Moisture damage susceptibility of asphalt mixtures
Experimental characterization and modelling

Varveri, Aikaterini (Katerina)

DOI
10.4233/uuid:9c25df0e-2df0-4d30-b9aa-d95a31fcaafd

Publication date
2017

Document Version
Final published version

Citation (APA)
Varveri, A. (2017). *Moisture damage susceptibility of asphalt mixtures: Experimental characterization and modelling*. [Dissertation (TU Delft), Delft University of Technology]. https://doi.org/10.4233/uuid:9c25df0e-2df0-4d30-b9aa-d95a31fcaafd

Moisture damage susceptibility of asphalt mixtures
-Experimental characterization and modelling-

Moisture damage susceptibility of asphalt mixtures
-Experimental characterization and modelling-

Proefschrift

ter verkrijging van de graad van doctor
aan de Technische Universiteit Delft,
op gezag van de Rector Magnificus prof. ir. K. C. A. M. Luyben,
voorzitter van het College voor Promoties,
in het openbaar te verdedigen
op vrijdag 17 maart 2017 om 10:00 uur

door

Aikaterini VARVERI

Master of Science in Civil Engineering
Aristotle University of Thessaloniki
geboren te Kavala, Griekenland.

This dissertation has been approved by the promotor:

Prof. dr. A. Scarpas

Composition of doctoral committee:

Rector Magnificus	Technische Universiteit Delft, chairperson
Prof. dr. A. Scarpas	Technische Universiteit Delft, promotor

Independent members:

Prof. dr. S. M. J. G. Erkens	Technische Universiteit Delft
Prof. dr. A. Bhasin	University of Texas at Austin
Prof. dr. G. Chehab	American University of Beirut
Prof. dr. B. Birgisson	Texas A&M University
Dr. X. Liu	Technische Universiteit Delft

Reserve member:

Prof. dr. C. Jommi	Technische Universiteit Delft

Rijkswaterstaat
Ministerie van Infrastructuur en Milieu

This research was financially supported by the Ministry of Infrastructure and Environment, Rijkswaterstaat.

Cover design: Vassiliki Dimaki and Michael Papadopoulos
Printed in the Netherlands by Ipskamp Drukkers

ISBN 978-94-92516-46-6
An electronic version of this dissertation is available at http://repository.tudelft.nl/.

to him,
who always stands by me.

to her,
who brought more joy to our life.

Acknowledgements

A lot of people contributed, in different ways, to this work. Though I have tried (and hopefully succeeded) to show my appreciation for their support over time, this is my opportunity to express my gratitude to them publicly.

I would like to thank my promotor, Prof. Tom Scarpas, for introducing me to the world of asphalt and giving me the opportunity to work with a team of talented researchers. Coming from a different scientific background, there were times in the start of my research that I felt lost, but Tom with his continuous support and encouragement helped me find my way and trusted me, sometimes more than I trusted myself.

I am also grateful to my committee members Prof. Sandra Erkens, Prof. Bjorn Birgisson, Prof. Amit Bhasin, Prof. Ghassan Chehab, Prof. Cristina Jommi, and Dr. Xueyan Liu for their time and effort. A very special thanks goes to Prof. Sandra Erkens for translating the summary and propositions into Dutch.

I want to thank my colleagues Alieh Alipour, Anupam Kumar, Cor Kasbergen, Greet Leegwater and former colleagues Alexander Schmets, Fani Lyrou, George Tzimiris, Jinlong Li, Mirella Villani, Santosh Srirangam and Sayeda Nahar for their company and encouragement during my PhD. It was a pleasure to work with you and share ideas and worries all these years. In particular, I want to thank Cor Kasbergen for standing me and for being eager to help, even in the late-night hours. Without his tremendous contribution the implementation of the model would not have been possible. I would also like to acknowledge the support of Prof. Niki Kringos. She was there in my first steps, and always cared about my progress and well-being. Your advice and encouragement have always been a source of inspiration to me. The secretaries and laboratory technicians of our section always provided a strong support network. I would like to thank Anneke Meijer and Jacqueline Barnhoorn for tackling the administration issues. I am also thankful to Jan-Willem Bientjes and Marco Poot for their willingness to help with my activities in the Stevin II Laboratory.

Friends have always played an important role in my life. My cherished friends back in Greece, Eletheuria, Christos, Giorgos, Nikos, Ilianna, Giorgos, Akis, and Roula supported me through this process and fill(-ed) my life with love and lots of good moments that help me through the hard days. I am so fortunate to have friends that I may not see in months, but every time we meet it feels like no day has passed by. I also want to express thanks to my “family” here in the Netherlands. Dimitri, Dora, Eirini, Gianni, Kimona, Lia, Niko, Petro, Strato, Tania, Tonia and Vangeli thank you for being there for me. Living away from home can be tough, but your friendship and support certainly made things easier! Special thanks to Stratos, Nikos and Petros for taking the time to proofread my thesis. Also, I am thankful to Vassiliki and Michael for designing the cover of this thesis.

My family has always been there for me throughout the years. I will always be indebted to my parents, Dimitris and Argyro, for raising me to become the person I am today and for their unconditional love and continuous support. I am grateful to my amazing sisters for their care and love; Vaso and Dimitra I cannot imagine my life without you. I also want to thank my in-laws and my

extended family for their encouragement and moral support. Αγαπημένοι μου, σας ευχαριστώ όλους από τα βάθη της καρδιάς μου!

There are no words to express my gratitude to my husband, Stavros. He has always been a source of love and happiness in my life. Thank you for growing together, for taking care of me, for believing in me, for being a wonderful partner in life and an incredible father to our daughter, Yro. You are both the joy of my life!

Katerina Varveri,

Delft, 15 December 2016

Ιθάκη

Σα βγεις στον πηγαιμό για την Ιθάκη,
να εύχεσαι νάναι μακρύς ο δρόμος,
γεμάτος περιπέτειες, γεμάτος γνώσεις.
Τους Λαιστρυγόνας και τους Κύκλωπας,
τον θυμωμένο Ποσειδώνα μη φοβάσαι,
τέτοια στον δρόμο σου ποτέ σου δεν θα βρεις,
αν μέν' η σκέψις σου υψηλή, αν εκλεκτή
συγκίνησις το πνεύμα και το σώμα σου αγγίζει.
Τους Λαιστρυγόνας και τους Κύκλωπας,
τον άγριο Ποσειδώνα δεν θα συναντήσεις,
αν δεν τους κουβανείς μες στην ψυχή σου,
αν η ψυχή σου δεν τους στήνει εμπρός σου.

Να εύχεσαι νάναι μακρύς ο δρόμος.
Πολλά τα καλοκαιρινά πρωιά να είναι
που με τι ευχαρίστησι, με τι χαρά
θα μπαίνεις σε λιμένας πρωτοειδωμένους·
να σταματήσεις σ' εμπορεία Φοινικικά,
και τες καλές πραγμάτειες ν' αποκτήσεις,
σεντέφια και κοράλλια, κεχριμπάρια κ' έβενους,
και ηδονικά μυρωδικά κάθε λογής,
όσο μπορείς πιο άφθονα ηδονικά μυρωδικά·
σε πόλεις Αιγυπτιακές πολλές να πας,
να μάθεις και να μάθεις απ' τους σπουδασμένους.

Πάντα στον νου σου νάχεις την Ιθάκη.
Το φθάσιμον εκεί είν' ο προορισμός σου.
Αλλά μη βιάζεις το ταξίδι διόλου.
Καλλίτερα χρόνια πολλά να διαρκέσει·
και γέρος πια ν' αράξεις στο νησί,
πλούσιος με όσα κέρδισες στον δρόμο,
μη προσδοκώντας πλούτη να σε δώσει η Ιθάκη.

Η Ιθάκη σ' έδωσε τ' ωραίο ταξίδι.
Χωρίς αυτήν δεν θάβγαινες στον δρόμο.
Άλλα δεν έχει να σε δώσει πια.

Κι αν πτωχική την βρεις, η Ιθάκη δεν σε γέλασε.
Έτσι σοφός που έγινες, με τόση πείρα,
ήδη θα το κατάλαβες η Ιθάκες τι σημαίνουν.

Κωνσταντίνος Καβάφης, Αλεξάνδρεια 1911

Ithaca

As you set out for Ithaca
hope your road is a long one,
full of adventure, full of discovery.
The Laestrygonians, the Cyclops,
fierce Poseidon-don't be afraid of them:
you'll never find things like that on your way
if you keep your thoughts raised high, if rare
excitement stirs your spirit and your body.
The Laestrygonians, the Cyclops,
wild Poseidon-you won't encounter them
unless you bring them along inside your soul, unless
your soul sets them up in front of you.

Hope your road is a long one.
May there be many summer mornings when,
with what pleasure, what joy,
you enter harbors you're seeing for the first time;
may you stop at Phoenician trading stations
to buy fine things,
mother of pearl and coral, amber and ebony,
sensual perfume of every kind
as many sensual perfumes as you can;
and may you visit many Egyptian cities
to learn and go on learning from their scholars.

Keep Ithaca always in your mind.
Arriving there is what you're destined for.
But don't hurry the journey at all.
Better if it lasts for years,
so that you're old by the time you reach the island,
wealthy with all you've gained on the way, not
expecting Ithaca to make you rich.

Ithaca gave you the marvelous journey.
Without her you wouldn't have set out.
She has nothing left to give you now.

And if you find her poor, Ithaca won't have fooled you.
Wise as you will have become, so full of experience,
you will have understood by then what these Ithacas
mean.

Konstantinos Kavafis, Alexandria 1911

Contents

1

Introduction

"The beginning is the most important part of the work."

— Plato (428 BC-348 BC)

The main purpose of this chapter is to provide the reader with the theoretical background of moisture-induced damage in asphalt pavements and show the significance of the research topic. In addition, Chapter one states the objectives of this research work and provides the outline of the thesis.

1.1 Moisture damage susceptibility of asphalt mixtures

The planning, design and construction of sustainable highway infrastructure is of vital importance, as it ensures the mobility of people and eases the transport of goods, while promoting economic and environmental sustainability, which will ultimately affect its social sustainability, considering the importance of a well-functioning and safe infrastructure network.

The development of sustainable highway infrastructure requires, among others, the construction of asphalt pavements with enhanced durability characteristics. From the moment of construction and during their service life, asphalt pavements are continuously exposed to a combination of traffic loading and environmental influences. Environmental conditions such as fluctuating temperature, humidity, precipitation, oxygen, freeze-thaw cycles and ultraviolet radiation constantly degrade the material properties and affect the performance of asphalt pavements. As a result, an increase in operational and maintenance costs is needed in order to fulfill the expected service life of the pavement system. Moreover, global warming and climate change events such as temperature extremes, high mean precipitation and rainfall intensity may further increase the probability and rate of pavement deterioration. There is thus a strong need to obtain an improved understanding of the influence of environmental factors on the long term performance of asphalt pavements.

Of all possible damages, moisture has been identified as an important contributor to various forms of damage such as ravelling, rutting and cracking. The intrusion of water into asphalt pavements is associated with their reduced performance, unexpected failures and shortened service life. As illustrated in Figure 1.1, water can accumulate in asphalt pavements due to a number of reasons (Kandhal 1992).

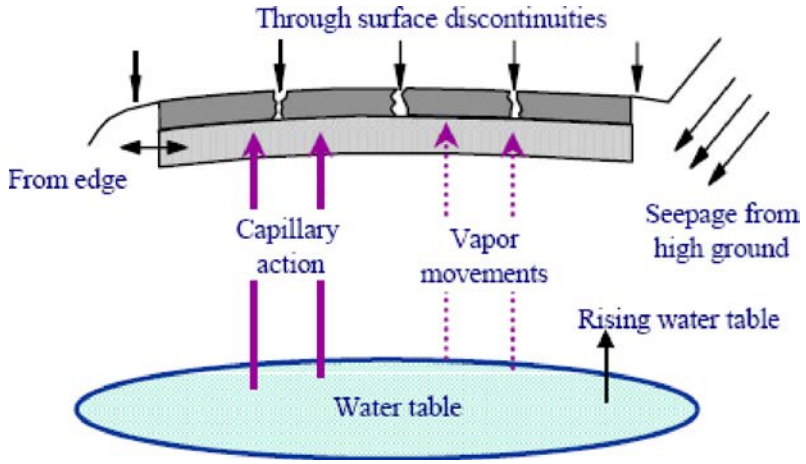

Figure 1.1. Sources of moisture in pavement structures (after Christopher et al. 2006).

The most common source is atmospheric precipitation, which supplies water in the form of rainfall, snow, hail, mist or dew. Water enters the body of the pavement through its surface discontinuities. Specifically the air voids and cracks in the surface of a pavement, the shoulder edges, as well as the joints formed between adjacent asphalt mats during construction provide easy access paths for surface water. Alternatively, water can enter into pavement structures due to

capillary action, water vapour movement or upward flow from a high groundwater table or an artesian aquifer. In the case of open graded pavements (also named drainage or silent asphalt pavements) the top mixtures are designed to have high levels of interconnected air voids to enable fast drainage of the surface water.

As soon as water enters in asphalt pavements a combination of physical, chemical, thermodynamic and mechanical processes (Caro et al. 2008, Kringos et al. 2008) occur during the interaction of water with the asphalt constituents. A great number of factors such as: the physico-chemical properties of bitumen and aggregates and their interaction, the mixture characteristics (percentage, size and interconnectivity of air voids and hence permeability), the type of traffic loading as well as the quality control during construction can influence the susceptibility of a mixture to moisture damage. The variability of the abovementioned factors introduces a high level of complexity to the problem and causes additional difficulties in predicting and preventing moisture induced damage in asphalt pavements. In the following section, the mechanisms related to moisture induced damage are discussed.

1.2 Mechanisms associated to moisture damage

Moisture damage in asphalt pavements is primarily observable through the loss of aggregates (commonly referred to as stripping or ravelling) and the appearance of potholes on their surface. Even though the failure of adhesion between different pavement layers due to moisture infiltration can also be a cause of pothole creation, potholes can also be attributed to the loss of bond between the mineral aggregate and the asphalt binder (i.e. bitumen plus mineral filler) and/or the loss of strength and stiffness of the mastic itself (Kiggundu & Roberts 1988). These modes of disintegration are often referred to as adhesive and cohesive failure, respectively. Figure 1.2 illustrates the effect that water can have on pavement wearing courses.

Figure 1.2. Deteriorated pavements due to water induced damage: (a) ravelling caused by segregation; (b) and (c) pothole formation (reprinted from Pavement Interactive http://www.pavementinteractive.org/).

In literature, five mechanisms are proposed in an attempt to explain moisture damage: detachment, displacement, spontaneous emulsification, hydraulic scouring and pore pressure development. Majidzadeh and Brovold (1968) define *detachment* as the separation of the bituminous film of the aggregate surface due to the presence of water assuming a continuous film without the presence of cracks. In this case, the existence of moisture in the interface can be only attributed to the molecular process of *diffusion* (Cheng et al. 2003). When a bituminous film is exposed to a moist environment, moisture gradually starts infiltrating through the film towards the adhesive interface zone. Depending on the moisture diffusion characteristics and the thickness of the bituminous film, the amount of moisture in the interface varies with time. Once moisture reaches the interface, it will progressively cause stripping of the asphalt binder from the aggregate. A schematic of the diffusion process is shown in Figure 1.3. An additional mechanism, which also results in separation of the binder film from the aggregate, is *displacement* (Tarrer & Wagh 1991) that in contrast to detachment, involves disruption in the bituminous film.

According to Stuart (1990) and Labib (1992) *spontaneous emulsification* is identified as a moisture damage mechanism for asphalt mixtures. Typically spontaneous emulsification occurs when two immiscible liquids emulsify without the aid of any external thermal or mechanical energy source (Lopez-Mantilla et al. 2002). Depending on the nature of the liquids involved, it may take from a few minutes to several days for the process to complete. Davies and Rideal (1963) discussed three mechanisms by which spontaneous emulsification can be produced i.e. interfacial turbulence, negative interfacial tension and 'diffusion and stranding'. According to diffusion theory, during the diffusion process regions of local supersaturation are produced and emulsion droplets are formed due to phase transformation at those regions. For asphalt mixtures, it has been observed that long conditioning periods can cause emulsification at the surfaces of the samples, which are in direct contact with water. In this case, water diffuses into the asphalt sample, weakens the binder and forms water-bitumen emulsions for asphalt binders that are unstable in water.

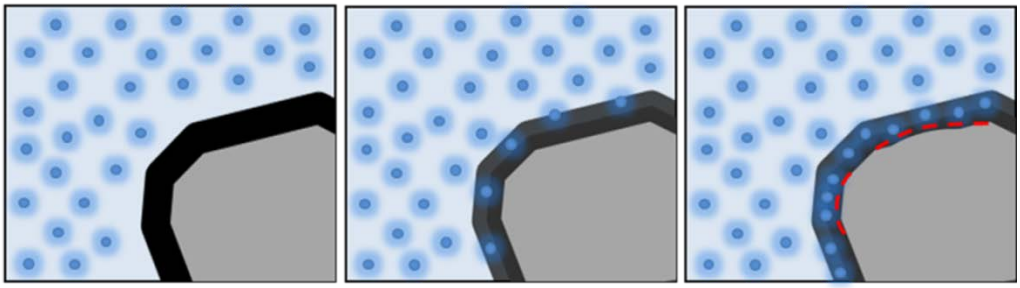

Figure 1.3. Damage of the asphalt binder and the binder-aggregate interface due to moisture diffusion (after Varveri et al. 2014).

Hydraulic scouring is identified as an additional water damage mechanism. The action of a vehicle tire over a saturated pavement can cause abrasion of the asphalt binder from the aggregates, resulting in fine aggregates to become loose and ultimately dislodge from the pavement. This mechanical scraping can be aggravated by the presence of abrasives, such as dust, on the surface of the pavement (Asphalt Institute 1987). Unlike hydraulic scouring, which is a phenomenon that occurs at the pavement surface, the repeated action of traffic loading over a saturated pavement can

result to excessive *pore pressure* build up in the macro pores or to internal erosion of the binder due to the presence of water flow depending on the drainage conditions. The latter process is also mentioned as desorption and was modeled by Kringos et al. (2008) using an advective transport model.

Generally it is assumed that the permeability of a pavement is proportionally related to its air void content. Past studies by Choubane et al. (1997), Cooley et al. (2001) and Chen et al. (2004), in which falling head permeability tests on dense and open graded asphalt mixtures were performed, demonstrated that in every case an exponential relationship exists between permeability and air void content. Though, in reality, permeability is also affected by other factors such as aggregate gradation and shape, lift thickness, density homogeneity, and compaction method (Mallick et al. 2003, Caro et al. 2008), it has been shown that the air void content has a strong effect on permeability and thus on the susceptibility of asphalt mixtures to water damage. As a result, the design of a mixture and consequently its permeability characteristics dictates the occurrence of either pressure development or binder erosion. In the undrained case, at which water is entrapped in the air void network of the pavement, water will dilate and contract, due to the incompressibility of the liquid, under the effect of dynamic traffic loading and will encourage high pressures in the saturated pores which may cause additional stresses in the material. The process of pore pressure build up will ultimately lead to cracking of the binder film or the growth of micro cracks in the asphalt mixture, facilitating thus the ingression of water to the asphalt binder-aggregate interface, as shown in Figure 1.4. In literature, this phenomenon is referred to as *pumping action* (Taylor et al. 1983, Kiggundu & Roberts 1988, Kandhal 1992). On the other hand, high permeable pavements have a high percentage of air voids which are interconnected and allow water to flow through the pore network. The design of pavements with high permeability ensures the reduction of surface runoff and improves driving safety. However, the action of fast water flow through the interconnected pores may create an *erosion* effect due to the high water pressure gradients against the binder film (Kringos et al. 2008).

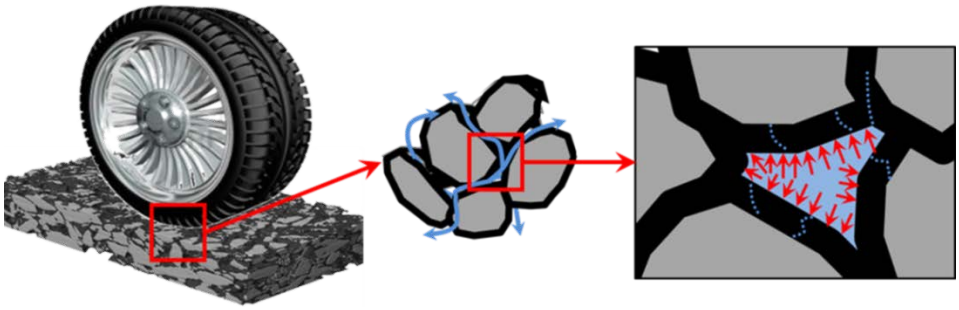

Figure 1.4. Cracking of the asphalt binder due to pumping action (after Varveri et al. 2014).

Though pumping action could often be related to mixtures with non-connected air voids, one can also consider that open graded mixtures that originally start with well-connected voids, will eventually clog with dirt from the pavement surface, thus increasing the risk of trapped water. Open graded mixtures can, therefore, first be exposed to a dominant erosion issue, followed by a pumping action challenge over time when their permeability reduces.

Moreover, frost damage may occur when water is present in the voids and micro-cracks in the top layers of a pavement or even at the interface between pavement layers and, at the same time, sub-zero temperatures are sustained during winter. Frost damage is the result of volume expansion due to the phase change of water into ice crystals. The expanded ice crystals impose additional internal stresses to the mixture, which can be detrimental to pavements. The magnitude of expansion, and consequently the extent of the resulting stresses and strains, depends on the degree of saturation (Mauduit et al. 2010).

From the above, it can be presumed that depending on the traffic loading and environmental conditions, as well as the binder and aggregate characteristics and mixture type, one moisture related damage mechanism or a combination thereof can lead to adhesive or cohesive failure. Adhesion is defined as the attraction process between unlike molecules that are brought into contact in such way that the adhesive binds to the applied surface or substrate. In contrast, cohesion is the attraction between similar molecules, mainly as the result of chemical bonds that are formed between the individual components of the substance. Thus, in bituminous mixtures cohesion may be defined as the internal strength of the asphalt binder due to various interactions that keep the mass together, whereas adhesion is the bonding of the mineral aggregate with the asphalt binder due to a number of interactions at the aggregate-binder interface.

In the presence of water, asphalt binder cohesion and binder-aggregate adhesion are adversely affected resulting to the distinct failure modes, as shown schematically in Figure 1.5. Considering that the load-carrying capacity of the mixture comes from the aggregate skeleton and the ability for the mixture to dampen the traffic loads comes from the mastic matrix, the adhesive and cohesive bonds are equally important and should be maintained at a high quality for as long as possible.

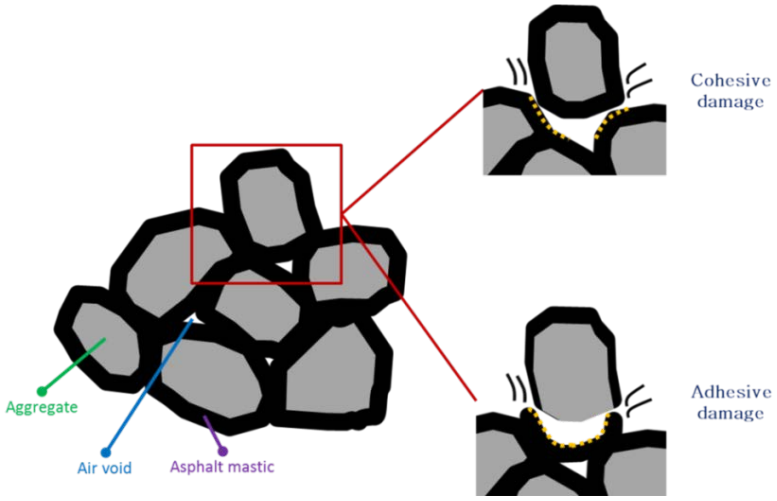

Figure 1.5. Adhesive and cohesive failure due to water damage.

According to Terrel and Shute (1989) four main theories exist to fundamentally describe adhesive bonding and failure between aggregates and asphalt binders, namely the chemical bonding (Kiggundu & Roberts 1988, Tarrer & Wang 1991), the molecular orientation (Hicks 1991, van Lent 2013), the thermodynamic (Cheng et al. 2002, Little & Jones 2003, Lytton et al. 2005, Masad et al. 2006, Bhasin & Little 2007, Fischer et al. 2012) and the mechanical theory (Hefer & Little 2005).

Also, the weak boundary layer theory (Bikerman 1967, Packham 1992) is used to describe poor adhesion in aggregate-bitumen systems.

On the other hand, cohesion failure refers to failure within the asphalt binder itself due to the interaction with water or moisture. Cohesion is defined as the internal strength of the binder due to the intermolecular forces between similar molecules and is influenced by the binder's rheological properties. Moisture enters into the binder film through diffusion and due to physico-chemical interactions softens the binder and therefore reduces its cohesive strength and stiffness (Hicks 1991). Cohesive failure can also occur due to spontaneous emulsification and expansion of the void system due to saturation (Stuart 1990). Additionally, the weakening of the binder due to moisture, alters its desorption characteristics and can actually assist the erosion effect due to fast water flow, sometimes referred to as dispersion of the binder (Kringos et al. 2008).

The occurrence of adhesive or cohesive failure strongly depends on the film thickness of the bitumen surrounding the aggregates (Marek & Hennin 1968, Lytton 2004). A thinner bituminous film results in lower adhesive strength, increasing the probability that the failure occurs in the binder-aggregate interface. A relation between the tensile strength of bitumen and the adhesive bond strength of the bitumen-aggregate interface with film thickness was established. Figure 1.6 shows that for thicker bitumen films the cohesive strength is lower than the adhesive strength.

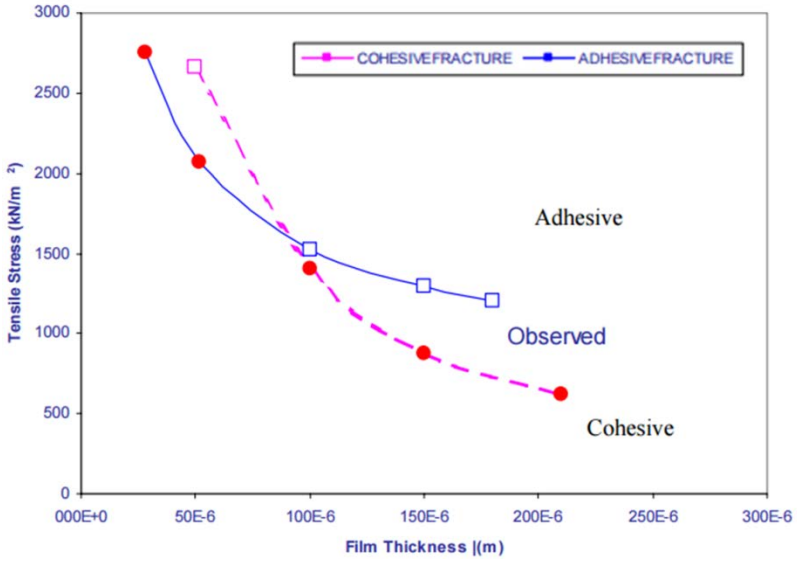

Figure 1.6. Adhesive and cohesive tensile strength versus binder film thickness (after Lytton 2004).

1.3 Experience with moisture damage in the Netherlands

An improved understanding of moisture induced damage phenomena in asphalt pavements can have a significant impact on road maintenance expenditure, particularly in countries that suffer from large amounts of rainfall, such as the Netherlands, as shown in Figure 1.7. Even though a logical step to mitigate moisture induced damage might be to avoid the infiltration of water using

dense mixtures with low air void content, there are mixtures that are in fact designed to lead the water through the pavement such as porous asphalt, which must retain a large content of air voids, approximately 20% to 25% by volume.

Since the early 1990s, porous asphalt mixtures (ZOAB: Zeer Open Asfalt Beton) were applied across the highway network in the Netherlands mainly due to policy changes with respect to noise reduction (Goubert et al. 2005), and at present over 80% of highways have porous asphalt as a wearing course. The use of porous asphalt entails several benefits, especially during wet seasons, including the reduction of hydroplaning and "splash and spray" effects and better quality of the runoff water. However, it has been realized that the use of porous asphalt is associated with reduced lifetimes and high maintenance costs. The average lifetime of porous asphalt is about 11 years in the right-hand lane and 17 years in the other traffic lanes, which is relatively shorter than the lifetime of dense asphalt.

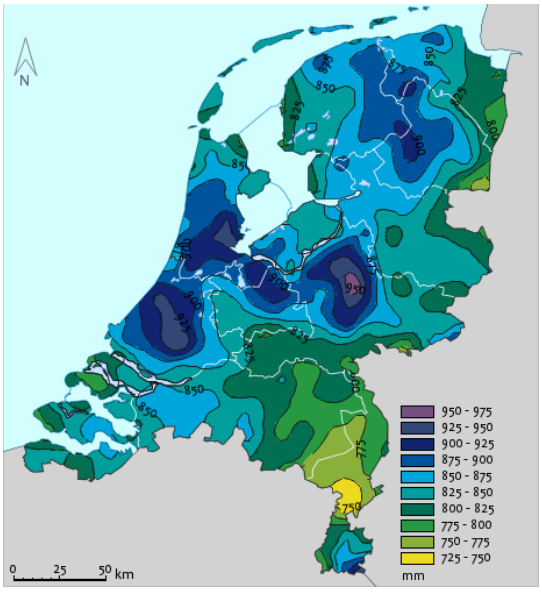

Figure 1.7. Long-term average annual rainfall (1981-2010).

The most common distress of porous asphalt is the loss of aggregates from the pavement surface named ravelling (Klomp 1996). Premature ravelling occurs in porous asphalt pavements primarily due to their open structure, which facilitates oxygen and water to access the pavement, thus degrading its material properties and decreasing its durability. Currently, in the Netherlands, the practices used to prevent moisture damage of porous asphalt pavements are restricted to the addition of calcium hydroxide and calcium carbonate fillers to the mixture, which is part of the standard ZOAB mix design (the use of liquid anti-stripping agents is not allowed). Apart from the continuous weakening effect of moisture on porous asphalt pavements, in the winter of 1998, a combination of moisture and low temperatures resulted to immense damage in the highway network, due to frost damage. A series of winters (2009, 2010) with several freeze-thaw cycles and overnight temperatures below zero, after that, lead to an interest in the additional effects of frost damage combined with moisture.

In Netherlands, which is a densely populated country, the use of porous asphalt in the road network is essential, mainly due to its excellent acoustic properties. It is, therefore, a priority to enhance the durability of porous asphalt pavements, while maintaining those characteristics that impart the desired acoustic and drainage properties to the material.

1.4 Research objectives

Even though the mechanisms related to moisture damage were identified in the early 1970s, they are today still not understood to the extent that we have been able to mitigate the problem. Current moisture damage evaluation methods for asphalt mixtures are still primarily based on empirical test methods and pavement engineers today do not have many new tools to assist them in mitigating moisture damage or to make accurate moisture damage predictions. In practice, some additives, e.g. hydrated lime and amines, have been used in the production of asphalt mixtures to minimize moisture damage related distresses. In the recent past, however, several new test methods and computational models were developed to characterize and predict moisture sensitivity of asphalt mixtures, based on fundamental and theoretical mechanisms, albeit not many of them are in fact used in daily engineering applications. It is, therefore, crucial for modern pavement engineers to understand the basic mechanisms in which moisture infiltrates and degrades the material components and ultimately the structural response of the pavement, both over short- and long-term periods. For this reason, the research community should focus on the proper explanation of new models, the potentially required new test methods and how to embed these in the current state-of-the- practice.

The scope of this thesis is to acquire an advanced understanding of the fundamental moisture damage processes. Based on this, a set of tools, i.e. experimental methods and computational models, are developed that can enable the optimization of the design of durable materials and the enhanced prediction of the durability characteristics of asphalt pavements. To this end, this research pursues the following objectives:

- investigate the effect of prolonged moisture conditioning on the cohesive characteristics of asphalt mortar;
- develop a moisture conditioning protocol that enables the quantification of long- and short-term moisture damage degradation mechanisms;
- formulate a computational algorithm to model moisture induced damage in asphalt mixtures and investigate the influence of mixture morphology and material properties on the mechanical performance of mixtures subjected to moisture diffusion;
- formulate a physical model that simulates the water-to-ice phase change driven expansion in asphalt mixtures.

1.5 Thesis outline

This dissertation consists of eight chapters that intend to cover the most fundamental aspects of moisture damage in asphalt mixtures. This *introductory chapter* highlights the great interest on

moisture-induced damage, describes the basic moisture damage processes, states the objectives of this research work and provides the outline of this thesis. A pertinent literature review is provided in the start of each chapter according to the corresponding topic treated in the chapter.

The *second chapter* provides an overview of the main parameters that influence moisture diffusion in asphalt mixtures. Moreover, the mathematics of modelling moisture diffusion are presented and formulated in a form that is appropriate for implementation using the finite element method.

The *third chapter* aims to investigate the effect of moisture on the cohesive strength of asphalt mortar. Mortar samples were prepared and then subjected to various combinations of moisture and thermal conditioning, before being tested in uniaxial tension. A detailed description of the sample geometry, testing setup and conditions, as well as the sample preparation protocol is included. A total of five conditioning protocols are employed in an attempt to reproduce various conditioning states that pavements undergo in the field. The changes in the mechanical properties of the mortar samples due to the various conditioning scenarios are evaluated using their tensile strength and fracture energy. Also, a new data analysis procedure is presented in order to obtain a more accurate calculation of fracture energy.

The *fourth chapter* focuses on quantifying the contributions of long- and short-term moisture damage to strength degradation of asphalt mixtures. A moisture conditioning protocol, which comprises two conditioning types, namely bath immersion and pore pressure application, is introduced. Subsequently, the effect of conditioning regime and exposure time, aggregate and binder type on the response degradation of the mixtures is evaluated. The last section of the chapter focuses on the investigation of the cyclic pore pressure mechanism. Computed tomography and image analysis techniques are employed to characterize damage due to dynamic pore pressure.

The *fifth chapter* is dedicated to the mathematical formulation of a finite element model, which simulates damage due to moisture infiltration, at micromechanical level. The three-dimensional energy-based elasto-visco-plastic model with softening due to moisture-mechanical damage introduces material damage as an internal state variable, which represents the irreversible physical processes within the microstructure of the material. In this chapter, the mathematical details of the damage model in addition to the numerical methodology followed for its implementation are provided. More information on the mathematical derivations of this chapter can be found in the appendices.

Chapter six studies the effect of mixture morphology on moisture sensitivity. To this end, finite element analysis is performed in a staggered scheme: first the moisture diffusion model, presented in Chapter two, is used to obtain the moisture profiles within the asphalt samples and then the elasto-visco-plastic model with softening due to moisture-mechanical damage, described in Chapter five, is used to investigate the influence and interconnectivity of air voids to moisture sensitivity of the mixtures. The analysis is carried out for a porous and a dense sample and the simulations were performed on 3D finite element meshes obtained via X-ray Computed Tomography scans.

Considering that frost damage is part of the moisture damage related mechanisms, *chapter seven* describes an energy-based micromechanical model for simulation of volume expansion that occurs during the water-to-ice phase change in the macro pores of an asphalt pavement. The phase-

change model is loosely coupled with a thermal conduction model. Again, the effect of air voids and pore connectivity on the asphalt binder damage, due to the volume change of water-to-ice in the pores, is investigated.

Finally, *chapter eight* concludes this thesis by providing a brief summary of results and conclusions and gives an outlook for potential use and further developments of the proposed experimental methods and computational tools.

1.6 References

Asphalt Institute (1987). Cause and Prevention of Stripping in Asphalt Pavements. Educational Series No.10 (ES-10) Second Edition, Maryland, U.S.A.

Bikerman J. J. (1967). Causes of poor adhesion. *Journal of Industrial & Engineering Chemistry,* 59:9, 40–44.

Bhasin, A. & Little, D. N. (2007). Characterization of aggregate surface energy using the universal sorption device. *Journal of Materials in Civil Engineering*, 19, 634–641.

Caro, S., Masad, E., Bhasin, A. & Little, D. N. (2008a). Moisture susceptibility of asphalt mixtures, part 1: mechanisms. *International Journal of Pavement Engineering,* 9:2, 81-98.

Chen, J. S., Lin, K. Y. & Young, S. Y. (2004). Effects of crack width and permeability on moisture-induced damage of pavements, *Journal of Materials in Civil Engineering*, 16:3: 276-282.

Cheng, D., Little, D. N., Lytton, R. L. & Holste, J. C. (2002). Use of surface free energy properties of the asphalt-aggregate system to predict damage potential. *Journal of the Association of Asphalt Paving Technologists*, 71, 59-88.

Cheng, D., Little, D. N., Lytton, R. L. & Holste, J. C. (2003). Moisture damage evaluation of asphalt mixtures by considering both moisture diffusion and repeated-load conditions. *Transportation Research Record: Journal of the Transportation Research Board*, 1832, 42-49.

Choubane, B., Page, G. C. & Musselman, J. A. (1997). Investigation of water permeability of coarse graded Superpave pavements. Research report FL/DOT/SMO/97-416, Florida Department of Transportation.

Christopher, B. R., Schwartz, C. & Boudreau, R. (2006). Geotechnical Aspects of Pavements. National Highway Institute, Federal Highway Administration, Washington, D.C.

Cooley Jr., L. A., Brown, E. R. and Maghsoodloo, S. (2001). Development of critical field permeability and pavement density values for coarse-graded Superpave pavements. Report 01-03, National Center for Asphalt Technology, Auburn University, Alabama.

Davies, J. T. & Rideal, E. K. (1963). Interfacial Phenomena. Academic Press, New York.

Fischer, H. R., Dillingh, E. C. & Hermse, C. G. M. (2012). On the interfacial interaction between bituminous binders and mineral surfaces as present in asphalt mixtures. *Applied Surface Science*, 265, 495–499.

Goubert, L., Hooghwerff, J., The, P. & Hofman, R. (2005). Two-layer porous asphalt: an international survey in the frame of the Noise Innovation Programme (IPG). 34th INTER-NOISE congress.

Hefer, A. & Little, D. N. (2005). Adhesion in bitumen-aggregate systems and quantification of the effects of water on the adhesive bond. Report ICAR/505-1; Texas Transportation Institute; Texas A&M University System, College Station, Texas, USA.

Hicks, R. G. (1991). Moisture Damage in Asphalt Concrete. NCHRP Synthesis of Highway Practice 175, TRB, National Research Council, Washington, D.C.

Kandhal, P. S. (1992). Moisture susceptibility of HMA mixes: Identification of problem and recommended solutions. Report 92-01, National Center for Asphalt Technology, Auburn University, Alabama.

Kiggundu, B. M. & Roberts, F. L. (1988). Stripping in HMA mixtures: state-of-the-art and critical review of test methods. Report 88-02, National Center for Asphalt Technology, Auburn University, Alabama.

Klomp A. J. G. (1996). Life period of porous asphalt. Dutch Road and Hydraulic Engineering Institute report.

Kringos, N., Scarpas, A., Kasbergen, C. & Selvadurai, P. (2008). Modelling of combined physical mechanical moisture-induced damage in asphaltic mixes, part 1: Governing processes and formulations. *International Journal of Pavement Engineering*, 9:2, 115-118.

Labib, M. E. (1992). Asphalt–aggregate interactions and mechanisms for water stripping. *American chemical society division of fuel chemistry*, 37, 1472–1481.

Little, D. N. & Jones, D. R. (2003). Chemical and mechanical processes of moisture damage in hot-mix asphalt pavements. Proceedings of the Moisture Sensitivity of Asphalt Pavements –A National Seminar, California.

López-Montilla, J. C., Herrera-Morales, P. E., Pandey, S. & Shah, D. O. (2002). Spontaneous Emulsification: Mechanisms, Physicochemical Aspects, Modeling and Applications. *Journal of Dispersion Science and Technology*, 23:1-3, 219-268.

Lytton, R. L. (2004). *Adhesive fracture in asphalt concrete mixtures*. Course Notes.

Lytton, R. L., Masad, E. A., Zollinger, C., Bulut, R. & Little, D. N. (2005). Measurements of surface energy and its relationship to moisture damage. Technical Report No. TX-05/0-4524-2, Texas A&M Transportation Institute, College Station, Texas.

Majidzadeh, K. & Brovold, F. N. (1968). Special report 98: State of the art: Effect of water on bitumen-aggregate mixtures. Highway Research Board, National Research Council, National Academy of Sciences and National Academy of Engineering, Washington D.C.

Mallick, R. B., Cooley, Jr., L. A., Teto, M. R., Bradbury, R. L. & Peabody, D. (2003). An evaluation of factors affecting permeability of Superpave designed pavements. Report 03-02, National Center for Asphalt Technology, Auburn University, Alabama.

Marek, C.R. & Herrin, M. (1968). Tensile behavior and failure characteristics of asphalt cements in thin films. Proceedings of Association of Asphalt Paving Technologists, 37, 1-54.

Masad, E., Zollinger, C., Bulut, R., Little, D. N. & Lytton, R. L. (2006). Characterization of HMA moisture damage using surface energy and fracture properties. *Journal of the Association of Asphalt Paving Technologists*, 75, 713-754.

Mauduit, C., Hammoum, F., Piau, J. M., Mauduit, V., Ludwig, S. & Hamon, D. (2010). Quantifying expansion effects induced by freeze-thaw cycles in partially water saturated bituminous mix. Road Materials and Pavement Design, 11:1, 443-457.

Packham, D. E. (1992). Handbook of adhesion. London: Longman Group, UK.

Stuart, K. D. (1990). Moisture damage in highway mixtures - a state of the art report. FHWA-RA-90-019, Washington, D.C.

Tarrer, A. R. & Wagh, V. (1991). The effect of the physical and chemical characteristics of the aggregate on bonding. Strategic Highway Research Program, National Research Council, Washington, D.C.

Taylor, M. A. & Khosla, N. P. (1983). Stripping of Asphalt Pavements: State-of-the-Art. *Transportation Research Record: Journal of the Transportation Research Board,* 911.

Terrel, R. L. & Shute, J. W. (1989). Summary Report on Water Sensitivity. SHRP-A/IR-89-003, Strategic Highway Research Program, National Research Council, Washington, D.C.

van Lent, D. Q. (2013). Interfacial interactions and mass transfer at the interfacial region of bituminous hydrocarbon mixtures. Technische Universiteit Delft, Netherlands.

Varveri, A., Avgerinopoulos, S., Scarpas, A., Collop, A. & Erkens, S. (2014). On the combined effect of moisture diffusion and cyclic pore pressure generation in asphalt concrete. 93rd TRB Annual Meeting Compendium of Papers, No. 14-1195, Transportation Research Board, Washington, D.C.

Varveri, A., Zhu, J. & Kringos, N. (2015). *Moisture Damage in Asphaltic Mixtures* in "Advances in Asphalt Materials: Road and Pavement Construction". ISBN: 9780081002698. Cambridge: Woodhead Publishing Ltd, UK.

2

Moisture diffusion in bituminous mixtures

"Everything must be made as simple as possible. But not simpler."
— Albert Einstein (1879-1955)

Modelling of moisture diffusion is commonly performed to develop an understanding of the accumulation of moisture in asphaltic components and allow for predictions with respect to the degradation of mechanical performance when coupled with the appropriate mechanical-based damage computational models. Such a numerical scheme, which couples damage due to mechanical loading and moisture diffusion, is discussed later in Chapter six. An understanding of the moisture diffusion process in asphaltic materials is essential for designing reliable asphalt binders and selecting constituent materials for use in demanding environments. Furthermore, a better knowledge of diffusion is important for developing testing methodologies and accelerated moisture conditioning protocols for asphalt mixtures.

2.1 Introduction

Asphalt mixtures are highly heterogeneous materials that comprise aggregates, mastic (bitumen, filler plus fine minerals) and air voids. Moisture diffusion has been recognised as a key mechanism for degradation in bituminous systems. The ingress of moisture into the asphaltic components may affect the mechanical performance of the asphalt mixture and decrease the overall loading capacity of the pavement, having thus a critical effect on the service performance of pavement structures. As moisture diffuses into the mixture, the properties of the binder change causing a decrease in the cohesive strength and consequently, an overall reduction in the stiffness and strength of the pavement. Additionally, in the presence of moisture, the adhesive bond characteristics between the aggregate and binder change in time and the integrity of the bond diminishes, hence resulting in stripping of the aggregates from the asphalt mixture (Adamson 1982, Labib 1992, Hefer 2004, Lytton et al. 2005).

2.1.1 Factors affecting moisture diffusion

Moisture transport processes in asphalt mixtures are influenced by various parameters, including environment conditions such as temperature, physicochemical properties of the mixture constituents and mixture microstructure, namely air voids and their interconnectivity. In the following, the relationship of moisture diffusion with the aforementioned parameters is described.

Temperature

Temperature has a strong effect on the coefficients and rate of diffusion in solids. Molecular diffusion is the result of random motion of individual molecules. Normally, according to the kinetic molecular theory, a molecule will travel with constant velocity along a straight line until it collides with another molecule, which results in a change of its velocity (Averill & Eldredge 2007). With increasing temperature the diffusion rates may increase due to the higher velocity of the molecule. As a general rule diffusion is low at low temperatures, but can become significantly higher as temperature rises. In solids, the temperature dependence of the diffusion coefficient normally conforms to the Arrhenius equation

$$D(T) = D_o e^{-E_\alpha / RT} \quad [2.1]$$

In equation [2.1] D_o denotes the temperature independent pre-exponential factor ($m^2\ s^{-1}$), E_α the activation energy of the diffusion process (kJ mol^{-1}), R the universal gas constant (equal to 0.0083 kJ $mol^{-1}\ K^{-1}$) and T (K) the absolute temperature. Vasconcelos (2010) investigated the effect of temperature on moisture uptake and diffusion coefficients. Figure 2.1 illustrates the water uptake for all fine aggregate mixtures. Six combinations of asphalt binders and aggregates contain 8.9% (by weight) of asphalt binder, with air voids content from 7% to 11%, were conditioned in a distilled water bath at room temperature (23.9°C) and at 37.8°C (100°F) for 21 and 14 months, respectively.

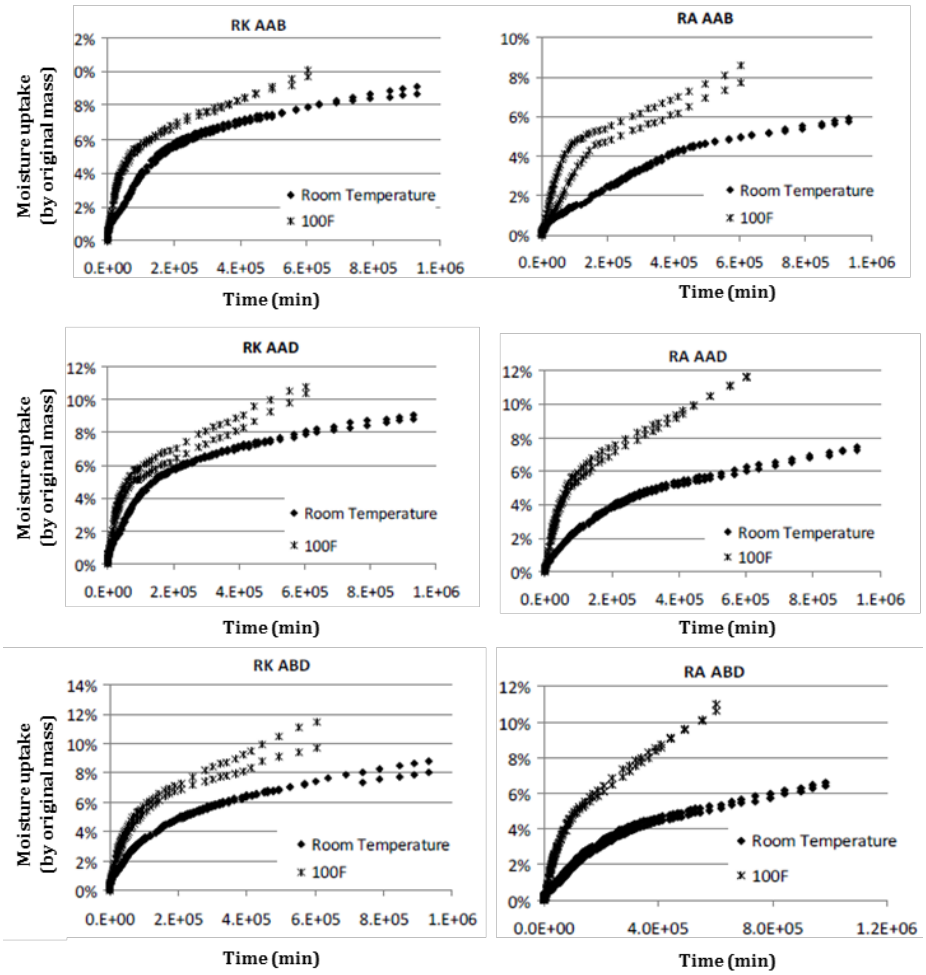

Figure 2.1. Effect of temperature on water uptake of fine aggregate mixtures (after Vasconcelos 2010).

Moreover, a dual mode diffusion model was used to determine the effective diffusivity of all samples at both temperatures. The average values are presented in Figure 2.2.

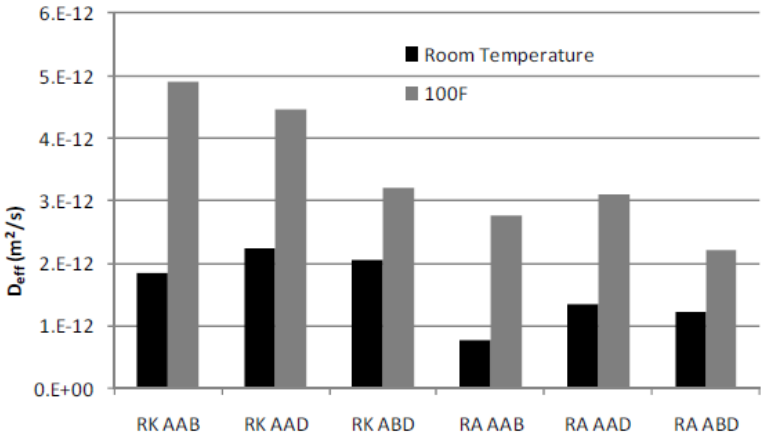

Figure 2.2. Effect of temperature on effective diffusivity of fine aggregate mixtures (after Vasconcelos 2010).

The results clearly show the influence of temperature on diffusion characteristics. Both the diffusion coefficient and moisture uptake were substantially greater at the higher temperature of 37.8°C than they were at room temperature. From the above, it can be deduced that there is an interrelation between temperature and moisture absorption. In the presence of a thermal gradient in an asphalt pavement, for example, the rate of moisture absorption can vary with location. Nevertheless, for typical applications of bituminous mixtures, heat conduction occurs faster than moisture diffusion, considering that the thermal diffusion coefficients of the mixtures have values of the order of 10^{-7} m^2/s (Apostolidis 2015), while moisture diffusion coefficients are of the order of 10^{-12} m^2/s (Kassem et al. 2006, Arambula et al. 2010, Kringos et al. 2008, Vasconcelos et al. 2011, Apeagyei et al. 2013). Consequently, temperature will reach an equilibrium state earlier than moisture concentration. This observation enables the numerical simulation of mass and energy transport phenomena independently.

Asphalt bitumen

Bitumen is a mixture of dissimilar hydrocarbon molecules, which may contain small amounts of heteroatoms like nitrogen, oxygen, sulphur, and trace metals (mainly nickel, vanadium and iron) (Read & Whiteoak 2003). The physicochemical characteristics of bitumen differ significantly depending on the crude oil origin and production process. Bitumen can be separated into chemical fractions using different separation techniques. A common technique is the SARA analysis, which separates the bitumen molecules into various fractions based upon their polarity. The fractions, based on their increase in molar mass, aromatic content and polarity, are saturates, aromatics, resins and asphaltenes (Lesueur 2009).

The chemical composition of bitumen will have a strong influence on the diffusion properties of moisture into bitumen, which can change further as asphalt binders (bitumen plus filler) are exposed to oxygen or ultraviolent radiation. Below, equation [2.7] shows that the rate of change of moisture concentration is proportional to the second derivative of concentration in space and the diffusion characteristics of the binders. In general, bitumen types with high polarity are expected to have a strong affinity to polar molecules, such as water. In contrast, water uptake will be lower for bitumen types with lower polarity. As a result, differences in the moisture diffusivity properties of bitumen can be anticipated, on the basis of the molecules that constitute their chemical composition.

Filler Particles

However, binder chemistry is not the only parameter that can influence moisture diffusivity. In practical applications, essentially every asphaltic material will contain filler particles and other additives, such as fibres, crumb rubber etc., introduced to modify their physical and handling properties. Filler particles are added to binder mixtures to increase their stiffness and consequently improve their fatigue life and resistance to permanent deformation (Kim et al. 2003, Faheem et al. 2008, Wang et al. 2011). Fibres are used to provide mechanical reinforcement (Wang et al. 2013), while rubber particles are used to enhance the binder's resistance to rutting, fatigue cracking and thermal cracking (Bahia & Davies 1994, Airey et al. 2003, Shen & Amirkhanian 2005).

Filler particles and additives can significantly influence the diffusion characteristics of binders. The presence of impermeable particles is a hindrance to diffusion and will reduce the moisture transport rates as the water molecules would need to travel around the particles, increasing thus the diffusion path lengths. In contrast, particles with higher diffusion coefficients, compared to those of bitumen, will facilitate the ingress of water into asphalt binders. The overall properties of the binders will, ultimately, depend on the concentration of the filler particles (or additives) and their diffusivity properties. Figure 2.3 shows the effect of filler type and content on the diffusivity of asphalt mastics. An increase in filler content is shown to increase the rate of moisture diffusion, while the filler type has a major impact on the overall diffusivity of the mastics.

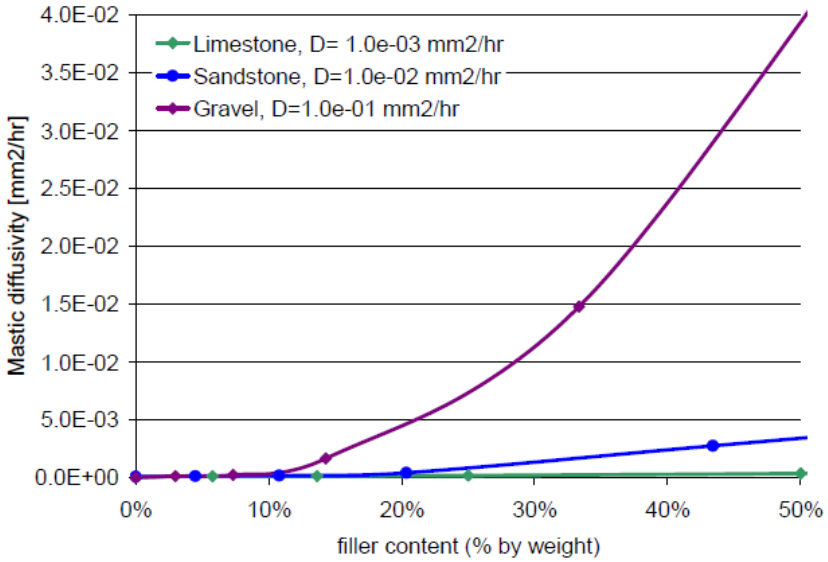

Figure 2.3. Mastic diffusivity as function of filler content and type (after Kringos 2007).

Aggregates

The influence of aggregate type on the creation of adhesive bond between binder and aggregate, as well as the effect of moisture on bond degradation, has been extensively studied in the past (Curtis 1992, Cheng et al. 2002, Hefer 2004, Hefer 2005, Copeland 2007, Bhasin & Little 2007, Fischer 2012, Cui et al. 2014). In addition to the physicochemical properties of mineral aggregates that dictate adhesion in bituminous systems, their mineralogical and microstructural characteristics, i.e. porosity and pore size, significantly influence diffusion and moisture transport processes into asphalt mixtures.

The diffusion coefficients of moisture for various types of aggregates were determined and are shown in Table 2.1. The results show the great influence of the aggregate nature and origin on the diffusion coefficients of moisture. Similarly, it is evident that the test methods and the selected diffusion species used for the experiments cause a great variability of the values for the same aggregate types (Arambula et al. 2010).

Table 2.1. Diffusion coefficients for various aggregate types (adapted from Arambula et al. 2010).

Reference	Aggregate type	Diffusion coefficient [mm²/hr]	Test method
Bradbury et al. (1982)	Ossian granite	5.04×10^{-3}	Used potassium iodine solution at ambient temperature.
	Scottish granite	1.44×10^{-3}	
Hénon et al. (2002)	Dolomitican marble	2.91×10^{2}	Average effective water vapor diffusivities.
	Pietra Serena sandstone	1.92×10^{3}	
	Pietra de Lecce limestone	6.73×10^{3}	
Jirickova & Cerny (2002)	Rock wool	1.04×10^{4}	Standard wet cup method on rock wool made of limestone, basalt, and coke at 20°C.
Dobchuck et al. (2014)	Montana waste rock	8.5×10^{4}	Average coefficient measured using a diffusion column at 24.5°C.
Kodikara & Chakrabarti (2005)	Basaltic rock	1.25×10^{-1} through $8.33\times10-^{1}$	Value at the oven-dry condition.
Kringos et al. (2008)	Norway sandstone	7.20×10^{-1}	Gravimetric method on specimens submerged in water at 18°C for 150 h.
	Scottish granite	4.40×10^{-1}	
Valkiainen et al. (1996)	Rapakivi granite	6.12×10^{-4} through 9.00×10^{-4}	Effective diffusion coefficient estimated using sodium chloride solution with tritium and anionic Cl as tracers.
Witthüser et al. (2006)	India granite	2.88×10^{-2}	Average effective diffusion coefficient estimated using strontium chloride at 26°C and 50% RH.
	Denmark chalk	4.23×10^{-1}	
	Israel chalk	2.39×10^{-1}	
Yokoyama & Nakashima (2005)	Kozushima rhyolite rock	3.20×10^{-2}	Average effective diffusion coefficient in the vertical direction using a potassium chloride solution.
Arambula et al. (2010)	Limestone	8.82×10^{-1}	Periodic weight measurements of samples conditioned at 35°C and 15% RH for 40 days.
	Sandstone	6.03×10^{-1}	
Cui et al. (2014)	Limestone	7.54×10^{-1}	Periodic weight measurement of samples conditioned at 20°C in liquid water for up to 14 days.
	Marble	5.04×10^{-2}	
	Granite-1	2.79×10^{-5}	
	Granite-2	1.08×10^{-6}	

Air voids

The presence of air voids in an asphalt mixture facilitates the ingress of oxygen and water (or moisture) into the pavement structure. The air voids offer space into which bulk water can easily flow and moisture molecules can move faster, as molecular diffusion progresses faster in gases rather than in liquids or solids. A high air void content is translated into greater connectivity among the voids, and consequently to high permeable pavements. The latter ensures rapid water infiltration, thus causing an acceleration of moisture damage occurrence. Denser mixtures, with lower void content, have more isolated pores, leading to substantially slower diffusion rates of moisture into the pavements, as the effective diffusion coefficient of the mixture decreases. Specifically, the air void content and void radius influence significantly the overall diffusivity of asphalt mixtures (Kassem et al. 2009). It has to be noted that it is the connectivity of the air void phase that dictates the diffusion rates in asphalt pavements, as discussed later in Chapter six.

The distribution of air voids in a mixture proves to be particularly important to moisture diffusion and, subsequently, to moisture susceptibility. Masad et al. (2006) established a relation between moisture damage and average air void diameter. The study investigated granite and limestone mixtures with varying aggregate gradations, so as to result in diverse air void distributions. Moisture resistance was evaluated on the basis of energy ratio and number of cycles to failure. The study concluded that there is a range of void sizes and permeability values in which mixtures are more sensitive to moisture. Moreover, low ranges of air void content, from 4% to 7%, and void radii were associated to higher rates of crack growth (Arambula et al. 2007). Alternatively, Kassem at al. (2011) used a fracture mechanics model to demonstrate that the levels of moisture damage were similar at 4% to 7% of air voids, but increased substantially for mixtures with 10% of air voids.

2.1.2 Moisture diffusion coefficients and moisture capacity of bituminous materials

To improve our understanding of moisture transport in bituminous mixtures, one has to obtain the physical properties related to the phenomenon, namely moisture diffusivity and moisture capacity at equilibrium of the constituent materials, such as bitumen, filler, aggregates, etc. The standard mechanical test methods, however, cannot provide this information that is essential for modelling moisture diffusion. Parameter determination for physicochemical models involves the use of specialized test methods, and therefore dedicated equipment, that allow the measurement of more fundamental material properties.

Few studies have focused on the determination of the diffusion properties of asphalt bitumen using a variety of test methods. Pettersson & Elert (2001) reported a value of $0.72 \cdot 10^{-2}$ mm^2/hr (at 25°C) for Mexphlate 40/50 bitumen used for encapsulation of radioactive waste. Cheng et al. (2003) used the Universal Sorption Device (USD) to measure the diffusivity of distilled water into two asphalt bitumens, namely AAD-1 and AAM-1. Moreover, they established a link between the diffusion characteristics of the two bitumen types with the results of accelerated moisture damage tests. They concluded by emphasizing the importance of the moisture holding capacity parameter, as they observed that mixtures containing binders with high capacity to absorb moisture appear to

be more prone to moisture damage. Later, Nguyen et al. (1992) used infrared spectroscopic techniques to measure diffusion coefficients of moisture into bitumen. The measurements were performed on bitumen coatings on siliceous Attenuated Total Reflectance (ATR) plates. The values reported are within a range of 0.50 to 1.19 ($\times 10^{-4)}$ mm^2/hr.

Lower values of moisture diffusion coefficients, from 5.54×10^{-8} to 1.51×10^{-4} mm^2/hr, were determined, in a study by Wei and Youtcheff (2008) using the Electrochemical Impedance Spectroscopy (EIS) method, as reported in Arambula et al. (2010). Finally, Vasconcelos (2010) used the Fourier transform infrared spectroscopy (FTIR) to determine the diffusivity of water through four asphalt bitumens. Table 2.2 provides an overview of the diffusivity values found in literature.

Table 2.2. Diffusion coefficients for various bitumens (adapted from Arambula et al. 2010).

Reference	**Asphalt bitumen type**	**Diffusion coefficient [mm^2/hr]**
Nguyen et al. (1992)	AAC-1	5.04×10^{-5}
	AAD-1	9.00×10^{-5}
	AAK-1	1.19×10^{-4}
Wei and Youtcheff (2008)	AAD-1	1.51×10^{-4}
	AAK-1	1.06×10^{-7}
	AAM-1	5.54×10^{-8}
Vasconcelos et al. (2010)	AAB-1	1.35×10^{-8}
	AAD-1	3.38×10^{-8}
	AAF-1	3.44×10^{-8}
	ABD-1	2.52×10^{-8}
Cheng et al. (2003)	AAD-1	4.78
	AAM-1	17.39
Pettersson and Elert (2001)	Mexphlate 40/50	0.72×10^{-2}

Apart from pure bitumen, studies also focused on the measurement of the diffusion properties of mastics and fine aggregate mixtures. Again, the two key parameters measured are the diffusion coefficient and the moisture uptake at equilibrium. Significant differences are found among the various methods. Kassem et al. (2006) monitored the change of total suction in cylindrical samples with time, sitting in a shallow water bath at 25°C, using a psychrometer embedded in the middle of the sample. Other methods included measurements of the weight increase of samples after being submerged under water (Vasconcelos et al. 2011) or the use of gravimetric techniques that aimed to measure the overall moisture sorption of a sample by means of a sensitive micro-balance (Kringos

et al. 2008, Arambula et al. 2010, Apeagyei et al. 2013). Table 2.3 provides an overview of the test methods and the reported moisture diffusion coefficients.

Table 2.3. Diffusion coefficients for various mastic and fine aggregate mixtures (adapted from Apeagyei et al. 2013).

Reference	**Blend proportions [w/w]**	**Diffusion coefficient [mm²/hr]**	**Equipment used**
Kassem et al. (2006)	Aggregates (1.18 mm sieve) Sandstones: 52.4, Igneous screening: 35.0% Hydrated lime: 4,6%, Bitumen: 8% PG 76-22	0.37×10^{-1}	Monitoring the change of total suction in specimens with time
	Aggregate: 66.2% Natural sand: 25.8% Limestone sand asphalt: 8.0% PG 64-22, PG 64-28	$0.35\text{-}0.87\times10^{-1}$	
Kringos et al. (2008)	Aggregates (1.18 mm sieve) Crushed sand: 50%, Lime filler: 25%, Bitumen: 25% Pen 70/100	$0.47\text{-}11.09\times10^{-3}$	Gravimetric sorption method
Arambula et al. (2010)	Aggregates (4.75 mm sieve) Diabase: 47.3% Sand: 42.5% Dust: 1.7% Bitumen: 8.5%, PG 70-22	0.92×10^{-1}	Periodic weight measurement of specimen-container ensembles
Vasconcelos et al. (2010)	Aggregates (1.18 mm sieve) Basalt or Granite Bitumen: 8.9% PG85-10, PG 85-22, PG85-28	$2.8\text{-}17.64\times10^{-3}$	Measuring the weight increase of specimens after being submerged under water
Apeagyei et al. (2013)	Aggregates (1.18 mm sieve) Granite or Limestone 25% Filler: 25% Granite or Limestone Bitumen 25% Pen 40/60	$4.79\text{-}17.1\times10^{-3}$	Measuring with manual and automated gravimetric sorption techniques

It is apparent that the diffusivity values for both bitumen (Table 2.2) and mastics (Table 2.3) vary significantly. This can be mainly attributed to the dissimilarities in the experimental set-up and testing conditions used to measure diffusivity (Arambula et al. 2010, Apeagyei et al. 2013). In addition, the analytical solutions used to obtain the diffusion properties did not always coincide. However, another influential factor could be the temperature at which the measurements were performed. Earlier, the substantial effect of temperature on the diffusion coefficient was discussed. Unfortunately, most of the abovementioned studies do not report the temperature, at which

diffusivity was determined. For the mastic measurements, other parameters such as the mix design and the amount of air voids could considerably influence the diffusivity values.

Finally, in the case of bitumen measurements, few attempts were made to quantify moisture capacity of bitumen, but most studies focused on the diffusion coefficient. Nevertheless, the concentration of moisture in bitumen is also a function of the maximum moisture it can absorb, and consequently both parameters should be considered for characterizing moisture susceptibility of bitumen considering that they are complementary.

2.2 Modelling moisture diffusion in bituminous mixtures

To study the ingress of moisture into bituminous materials and to improve the understanding of how diffusion rates are influenced by the various parameters, namely environmental conditions, diffusion properties of the constituents, microstructure etc., a moisture diffusion model is implemented. The model enables the calculation of moisture accumulation in bituminous materials and allows for predictions with respect to the degradation of their mechanical performance, when coupled with the appropriate mechanical computational models. Such a numerical scheme, which couples damage due to mechanical loading and moisture diffusion, is discussed later in Chapter five.

An understanding of the process of moisture diffusion in bituminous materials is essential for the design of reliable asphalt binders and the selection of constituent materials, i.e. fillers, polymer additives etc., for use in demanding environments. Furthermore, deeper understanding of diffusion is critical in the development of better testing methodologies and accelerated moisture conditioning protocols for asphalt mixtures. For this reason, a three-dimensional finite element model is implemented, which simulates moisture diffusion. The model can be used to determine the moisture profiles and predict fluctuations in moisture content over time at various locations in bituminous mixtures.

In the following section, a detailed mathematical description of the moisture transport model is presented. The model is implemented in the CAPA-3D (Scarpas 2005) finite element (FE) software developed in Delft University of Technology.

2.2.1 Description of moisture transport equation

In general, the mass transfer of a substance can be described by the transport equation [2.2],

$$\frac{\partial c}{\partial t} = \nabla \cdot f + R \qquad [2.2]$$

, where c denotes the concentration, f the flux of the substance and R the sinks or sources of variable c. The aforementioned equation states that the rate of change of the concentration of the substance in a differential volume is given by the balance of the flux that enters into or exits out of the volume in addition to any accumulation and depletion of the substance (for example due to chemical reactions) that may occur over time. The net flux into the volume element is normally a result of two

types of transport processes, i.e. advection and diffusion. *Advection* is the transport of a substance due to the bulk flow of a fluid, while in *diffusion* mass is primarily transferred by means of random molecular motion, the so-called Brownian motion. If one considers both advection and diffusion, then the transport equation becomes

$$\frac{\partial c}{\partial t} + \nabla \cdot (vc + J) = R \qquad [2.3]$$

, where *v* denotes the velocity vector of the fluid and *J* the diffusive flux. It is generally accepted that the controlling mechanism of moisture transport, into the constituents of an asphalt mixture, is the molecular diffusion of moisture due to concentration gradients. In the absence of water flow, the transport equation further reduces to

$$\frac{\partial c}{\partial t} + \nabla \cdot J = R \qquad [2.4]$$

Moisture diffusion in bituminous mixtures is a long-term process (Cheng et al. 2003), which depends on the diffusivity characteristics of the mixture components. Mass transfer of moisture expresses essentially the spatial and temporal evolution of moisture concentration in the asphaltic components. The concentration of moisture is initially not uniform (moisture concentration is greater in the environment surrounding the mixture than in the mixture itself) then, with time, mass transfer occurs, from regions of high concentration to low concentration, which acts to balance the differences in concentration and eventually results in an equilibrium state of concentration, as shown in Figure 2.4.

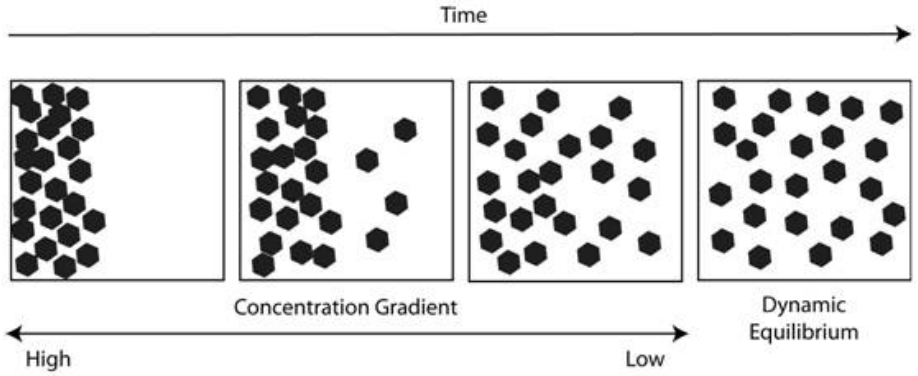

Figure 2.4. Diffusion process in time (reprinted from BCA Chemistry https://bcachemistry.wordpress.com).

The constitutive relation that describes the steady-state flux of moisture per unit area, while concentration is not varying with time, is known as the Fick's first law of diffusion

$$J = -D\nabla c \qquad [2.5]$$

, where *J* denotes the moisture flux across the unit area per unit time (mol/m^2·s or kg/m^2·s), *c* the moisture concentration (mol/m^3 or kg/m^3) and *D* the diffusion coefficient (m^2/s). As follows from equation [2.5], the moisture flux is proportional to the moisture concentration gradient and is

controlled by the diffusion coefficient. Physically, the coefficient of moisture diffusion is indicative of the rate of moisture ingress into the material. Higher values of diffusivity result in higher rates of moisture diffusion. In the case of anisotropic diffusion we can define the diffusivity tensor, which is expressed as (Kringos 2007)

$$\underset{\sim}{D} = \sum_{i,j} D_{ij} \underset{\sim}{e}_i \otimes \underset{\sim}{e}_j = \alpha_m \tau \delta_{ij} \quad [2.6]$$

, where α_m denotes the molecular diffusion coefficient, τ the tortuosity of the material and δ_{ij} the Kronecker delta. Fick's second law of diffusion is derived by combining the reduced transport equation [2.4] and the constitutive equation [2.5], which describes the flux of moisture, in addition to presuming that moisture is a conserved quantity and hence there are no internal or external sources or sinks (namely R=0)

$$\frac{\partial c}{\partial t} = D\Delta c \quad [2.7]$$

, where $\Delta=\nabla^2$ denotes the Laplace operator. Equation [2.7] postulates that the diffusion coefficient is isotropic and constant in time, i.e. $D=D_{xx}=D_{yy}=D_{zz}$=const. When two material phases with dissimilar moisture capacities are joined together, for example aggregates and binder, the concentration of moisture is discontinuous at their interface. To ensure the continuity of the equation across the interface a normalized variable, the normalized moisture concentration θ, is introduced. Then equation [2.7] can be written as

$$\frac{\partial \theta}{\partial t} - D\Delta\theta = 0 \text{ , with } \theta = \frac{c_t}{c_{t\to\infty}} \quad [2.8]$$

, where θ denotes the normalized moisture concentration, c_t the concentration at any time and $c_{t\to\infty}$ the maximum concentration of moisture that the material can absorb.

2.2.2 Boundary conditions

To define the boundary value problem, it is required that equation [2.8] is satisfied within the domain Ω and boundary conditions are satisfied on the boundary Γ of the domain. Dirichlet and Neumann boundary conditions are applied. Dirichlet boundary condition specifies that the moisture applied on boundary Γ should be equal to the corresponding prescribed values such as $\theta=\theta^p$, where θ^p is the prescribed moisture content on the specific boundary. According to the equation of energy conservation the moisture inflow rate across the boundary Γ should be equal to the outflow rate. Therefore the Neumann boundary condition is defined as

$$-n^T D\nabla\theta - Q = 0 \quad \text{on } \Gamma \quad [2.9]$$

, where n is the normal unit vector and Q is the outflow rate per unit area of the boundary surface.

2.2.3 Finite element formulation

To solve equation [2.8] we need to transform the equation into an appropriate form. The appearance of second derivatives in equation [2.8] requires that there is a smooth transition in space. For this reason, the variational (weak) form of the equation should be derived. To construct the variational form, the equation should be multiplied by an appropriate arbitrary function, then integrated over the domain of interest and set the result to zero (Zienkiewicz & Taylor 2000).

The weak residual form of equation [2.8] that applies on the continuum and equation [2.9] that applies on the boundary is written as

$$\int_{\Omega} m^T \left(\frac{\partial \theta}{\partial t} - D\nabla^2\theta\right)\, d\Omega + \int_{\Gamma} p^T \left(-n^T D\nabla\theta\ - Q\right)\, d\Gamma = 0 \qquad [2.10]$$

, where *m* and *p* are arbitrary weighting functions. Performing integration by parts yields

$$\int_{\Omega} m^T \frac{\partial \theta}{\partial t} d\Omega - \left(\int_{\Omega} \nabla(m^T D\nabla\theta)\, d\Omega - \int_{\Omega} (\nabla^T m^T) D\nabla\theta\, d\Omega \right) + \int_{\Gamma} p^T \left(-n^T D\nabla\theta\ - Q\right)\, d\Gamma = 0 \qquad [2.11]$$

Using the divergence theorem, the volume integral over the divergence, in equation [2.11] can be changed into a surface integral

$$\int_{\Omega} \nabla(m^T D\nabla\theta)\, d\Omega = \int_{\Gamma} m^T b^T D\nabla\theta\, d\Gamma \qquad [2.12]$$

Therefore equation [2.11] can be written as

$$\int_{\Omega} m^T \frac{\partial \theta}{\partial t} d\Omega + \int_{\Omega} (\nabla m)^T D\nabla\theta\, d\Omega - \int_{\Gamma} m^T b^T D\nabla\theta\, d\Gamma + \int_{\Gamma} p^T [-n^T D\nabla\theta - Q]\, d\Gamma = 0 \qquad [2.13]$$

, where *n* and *b* are identity tensors. In order to minimise the integrals to be evaluated and since *m* and *p* are arbitrary weighting functions, we choose *m=-p*. Then equation [2.13] reduces to the final variational form of the moisture diffusion equation

$$\int_{\Omega} m^T \frac{\partial \theta}{\partial t} d\Omega + \int_{\Omega} (\nabla m)^T D\nabla\theta\, d\Omega + \int_{\Gamma} m^T Q\, d\Gamma = 0 \qquad [2.14]$$

The Galerkin finite element method is used to solve the diffusion equation. In the FE method, the domain of interest is discretized in space and represented as an assembly of finite elements. Approximating functions are determined for the moisture content nodal values, at finite number of points within the continuum and on the boundary, using interpolation functions, known as shape functions. Shape functions are attached to each node and are usually chosen to be locally defined polynomials within each element and being zero outside the element under consideration. Typically, they vary for different element types. The expression for moisture content can take the form

$$\theta = N\bar{\theta} \qquad [2.15]$$

, where *N* denotes the shape function and $\bar{\theta}$ the moisture content at node *i*.

Following the Galerkin method, the approximating shape functions are chosen to be identical to the weighting functions, hence equation [2.14] becomes

$$\int_{\Omega} N^T N \, d\Omega \frac{d\overline{\theta}}{dt} + \int_{\Omega} (\nabla N)^T D \nabla N \, d\Omega \overline{\theta} + \int_{\Gamma} N^T Q \, d\Gamma = 0 \qquad [2.16]$$

For brevity, the spatial discretization of equation [2.14] can be written in matrix form as

$$A \frac{d\,{}^t\overline{\theta}}{dt} + B\,{}^t\overline{\theta} = C \qquad [2.17]$$

, where

$$A = \int_{\Omega} N^T N \, d\Omega \qquad [2.18]$$

$$B = \int_{\Omega} \left(\nabla N\right)^T D \nabla N \, d\Omega \qquad [2.19]$$

$$C = -\int_{\Gamma} N^T \, Q \, d\Gamma \qquad [2.20]$$

The diffusion equation is discretised (Lewis & Schrefler 1987) in the time domain by approximating $\overline{\theta}$ with a linear variation at each time step Δt

$$[\overline{\theta}] = [N_1^t \;\; N_2^t] \begin{bmatrix} \overline{\theta}^{t-\Delta t} \\ \overline{\theta}^{t} \end{bmatrix} \qquad [2.21]$$

, where $N_1 = 1 - \varepsilon$, $N_2 = \varepsilon$, $\varepsilon = \frac{t - t_k}{\Delta t_k}$ and Δt_k is the length of the time step. The time derivatives of N_1 and N_2 are

$$\frac{d}{dt}[N_1^t \;\; N_2^t] = \begin{bmatrix} -\frac{1}{\Delta t_k} & \frac{1}{\Delta t_k} \end{bmatrix} \qquad [2.22]$$

A step-by-step integration method is used. The integration follows the same form as used for the spatial discretization, hence if *F=0* then $\int \overline{g} F \; dt = 0$, where $\overline{g}$ is an arbitrary function in time. Therefore, by applying this scheme, equation [2.17] becomes

$$\int_{t_k - \Delta t_k}^{t_k} \overline{g} A \frac{d\,{}^t\overline{\theta}}{dt} \; dt + \int_{t_k - \Delta t_k}^{t_k} \overline{g} B\,{}^t\overline{\theta} \; dt = \int_{t_k - \Delta t_k}^{t_k} \overline{g} C \; dt \qquad [2.23]$$

Using equations [2.21] and [2.22], equation [2.23] becomes

$$\int_{t_k-\Delta t_k}^{t_k} \bar{g}A\left[-\frac{1}{\Delta t_k}\bar{\theta}^{t-\Delta t}+\frac{1}{\Delta t_k}\bar{\theta}^{t}\right]dt+\int_{t_k-\Delta t_k}^{t_k} \bar{g}B\left[(1-\varepsilon)\bar{\theta}^{t-\Delta t}+\varepsilon\bar{\theta}^{t}\right]dt = \int_{t_k-\Delta t_k}^{t_k} \bar{g}C\ dt \quad [2.24]$$

, where ε is parameter ranging in [0, 1). For $\varepsilon=0$, the above transforms to the explicit forward Euler method. While, for $\varepsilon=0.5$ and $\varepsilon=1.0$ this formulation results to the Crank-Nicholson and the implicit backward Euler methods, respectively. Finally, after it is integrated and divided by $\bar{g}$, equation [2.24] becomes

$$[A\frac{1}{\Delta t_k}+\varepsilon B]\ \bar{\theta}^{t}=[A\frac{1}{\Delta t_k}-(1-\varepsilon)B]\ \bar{\theta}^{t-\Delta t}+C \quad [2.25]$$

, where the definition $\Delta^t\bar{\theta}=\bar{\theta}^{t}-\bar{\theta}^{t-\Delta t}$ is introduced. By rearranging the terms, equation [2.25] becomes

$$A\frac{\Delta^t\bar{\theta}}{\Delta t}+B(\varepsilon\bar{\theta}^{t}+(1-\varepsilon)\bar{\theta}^{t-\Delta t})=C \quad [2.26]$$

2.2.4 Stability of diffusion equation

The moisture diffusion equation can be unstable for large time steps. A large time step will overshoot the solution, due to the fact that the rate of moisture diffusion at present time is always greater than at later times. Therefore it is required to set a stability criterion that bounds the time step. First equation [2.26] is pre- and post-multiplied by Δt , which leads to

$$A\Delta^t\bar{\theta}+B(\varepsilon\bar{\theta}^{t}+(1-\varepsilon)\bar{\theta}^{t-\Delta t})\Delta t=C\Delta t \quad [2.27]$$

Rearranging the terms in Eq. (19) the following expression is derived

$$A\Delta^t\bar{\theta}+B(\varepsilon(\bar{\theta}^{t}-\bar{\theta}^{t-\Delta t})+\bar{\theta}^{t-\Delta t})\Delta t=C\Delta t \quad [2.28]$$

, which further becomes

$$A\Delta^t\bar{\theta}+\varepsilon B\Delta^t\bar{\theta}\Delta t=C\Delta t-B\bar{\theta}^{t-\Delta t}\Delta t \quad [2.29]$$

Solving equation [2.29] for $\Delta^t\bar{\theta}$ gives

$$\Delta^t\bar{\theta}=\frac{C\,\Delta t-B\,\bar{\theta}^{\,t-\Delta t}\Delta t}{A+\varepsilon\,B\,\Delta t} \quad [2.30]$$

For the special case that no external heat source is present, $C=0$ and equation [2.30] changes into

$$\Delta^{t}\overline{\theta} = \frac{-B\ \Delta t}{A+\varepsilon\ B\ \Delta t}\ \overline{\theta}^{\,t-\Delta t} \qquad [2.31]$$

The updated moisture content ${}^{t}\overline{\theta}$ is now expressed as

$${}^{t}\overline{\theta} = \overline{\theta}^{\,t-\Delta t} + \Delta^{t}\overline{\theta} = \overline{\theta}^{\,t-\Delta t} + \frac{B\,\Delta t}{A+\varepsilon\ B\ \Delta t}\overline{\theta}^{\,t-\Delta t} = \frac{A-\left(1-\varepsilon\right)B\ \Delta t}{A+\varepsilon\ B\ \Delta t}\overline{\theta}^{\,t-\Delta t} \qquad [2.32]$$

To prevent getting irregular moisture contents in successive steps, it should hold that

$$\frac{A-\left(1-\varepsilon\right)B\ \Delta t}{A+\varepsilon\ B\ \Delta t} \geq 0 \qquad [2.33]$$

The stability condition can be reduced to the following expression, as matrices A and B, as well as the denominator of equation [2.33] are all positive

$$A-\left(1-\varepsilon\right)B\,\Delta t \geq 0 \qquad [2.34]$$

This means that the time step should be bound by the following condition to ensure a stable analysis

$$\Delta t \leq \frac{A}{\left(1-\varepsilon\right)B} \qquad [2.35]$$

2.2.5 Model validation

The governing equation of moisture diffusion into asphalt pavements and its finite element formulation are presented in the previous section. Following this, a benchmark solution is used for the verification of the model before using the implementation to simulate moisture diffusion phenomena in bituminous mixtures,. General solutions of the diffusion equation can be found in literature for various initial and boundary conditions, under the assumption that the coefficient of moisture diffusion is constant. A comparison between the results of the moisture diffusion model and the analytical solution for diffusion into a semi-infinite medium is presented below.

Crank (1975) provides the analytical solution of diffusion in a semi-infinite medium, $x > 0$, when the boundary is kept at a constant concentration, C_o, and the initial concentration is zero throughout the medium. Figure 2.5 shows the definition of the problem, as modified in the case of moisture diffusion in a semi-infinite bar.

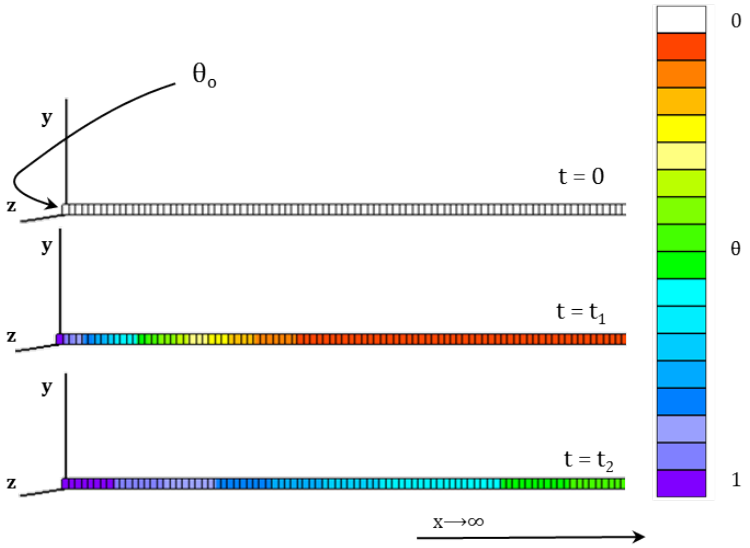

Figure 2.5. One dimensional diffusion of moisture into a semi-infinite medium.

The diffusion equation for a one dimensional (1D) flow reduces to

$$\frac{\partial \theta}{\partial t} = D\frac{\partial^2 \theta}{\partial x^2} \qquad [2.36]$$

To solve the problem, the Laplace transform is used and the solution for the calculation of the moisture concentration field in the semi-infinite system can be found below

$$\theta(x,t) = \theta_t erfc\left(\frac{x}{2\sqrt{Dt}}\right) \qquad [2.37]$$

, where the function *erfc(z)* can be found from the error function *erf(z)* as

$$erfc(z) = 1 - erf(z) = 1 - \frac{2}{\sqrt{\pi}}\int_0^z e^{-\eta^2} d\eta \qquad [2.38]$$

Equation [2.37] was used to validate the results of the FE implementation. The diffusion problem was computationally solved using a diffusion coefficient equal to 0.05 m/s² and a 100 mm for the total length of the medium. A Dirichlet boundary condition of $\theta=\theta_o=1$, at x=0 and t>0 , was applied. Figure 2.6 presents the results obtained from the analytical solution and the numerical model; a good agreement was found between the two.

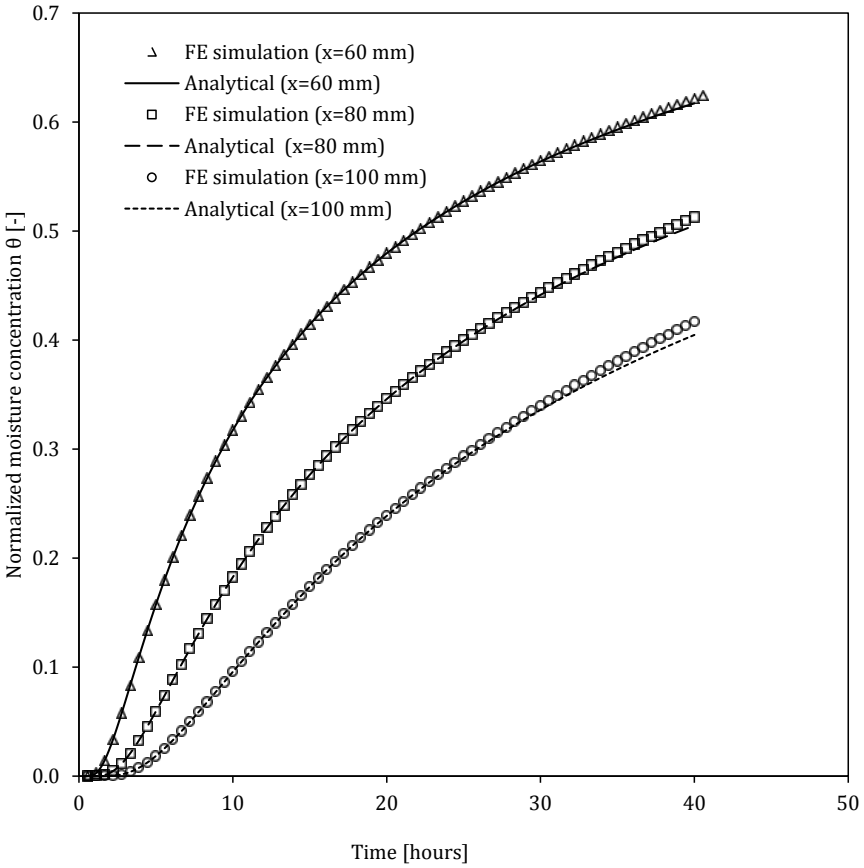

Figure 2.6. Results obtained from analytical solution and FE model simulation.

2.3 Summary

Moisture diffusion is an important process when discussing moisture susceptibility in asphalt mixtures. Moisture transport into a mixture, and through its constituents, is influenced by a number of parameters, namely the physicochemical properties of the constituents, the mixture microstructure, and the environmental conditions. The interplay among these parameters is essentially what imparts the particular moisture sensitivity characteristics to a mixture.

Nowadays, the determination of the constituents' properties related to moisture absorption is not part of the standard practice. Research studies have been undertaken to measure the diffusion coefficients and capacity of moisture of bituminous materials; nevertheless the values often appear to vary significantly, mainly due to inconsistencies among the employed test methods. To overcome this problem, the pavement community should focus on the development of easily implementable testing protocols, similar to those available for mechanical asphalt tests, which designate the test conditions, sample preparation and provide the analytical tools to determine the physical properties related to moisture. Thus, the vital information required to prevent the use of constituents with inherent sensitivity against moisture in mix design will be made available.

Moreover, this information will be particularly interesting for developing accelerated moisture conditioning protocols for the evaluation of asphalt mixtures against moisture, while being used as an input to computational models. By expanding our knowledge of the way moisture accumulates in asphaltic materials will allow the selection of constituents for the design of asphalt mixtures with enhanced properties against moisture. The diffusion model, presented in this chapter, especially contributes to the improved understanding of the influence of physical properties of bitumen and mix constituents to the moisture sensitivity of asphalt mixtures. The model results will lead to establishing a link between the mixture structure and composition to its macroscopic behaviour. Such an example is presented later in Chapter six.

2.4 References

Adamson, A.W. (1982). Physical Chemistry of Surfaces. John Wiley & Sons, Inc., New York.

Airey G. D. , Rahman, M. M. & Collop, A. C. (2003). Absorption of bitumen into crumb rubber using the basket drainage method. *International Journal of Pavement Engineering*, 4:2, 105-119.

Apeagyei, A. K., Grenfell, J. R., & Airey, G. D. (2013). Evaluation of moisture sorption and diffusion characteristics of asphalt mastics using manual and automated gravimetric sorption techniques. *Journal of Materials in Civil Engineering*, 26:8.

Apostolidis, P. (2015). Experimental and numerical investigation of induction heating in asphalt mixes. MSc Thesis, Delft University of Technology, the Netherlands.

Arambula, E., Masad, E. A. & Martin, A. (2007). Influence of air void distribution on the moisture susceptibility of asphalt mixes. *Journal of Materials in Civil Engineering*, 19:8, 655–664.

Arambula, E., Caro, S., & Masad, E. A. (2010). Experimental measurement and numerical simulation of water vapor diffusion through asphalt pavement materials. *Journal of Materials in Civil Engineering*, 22:6, 588-598.

Averill, B. A. & Eldredge, P. (2007). Chemistry: Principles, Patterns, and Applications. Publisher: Prentice Hall. ISBN: 978-0805337990.

Bahia, H. U. & Davies, R. (2014). Effect of crumb rubber modifiers (CRM) on performance related properties of asphalt binders. *Journal of the Association of Asphalt Paving Technologists*, 63, 414-449.

Bhasin, A. & Little, D. N. (2007). Characterization of aggregate surface energy using the universal sorption device. *Journal of Materials in Civil Engineering*, 19, 634–641.

Cheng, D., Little, D. N., Lytton, R. & Holste, J. (2002). Use of surface free energy properties of the asphalt-aggregate system to predict damage potential. *Journal of the Association of Asphalt Paving Technologists*, 71, 59-88.

Cheng, D., Little, D. N., Lytton, R. L. & Holste, J.C. (2003). Moisture damage evaluation of asphalt mixtures by considering both moisture diffusion and repeated-load conditions. *Transportation Research Record: Journal of the Transportation Research Board*, 1832, 42-49.

Copeland, A. (2007). Influence of moisture on bond strength of asphalt-aggregate systems. PhD dissertation. Vanderbilt University, Nashville, Tennessee.

Crank, J. (1975). The mathematics of diffusion. Second edition. Oxford Science Publication.

Cui, S., Blackman, B. R. K., Kinloch, A. J. & Taylor, A. C. (2014). Durability of asphalt mixtures: Effect of aggregate type and adhesion promoters. *International Journal of Adhesion & Adhesives,* 54, 100–111.

Curtis, C.W. (1992). Investigation of asphalt-aggregate interactions in asphalt pavements. American Chemical Society, Fuel, 37, 1292-1297.

Faheem, A., Wen, H. Stephenson, L. & Bahia, H. U. (2008). Effect of mineral filler on damage resistance characteristics of asphalt binders. *Journal of the Association of Asphalt Paving Technologists*, 77, 885-908.

Fischer, H. R., Dillingh, E. C., and Hermse, C. G. M. (2012). On the interfacial interaction between bituminous binders and mineral surfaces as present in asphalt mixtures. *Applied Surface Science*, 265, 495–499.

Hefer, A. (2004). Adhesion in bitumen-aggregate systems and quantification of the effects of water on the adhesive bond. PhD dissertation. Texas A&M University, College Station, Texas.

Hefer, A. & Little, D. N. (2005). *Adhesion in bitumen-aggregate systems and quantification of the effects of water on the adhesive bond.* Report ICAR/505-1. Texas Transportation Institute, Texas A&M University System, College Station, Texas.

Kassem, E., Masad, E. A., Bulut, R. & Lytton, R. (2006). Measurements of moisture suction and diffusion coefficient in hot-mix asphalt and their relationships to moisture damage. *Transportation research record: Journal of the Transportation Research Board*, 1970:1, 45-54.

Kassem, E., Masad, E. A., Lytton, R. L. & Bulut, R. (2009). Measurements of the moisture diffusion coefficient of asphalt mixtures and its relationship to mixture composition. *International Journal of Pavement Engineering*, 10:6, 389-399.

Kassem, E., Masad, E. A., Lytton, R. L. & Chowdhury, A. (2011). Influence of air voids on mechanical properties of asphalt mixtures. *Road Materials and Pavement Design*, 12:3, 493-524.

Kim, Y. R., Allen, D. H. & Little, D. N. (2005). Damage-induced modeling of asphalt mixtures through computational micromechanics and cohesive zone fracture. *Journal of Materials in Civil Engineering*, 17:5, 477-484.

Kringos, N. (2007). Modeling of combined physical-mechanical moisture induced damage in asphaltic mixes. PhD dissertation. Delft University of Technology, The Netherlands.

Kringos, N., Scarpas, A., Copeland, A., & Youtcheff, J. (2008). Modelling of combined physical–mechanical moisture-induced damage in asphaltic mixes, part 2: moisture susceptibility parameters. *International Journal of Pavement Engineering*, 9:2, 129-151.

Labib, M. E. (1992). Asphalt-aggregate interactions and mechanisms for water stripping. *American Chemical Society Division of Fuel Chemistry*, 37, 1472-1481.

Lesueur, D. (2009). The colloidal structure of bitumen: Consequences on the rheology and on the mechanisms of bitumen modification. *Advances in Colloid and Interface Science*, 145, 42–82.

Lewis, R. W. & Schrefler, B. A. (1987). The finite element method in the deformation and consolidation of porous media. Publisher: John Wiley & Sons. ISBN: 0471912107.

Lytton, R. L., E. A. Masad, C. Zollinger, R. Bulut & Little, D. N. (2005). Measurements of surface energy and its relationship to moisture damage. Technical Report No. FHWA/TX-05/0-4524-2, FHWA, Washington D.C.

Masad, E. A., Castelblanco, A. & Birgisson, B. (2005). Effects of air void size distribution, pore pressure, and bond energy on moisture damage. *Journal of Testing and Evaluation*, 34:1, 1-9.

Nguyen, T., Byrd, W. E., Bentz, D. & Seiler, J. (1992). *Development of a technique for in situ measurement of water at the asphalt/model siliceous aggregate interface.* SHRPID/URF-92-611, Strategic Highway Research Program, Washington, D.C.

Pettersson, M. & Elert, M. (2001). *Characterisation of bituminised waste in SFR 1*. SKB Report R-01 - 26. Swedish Nuclear Fuel and Waste Management Co. Stockholm, Sweden.

Read, D. & Whiteoak, J. (2003). The Shell Bitumen Handbook. Publisher: Thomas Telford. ISBN: 9780727732200.

Scarpas, A. (2005). *CAPA-3D: A mechanics based computational platform for pavement engineering*, PhD dissertation. Delft University of Technology, the Netherlands.

Shen, J. & Amirkhanian, S. N. (2005). The influence of crumb rubber modifier (CRM) microstructure on the high temperature properties of CRM binder. *International Journal of Pavement Engineering*, 6:4, 265-271.

Vasconcelos, K. L., Bhasin, A., Little, D. N., & Lytton, R. L. (2011). Experimental measurement of water diffusion through fine aggregate mixtures. *Journal of Materials in Civil Engineering*, 23:4, 445-452.

Vasconcelos, K. L. (2010). Moisture diffusion in asphalt binders and fine aggregate mixtures. PhD dissertation. Texas A&M University, College station, Texas.

Wang, H., Al-Qadi, I. L., Faheem, A. F., Bahia, H. U., Yang, S. H. & Reinke, G. H. (2011). Effects of mineral filler characteristics on asphalt mastic and mixture rutting potential, *Journal of the Transportation Research Board*, 2208, 33-39.

Wang, D., Wang, L., Gu, X. & Zhou, G. (2013). Effect of basalt fiber on the asphalt binder and mastic at low temperature. *Journal of Materials in Civil Engineering*, 25:3, 355-364.

Wei, J. & Youtcheff, J. (2008). *Ongoing research to determine moisture diffusion coefficients of asphalt binders.* Internal Report. Federal Highway Administration, Washington, D.C.

Zienkiewicz, O. C. & Taylor, R. L. (2000). The finite element method for solid and structural mechanics, Sixth edition. Publisher: Elsevier Ltd. ISBN: 9780750663212.

3

Cohesion properties of asphalt mortar

"See now the power of truth; the same experiment which at first glance seemed to show one thing, when more carefully examined, assures us of the contrary."
— Galileo Galilei (1564-1642)

The mechanical response of asphalt pavements strongly depends on the performance of asphalt mortars, considering that they serve as the binding medium that holds the coarser aggregate matrix together. During their service life asphalt pavements, and consequently asphalt mortars, are exposed to a variety of environmental conditions that can change their physicochemical characteristics, and hence compromise their performance. Moisture diffusion is well-known to degrade the mechanical properties of asphalt mortars, thus increasing their propensity to cracking. It is, therefore, essential to characterize the cohesion properties of mortars and how these can alter under the influence of environmental conditions. This chapter aims to investigate the changes in the cohesive characteristics of asphalt mortars, after various combinations of moisture conditioning and thermal cycles, through a series of uniaxial tension tests.

3.1 Introduction

Asphalt pavements experience a complex state of stresses under traffic loading. The nature and the magnitude of the developed stresses vary with the distance from the wheel path and the pavement depth. As shown in Figure 3.1, the pavement structure deflects under the wheel load and vertical compressive stresses are developed in the top of the surface layer, while horizontal tensile stresses are developed in the bottom part directly underneath the applied load. The stresses profile changes as we move away from the wheel path; in this case, tension is developed in the top layers and compression in the layers below. When the applied stresses exceed the strength of the material and its resistance to deformation, pavement distresses can occur. Specifically, the repetitive traffic action can lead to fatigue or bottom-up cracking in those locations where high tensile stresses are present, while compressive stresses and strains can cause rutting on the pavement surface. Asphalt pavements are mainly designed to withstand the traffic induced stresses and strains and eliminate common distress mechanisms, such as fatigue cracking and permanent deformation. However, the degradation of asphalt pavements results from a combination of traffic loading and environmental conditions such as temperature, oxygen and moisture.

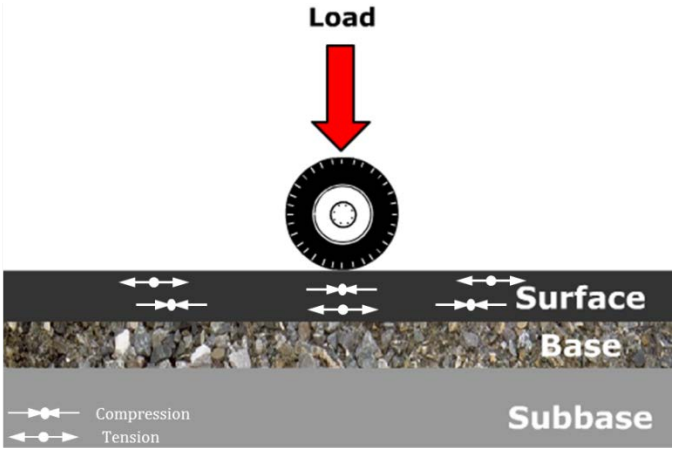

Figure 3.1. Stress profile under traffic loading (reprinted from Pavement Interactive©2003 - Steve Muench).

The presence of water (or moisture) has been recognized as a primary cause of distress in asphalt pavement structures. Apart from the direct effects of moisture on the performance of asphalt pavements, which results in stripping of the aggregates from the surface, moisture damage can accelerate other types of pavement distresses, such as rutting and fatigue cracking, due to decreased strength and stiffness of the asphalt mixture (Hicks et al. 2003). As described in Chapter one, moisture diffusion has been identified as a dominant process that can alter the physicochemical and mechanical properties of asphalt mortars, thus causing degradation of their functional performance (Kringos et al. 2008a, Caro et al. 2008).

Asphalt mortar is the binding medium that holds the coarser aggregates of an asphalt mixture together and ensures its structural integrity. It is the asphalt mortar phase that deforms under loading and can fracture at low-temperature or under repetitive loading. Thus, the tensile properties of mortars play an important role in the mechanical performance of asphalt mixtures and

are imperative for the study of pavement structures under the state of tensile stresses, such as those due to traffic loads, temperature differentials and pumping action.

The design of asphalt pavements with enhanced durability characteristics requires a better understanding of the cohesion properties of asphalt mortars and how those change under the influence of environmental conditions. According to Hicks (1991) moisture enters into the binder film through diffusion and due to physicochemical interactions degrades the binder, and therefore its cohesive strength and stiffness reduces. The binder, and consequently the mortar, is then more prone to cracking due to traffic loading, as well as due to the additional internal stresses that develop as a result of pumping action or freeze-thaw cycles. Moreover, it is expected that the deteriorated mortar will be easily eroded by fast water flows that may develop in asphalt pavements, especially in those with a highly interconnected air voids network.

The most common testing methods, which are also part of the Superpave specification testing in US, comprise traditional tests such as the Dynamic Shear Rheometer (DSR) that is used to characterize the rheological properties of binders and mortars, in addition to the Bending Beam Rheometer (BBR) and the Direct Tension (DT) test that are mainly performed at low temperatures in order to investigate their thermal cracking characteristics. Over the past years a number of studies were undertaken in order to evaluate the feasibility of the aforementioned methods in determining the fracture characteristics of asphalt binders and mortars at low and intermediate temperatures.

Ponniah et al. (1996) used a notched three point bending beam test to determine the fracture toughness K_{IC} and fracture energy G_{IC} for modified binders. They showed that the fracture energy of four binder types correlated well with the low temperature performance as obtained through the Thermal Stress Restrained Specimen (TSRS) test, and hence concluded that the use of fracture energy is a promising parameter on the basis of which low temperature performance specifications for modified binders can be developed. In another study, Hoare and Hesp (2000) investigated the effect of sample size and the presence of a notch on fracture toughness and energy for unmodified and polymer modified binders. The study concluded that there were not significant differences in the fracture toughness values between samples with different sizes. However, a high variability on the results obtained from the tests with notched and unnotched samples was observed; the authors concluded that the use of notched samples may result in a more accurate prediction of fracture energy at low temperatures, which in turn may provide better predictions with respect to fracture performance.

Anderson et al. (2007) also used a single notched beam test to determine the fracture toughness of fourteen different binder types. The results suggested that fracture toughness provides a better tool for ranking asphalt binders with respect to their low temperature cracking performance, in comparison with the current Superpave specification criteria. Moreover, Ohio University developed the Asphalt Binder Cracking Device (ABCD) as an alternative test method to characterize the low temperature properties of modified asphalt binders (Kim 2007). This test method was designed in a way that replicates better the conditions in the field and thus, correlate well with the performance of actual test pavements.

Together these studies provide important insights into the fracture properties of asphalt binders, mainly at low temperature and without considering the effect of moisture. Nevertheless, moisture can substantially change the rheological properties of binders and mortars in time and therefore, their mechanical properties and performance characteristics. In literature, however, there are only a few studies on the influence of moisture on the degradation of the mechanical properties of asphalt binders or mortars. Cheng et al. (2003) used the Universal Sorption Device (USD) to measure the amount of vapor water in a thin binder film. They developed a diffusion model that distinguishes between adsorption at the binder surface and absorption within the binder. Figure 3.2 shows the mass increase of water in a binder film with moisture conditioning time due to adsorption and absorption. After a relatively short time, water is adsorbed on the surface of the film; consequently any additional gain in the weight is attributed to absorption of moisture into the bulk of the binder. The model was used to determine the total sorption of moisture with time for two binder types. Moreover, they performed repeated load mechanical tests on mixtures prepared with the same binders. The results showed that the rate of damage was higher rate for the binder that absorbed a greater amount of moisture, indicating thus that, ultimately, it is the amount of moisture in the binder that significantly influences the progression of damage and not the rate of moisture diffusion.

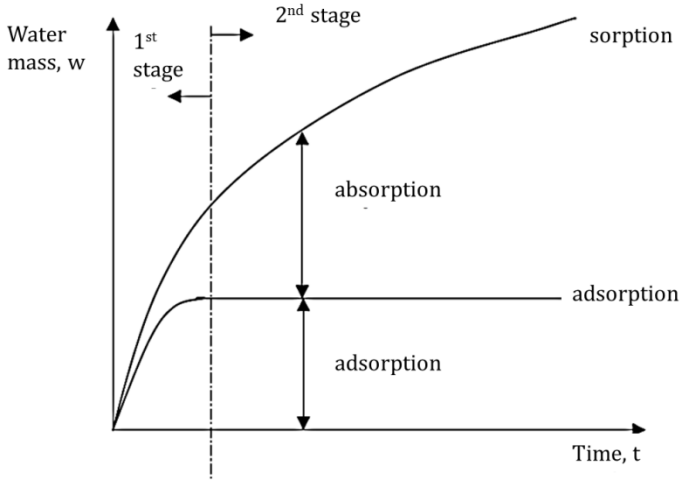

Figure 3.2. Moisture sorption in a thin binder film (after Cheng et al. 2003).

In Delft University of Technology, Kringos et al. (2011) developed a methodology that allowed the determination of adhesive and cohesive strength as a function of moisture content, based on a combination of numerical analysis and experimental tests, as shown schematically in Figure 3.3. This approach allowed the comparison of cohesive and adhesive damage strength and enabled the determination of the prevailing failure mode in an asphalt mixture. For the cohesive strength tests, a special sample geometry was developed and tested at various moisture conditioning intervals. Subsequently the strength results for the mortars were compared to those obtained from adhesive tests, for the same mortars and under the specified testing conditions, resulting thus in a more fundamental material selection procedure.

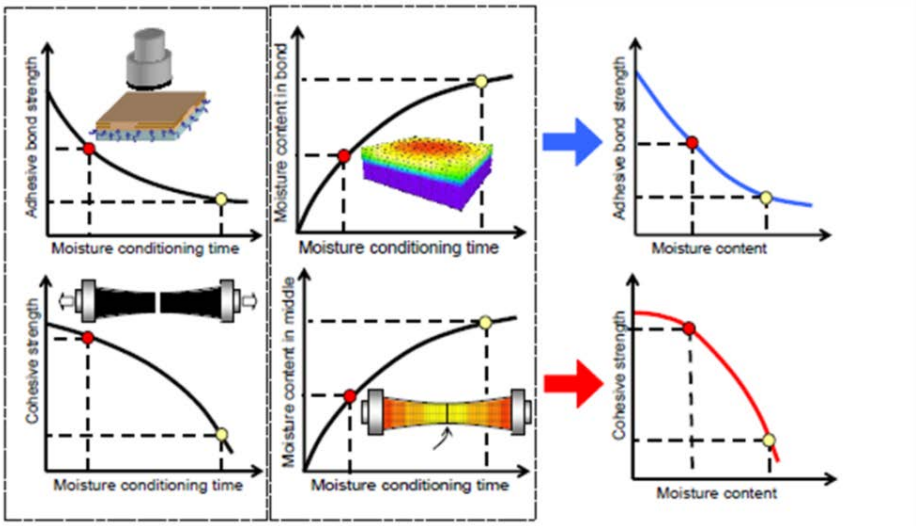

Figure 3.3. A method for the determination of adhesive and cohesive strength at various moisture contents (after Kringos et al. 2011).

It has been demonstrated that adhesion and cohesion failure modes are related to each other, and depending on the conditions the failure mode may change or a mixed failure mode can occur (Copeland 2007, Moraes et al. 2011, and Bahia et al. 2012). Copeland (2007) measured the bond strength of various aggregate-binder combinations, under dry and wet conditions, using a modified version of the ASTM D4541 pull-off test that is typically used in the coating and adhesives industry. Moisture conditioning was found to decrease the strength of the adhesive bond; however in most cases the failure mode was cohesive. The study, hence, concluded that the use of pull-off tests alone cannot be used to describe the failure characteristics of bituminous systems, but tests to determine the cohesive properties of asphalt binders are also required. More recently, Moraes et al. (2011) utilized another variant of the PATTI test (Youtcheff & Aurilio 1997, Kanitpong & Bahia 2005) to characterize damage in aggregate-binder systems. The findings showed that bond strength decreases under wet conditions for all binder-aggregate combinations and moreover, depends significantly on the moisture conditioning time and the type of binder modification. In addition, an alteration of the failure mode was observed to occur after moisture conditioning, changing from cohesive failure, at dry conditions, into adhesive failure in the presence of water.

The studies presented thus far provide evidence that the use of adhesion tests alone cannot fully described the moisture susceptibility characteristics of asphalt mixtures, but tests for the determination of the cohesive properties of asphalt binders or mortars should be also considered. To this end, the objective of this chapter is to investigate the cohesive properties of asphalt mortars and how these can change under the influence of moisture, at low and intermediate temperatures, through a series of uniaxial tension tests. In addition, a new data analysis procedure is introduced to allow the determination of fracture energy of the mortar samples at low and intermediate temperatures.

3.2 Characterization of mortar cohesion properties

The direct tension test has been known to be an appropriate test method to measure the cohesion properties of asphalt binders. However, the conventional direct tension test, as performed based on the AASHTO T314 (2000) test procedure, demonstrates low repeatability, mainly due to the geometry of the testing sample, which results in a long middle section as shown in Figure 3.4. Failure can occur anywhere in the middle section, due to the uniformity of the stress field there, but it is also possible that the samples fracture in the location of changing geometry where stress concentrations can develop. The fact that it is not possible to effectively control the fracture plane precludes the accurate positioning of the instrumentation used for data collection.

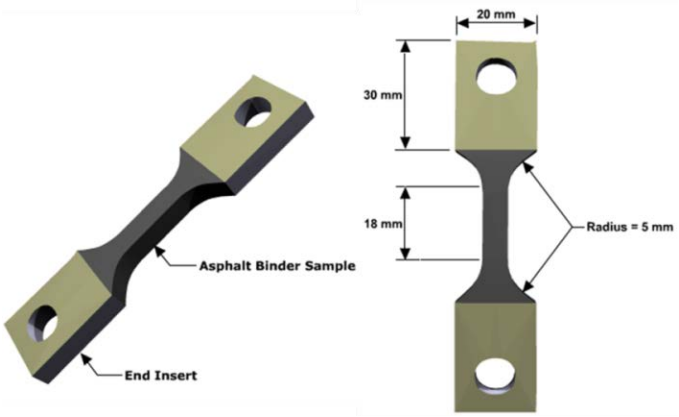

Figure 3.4. Geometry of the testing sample used in direct tension tests (reprinted from Pavement Interactive-http://www.pavementinteractive.org/).

For this reason, and on the basis of earlier experience in Delft by Erkens (2002) and Kringos (2011), parabolic dogbone-shaped samples were used for uniaxial tension tests, which ensure prevent the development of the fracture plane in the middle of the sample and hence enable the positioning of instrumentation. Except from sample geometry, other factors such as the testing setup and the sample preparation procedure were considered and further modified to ensure reproducibility and repeatability of the test results. The protocol developed for direct tension testing was then used to assess the mechanical strength and fracture energy of asphalt mortars under the influence of moisture conditioning and freeze-thaw cycles.

3.2.1 Sample geometry

Taking into consideration the drawbacks of the traditional sample geometry for the direct tension test, a parabolic dogbone sample was developed. The parabolic geometry of the dogbone sample has been used earlier in a study by Erkens (2002) and Kringos et al. (2011). The sample geometry, however, was modified for this study as the previous geometries were relatively large in size. Given that this test was meant to study moisture susceptibility, a large sample size would increase significantly the time for water bath conditioning. The proposed sample geometry has smaller size, which allows for shorter moisture conditioning times and for less binder material to be used.

The sample has a cylindrical parabolic shape, as shown in Figure 3.5; the largest cross-sectional diameter of 21 mm (excluding the thickness of the rings) is at the ends and it is gradually reduced to 16.5 mm at the middle part of the sample. The gauge length of the sample was 34 mm. The reduction of the cross-section is nearly 30% and it is considered large enough to induce crack initiation at the centre of the sample. Considering that the horizontal line of symmetry and the vertical directrix of the parabolic curve pass through the middle cross-section of the sample and the longitudinal axis, respectively, the radius of the cross section at any height z can be calculated by means of the following equation

$$R(z) = 0.00778z^2 + 8.25 \quad [3.1]$$

During sample preparation, stainless steel rings were used, at the top and bottom part, to enable clamping of the sample onto the test setup. The clamping rings were 1.5 mm in thickness and 15 mm in height.

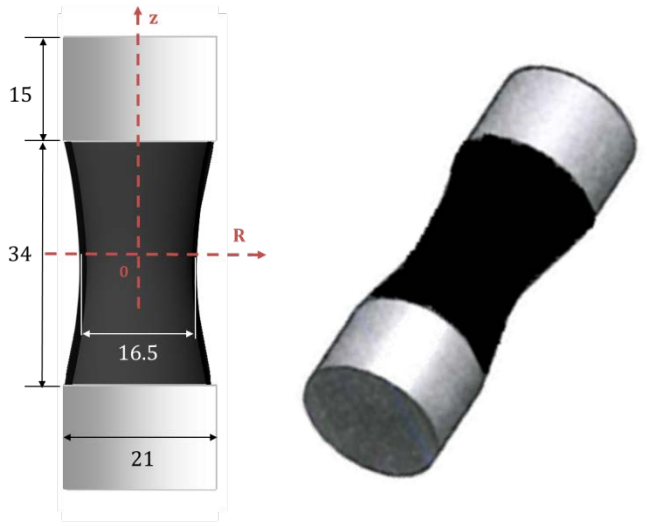

Figure 3.5. Sample geometry and dimensions, in mm.

3.2.2 Mix design and sample preparation

The production of asphalt mortar samples involved three steps, explicitly the fabrication of contra-moulds and moulds, the mix design and finally the actual production of the samples. Two types of moulds were produced, namely a special mould for obtaining the desired sample geometry and a mould for hosting the samples during bath conditioning and before testing so as to avoid any deformations. Initially contra-moulds with the chosen dimensions were produced, which were then used for the production of the moulds. At this point, special attention was placed on the selection of the material used for making the moulds considering of three particular issues: (a) the moulds had to be stiff, so they could carry the weight of the samples, (b) they had to be flexible enough in order to easily remove the samples without destroying them and (c) sticking of the mortar on the walls of

the mould had to be avoided. To overcome these problems, the moulds were prepared using two types of silicon rubber, a soft and harder one, which were mixed in appropriate proportions in order to achieve the desired stiffness of the silicon moulds.

In total, four mortar types were prepared using a virgin PEN 70/100 bitumen (source: Total) and two Styrene-Butadiene-Styrene (SBS) polymer modified bitumens (source: Shell and Ooms), two types of mineral filler, i.e. a limestone Wigras 60 and a hydrated lime Wigro 60K (25% hydrated lime) filler, and crushed Norwegian sand (125 μm<d<1 mm). The constituents were mixed in a ratio of 25:25:50 (bitumen: filler: sand) by weight of mixture and were selected so as to imitate the mix design of mortar typically used in porous asphalt mixtures in the Netherlands (Kringos et al. 2008b). Table 3.1 summarizes the specific properties of all bitumens and Table 3.2 shows the mix design of the mortars.

Table 3.1. Bitumen specifications

Property	**Neat bitumen**	**Cariphalte XS**	**Sealoflex 5-50 (PA)**
Penetration at 25°C (0.1. mm)	70 - 100	45 - 80	60 - 90
Density at 25°C (kg/m^3)	1027	1010	1025
Kinematic viscosity at 135°C (mm^2/s)	≥ 230	> 900	150 - 250
Softening point (°C)	43 - 51	> 65	> 65

Before sample preparation, the mixture components as well as the moulds and the steel rings were placed in the oven at 180°C for 2 hrs. Then bitumen, filler and sand were mixed in the following order; first the filler was added in the hot bitumen and mixed using a hand shear mixer and next the sand was added. A mixing temperature of 165°C was used for the mortar types prepared with the unmodified bitumen, while the temperature was increased to 185°C for the polymer modified bitumen types.

Table 3.2. Asphalt mortar mix design

Mortar ID	**Bitumen [25% w/w]**	**Filler [25% w/w]**	**Sand [50% w/w]**
A	Pen 70/100	Wigras 60	Norwegian crushed sand
B	Pen 70/100	Wigro 60K	Norwegian crushed sand
C	Cariphalte XS	Wigro 60K	Norwegian crushed sand
D	Sealoflex 5-50 (PA)	Wigro 60K	Norwegian crushed sand

Subsequently, the mixtures were poured in the moulds and were again placed in the oven at high temperature so as to reduce the mixture viscosity and suppress air void formation during the consolidation process (no compaction effort was applied). Then, the mortar samples were allowed

to cure for 24hrs at 20°C, the excess material was removed. Finally, the samples removed from the moulds in a cold chamber, at 5°C, in order to prevent any distortion. Then all samples were placed in the accommodating moulds and stored in temperature controlled chamber (at 20°C), until placed in the bath for conditioning and testing.

3.2.3 Tension test setup

The design of the test setup is of paramount importance so as to perform properly a direct tension test. A numbers of aspects have to be considered such as the proper gripping and alignment of the test sample, the force capacity and the sensitivity of the load cell, the rigidity of the loading frame and the appropriate installation of the measuring instruments.

During the tension test, the loading axis must, continuously, coincide with the longitudinal symmetry axis of the sample. If any misalignment occurs, then the sample will be subjected to a combination of axial loading and bending. As a result, apart from axial stresses, bending stresses will also develop along the height of the sample and fracture may occur at a stress level considerably lower than the true tensile one. There is a variety of methods that are used to fix the samples onto the testing machine; for example bonding the sample directly to the MTS actuator using an epoxy adhesive (Kringos et al. 2008b), using end inserts that are moulded with the samples as shown in Figure 3.4 (AASHTO T314 2000, Niu et al. 2014) or using gripping fixtures. The choice of the gripping method mainly depends on the sample geometry. However, each method entails possible problems. For example the use of an adhesive to glue the samples increases the time for test preparation and also care should be taken with regard to the type as well to the amount of the adhesive in order to prevent non-uniform gluing of the sample (Bolzan & Huber 1993). In the case of end inserts, possible drawbacks are related to the adhesion of the insert with the asphalt binder that can result in failure in the insert-binder interface rather than in the middle of the sample (Niu et al. 2014).

In this study, a tailor-made clamping fixture was developed for fixing the sample on the testing machine. The tension test setup comprises a highly rigid loading frame in which a servo hydraulic universal testing machine (UTM 12) with a 15kN actuator was mounted. The device consisted of two clamping heads with attached hinges that were used to fix the sample, and therefore keep it aligned so as the forces to be applied along the specimen axis. The sample is fixed to the clamping heads using screws and then the hinges are attached to the actuator, as shown in Figure 3.6. The use of screws ensures that the sample will not slip out of the clamping head and is placed perpendicular; therefore any deviation from its proper position is avoided. Moreover, the clamping heads were designed in such way, that unless the sample is perfectly aligned and the ends of the sample are in parallel, it cannot be fixed to the setup. The tension testing setup was placed in a temperature controlled chamber to maintain a constant temperature during testing.

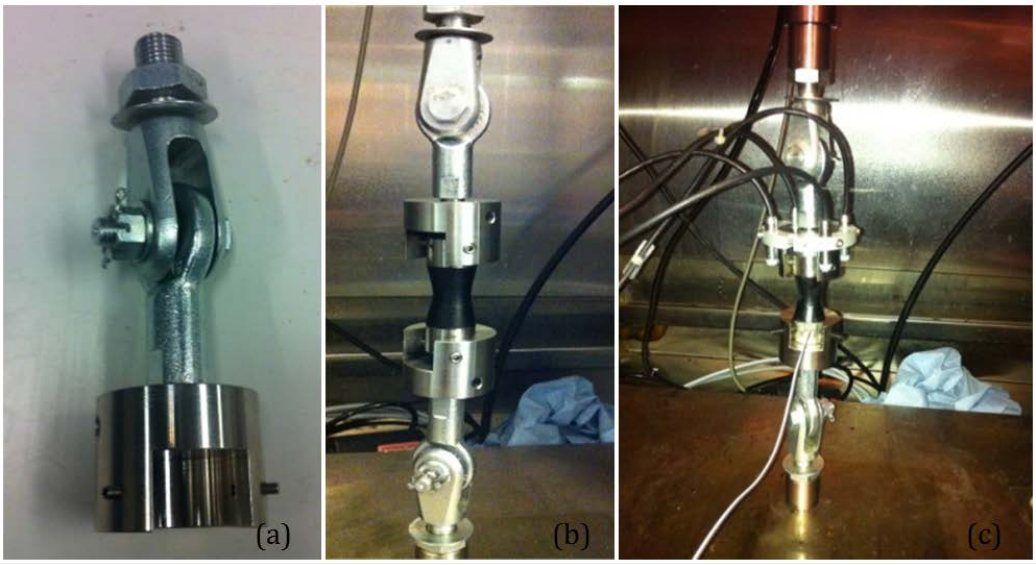

Figure 3.6 (a) The tailor-made clamping head, (b) the sample fixed onto the testing machine and (c) details of the positioning of LVDTs on the sample.

During the test, the applied load and the axial deformation were recorded. The axial deformation was measured using three LVDTs. For the specific test conditions, ±0.5 mm LVDTs were used. In this research, three Solarton displacement transducers were used to control the applied deformation signal and record the total deformation of the sample. Also, a calibration procedure was performed, so as to ensure that the measuring control system records the real deformation of the sample. Using a calibration unit the transducers were set to a given deformation and the corresponding voltage was registered. The displacement transducers were attached to a ring with holes, and were fixed directly to the sample. The measuring devices were connected to an input/output board, which consisted of a BNC connection panel, and then the data were collected via a data acquisition board installed in the computer. The measurement system was connected to a PC-based data acquisition system, which produced a single ASCII output file for each test. The data acquisition procedure was controlled through TestPoint data acquisition software.

3.3 Conditioning and testing protocols

The interaction of moisture with asphalt mortars is known to reduce the strength and stiffness, leading thus to mortars with low performance characteristics under mechanical loading. Apart from moisture, asphalt mortars are subjected to thermal cycles due to temperature variations that can fatigue the material. At extremely low temperatures cracking can occur once the developed tensile stress exceeds the tensile strength of the mortar. The effect of temperature, moisture and of their combination on the cohesive (tensile) strength of the mortars was investigated after the samples were subjected to five different conditioning regimes, explained in detail below.

Protocol I: In this protocol the mortar samples were tested at dry conditions, after one week of curing at 20°C. The aim of protocol I was to provide a reference value without any moisture or thermal conditioning.

Protocol II: This protocol involved conditioning of the mortar samples in a water bath and was used to study the influence of moisture conditioning on their cohesion properties. First, the dry weight of the samples was recorded. Following this, the samples were fully submerged in a water bath at room temperature (20°C). Next, the weight of each sample at saturated surface-dry conditions (SSD) was measured, using a sensitive microbalance, at periodic time intervals. Immediately after the weight measurement, the samples were placed back in the bath. After 203 days of conditioning the samples were removed from the water bath.

Protocol III: The samples were partially dried for 165 days following the 203-days moisture conditioning phase (protocol II). A subset of the mortar samples were removed from the water bath and placed in a climate chamber with relative humidity of 20% at 20°C. During the drying phase, the weight loss of the samples was recorded at regular time intervals. The aim of the protocol was to investigate the reversibility of mortar strength upon drying.

Protocol IV: The aim of the protocol was to study the effect of differential thermal expansion on the tensile strength of the mortar samples. Dry samples were tested after the application of freeze-thaw cycles. The protocol was based on the NEN-EN 1239 (2011), which is a standard method for the evaluation of freeze-thaw stability of adhesives. The samples, without any prior moisture conditioning, were placed in sealed containers and then they were kept in the freezer at -10±1°C for 16 hours. Afterwards, the samples were removed from the freezer and were allowed to thaw at room temperature for 8 hours. This procedure was repeated five times.

Protocol V: Protocol VI is a combination of protocols II and IV and aims to investigate the effect of thermal loading on the strength of moisture conditioned mortar samples. Consequently, the samples were tested after 203 days of moisture conditioning followed by application of freeze-thaw cycles.

Overall the samples were tested at three loading rates (1.5%/s, 0.5%/s and 0.05%/s) and two temperatures, namely 20°C and -10°C. For each temperature-loading condition three replicate samples were used. To assess the effects of moisture and temperature on the tensile properties of asphalt mortars 90 samples per mortar type were tested, which resulted in a total of 360 samples.

3.4 Moisture uptake measurements

Moisture uptake tests were performed to determine the response of asphalt mortars to moist environments. The weight increase as a function of time, due to moisture ingress when the material is fully submerged in water, was measured. The results apply directly when the moisture content and temperature of the environment are constant. To investigate the effect of filler and bitumen on the amount of moisture the mortars can hold, the constituents were mixed in the same proportions for all mortar types (please refer to Table 3.2). The weight measurements were then used to

determine the moisture uptake, which is given as the ratio of the amount of moisture absorbed to the initial mass of the sample at dry conditions

$$moisture\ uptake\ (\%) = \frac{m^t - m^o}{m^o} \times 100 \quad [3.2]$$

, where m^t is the weight of the samples at time t and m^o is the initial weight at dry conditions. For each mortar type, 18 samples were conditioned in the water bath. The average dry weight of the samples was 65gr.

Figure 3.7 shows the kinetics of moisture uptake for the four mortar types. Overall, the amount and rate of water uptake varied with mineral filler and bitumen type. It is clear that moisture uptake has not reached an asymptote; hence the samples were not fully saturated. The results show that mortar A, which was prepared with limestone (quicklime) filler, absorbed approximately three times much water than mortar B containing hydrated lime. It is, thus, apparent that the increased water permeability of mortar A can be attributed to the use of quicklime filler. On the other hand, hydrated lime has been known to enhance the resistance of bituminous mixtures against moisture (Plancher et al. 1976, Little and Epps 2001, Little and Petersen 2005, Sebaaly 2007, Lesueur et al. 2013). The moisture damage resistivity of mixtures containing hydrated lime can be mainly attributed to the improved bitumen-aggregate adhesion due to the formation of calcium ions that modify the aggregate surface properties and due to chemical interactions with the bitumen, which also result in the improvement of its adhesive properties (Lesueur at al. 2013). The results of the moisture uptake tests, however, suggest that the low moisture uptake of asphalt mortars achieved with the use of hydrated lime, might be an added mechanism to explain the improvement of mixture mechanical performance.

It was also observed that the moisture uptake of the two SBS polymer modified bitumens varied. In general, the weight increase due to moisture ingress for both SBS modified mortars was substantially lower, approximately two times lesser, than for mortar B containing a straight run 70/100 bitumen. The presence of styrenic blocks copolymers in the SBS modified bitumen, which are hydrophobic in nature (Kennedy & Higginbotham 2011), might act as a hindrance to moisture diffusion and explain the lower moisture absorption. The water uptake profiles of mortars C and D were dissimilar, even though both contained SBS modified bitumen. This might be a result of the variability of the SBS content or of the differences in the density of the bitumens. However, no data are available with respect to the percentage of SBS modifier used.

Similarly, the rate of moisture absorption varied significantly for the various asphalt mortars. Mortar A, containing limestone (quicklime) filler, had a higher absorption rate compared to all other mortars. The results show that the polymer modified mortars demonstrated different absorption behaviour; the SBS modified mortar D (Sealoflex 5-50) was found to absorb moisture in a lower rate compared to mortar C. Figure 3.7 shows that after 20 days of moisture conditioning, no moisture uptake was recorded for mortar D, while mortar C had 0.15% of weight increase due to moisture. The results suggest that mortar D will saturate slowly, as the rate of moisture uptake and the moisture content are low, while the opposite can be assumed for mortar A.

Overall, the rates of moisture absorption reduced after roughly 120 days of conditioning in the water bath. Considering that diffusion is a gradient driven process, moisture diffuses down to the concentration gradient. Initially, high moisture concentrations were applied on the surface of the mortars (which were at a dry state), causing thus large concentration gradients (at the mortar-atmosphere interface) and hence, rapid diffusion. As time progressed, moisture concentration inside the material increased and consequently, the concentration gradient gradually diminished (at equilibrium it tends to zero), reducing thus the diffusion rate.

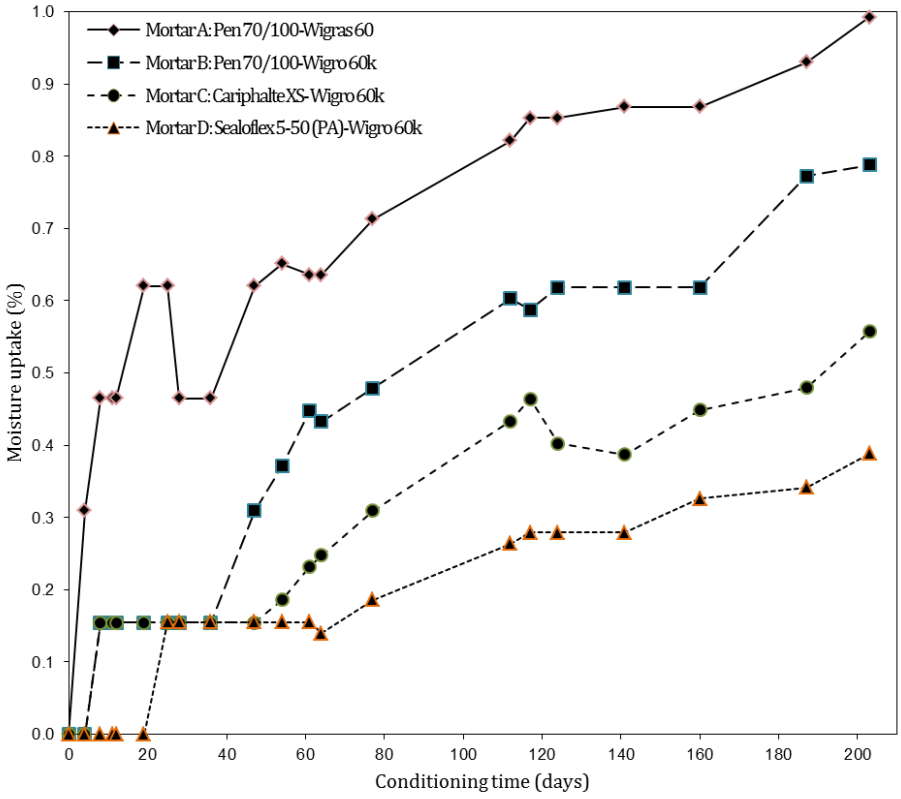

Figure 3.7. Average moisture uptake of asphalt mortars containing different filler and bitumen types.

After the samples were moisture conditioned, they were subjected to a drying process. As described in protocol III the samples were kept at a climate chamber with relative humidity of 20%, so as to create appropriate conditions for desorption to occur. Moisture desorption typically occurs when a material is placed in an environment, at which the moisture concentration is less than the concentration required for maintaining its current saturation level. The greater the difference between the moisture concentration on the mortar surface and the atmosphere, the higher the drying rate. For polymers, however, considerable hysteresis may occur if absorbed molecules are strongly bounded in the polymer. Therefore, higher energies or longer times may be required for this material to return to the dry state (Duncan et al. 2005). Figure 3.8 shows the average mass loss of all mortar types after 165 days of drying.

In all cases, a high desorption rate was observed at the beginning of the drying phase. This indicates that moisture adsorbed on the surface was released first, followed by desorption of moisture from the bulk of the mortars. Overall, the drying rates of the polymer modified mortars C and D were higher compared to those of mortars A and B. With respect to the amount of moisture lost, mortars A, C and D showed the greater loss, which was approximately three times higher than the amount of moisture lost for mortar B. Based on the moisture uptake and loss measurements, it is anticipated that mortars C and D would be less susceptible to moisture damage, as they can hold less moisture and moreover release moisture easier upon drying.

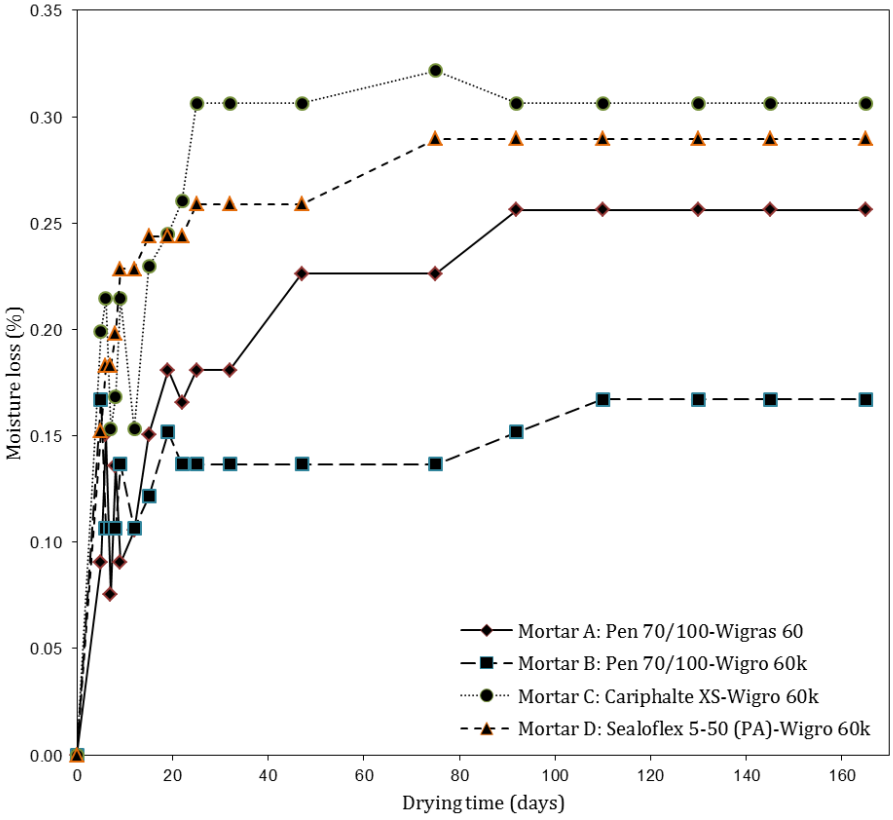

Figure 3.8. Average moisture loss during drying process.

3.5 Uniaxial tension tests

Direct displacement-controlled tension tests were performed at constant loading rates of 1.5%/s, 0.5%/s and 0.05%/s (or 0.50 mm/s, 0.17 mm/s and 0.017 mm/s, respectively), considering an effective length of 34 mm (length between the clamping rings). The tests were performed at 20°C and -10°C. Figure 3.9 shows typical results of the mortar tension tests at intermediate and low temperatures.

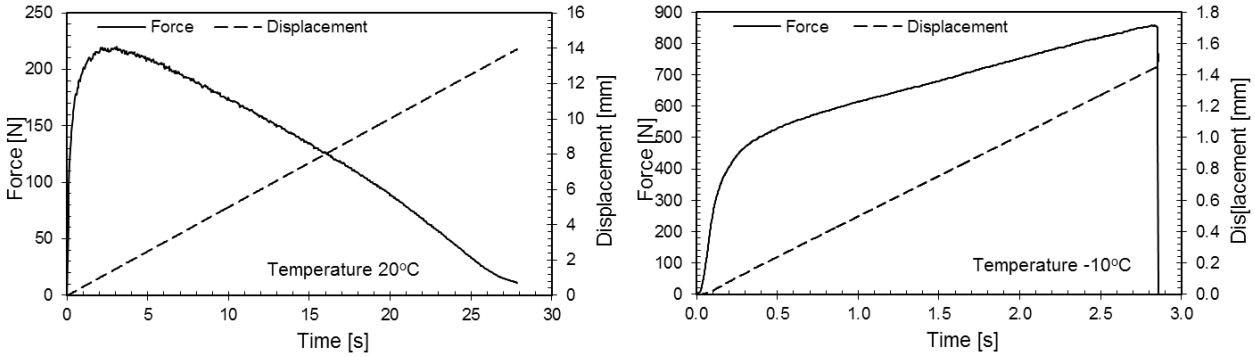

Figure 3.9. The right and left graph show the DTT results at 20°C and -10°C, respectively.

At low temperature, the samples were in a brittle state; as a result a clear fracture plane at the centre of the sample was observed. On the other hand, at intermediate temperature, the samples exhibited large deformation (necking) before fracture. Figure 3.10 demonstrates the distinct differences between the failure modes.

Figure 3.10. Mortar samples after testing at a temperature of (a) -10°C and (b) 20°C.

The behaviour of a viscoelastic material during a direct tension test is illustrated in Figure 3.11. The material is assumed to be homogeneous at the macroscale and the test is performed in a displacement-controlled mode. The parabolic shape promotes concentration of damage and, eventually, tensile fracture at the middle of the sample where the longitudinal stress is highest. Up to the peak load, the integrity of the sample is maintained. Beyond the peak load, necking occurs at the middle of the sample and as the total applied displacement increases, damage within the fracture zone increases rapidly causing a reduction in the longitudinal stress of the sample. Because of this stress reduction, the parts of the sample on either side of the fracture zone unload. The graph in Figure 3.11 distinguishes the individual responses beyond the peak load; the solid line denotes the cracking response in the failure zone and the dashed line represents the unloading of the uncracked parts.

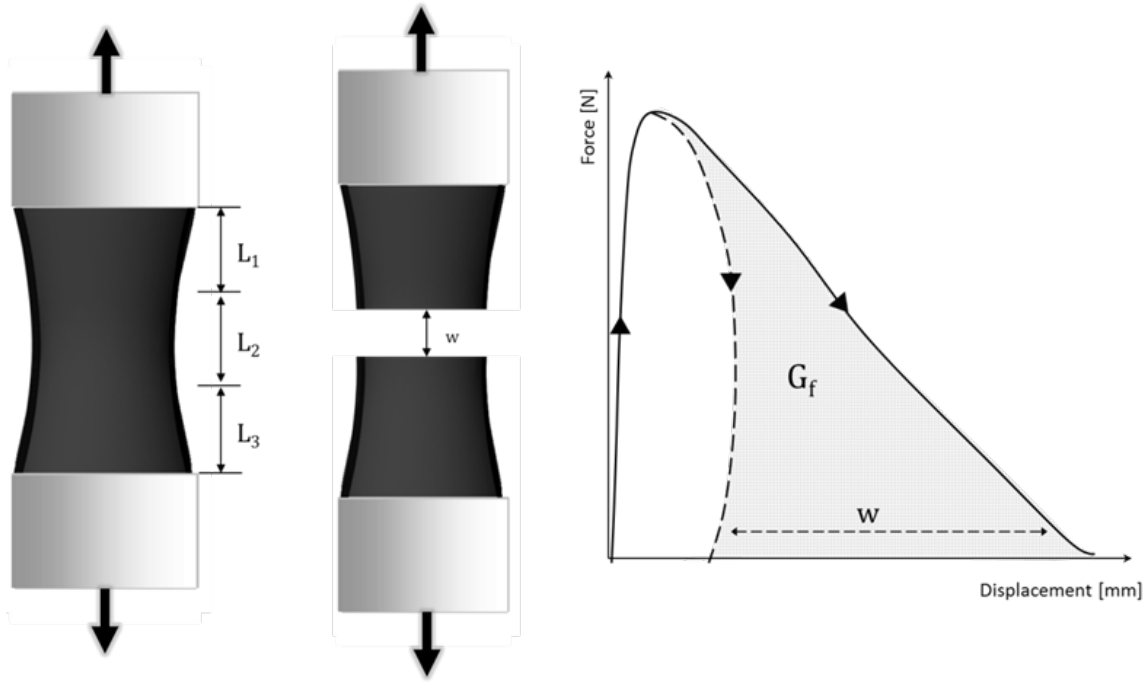

Figure 3.11. Behaviour of a viscoelastic material during a direct tension test.

Here, the definition of crack width *w* is given as the difference between the total deformation and the deformation of the uncracked parts. The area under the load-crack width curve, which can be given as the difference between the overall and unloading descending branches, is considered to be the energy per unit area in the fracture zone (G_f). Hillerborg (1985) provides the definition of the total energy absorption W, during a tension test, as the area below the load-deformation curve; one part of the absorption energy is related to the area below the stress-strain curve and another part to the area below the stress-crack width curve. In the complete stress-deformation diagram the two parts are separated by the unloading curve from the peak load.

The calculation of fracture energy requires that the true stress-strain curve is determined after necking initiates. This is not possible only from the force-displacement data, unless measurements of the length change and reduction of the cross-sectional are obtained in time. Then the expressions [3.3] and [3.4] can be used to obtain the true stress and strain of the material.

$$\sigma_t(t) = \frac{F(t)}{A_t} \qquad [3.3]$$

$$d\varepsilon = \int_{L_o}^{L_t} \frac{1}{L}\, dL \Rightarrow \quad \varepsilon = \ln\left(\frac{L_t}{L_o}\right) \qquad [3.4]$$

, where σ_t is the true tensile stress (MPa), F is the applied force (N), A_t is the cross-sectional area of the sample (mm^2) at time t, ε is the true strain (%), L_o is the original length of the sample (mm) and L_t is the measured length at time t (mm).

Alternatively, the true stress and strain curve can be estimated by defining the relation of total axial deformation (extension) with the changes in the length and cross-sectional area of the part of the sample that undergoes necking by means of finite element large deformation viscoelastic models. Such an approach was adopted by Niu et al. (2014) with the aim of calculating fracture energy from direct tension tests at intermediate temperatures. However, in this case, there were limitations related to the accurate simulation of large-strain and fracture phenomena in viscoelastic materials, as well as to the variability of binder properties.

A more straightforward way to calculate fracture energy is to register the unloading response during testing (Erkens 2002). Nevertheless, obtaining the different responses in the post-peak regime is not always a trivial task to perform. Recording the recovery in ductile materials is difficult as unloading occurs gradually. Also, the instrumentation of specific geometries can be very difficult, especially since nowadays more tests are performed at micromechanical (material) level. Therefore, a new data analysis procedure was developed to allow for the calculation of fracture energy when only force-displacement data from a direct tension test are available. The following section presents a detailed description of the procedure.

3.5.1 Calculation procedure for fracture energy

The aim of the data analysis procedure is to obtain an accurate measure of the total energy absorption and energy per unit area in the fracture zone, when only force-displacement data are available and consequently the estimation of the true stress-strain curve is not feasible. The procedure uses nonlinear finite element analysis to specify the unloading response outside the fracture zone, and then utilize this information to calculate the energy absorption and fracture energy of the material.

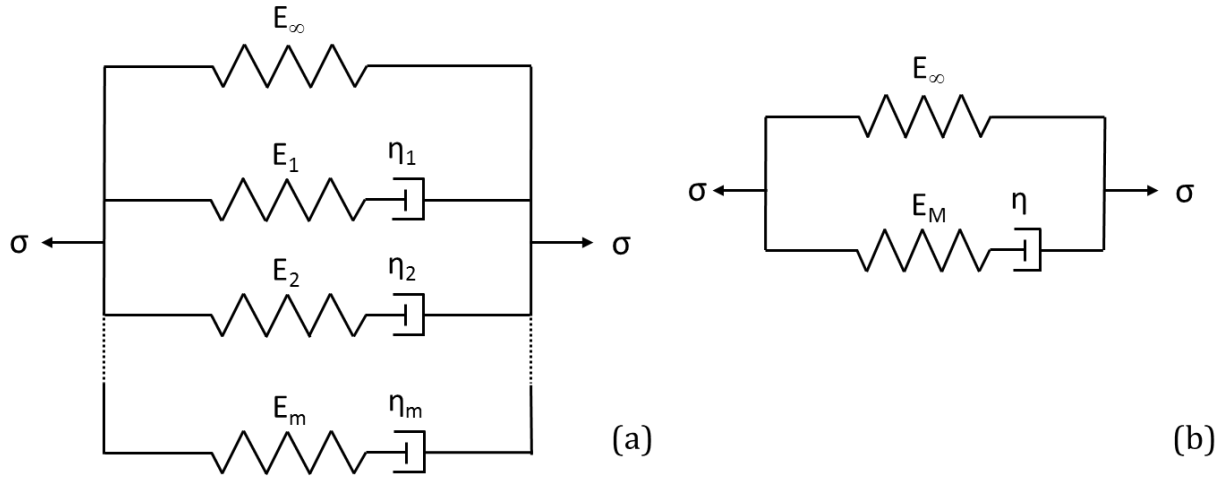

Figure 3.12. Schematic of the (a) Generalized Maxwell model and (b) Zener model.

A simplified version of the Generalized Maxwell viscoelastic model, Figure 3.12(a), the Zener model, was used to model the behaviour of the mortar samples. The Zener model was chosen

because its constitutive relation is simple and the analytical solution for conventional laboratory tests, namely creep or relaxation tests, uniaxial tension and compression tests, can be easily derived. Figure 3.12(b) shows that the model consists of two parallel components, i.e. an elastic spring with modulus E_∞ and a viscoelastic Maxwell component, which consists of a spring with modulus E_M in series with a dashpot with viscosity coefficient η.

The *first step of the data analysis* involved the determination of the model parameters for each mortar type; for this reason the analytical solution for the Zener model for a uniaxial displacement-controlled tension test was derived.

Zener solution for uniaxial displacement-controlled tension test

Since the elastic spring and the Maxwell component are in parallel, the total stress σ in the Zener model is equal to the addition of the individual element stresses

$$\sigma = \sigma_\infty(t) + \sigma_{\mathrm{M}}(t) = E_\infty \varepsilon(t) + E_M[\varepsilon(t) - \varepsilon_v(t)] \qquad [3.5]$$

, where σ_∞ denotes the stress of the spring, σ_M the stress of the Maxwell component, $\varepsilon(t)$ and $\varepsilon_v(t)$ the total strain and the strain at the Maxwell component, respectively. The stress at the Maxwell element is expressed as

$$\sigma_{\mathrm{M}}(t) = E_M[\varepsilon(t) - \varepsilon_v(t)] = \eta\dot{\varepsilon}_v \qquad [3.6]$$

, which can be further written as

$$E_M\varepsilon(t) - E_M\varepsilon_v(t) = \eta\dot{\varepsilon}_v \Rightarrow \dot{\varepsilon}_v + \frac{E_M}{\eta}\varepsilon_v(t) = \frac{E_M}{\eta}\varepsilon(t) \qquad [3.7]$$

, where $\dot{\varepsilon}_v(t)$ denotes the time derivative of the strain at the Maxwell component. Considering that in the beginning of the test (at time $t=0$) the total strain is equal to zero the general (or homogeneous) solution of non-homogeneous differential equation [3.7] is

$$\dot{\varepsilon}_v + \frac{E_M}{\eta}\varepsilon_v(t) = 0 \Rightarrow \varepsilon_{v,h} = c_1 e^{\frac{E_M}{\eta}t} \quad , c_1 \in \mathbb{R} \qquad [3.8]$$

The particular solution of equation [3.7] is the convolution integral

$$\varepsilon_{v,p} = \int_0^t e^{-\frac{E_M}{\eta}(t-s)} \frac{E_M}{\eta}\varepsilon(s)\ ds \qquad [3.9]$$

Integrating by parts yields

$$\begin{aligned}\varepsilon_{v,p} &= \int_0^t e^{-\frac{E_M}{\eta}(t-s)} \frac{E_M}{\eta}\varepsilon(s)\ ds \\ &= \frac{E_M}{\eta} e^{-\frac{E_M}{\eta}(t)} \int_0^t e^{\frac{E_M}{\eta}(s)} \varepsilon(s)\ ds \\ &= \frac{E_M}{\eta} e^{-\frac{E_M}{\eta}(t)} \left[\frac{\eta}{E_M} e^{\frac{E_M}{\eta}(s)} \varepsilon(s) \Big|_0^t - \int_0^t \frac{\eta}{E_M} e^{\frac{E_M}{\eta}(s)} \dot{\varepsilon}(s)\ ds \right] \\ &= e^{-\frac{E_M}{\eta}(t)} \left[e^{\frac{E_M}{\eta}(s)} \varepsilon(t) - \varepsilon(0) - \int_0^t e^{\frac{E_M}{\eta}(s)} \dot{\varepsilon}(s)\ ds \right]\end{aligned} \quad [3.10]$$

Given that that $\varepsilon_v(t=0) = 0$, as at time t=0 when the load is applied the dashpot is not active yet, equation [3.10] becomes

$$\varepsilon_{v,p} = \varepsilon(t) - \int_0^t e^{\frac{E_M}{\eta}(t-s)} \dot{\varepsilon}(s)\ ds \quad [3.11]$$

Adding the homogenous solution [3.8] to the particular solution [3.9] yields a general solution of equation [3.7] with arbitrary constants, which can be solved for to meet a given initial condition.

$$\varepsilon_v = c_1 e^{\frac{E_M}{\eta}t} + \varepsilon(t) - \int_0^t e^{\frac{E_M}{\eta}(t-s)} \dot{\varepsilon}(s)\ ds \quad [3.12]$$

Using the condition $\varepsilon_v\ (t=0) = 0$, in equation [3.12], constant c_1 is defined as

$$\varepsilon_v(0) = 0 \ \Rightarrow\ 0 = c_1 + 0 - 0 \ \Rightarrow\ c_1 = 0 \quad [3.13]$$

Therefore equation [3.12] becomes

$$\varepsilon_v = \varepsilon(t) - \int_0^t e^{\frac{E_M}{\eta}(t-s)} \dot{\varepsilon}(s)\ ds \quad [3.14]$$

Substituting equation [3.14] into [3.6] yields

$$\begin{aligned}\sigma_M(t) &= E_M[\varepsilon(t) - \varepsilon_v(t)\ ] \\ &= E_M[\varepsilon(t) - \varepsilon(t) + \int_0^t e^{\frac{E_M}{\eta}(t-s)} \dot{\varepsilon}(s)\ ds] \\ &= E_M \int_0^t e^{\frac{E_M}{\eta}(t-s)} \dot{\varepsilon}(s)\ ds\end{aligned} \quad [3.15]$$

Subsequently the total stress in the Zener model becomes

$$\sigma = \sigma_{\infty}(t) + \sigma_{\mathrm{M}}(t) = E_{\infty}\varepsilon(t) + E_M \int_0^t e^{\frac{E_M}{\eta}(t-s)} \dot{\varepsilon}(s)\ ds \qquad [3.16]$$

In the case of a constant strain rate (displacement-controlled test) the following quantities are defined

$$\begin{aligned} \dot{\varepsilon}(t) &= \varepsilon_{cnst} \\ \varepsilon(t) &= \varepsilon_{cnst} t \end{aligned} \qquad [3.17]$$

Consequently equation [3.16] yields

$$\begin{aligned} \sigma &= E_{\infty}\varepsilon_{cst} t + E_M \varepsilon_{cst} \int_0^t e^{\frac{E_M}{\eta}(t-s)} \dot{\varepsilon}(s)\ ds \\ &= E_{\infty}\varepsilon_{cst} t + E_M \varepsilon_{cst} e^{-\frac{E_M}{\eta}t} \left(\frac{\eta}{E_M} (e^{\frac{E_M}{\eta}t} - 1) \right) \\ &= E_{\infty}\varepsilon_{cst} t + \varepsilon_{cst}\eta e^{-\frac{E_M}{\eta}t} \left(e^{\frac{E_M}{\eta}t} - 1 \right) \\ &= E_{\infty}\varepsilon_{cst} t + \varepsilon_{cst}\eta \left(1 - e^{-\frac{E_M}{\eta}t} \right) \end{aligned} \qquad [3.18]$$

As a result the total stress of the Zener model can be calculated using the expression

$$\sigma = E_{\infty}\varepsilon_{cst} t + \varepsilon_{cst}\eta \left(1 - e^{-\frac{E_M}{\eta}t} \right) \qquad [3.19]$$

Then a methodology was followed to back-calculate the parameters E_{∞}, E_M , η and ε_{cnst} of the Zener model using a non-linear constraint optimization procedure. This process is based on the generalized reduced gradient method that minimizes the difference between the values predicted by the analytical model and the experimental values. For the optimization all model parameters were considered to be positive. Typically when a nonlinear optimization algorithm is applied to minimize the error, the algorithm may find a locally optimum solution to the problem. To overcome this problem, one should use a set of initial values for the decision variables very close to the global optimal set. However, in the present work, it was not possible to know the model parameters in advance; therefore the algorithm was triggered repeatedly, starting from different starting values (seeds) for the decision variables, thus reaching to a solution closer to the global optimum solution.

Parameter determination was performed on the basis of the experimental data until the peak load was reached during the test. However, the parabolic shape of the sample did not allow for a straightforward relation between the overall deformation and the strain over the height of the

sample to be defined, since the specific geometry causes the strain to vary with height (Erkens 2002). As a result, the total displacement was calculated additively by means of the analytical model. Suppose that the sample height is divided into a number of slices with infinitesimal thickness Δl_k (k=1,2,...,m). At every time t_i (i=1,2,..,n) the total displacement δ_{total} of the sample is the sum of the displacement δ_k at every slice

$$\delta_{total}^{t_i} = \sum_{k=1}^{m} \delta_k^{t_i} \quad [3.20]$$

The displacement of each slide (assuming that necking does not occur before peak load is achieved) is defined as the product between the strain at this slice and the original slice thickness Δl_k

$$\delta_k^{t_i} = \varepsilon_k^{t_i} \Delta l_k \quad [3.21]$$

Therefore the total displacement of the sample at every time interval t_i is

$$\delta_{total}^{t_i} = \sum_{k=1}^{m} \varepsilon_k^{t_i} \Delta l_k \quad or \quad \delta_{total}^{t_i} = \sum_{k=1}^{m} \dot{\varepsilon}_k^{t_i} t_i \Delta l_k \quad [3.22]$$

, where $\dot{\varepsilon}_k^{t_i}$ is the strain rate at each slice Δl_k at every time t_i. The parameter determination methodology was organized in two phases. In the first phase, the variables E_∞, E_M , η and ε_{cnst} were obtained by minimizing equation [3.23] at one slice (located at the top of the sample).

$$\min f(E_\infty, E_M, \eta, \dot{\varepsilon}^{t_i}) = \sum_{i=1}^{n} \left(\frac{\sigma_{\exp}^{t_i}}{\sigma_{model}^{t_i}} - 1 \right)^2 \quad [3.23]$$

The first minimization step produces the model parameters that approximately define the stress-time curve, at the top of the sample, as shown in Figure 3.13.

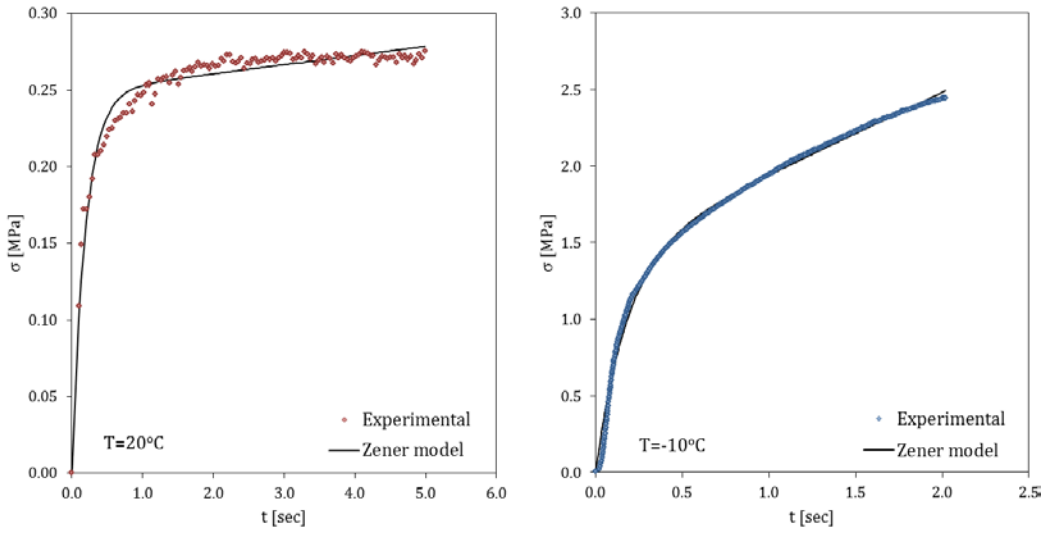

Figure 3.13. Comparison of experimental and estimated stress with time up to peak load at two temperatures.

In the second phase, the same minimization procedure was used to determine the strain rate at each slice at every time. In this phase, the values E_∞, E_M and η were not allowed to vary; in contrast they were equal to those obtained in the first phase. The minimization equation was described as

$$\min f(\dot{\varepsilon}_k^{t_i}) = \sum_{i=1}^{n} \left(\frac{\sigma_{\exp}^{t_i}}{\sigma_{\mathrm{mod}\,el}^{t_i}} - 1 \right)^2, \quad for \quad every \quad k = 1, 2, \ldots, m \qquad [3.24]$$

The total displacement of the sample was then calculated on the basis of equation [3.22]. The thickness of each slice was Δl_k = 0.1 mm. Figure 3.14 shows a comparison of the stress at the top of the sample against the total displacement as obtained from the experiment and predicted by the analytical solution of the Zener model.

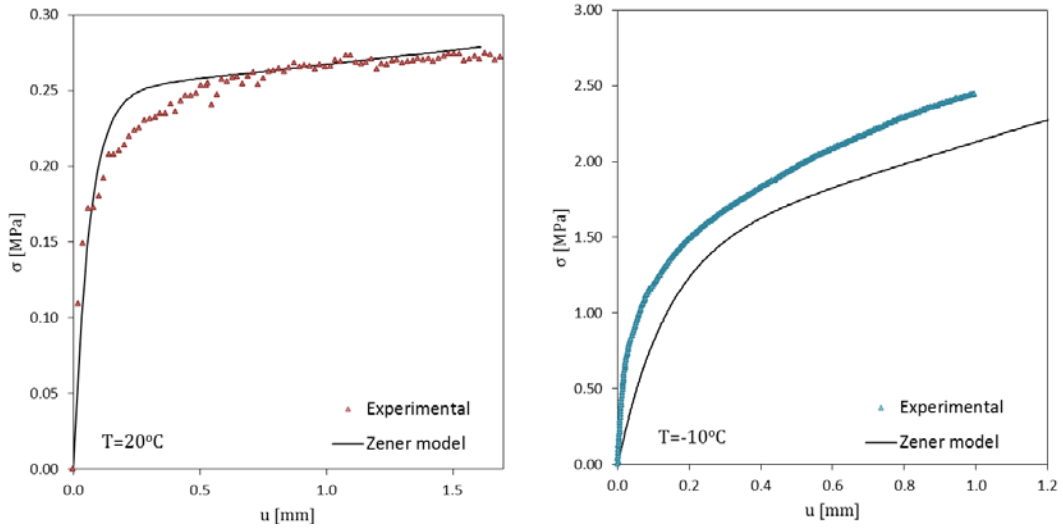

Figure 3.14. Experimental and estimated stress with total displacement at two temperatures.

In the *second step of the data analysis procedure* finite element simulations of the direct tension test were performed. A finite element mesh of the sample geometry, as illustrated in Figure 3.5, was used. The material properties determined in the first step of the optimization process were used for the analysis. Force-controlled tension tests were performed using the viscoelastic Zener material model. For each test the force-time curve as registered during the experiment was imposed on the mesh and the determination of the unloading curve after the peak load was possible.

In the *final step of the data analysis procedure* the fracture energy was calculated on the basis of the experimental and computational results. The difference between the unloading branch, as simulated using the FE method, and the experimental curve after the peak load was reached is defined as the energy in the fracture zone per unit area of the material, as shown schematically in Figure 3.15.

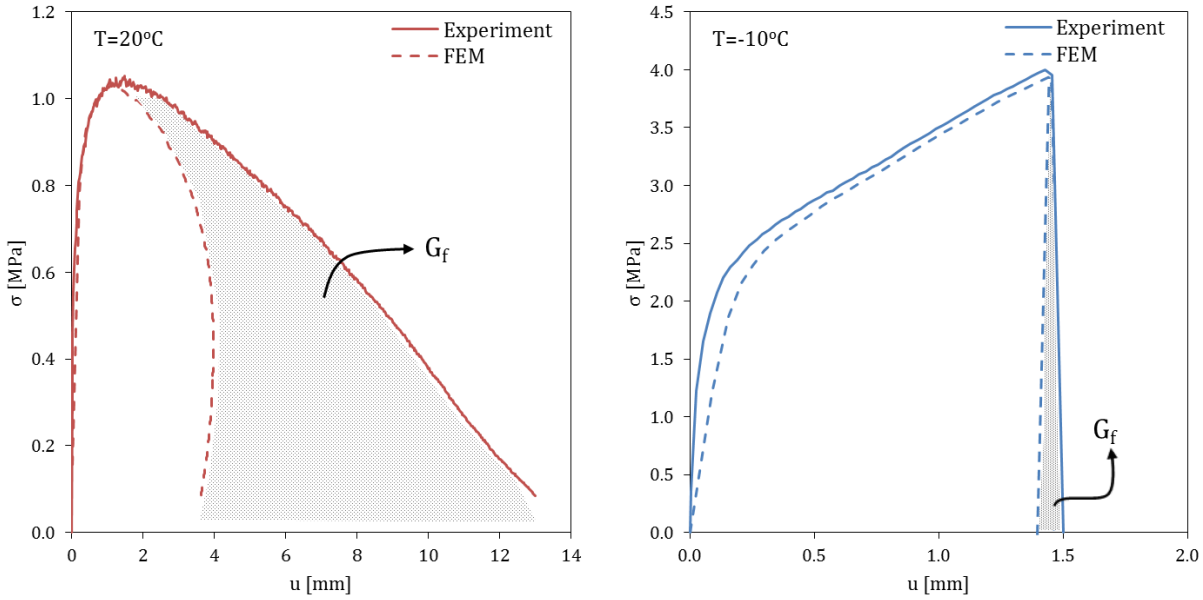

Figure 3.15. Determination of energy per unit area in the fracture zone.

3.6 Test results and discussion

Overall the mortar samples were tested at three loading rates (1.5%/s, 0.5%/s and 0.05%/s) and two temperatures, namely 20°C and -10°C. For each temperature-loading condition three replicate samples were used. To assess the effects of moisture and temperature on the tensile properties of asphalt mortars, five different protocols were used that resulted in a total of 360 samples to be tested. The *data analysis procedure* was used for determining the energy in the fracture zone and total energy absorption for all direct tension tests performed after every conditioning regime. The material properties of each mortar were determined only one time for the highest loading rate. For the remaining two loading rates the material properties were considered to be the same, and therefore only the second phase of the minimization procedure was realized.

3.6.1 Dry response: Influence of filler and bitumen type

Table 3.3 summarizes the results from the direct tension tests at dry conditions. Three replicate samples were tested for each temperature-loading rate combination. The mean tensile strength, total energy absorption and fracture energy at the middle of the sample were estimated for each mortar type. The standard deviation (SD) and coefficient of variation (CV) are also reported. Overall, the variability was observed to be higher for the tests performed at low temperature. To enhance the reproducibility of the direct tension test, apart from changes in sample geometry and testing setup, it is important to maintain a strict testing protocol with regard to sample preparation and testing conditions.

Table 3.3. Results of direct tension test at dry conditions

Mortar ID	Testing conditions		Tensile strength (Nominal stress σ) [MPa]		Total energy absorption W [N mm]		Fracture energy G_f [N mm/mm²]	
	T [°C]	Loading rate [mm/s]	Mean ± SD [MPa]	CV [%]	Mean ± SD [MPa]	CV [%]	Mean ± SD [MPa]	CV [%]
A	20	0.5	0.60±0.14	24.04	99.0±29.0	29.4	2.66±0.84	31.58
		0.17	0.36±0.02	5.98	85.6±7.3	8.4	2.30±0.10	4.33
		0.017	0.11±0.02	21.67	30.2±3.8	12.7	0.81±0.11	13.71
	-10	0.5	4.11±0.71	17.27	23.4±7.8	33.3	0.68±0.33	48.57
		0.17	3.49±0.59	16.92	16.7±6.7	40.1	0.48±0.30	61.47
		0.017	3.29±0.72	21.76	4.95±2.3	47.3	0.14±0.07	47.34
B	20	0.5	0.58±0.02	2.67	106.3±3.8	3.5	3.92±0.01	0.14
		0.17	0.25±0.02	7.57	70.8±3.5	4.9	2.61±0.00	0.00
		0.017	0.06±0.00	6.60	16.5±1.1	6.6	0.61±0.001	0.26
	-10	0.5	3.43±1.17	34.06	6.93±2.9	41.8	0.01±0.002	24.10
		0.17	4.13±0.82	19.76	21.12±7.26	34.4	0.03±0.011	34.31
		0.017	3.75±0.78	20.89	17.65±11.05	62.6	0.03±0.016	63.20
C	20	0.5	1.06±0.03	3.30	135.1±13.2	9.8	5.68±0.03	0.58
		0.17	0.63±0.06	9.30	100.6±3.1	3.1	4.22±0.00	0.01
		0.017	0.21±0.02	11.59	50.2±0.99	1.8	2.10±0.00	0.11
	-10	0.5	4.11±0.15	3.58	45.2±4.5	9.9	0.11±0.02	14.92
		0.17	3.99±1.14	28.48	32.5±13.2	40.6	0.08±0.04	53.70
		0.017	3.83±0.47	12.19	22.4±18.9	84.4	0.06±0.05	85.15
D	20	0.5	0.84±0.06	7.04	174.2±9.6	5.5	2.66±0.31	11.76
		0.17	0.63±0.01	1.99	135.0±16.3	12.2	2.06±0.29	14.17
		0.017	0.30±0.01	3.33	68.8±9.7	14.2	1.05±0.32	30.59
	-10	0.5	5.13±0.37	7.24	30.5±7.6	24.9	1.00±0.25	25.04
		0.17	5.05±0.29	5.83	47.8±6.4	13.4	1.57±0.21	13.55
		0.017	3.05±0.18	6.01	15.4±5.8	37.7	1.76±1.17	66.48

Figures 3.16-3.19 clearly show the significant influence of loading rate and temperature on the response of asphalt mortars. A higher loading rate always generates higher peak stress and fracture energy. At low temperature, however, the effect of loading rate on fracture energy was not that significant; the fracture energy-loading rate curve gets flatter with a decrease in testing temperature, which indicates that the influence of loading rate on the energy required to break the sample is diluted with the reduction in temperature.

The test results also confirm the significant effect of temperature on the material tensile strength, since tensile strength increased as temperature reduced. Overall, asphalts mortars tested at low temperature exhibited a more brittle behaviour and resulted in lower values of fracture energy. On the other hand, at intermediate temperature, the mortars underwent larger deformations in addition to lower strength levels and higher fracture energy, indicating thus a more ductile behaviour.

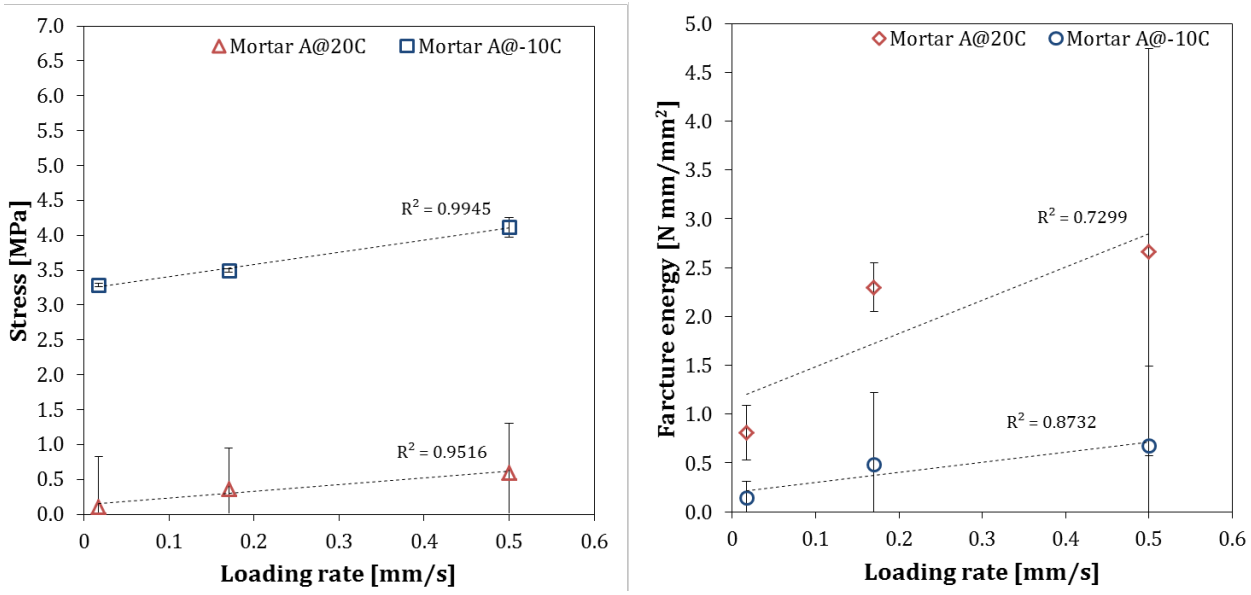

Figure 3.16. Tensile strength and fracture energy for mortar A at each loading rate and temperature.

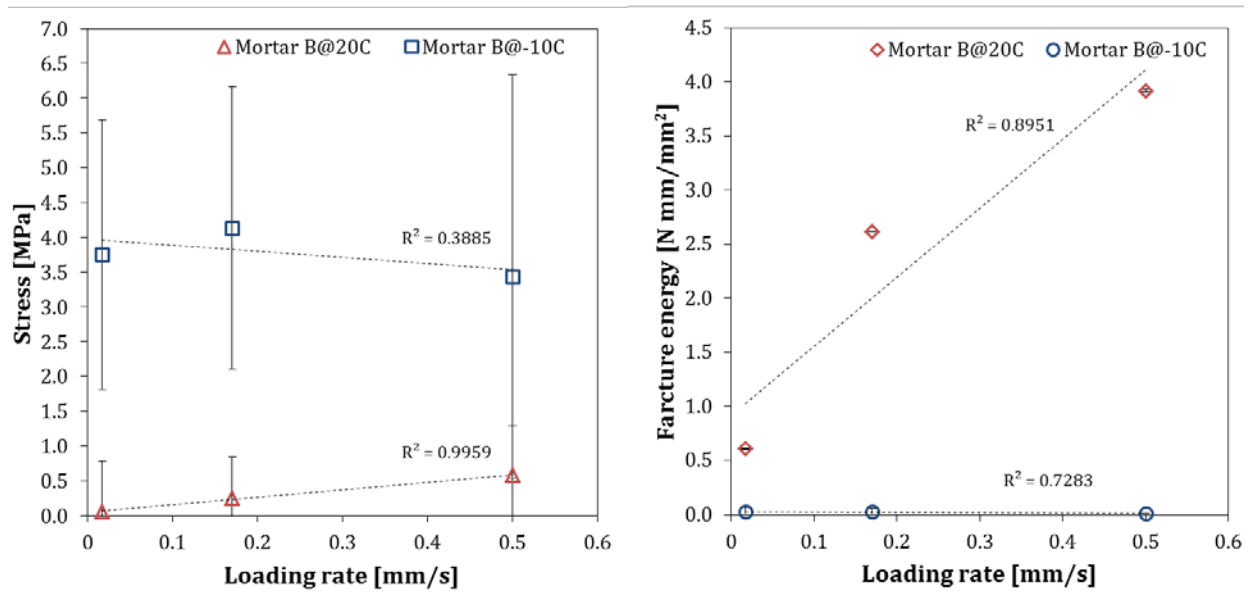

Figure 3.17. Tensile strength and fracture energy for mortar B at each loading rate and temperature.

The effect of filler type on the dry response of the mortars was not significant as follows from a comparison between Figure 3.16 and Figure 3.17. Similar values of strength and fracture energy were measured for mortars A and B. The use of SBS polymer modifier, however, improved the cohesion properties of the mortar samples. Generally, SBS is a polymer that improves the overall performance of asphalt pavements as SBS modified binders have increased stability and elasticity, and hence reduced propensity to rutting and cracking (Tarefder & Zaman 2010).

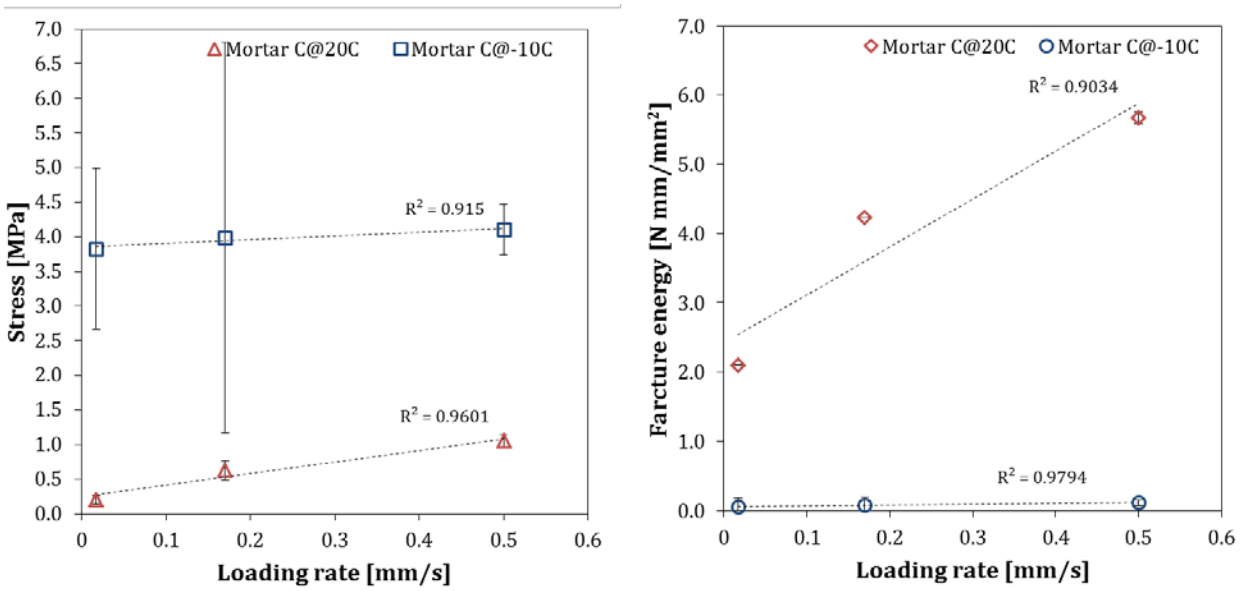

Figure 3.18. Tensile strength and fracture energy for mortar C at each loading rate and temperature.

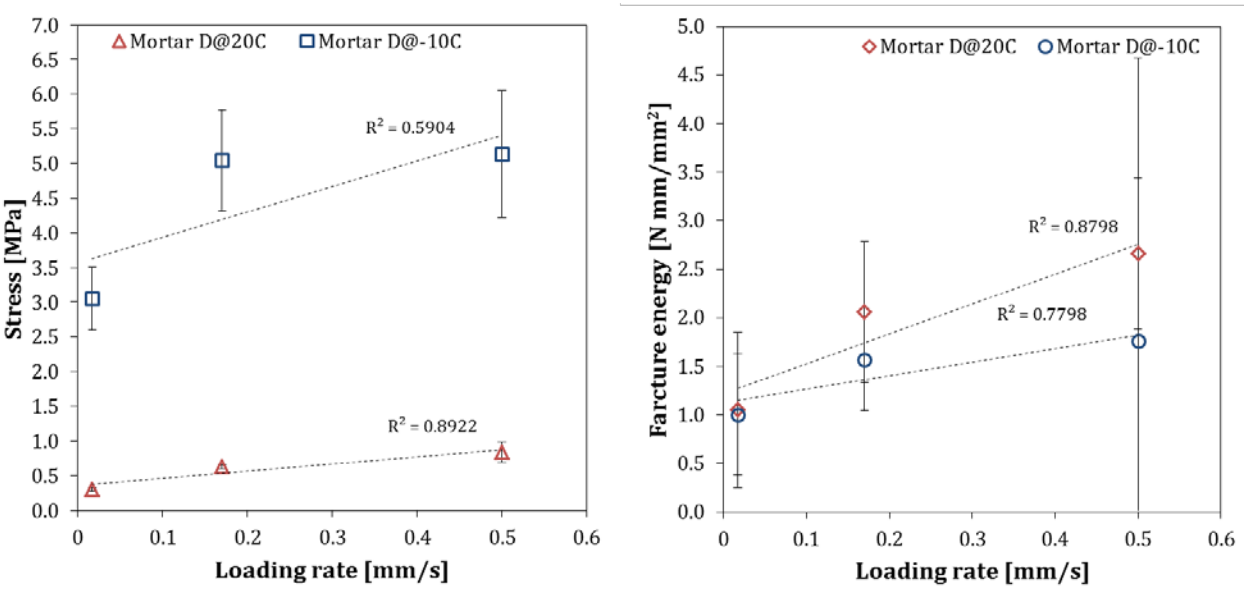

Figure 3.19. Tensile strength and fracture energy for mortar D at each loading rate and temperature.

At intermediate temperature, the uniaxial test results show that cohesive strength and fracture energy increased for both modified mortars C and D, suggesting that SBS modifiers had a positive effect on their cracking behaviour. At low temperature, however, the use of SBS did not affect significantly the strength of the mortars, as similar strength levels were observed for the unmodified and modified mortar types; nevertheless polymer modification resulted in an increase in fracture energy, and therefore modified mortars are expected to demonstrate a better fracture resistance at low temperatures in the field.

3.6.2 Influence of moisture conditioning

This section presents the effect of bath conditioning on the fracture properties of asphalt mortars. The graphs in Figures 3.20-3.21 provide the mean values of strength and fracture energy out of three replicate samples. The error bars represent a 95% confidence interval.

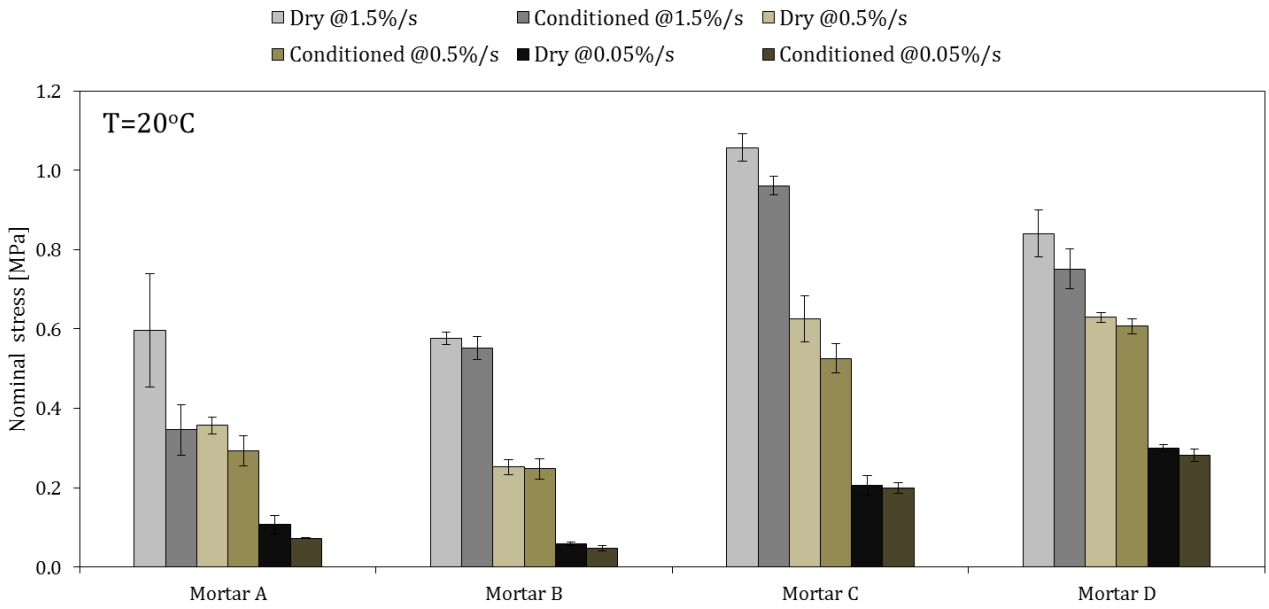

Figure 3.20. Tensile strength results at dry and moist conditions. The testing temperature was 20°C.

It is apparent from the results that, at dry conditions, the SBS modified mortars had a better mechanical behaviour in comparison to the unmodified mortars, as they exhibited higher strength and fracture energy values. Figure 3.20 clearly shows that moisture had an adverse effect on cohesion. The tensile strength of the samples, at intermediate temperature, decreased after moisture conditioning. Strength loss was comparable for all mortars and varied from 4 % to 11%. The results show that the wet strength of mortars prepared with PmB was higher compared to the unmodified ones.

Based on the results obtained for the fracture energy of the mortars, as shown in Figure 3.21, moisture had a significant effect on their fracture characteristics. Interestingly, fracture energy was observed to increase at wet conditions, suggesting that moisture had a softening effect on the mortars that lead to a more ductile behaviour. This observation was more pronounced for the SBS modified mortars. The use of SBS is considered to improve the cracking resistance during winter and the rutting potential at higher ambient temperatures. Nevertheless, it has not been clear yet what is the effect of SBS modification on moisture susceptibility (Tarefder & Zaman 2010). From this data, it can be seen that the use of SBS modified bitumen had a positive effect on the fracture resistance of the moisture conditioned mortars. Overall, a higher increase in fracture energy between dry and wet samples was observed for the polymer modified mortars.

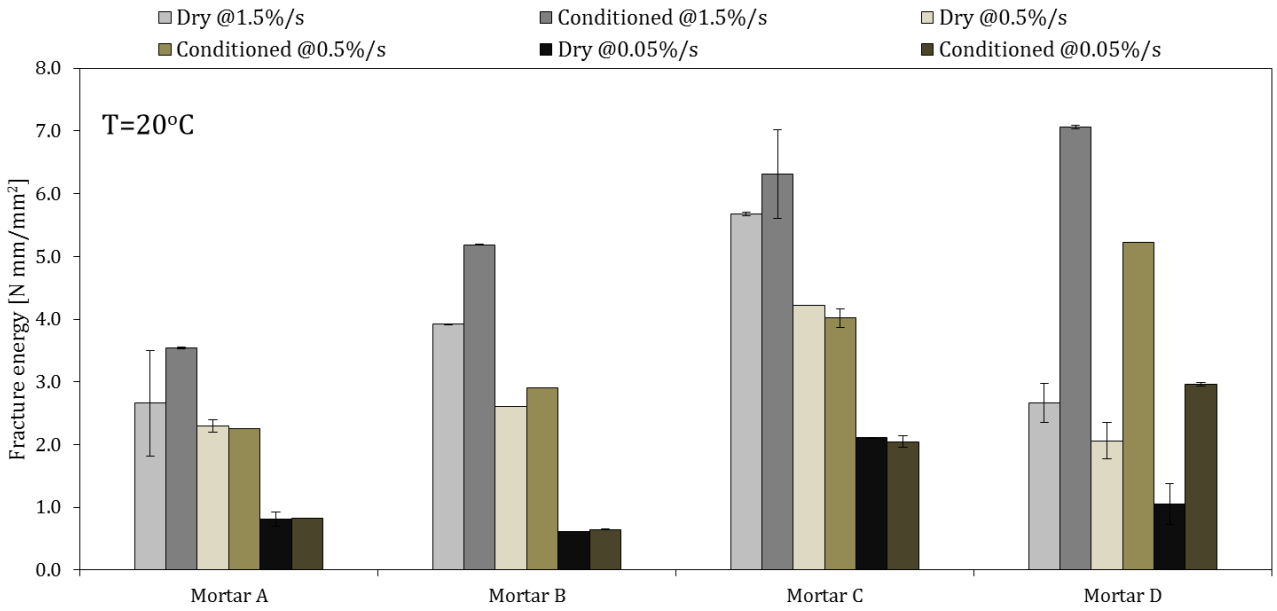

Figure 3.21. Fracture energy of mortars at dry and moist conditions. The testing temperature was 20°C.

Moreover, no substantial differences were found between mortars A and B, which were prepared with different filler types. A previous study by Stroup-Gardiner and Epps (1987) reported that asphalt mixtures prepared with quicklime filler were more moisture susceptible. In their research, they substituted hydrated lime with quicklime filler and observed that this change had an unfavorable effect on the performance of asphalt mixtures against moisture damage. Nonetheless, the results of this study does not support those findings, considering that mortar A, which contained quicklime filler, showed similar performance to mortar B for which hydrated lime filler was used.

The first set of data examined the impact of moisture on the response of the mortars at intermediate temperature. Figure 3.22 and Figure 3.23, present the test results at low temperature. Overall, the data reveal the strong effect of testing temperature on the mechanical response of asphalt mortars. The mortar samples exhibited a more brittle behaviour when tested at low temperatures, as they presented high tensile strength and significantly low fracture energy.

Generally, moisture conditioning was found to affect significantly the low temperature properties of asphalt mortars. After 203 days of bath conditioning, the tensile strength and fracture energy of the mortars decreased, hence the mortars became weaker and less deformable in the presence of moisture, and hence more susceptible to low temperature cracking. The only exception was mortar C, which exhibited an increase in both strength and fracture energy after conditioning. Also, even though the fracture energy of mortar D decreased after conditioning, it still remained above that of the unmodified mortars A and B.

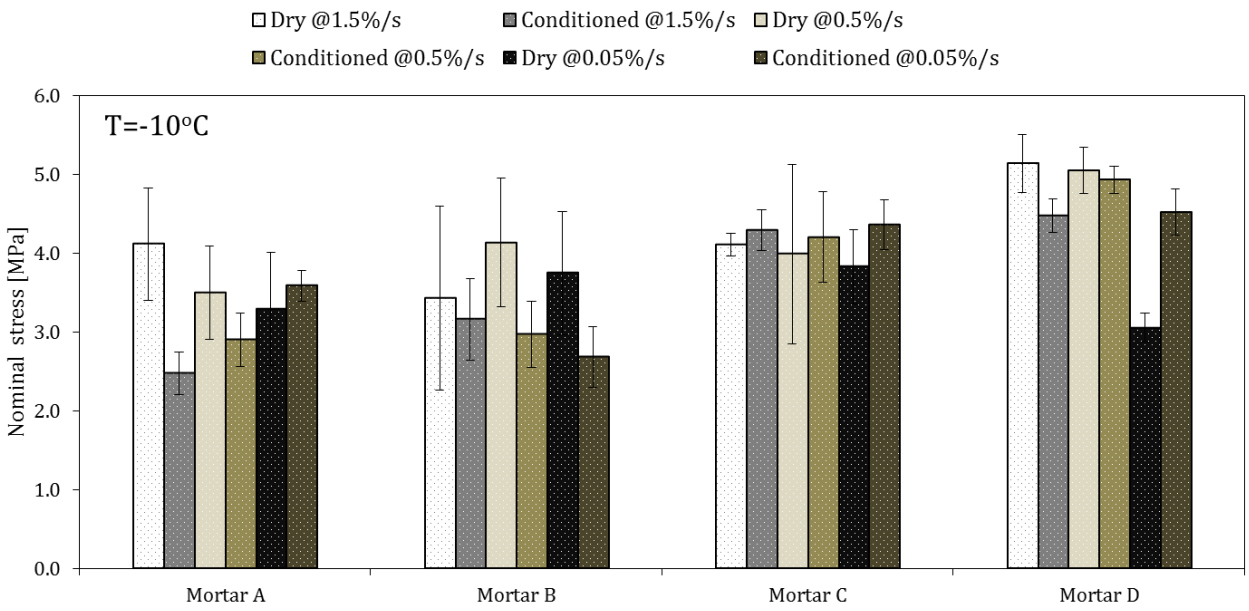

Figure 3.22. Tensile strength results at dry and moist conditions. The testing temperature was -10°C.

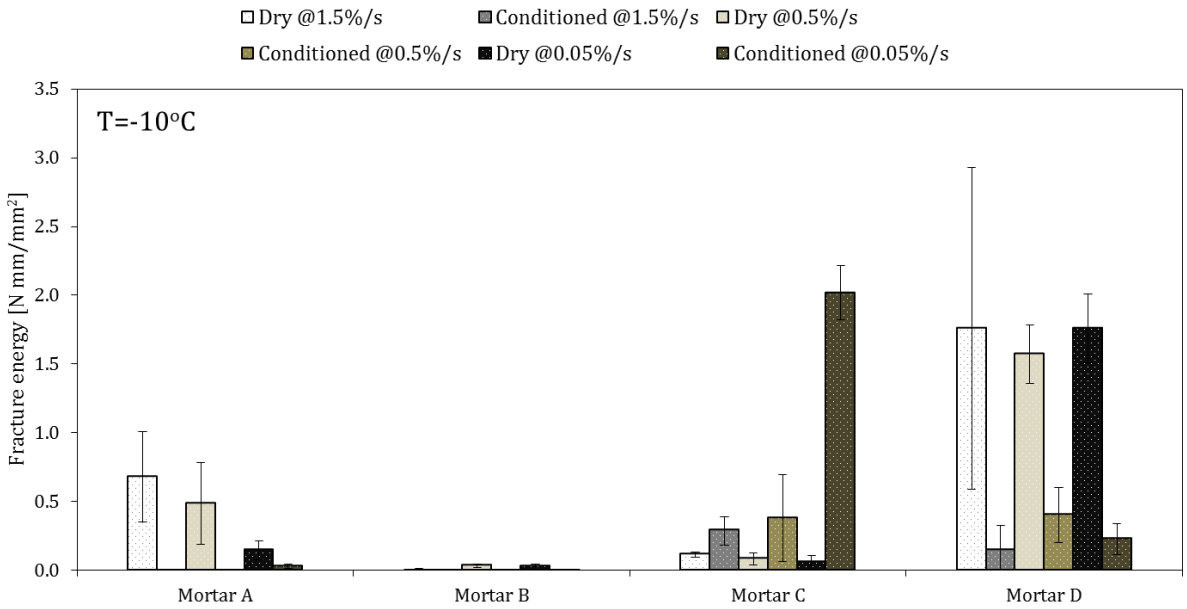

Figure 3.23. Fracture energy of mortars at dry and moist conditions. The testing temperature was -10°C.

In general, the results showed that there is a positive correlation between the use of PmB and moisture susceptibility. The dry and wet cohesive strength of the SBS modified mortars was higher than the strength of the unmodified mortars. What is more interesting in these results is the fact that fracture energy was significantly higher for modified mortars. This finding suggests that mortars with modified bitumen have a lower propensity to cracking even in the presence of moisture; this is a desired characteristic in terms of their performance at low temperatures.

3.6.3 Mechanical response upon drying

Asphalt mixtures are not always at moist conditions in the field, but undergo a number of wet and drying cycles depending on the environmental conditions of the specific geographical area. The question then arises as to whether the material restores the initial mechanical properties that it had before moisture conditioning. Hence, in this work, the reversibility of fracture properties of asphalt mortars was investigated by testing the samples after subjected to a drying phase as described in protocol III. Previous studies reported a recovery of stiffness and strength of asphalt mixtures upon drying. Schmidt and Graf (1972) observed that stiffness degradation of wet asphalt mixture samples was fully recovered upon drying. In a more recent study, Apeagyei et al. (2014) reported that the effect of moisture on the stiffness and strength of asphalt mixtures was reversible upon drying, indicating that cohesive failure dominates the durability of asphalt mixtures under long-term moisture conditioning.

The graphs below provide an overview of the results obtained after three conditioning regimes, namely at dry conditions (original state), after moisture conditioning and after drying. Figure 3.24 and Figure 3.25 show the tensile strength and fracture energy at each strain rate and at intermediate temperature. The results show that cohesive strength was recovered upon drying; in most of the tests the strength of the desiccated samples was higher than their dry strength. Overall, depending on the mineral filler and bitumen type, the cohesive strength of the mortars subjected to 165 days of drying increased by 19% to 60% compared to their wet strength. This finding is significant as it demonstrates the existence of reversible strength degradation in asphalt mortars. However, strength recovery was accompanied by a reduction (or no change) in fracture energy, which suggests the embrittlement of the mortar samples upon drying and hence a decrease in their fracture resistance.

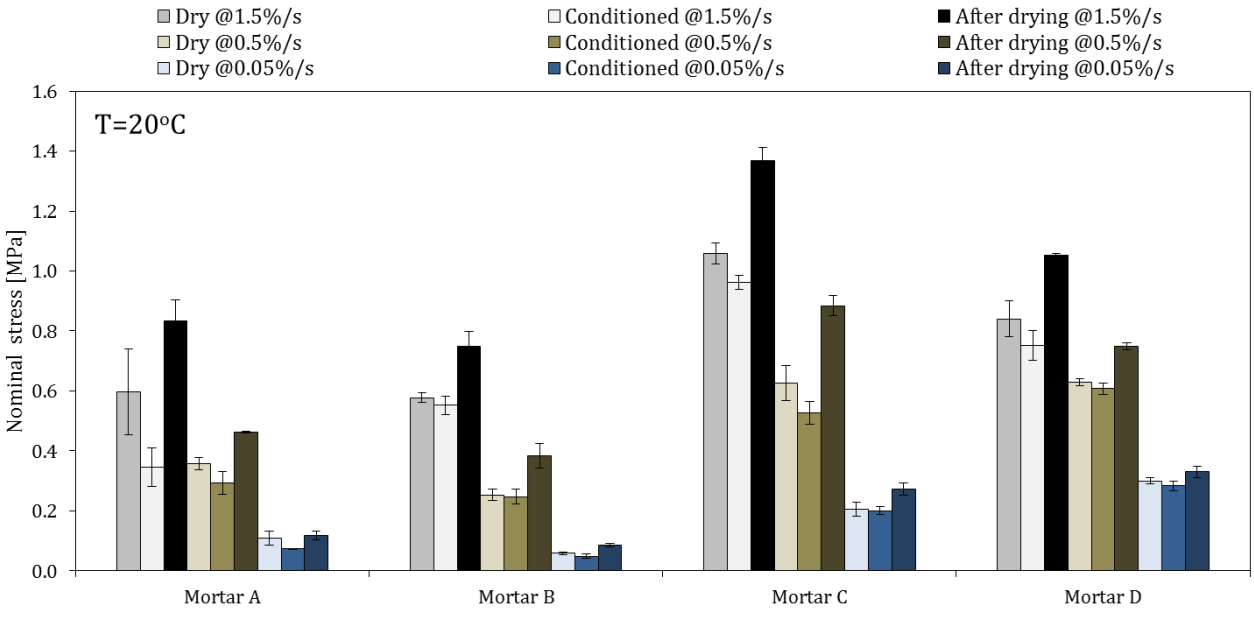

Figure 3.24. Tensile strength of mortars at dry conditions, after moisture conditioning and after drying. The testing temperature was 20°C.

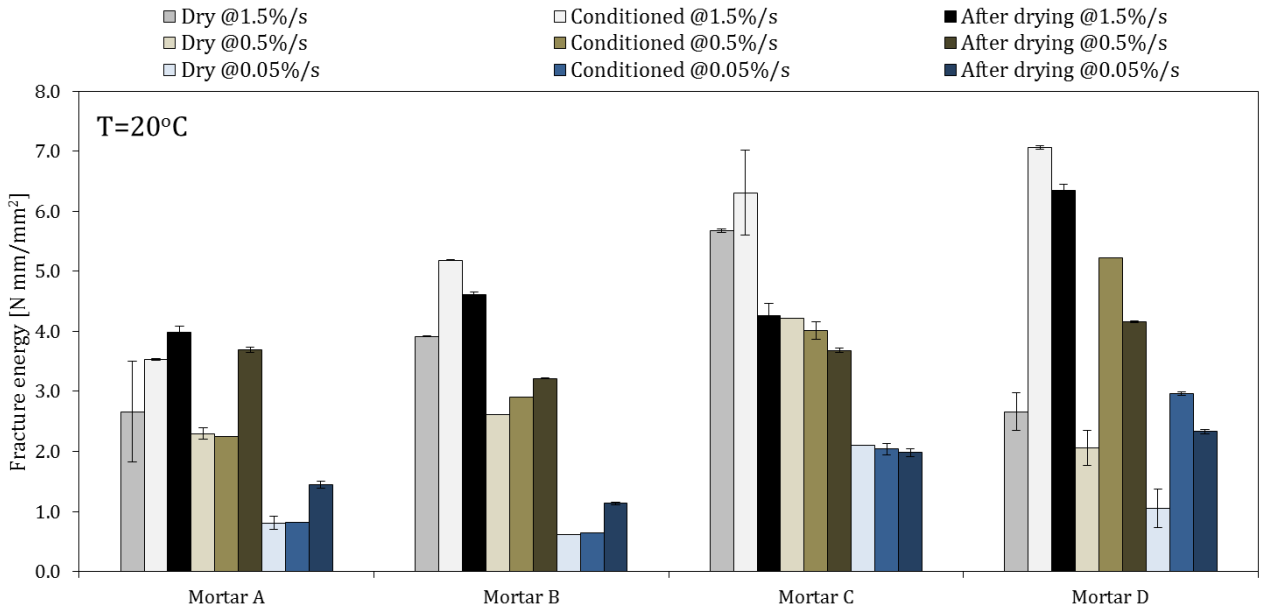

Figure 3.25. Fracture energy of mortars at dry conditions, after moisture conditioning and after drying. The testing temperature was 20°C.

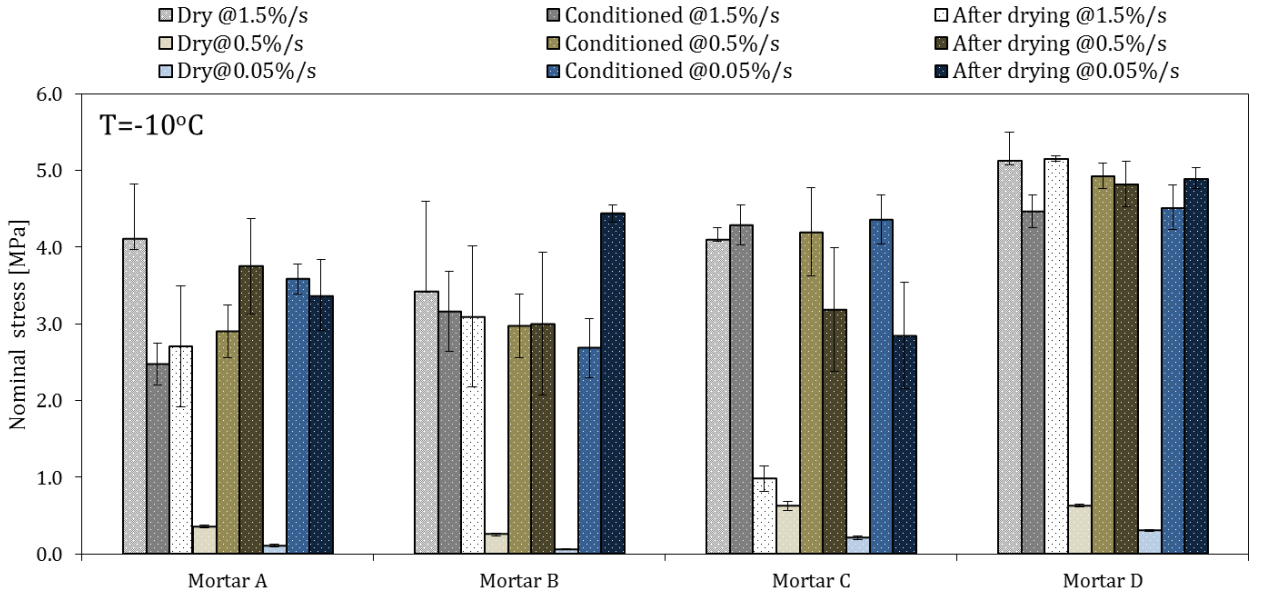

Figure 3.26. Tensile strength of mortars at dry conditions, after moisture conditioning and after drying. The testing temperature was -10°C.

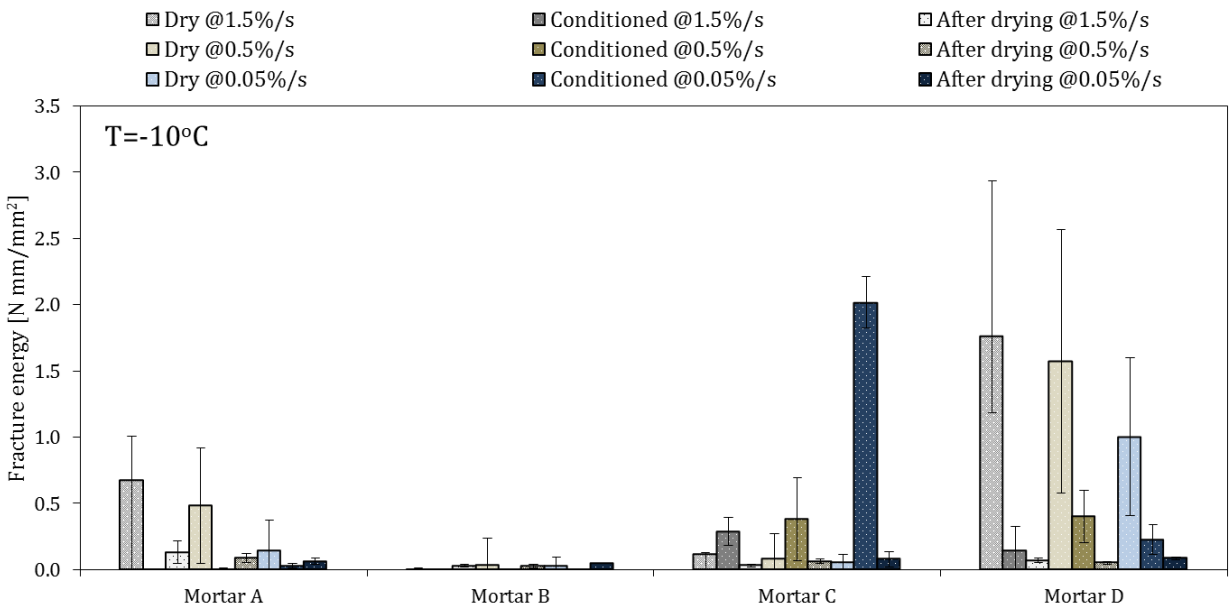

Figure 3.27. Fracture energy of mortars at dry conditions, after moisture conditioning and after drying. The testing temperature was -10°C.

The graphs in Figure 3.25 and Figure 3.26 provide the results of the tests performed at low temperature. As can be seen from the graph below the cohesive strength values of the desiccated samples were found to be similar or lower to the wet strength, in contrast to the results obtained at intermediate temperature. Moreover, fracture energy decreased significantly after the drying phase, thus suggesting that mortars became more brittle. Therefore, the results indicate that the low temperature properties were not restored after drying of the mortars, but quite the opposite the mortars had poorer fracture properties.

Taken together, these results suggest that it is likely that continuous wet and drying cycles can have a fatigue-like effect on the material, which may result in materials with inferior performance characteristics.

3.6.4 Influence of freeze-thaw cycles

Due to their viscoelastic nature, asphalt mortars highly depend on temperature fluctuations, which in turn influence pavement performance. In order to investigate the effect of freeze-thaw cycles, and account for the combined effect of moisture and low temperatures which often occurs during winter periods, protocols IV and V were employed. The two protocols differed in terms of the conditioning applied on the samples before subjected to thermal cycles. According to protocol IV freeze-thaw cycles were applied on the samples without any prior moisture conditioning (at dry state), while protocol V involved first bath conditioning followed by freeze-thaw cycles application. The graphs in Figures 3.28-3.31 show the results of the direct tension tests after the application of freeze-thaw

cycles. Overall, the fracture properties after the application of freeze-thaw cycles varied with respect to the conditioning state (dry or wet) of the samples.

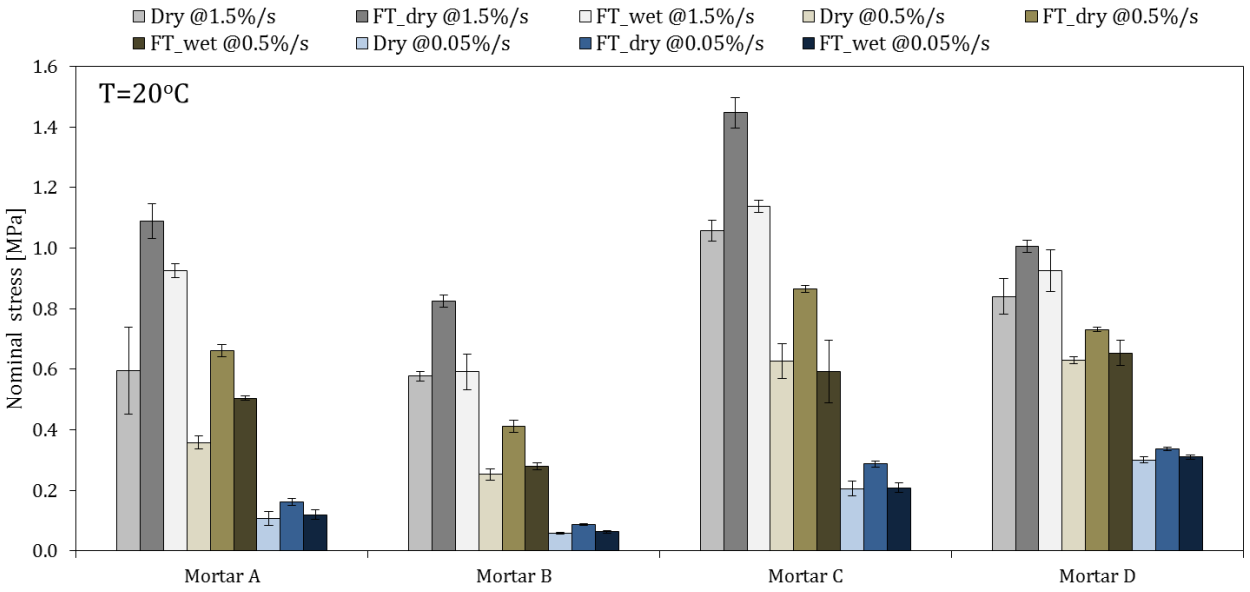

Figure 3.28. Tensile strength of mortars at dry conditions and after freeze-thaw cycles on dry and wet samples. The testing temperature was 20°C.

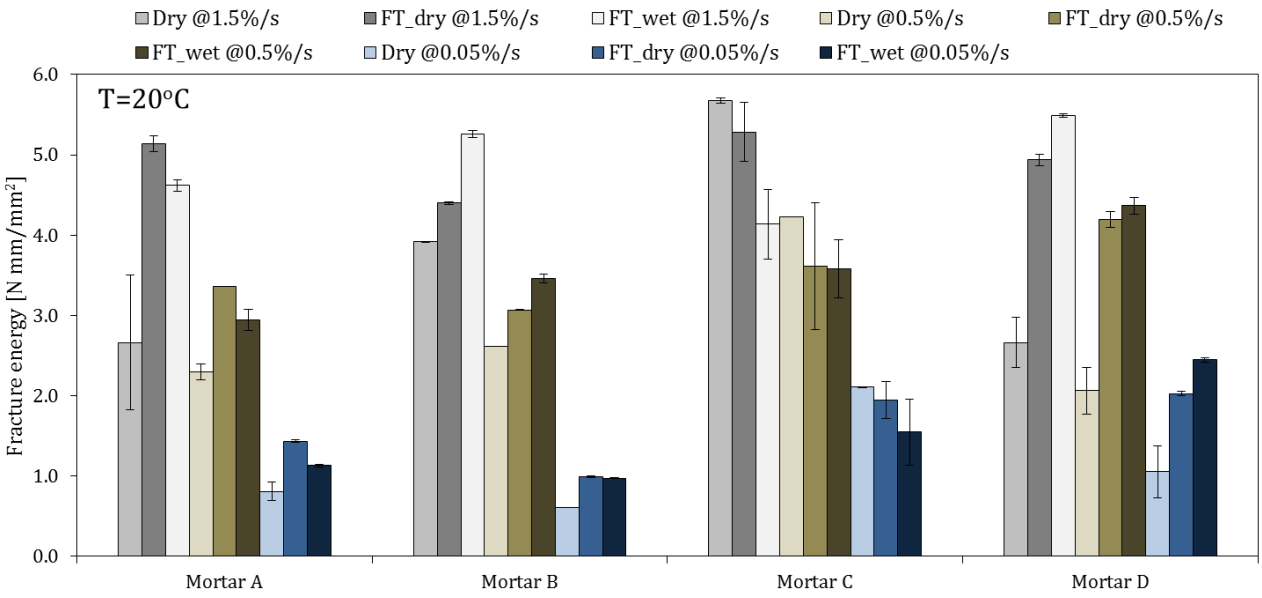

Figure 3.29. Fracture energy of mortars at dry conditions and after freeze-thaw cycles on dry and wet samples. The testing temperature was 20°C.

At intermediate testing temperature, the application of thermal cycles leads to a change in the fracture properties of the mortars depending on their composition. On the whole, a significant

increase in the strength of all mortar types was observed after freeze-thaw (FT) cycles were applied without prior moisture conditioning. However, the fracture energy values differed among the mortars; for the unmodified mortar A and the SBS modified mortar D fracture energy increased significantly, suggesting that the mortars became stronger and their fracture resistance increased. In contrast, the fracture energy of mortars B and D slightly decreased or remained stable, which in combination with the rise in their strength values, indicates that the mortars became more brittle and hence more prone to cracking.

A comparison between the test results after the application of FT cycles on dry (in the graph it is denoted as FT_dry) and wet samples (denoted as FT_wet) reveals the detrimental effect of moisture on the mechanical response of asphalt mortars. The presence of moisture, in combination with thermal cycles, caused a decrease of the mortar tensile strength. Again, different trends in the values of fracture energy were obtained. For mortars A and C the energy values decreased suggesting that these mortars became weaker, while mortars B and D were more ductile as their fracture energy of increased. With respect to the reference dry values (protocol I), slight differences were observed in the tensile strength of all mortars subjected to freeze-thaw cycles at moist state (protocol V). However, their fracture energy increased, thus indicating that moisture had a softening effect on the mortars.

Figure 3.30 and Figure 3.31 show the tensile strength and fracture energy, respectively, at low temperature. The results show that low temperature strength was not significantly influenced by the application of freeze-thaw cycles.

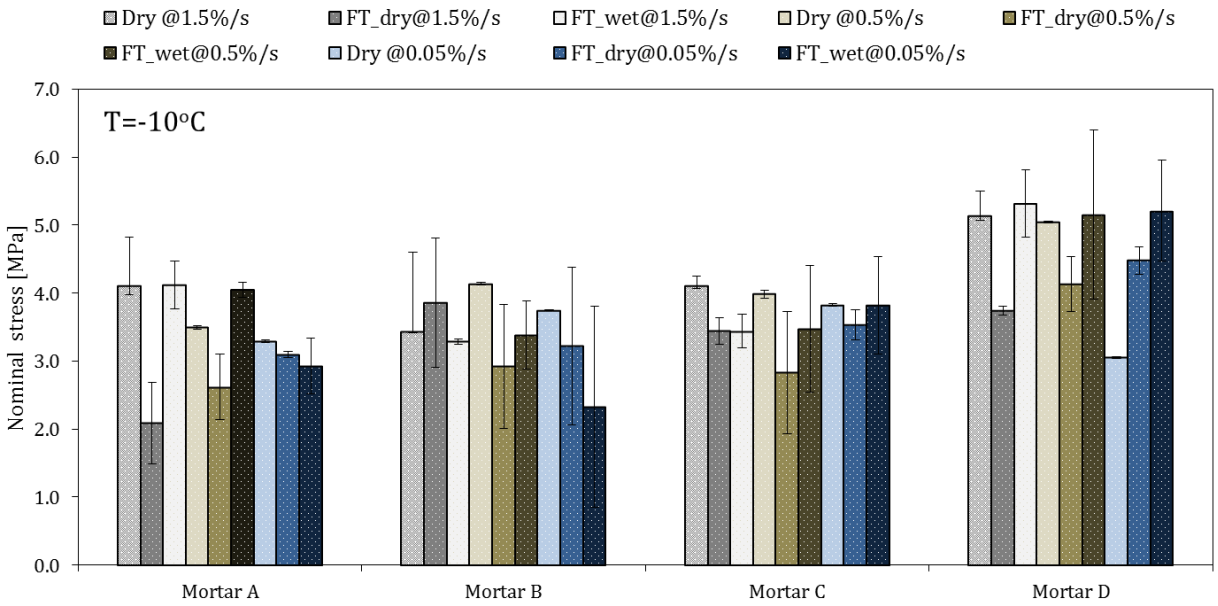

Figure 3.30. Tensile strength of mortars at dry conditions and after freeze-thaw cycles on dry and wet samples. The testing temperature was -10°C.

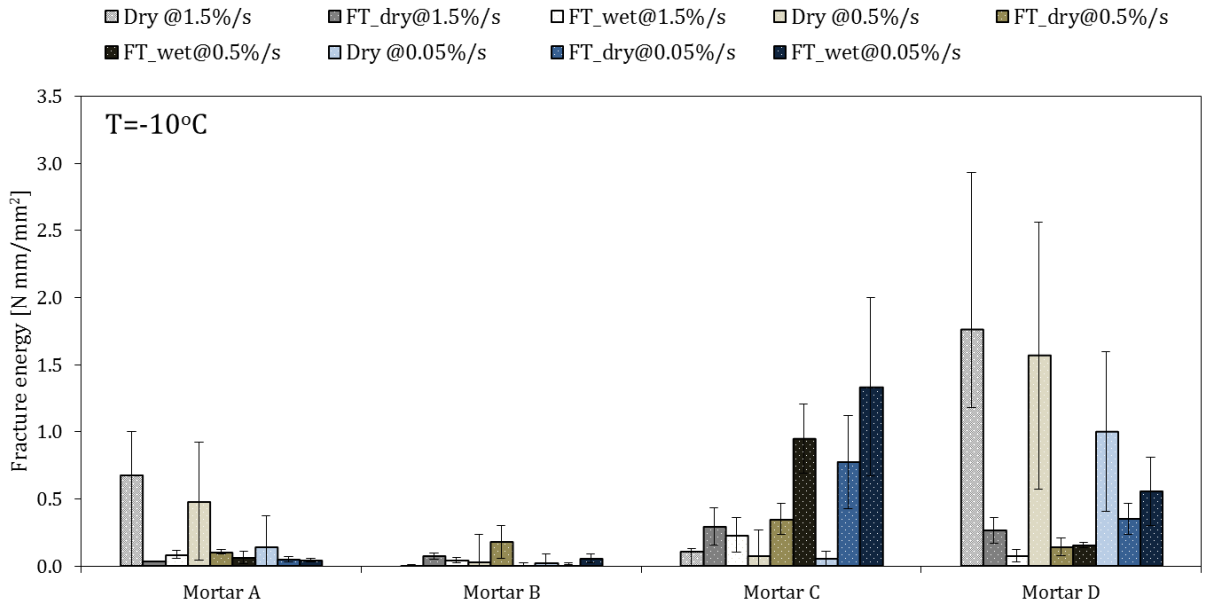

Figure 3.31. Fracture energy of mortars at dry conditions and after freeze-thaw cycles on dry and wet samples. The testing temperature was -10°C.

Even though the changes in strength were negligible, all four mortars became less resistant to fracture as indicated by their fracture energy values, suggesting that the application of freeze-thaw cycles had an unfavourable effect on the materials. The SBS modified mortar C was the only that exhibited an increase in its fracture energy, suggesting that polymer addition can improve low temperature behaviour. Even though a PmB (SBS modifier) was used also for mortar D, the effect was not the same; this can be attributed to the polymer content used for the preparation of the two mortars. The application of freeze-thaw cycles in the presence of moisture (protocol V) caused an additional reduction in cohesive strength for the majority of the mortar samples. Nevertheless, the combination of moisture and thermal conditioning was found to have a softening effect for the SBS modified mortars, as their fracture energy increased; in contrast, the unmodified mortars demonstrated a further decrease in their fracture energy.

3.6.5 Mechanical response as a function of moisture uptake

An attempt was also made to relate the behaviour of the mortars to the results obtained from the moisture uptake measurements. After 203 days of moisture conditioning, mortar A (which was prepared with quicklime filler) absorbed the highest amount of moisture, while the SBS modified mortars had substantially lower moisture absorption. Correspondingly, mortar A performed poorly in the direct tension tests, while, on the other hand, mortar D exhibited the best mechanical performance. Figure 3.32 shows the reduction in strength and the corresponding fracture energy, at intermediate testing temperature, as a function of moisture uptake. Each data point shows the maximum moisture absorbed for a particular mortar type and the equivalent decrease in cohesive

strength. It was observed that a linear relation exists between the ability of a mortar sample to absorb moisture and its degradation in strength.

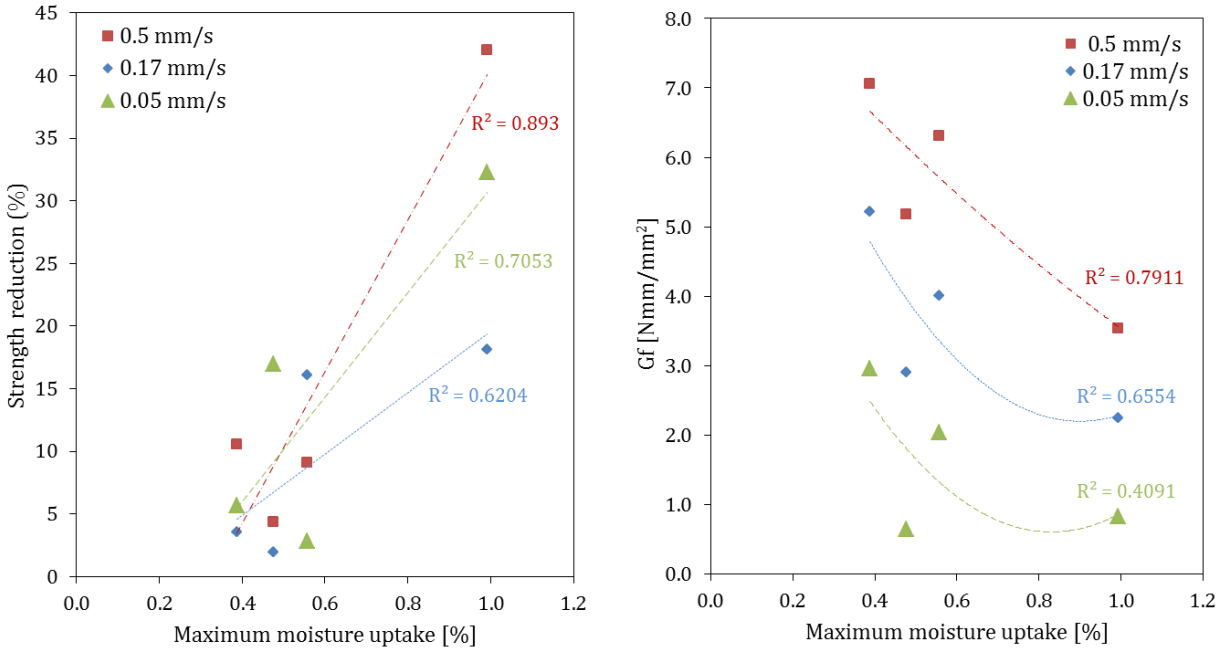

Figure 3.32. (a) Reduction in cohesive strength and (b) fracture energy values as a function of maximum moisture uptake. The tests were performed at intermediate temperature (20°C).

These findings suggest that the maximum amount of moisture a mortar can absorb is a key factor for the evaluation of moisture susceptibility of asphalt mortars. Naturally, asphalt mortars with dissimilar chemical compositions will interact differently with moisture and may result in diverse levels of strength degradation. However, it is anticipated that the greater the amount of moisture the mortar can hold, the higher the strength degradation. Similar findings were reported for asphalt binders by Cheng et al. (2003); the rate of damage was higher rate for binders that absorbed a greater amount of moisture, indicating thus that, ultimately, it is the amount of moisture in the binder that significantly influences the progression of damage and not the rate of moisture diffusion.

For the tests performed at low temperature, a correlation between strength reduction and moisture uptake could not be established, since for the polymer modified mortars an increase, and not a reduction, in strength was observed after moisture conditioning at low loading rates (0.17 mm/s and 0.05 mm/s). The results for fracture energy are also not conclusive with respect to establishing a relation between moisture uptake and fracture properties. It appears that there is not a clear relationship between low temperature behaviour and moisture uptake; it may be that at low temperature other phenomena dominate.

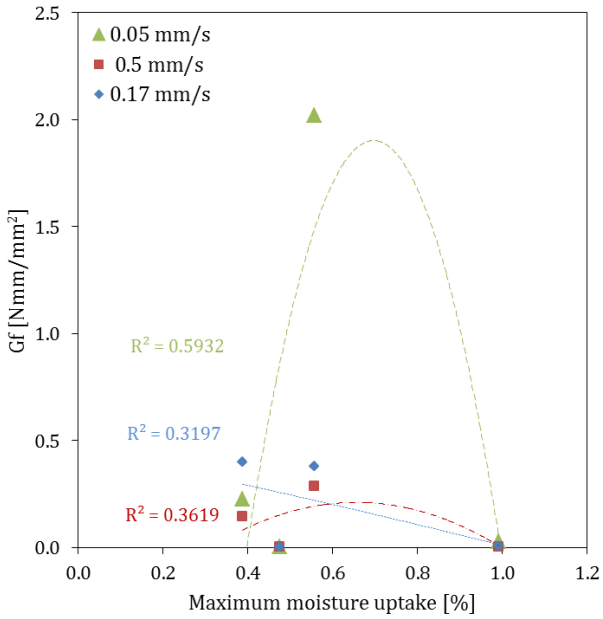

Figure 3.33. Fracture energy values as a function of maximum moisture uptake. The tests were performed at low temperature (-10°C).

3.7 Summary

The main objective of this study was to investigate the effect of moisture on the mechanical response of asphalt mortar samples. Four mortar types were prepared that varied in terms of mineral filler and bitumen type. Uniaxial tension tests were used to characterize the fracture properties of the mortar samples for various combinations of moisture and thermal conditioning. The effect of applying a drying cycle on the mortar properties was also studied. Given the fact that asphalt mortars are viscoelastic materials, and consequently have a strong dependency on loading rate and temperature, testing was performed at two different testing temperatures and three loading rates.

In addition to the mechanical tests, moisture uptake measurements were carried out. In this manner, a better understanding of the moisture diffusion characteristics of the individual mortar types was obtained and an attempt was made to establish a link between material response and maximum moisture uptake. In summary, the results show that the diffusion characteristics, i.e. maximum moisture uptake and rate of diffusion, were substantially different among the various mortar types; one mortar type absorbed considerably more moisture, and in a higher rate, than the other three mortars indicating that diffusivity varies with mortar composition. The use of quicklime filler resulted in mortars with high water permeability, whereas hydrated lime filler improved significantly the diffusivity characteristics of the mortars (lower moisture absorption). Another observation was that the use of SBS-modified bitumen had a favorable effect on the diffusion properties; the overall diffusivity of the mortars significantly reduced likely due to the presence of SBS copolymers that are extremely hydrophobic in nature. Similar results were obtained for the

drying process, indicating that the moisture absorption and desorption rates are highly dependent on mortar composition.

The tensile strength and fracture energy were used to evaluate the changes in the mechanical properties of the mortars due to the various conditioning protocols. A new data analysis procedure was developed in order to obtain a more accurate calculation of fracture energy. The procedure uses nonlinear finite element analysis to specify the unloading response outside the fracture zone, and then utilize this information to calculate the fracture energy of the material. This methodology can be used when only force-displacement data are available and therefore the estimation of the true stress-strain curve is not feasible.

Overall, the test results at dry conditions clearly show that an inverse relationship exists between testing temperature and strength or fracture energy. Strength and fracture energy increased with decreasing testing temperature, irrespective to the mortar composition. Similar observations can be made for loading rate, even though the effect is less pronounced at lower testing temperatures. Another observation was that fracture properties improved with the use of SBS modified bitumen. At intermediate temperature, the cohesive strength and fracture energy of the modified mortars increased significantly; also at low temperature the fracture resistance of the modified mortars improved as they could sustain larger deformations until failure. On the other hand, no significant differences on the strength and fracture energy values were found due to the type of mineral filler used.

The presence of moisture was found to have an adverse effect on the cohesive strength of asphalt mortars. At intermediate testing temperatures, the strength of the mortars reduced by 2% to 42% compared to their dry strength, while in contrast their fracture energy increased. It can thus be suggested that moisture has a softening effect on asphalt mortars. One interesting finding is that, at low temperature, the mortars degraded significantly after subjected to moisture conditioning. Moisture was associated with a significant reduction in strength and fracture energy, indicating that moisture increases the propensity to low temperature cracking. The addition of hydrated lime filler did not have a substantial effect on moisture susceptibility of the mortar samples. Conversely, the results showed that the use of SBS modified bitumen improved the fracture resistance of moisture conditioned mortar samples. The effect was more pronounced when the mortar samples were tested at low temperature, and could be explained by the increase in elasticity due to the addition of the SBS modifier. Furthermore, an attempt was made to find a correlation between moisture uptake and mechanical response. At intermediate temperature, according to these obtained relations, it can be inferred that the amount of moisture is strongly related to the level of moisture damage in spite of the chemical composition of the mortars. At low temperatures, however, such a relation could not be established.

The reversibility of fracture properties of mortars upon drying was also investigated. Cohesive strength was observed to recover after one drying cycle; specifically in most of the tests the strength of the desiccated mortar samples was higher than their dry strength. However, strength recovery was accompanied by a reduction (or no change) in fracture energy, which suggests the embrittlement of the mortars upon drying and hence a decrease in their fracture resistance. At low temperature, the degradation was more pronounced as the low temperature properties were not restored after drying, but quite the opposite they resulted in mortars with poorer fracture

properties. It is therefore likely that continuous wet and drying cycles can have a fatigue-like effect on the material, which may result in obtaining materials with inferior performance characteristics.

Besides moisture, thermal cycles also influence the fracture properties of mortars. Nevertheless, the response after the application of freeze-thaw cycles was found to vary with respect to the conditioning state (dry or wet) of the samples. Also, at intermediate testing temperature, the behaviour of the mortars differed depending on their composition. At low temperature, the application of freeze-thaw cycles on both dry and wet samples did not considerably influence their strength. However, all four mortars became less resistant to fracture as indicated by their fracture energy values. In general, therefore, it seems that thermal conditioning results in embrittlement of the materials, hence mortars become more susceptible to cracking. Overall, the polymer modified mortars were found to be less susceptible to thermal cycles as their strength and energy levels were comparable to those obtained at dry conditions (protocol I). The application of freeze-thaw cycles in the presence of moisture resulted in an additional reduction in cohesive strength for the majority of the mortars. Nevertheless, the combination of moisture and thermal conditioning was found to have a softening effect for the SBS modified mortars, as their fracture energy increased; in contrast, the unmodified mortars demonstrated a further decrease in their fracture energy.

In this chapter, the principal aim was to investigate the effects of long-term moisture diffusion on the cohesion properties of asphalt mortars. However, as explained in the introductory chapter, it is clear that moisture damage of asphalt mixtures results from a combination of long-term moisture diffusion and short-term phenomena, such as pumping action. To account also for the short-term processes, Chapter four investigates moisture susceptibility at mixture level, at which also the aggregates and consequently the air voids network are present. Hence, asphalt mixture samples were prepared using three of the mortar types investigated in this study. An attempt was made to correlate the performance of mortars against moisture with the moisture susceptibility of asphalt mixtures.

3.8 References

AASHTO T314 (2000). *Standard Method of Test for Determining the Fracture Properties of Asphalt Binder in Direct Tension (DT).* American Association of State Highway and Transportation Officials. Washington, D.C.

Anderson, D.A., Lapalu, L., Marasteanu, M.O., Hir, Y.M.L., Planche, J.P. & Martin, D. (2001). Low temperature thermal cracking of asphalt binders as ranked by strength and fracture properties. *Transportation Research Record: Journal of the Transportation Research Board*, 1766, 1–6.

Apeagyei, A.K., Grenfell, J.R.A. & Gordon D.A. (2014). Observation of reversible moisture damage in asphalt mixtures. *Construction and Building Materials*, 60, 73-80.

Bahia H.U., Moraes, R. & Velasquez, R. (2012). The effect of bitumen stiffness on the adhesive strength measured by the Bitumen Bond Strength test. 5th Eurasphalt & Eurobitumen Congress, Istanbul.

Bolzan, P.E. & Huber, G. (1993). Direct tension test experiments. Strategic Highway Research Programme, Report SHRP-A-641. National Research Council, Washington, D.C.

Caro, S., Masad, E., Bhasin, A. & Little, D.N. (2008). Moisture susceptibility of asphalt mixtures, part 1: mechanisms. *International Journal of Pavement Engineering*, 9:2, 81-98.

Cheng, D., Little, D.N., Lytton, R.L. & Holste, J.C. (2003). Moisture damage evaluation of asphalt mixtures by considering both moisture diffusion and repeated-load conditions. *Transportation Research Record: Journal of the Transportation Research Board,* 1832, 42–49.

Copeland, A.R. (2007). Influence of moisture on bond strength of asphalt-aggregate systems. PhD dissertation. Vanderbilt University, Nashville, Tennessee.

Duncan, B., Urquhart, J. & Roberts, S. (2005). Review of measurement and modelling of permeation and diffusion in polymers. NPL report DEPC-MPR-012. National Physical Laboratory, UK.

Erkens, S. J. M. C. (2002). Asphalt Concrete Response (ACRE): Determination, modelling and prediction. PhD dissertation. Delft University of Technology, The Netherlands.

Hicks, R.G. (1991). Moisture Damage in Asphalt Concrete. NCHRP Synthesis of Highway Practice 175. TRB, National Research Council, Washington, D.C.

Hicks, R.G., Santucci, L. & Aschenbrener, T. (2003). Introduction and Seminar Objectives, Topic 1, National Seminar on Moisture Sensitivity of Asphalt Pavements. TRB, Washington, D.C.

Hillerborg, A. (1985). Numerical methods to simulate softening and fracture of concrete. Chapter in *Fracture mechanics of concrete: Structural application and numerical simulation* (Eds: G. C. Sih and A. DiTommaso). Martinus Nijhoff publishers, Dordrecht.

Hoare, T.R. & Hesp, S.A. (2000). Low-temperature fracture testing of asphalt binders. *Transportation Research Record: Journal of the Transportation Research Board*, 1728, 36–42.

Kanitpong, K. & Bahia, H. (2005). Relating Adhesion and Cohesion of Asphalts to Effect of Moisture on Laboratory Performance of Asphalt Mixtures. *Transportation Research Record: Journal of the Transportation Research Board,* 1901, 33-43.

Kennedy, J. E. & Higginbotham, C. L. (2011). Synthesis and characterisation of styrene butadiene styrene based grafted copolymers for use in potential biomedical applications in "Biomedical Engineering, Trends in Materials Science". ISBN: 9789533075136. InTech, Croatia.

Kim, S. (2007). Development of an Asphalt Binder Cracking Device. Final Report for NCHRP IDEA Project 99, Transportation Research Board of the National Academies, Washington, D.C.

Kringos, N., Scarpas, A., Kasbergen, C. & Selvadurai, P. (2008a). Modelling of combined physical mechanical moisture-induced damage in asphaltic mixes, part 1: Governing processes and formulations. *International Journal of Pavement Engineering*, 9:2, 115-118.

Kringos, N., Scarpas, A. & de Bondt, A. (2008b). Determination of moisture susceptibility of mastic-stone bond strength and comparison to thermodynamical properties. *Journal of the Association of Asphalt Paving Technologists*, 77, 435-478.

Kringos, N., Khedoe, R., Scarpas, A. & de Bondt, A. (2011). A new asphalt concrete moisture susceptibility test methodology. Transportation Research Board 90th Annual Meeting Compendium of Papers, Washington, D.C.

Lesueur, D., Petit, J. & Ritter, H. J. (2013). The mechanisms of hydrated lime modification of asphalt mixtures: a state-of-the-art review, Road Materials and Pavement Design, 14:1, 1-16.

Little, D.N. & Epps, J.A. (2001). The benefits of hydrated lime in Hot Mix Asphalt. National Lime Association, Arlington, Virginia, USA.

Little, D.N. & Petersen, J.C. (2005). Unique effects of hydrated lime filler on the performance-related properties of asphalt cements: Physical and chemical interactions revisited. *Journal of Materials in Civil Engineerin*g, 17:2, 207-218.

Moraes, R., Velasquez, R. & Bahia H.U. (2011). Measuring the effect of moisture on asphalt–aggregate bond with the Bitumen Bond Strength test. *Transportation Research Record: Journal of the Transportation Research Board,* 2209, 70–81.

NEN-EN 1239 (2011). Adhesives Freeze-thaw stability. Nederlands Normalisatie Instituut.

Niu, T., Roque, R. & Lopp, G.A. (2014). Development of a binder fracture test to determine fracture energy properties. *Road Materials and Pavement Design*, 15:1, 219-238.

Plancher, H., Green, E.L. & Petersen, J.C. (1976). Reduction of oxidative hardening of asphalts by treatment with hydrated lime: A mechanistic study. Asphalt Paving Technology (AAPT) Proceedings, 1-24.

Ponniah, J.E., Cullen, R. & Hesp, S.A. (1996). Fracture energy specifications for modified asphalts. Symposium on Modified Asphalts, *Prepr., Am. Chem. Soc., Division of Fuel Chemistry*, 1317-1321.

Schmidt R.J. & Graf P.E. (1972). The effect of water on the resilient modulus of asphalt treated mixes. Proceedings of Association of Asphalt Paving Technologists, 41, 118–62.

Sebaaly, P.E. (2007). Comparison of lime and liquid additives on the moisture damage of Hot Mix Asphalt Mixtures. National Lime Association, Arlington, Virginia, USA.

Stroup-Gardiner, M. & Epps, J.A. (1987). Four variables that affect the performance of lime in asphalt-aggregate mixtures. *Transportation Research Record: Journal of the Transportation Research Board*, 1115, 12-22.

Tarefder, R. A. & Zaman, A. M. (2010). Nanoscale evaluation of moisture damage in polymer modified asphalts. *Journal of Materials in Civil Engineering,* 22:7, 714– 725.

Youtcheff, J. & Aurilio, V. (1997). Moisture sensitivity of asphalt binders: Evaluation and modelling of the pneumatic adhesion test results. 42nd Annual Conference of Canadian Technical Asphalt Association, Ottawa, Ontario.

4

Moisture susceptibility of asphalt mixtures

"Every experiment proves something. If it doesn't prove what you wanted it to prove, it proves something else"
— Anonymous

This chapter investigates the contributions of long- and short-term moisture damage to strength degradation of asphalt mixtures. The susceptibility of asphalt mixtures to moisture was evaluated using a moisture conditioning protocol, which comprises two conditioning types namely bath immersion and pore pressure application, and mimics the processes occurring when water interacts with an asphalt pavement. Asphalt samples, with different aggregate and bitumen types, were conditioned in combinations of water immersion and cyclic pore pressures, and subsequently tested using indirect tensile tests. In addition, X-ray computed tomography and image analysis techniques were employed to characterize and provide a better understanding of damage due to the pore pressure mechanism.

Part of this chapter contains published material from the article "Experimental evaluation of long and short term moisture damage characteristics of asphalt mixtures" (http://dx.doi.org/10.1080/14680629.2015.1066705) by A. Varveri, S. Avgerinopoulos and A. Scarpas, published in the *Road Materials and Pavement Design* © 2015.

4.1 Why use a different moisture conditioning approach?

Moisture damage is a key factor for the design of durable asphalt pavements. Water at all its physical states i.e. liquid, vapour and solid is considered to be an important contributor to various forms of damage such as ravelling and cracking. As explained in the introductory chapter, three main physico-mechanical moisture damage processes, which can deteriorate the performance of asphalt pavements, are found in literature: moisture diffusion, asphalt binder erosion due to fast water flows and cyclic pore pressure development (Hicks 1991, Kringos & Scarpas 2005). Depending on traffic loading, environmental conditions and mixture characteristics (percentage, size and interconnectivity of air voids, and hence permeability), one of the aforementioned processes or a combination thereof can occur in a pavement. However, a clear distinction between long- and short-term moisture damage processes can be made based on the time frame over which each process occurs.

Moisture diffusion is defined as long-term moisture damage inducing process, as it is a molecular process, in which long times are required for moisture to diffuse into the asphaltic components of the mixture. As discussed in the second chapter, the magnitude of moisture flux depends on the moisture concentration gradient, temperature and the diffusion properties of the asphaltic components. Particularly for asphalt mixtures, moisture diffusion is also influenced by the percentage of air voids, as well as their distribution and interconnectivity (Varveri et al. 2015). As moisture penetrates an asphalt pavement, the physico-chemical properties of the binder can change, and hence reduce its cohesion strength. Additionally, in the presence of moisture, the adhesive bond between aggregate and binder deteriorates, and eventually results to stripping of aggregates from the pavement surface (Caro et al. 2008a, Kringos et al. 2008).

In contrast, pumping action is a short-term moisture damage mechanism. Dynamic water flow phenomena are developed in asphalt pavements in shorter times and can act cumulatively, or even accelerate the long-term damage processes (Kringos et al. 2008, Hicks 1991, and Kandhal & Rickards 2001). The presence of water flow in the body of a pavement may result in diverse phenomena to occur; depending on mixture type, the geometry and topology of air voids and the drainage conditions, generation of pore pressure and erosion of the asphalt binder may take place. Kandhal et al. (1989) reported several field observations that confirm that stripping is a rather localized phenomenon in trafficked areas of pavements which are oversaturated with water. Typically, dynamic traffic loading can cause intense local water pressure fields when the macro pores and existing cracks in a pavement are saturated with water. Due to water being (nearly) incompressible, additional stresses are developed within the asphaltic material, resulting in more mechanical damage in contrast to the dry unsaturated case. The extra stresses can cause the binder film to crack, and hence facilitate the ingression of moisture towards the binder-aggregate interface or mechanically remove the binder due to the abrasive action of water.

Pore pressures can affect porous asphalt pavements as well as newly constructed pavements. In porous pavements, the presence of a highly interconnected pore network allows water to move through the pavement structure, causing thus binder erosion. In case, the pores of a porous mixture are clogged by dirt and other pollutants, then water can accumulate in the clogged pores and pore pressures can develop locally due to traffic. For a newly constructed pavement, water may also be

entrapped in the voids because of the reduction of air void content with time due to field compaction (Terrel & Al-Swailmi 1994).

Moisture susceptibility of asphalt mixtures typically depends on mixture design and on the physico-chemical properties, interaction and in-time degradation characteristics of the constituent materials. For instance, mixtures with poor aggregate-binder bond strength may display low moisture susceptibility during their service life provided that their design prevents moisture to easily penetrate or moisture takes a long time to diffuse through the binder towards the interface due to the low binder diffusivity. Similarly, mixtures with high permeability, but with asphalt components that experience slow mechanical degradation when exposed to moisture may not be moisture sensitive. Therefore, it is essential to determine the degree of performance deterioration for a given asphalt mixture and its individual components under a relevant time frame.

In practice, threshold values are used in specifications and standards to distinguish between bituminous mixtures that are susceptible, or not, to moisture damage. The complexity of moisture induced damage phenomena makes it difficult to find a unique way to comprehensively evaluate and estimate the future performance of the materials (Solaimanian et al. 2003). Nevertheless, several test methods have been developed to characterize the moisture susceptibility of asphalt mixtures (Airey & Choi 2002). The test methods can be classified in many ways, for example on the basis of their generic nature: subjective qualification, quantification by a performance index and tests that use the ratio of a single or multiple performance parameters to assess moisture damage (Caro et al. 2008b) or based on whether the tests are performed on loose or compacted mixtures (Solaimanian et al. 2003).

Among the various test methods, the boiling water (ASTM D3625), static immersion (AASHTO T182) and rolling bottle (CEN prEN 12697-11) tests are used to assess the propensity of bituminous mixtures to moisture damage by visual estimation of the amount of binder lost (or retained) from coated aggregates. These tests can provide a qualitatively measure for addressing adhesion between binder and aggregates. The interpretation of the results, however, can vary significantly as the degree of bitumen coverage is estimated by individual operators. More recently, computer-aided techniques were employed to minimize the subjectivity of the rolling bottle test method (Grönniger et al. 2010). Even though imaging techniques were found to be promising for standardizing the visual inspection method, further improvements are required as these techniques take into account only one surface of the aggregate, which is part of its total surface area that interacts with the binder material. Moreover, strict protocols are needed with respect to the quality of the image and the conditions under which imaging was made (camera position, lighting etc.). Therefore, one should be careful when drawing to conclusions for the moisture susceptibility of the whole asphalt mixture based on the tests results.

Other test procedures that are commonly used for the evaluation of asphalt mixtures with respect to moisture susceptibility include the Tunnicliff and Root conditioning (NCHRP 274), the modified Lottman (AASHTO T283), the saturation ageing tensile stiffness (EN 12697-45) and the Hamburg wheel tracking (AASHTO T234) tests (Hicks et al. 2003). Of all test methods, the modified Lottman test is the most popular test for characterizing moisture susceptibility of asphalt mixtures. The test resulted from the combination of the Lottman and Tunnicliff and Root tests. Other variants of the modified Lottman test method are being used all over the world. The test involves the

comparison of a dry control set of samples with samples subjected to vacuum saturation and freeze thaw conditioning. The damage due to moisture is evaluated on the basis of the indirect tensile strength test. The percentage loss of tensile strength of the mixture, widely known as tensile strength ratio (TSR), is used to evaluate moisture sensitivity of the mixtures. The tensile strength ratio is expressed as

$$TSR(\%) = \frac{S_2}{S_1} \times 100 \qquad [3.1]$$

, where S_1 and S_2 are the average tensile strengths of the control and the conditioned set of samples, respectively. The minimum TSR values, which are required to determine if a mixture is moisture susceptible, are typically between 0.70 and 0.90.

Nevertheless, despite its popularity, modified Lottman test results are known to be rather variable and do not necessarily describe accurately moisture susceptibility. Several drawbacks have been reported about the test, i.e. poor correlation with field performance, ineffective moisture conditioning protocols. Kringos et al. (2009) and Azari (2010) analyzed the moisture infiltration process and the structural nature of the modified Lottman test. Both studies concluded that the micro-cracks induced by the vacuum suction procedure may increase the variability of the test. In addition, the conditioning protocol of the test fails to capture the time frame over which moisture infiltration occurs and disregards the short-term moisture processes related to pumping action. Kanitpong and Bahia (2008) investigated the relation between pavement field performance (as given by the pavement distress index, PDI) and TSR values measured in the laboratory. The analysis indicated that no relation exists between PDI indices and TSR values for a total of 21 pavement sections under study. In addition, the TSR values could not correlate to common distresses, such as rutting and raveling, which are associated to moisture damage. It was also reported that the TSR data could only show the effect of antistripping additives, but then again did not correlate to field performance. In another study, Birgisson et al. (2005) also found that permeability did not correlate well with the TSR values; this result was attributed to the high variability of the indirect tensile tests and the microstructural characteristics of the mixtures. Differences were also observed during the saturation procedure of fine and coarse graded mixtures. The requirement of a minimum level of saturation could not be achieved with the same number of vacuum cycles for all mixtures. The researchers suggested that the mixture should be subjected to a single vacuum saturation cycle and find its own level of saturation, which reflects better its physical sensitivity to moisture.

Another test method is the saturation ageing tensile stiffness (SATS) test. The SATS method involves conditioning of the samples in a pressurized chamber at high temperature and humid conditions. Moisture sensitivity is evaluated using the retained stiffness modulus, which is calculated by dividing the stiffness of the conditioned by the stiffness of the unconditioned sample. Past research has shown that the method is able to differentiate between good and poor performing aggregates (Collop et al. 2004, Choi 2005, and Collop et al. 2007). In their study, Airey et al. (2005) reported that the SATS results agreed with the ranking as given by the modified Lottman method for six high modulus base mixtures. Yet the relative performance of mixtures prepared with highly moisture susceptible aggregates was considerably lower in the SATS test; this finding suggests that SATS conditioning is more severe compared to the modified Lottman conditioning (bath conditioning followed by freeze-thaw cycles). This indication is not unlikely if one considers that, in

SATS, mixtures are moisture conditioned at an elevated temperature and pressure, which as discussed in the second chapter can accelerate long-term moisture diffusion. Nevertheless, SATS does not consider pumping action, as conditioning does not simulate cyclic pressures in the pores of the mixture.

A different test, which is used in practice today especially from researchers and state highway agencies in the USA, is the Hamburg wheel tracking (HWT) test. The test involves repetitive loading of laboratory compacted samples or slabs using a steel wheel. During the test, the samples are submerged in a temperature controlled water bath. Stripping is identified with the presence of a sudden inflection point in plastic deformation during the application of cyclic loading, known as stripping inflection point. Similarly to the modified Lottman test, the HWT test shows low repeatability and is not able to predict pavement performance, mainly due to the lack of standardization in the sample preparation procedure (Cox et al. 2013). Moreover, it has been reported that the severity of the test may actually lead to the rejection of mixtures that are known to perform adequately in the field against moisture damage (Aschenbrener et al. 1994, Lu & Harvey 2006).

The studies presented thus far provide evidence that the test methods currently used to characterize a mixture in terms of its sensitivity to moisture damage show poor repeatability and do not correlate well with field observations. Hence the development of a new test that simulates the various moisture induced damage processes in the field and takes into account the moisture failure mechanisms in a relevant timeframe is necessary. Such a test could possibly provide the asphalt community with results that can be used in performance prediction.

This chapter focuses on the design of a conditioning protocol that combines the main moisture degradation processes. The results are used to quantify the contribution of each mechanism to the overall damage of the mixtures. In addition, this study provides some observations on the effect of pressure cycles on asphalt mixtures on the basis of X-ray computed tomography. Eventually, these results may contribute to the establishment of a protocol for the assessment of moisture sensitivity of bituminous mixtures.

4.2 Development of a new moisture conditioning protocol

The new moisture conditioning protocol addresses the individual damage mechanisms that are associated with (a) long-term moisture diffusion and (b) pore pressure generation due to traffic loading and aims to quantify their contributions to strength degradation of asphalt mixtures. In the following, the conditioning protocol is described in detail and the various parameters, for instance the duration of bath conditioning and the number of pressure cycles are defined.

4.2.1 Moisture damage susceptibility protocol

In the new protocol, the conditioning of asphalt mixtures was achieved by a combination of two moisture conditioning methods: (a) immersion in a water bath and (b) cyclic pore pressure

application. Bath conditioning was performed at elevated temperatures so as to facilitate moisture diffusion into the mixture (since diffusion is faster at higher temperatures), accelerating thus the long-term degradation of material properties. The duration of the bath conditioning phase was decided on the basis of finite element analyses. Simulations of moisture diffusion into a cylindrical porous asphalt sample were performed and are discussed in paragraph 4.2.2. Cycles of pore pressure were applied on the asphalt samples by means of the moisture induced stress tester (MiST). MiST is a self-contained unit, Figure 4.1, which includes a hydraulic pump and a piston mechanism that is designed to cyclically apply pressure inside a sample chamber. Moisture conditioning is performed by placing a compacted asphalt sample in the chamber and filling it with water. Then the water is pushed through and pumped out from the sample, thus creating pressure cycles between zero and the chosen pressure. One can choose the pressure, temperature and the number of conditioning cycles to replicate different combinations of traffic and environmental conditions (InstroTek Inc. 2012).

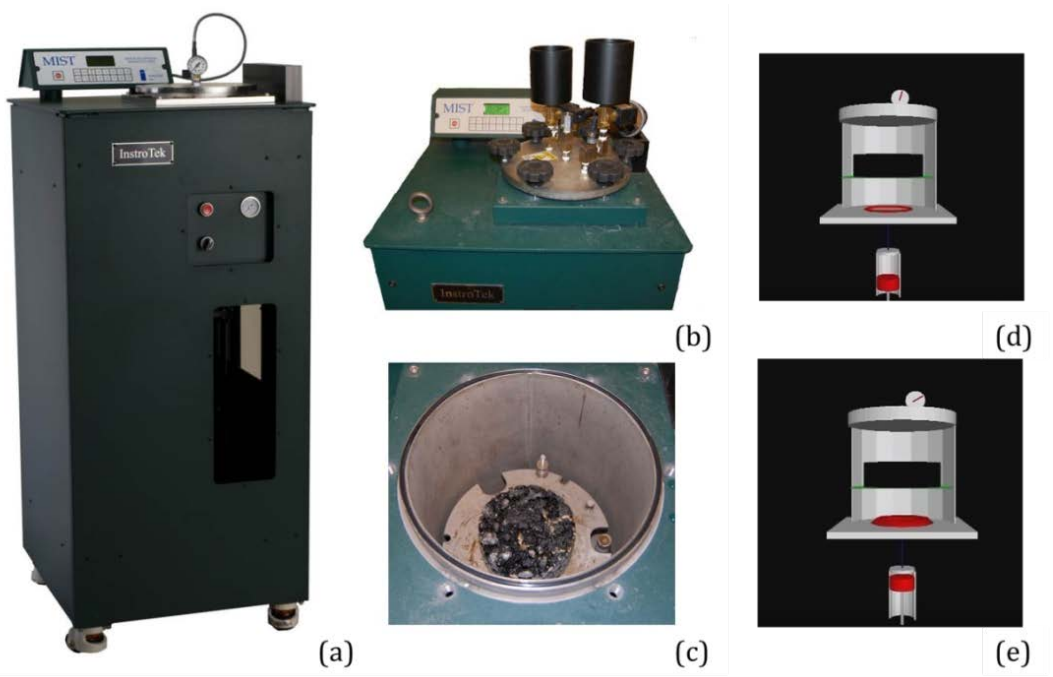

Figure 4.1. (a, b) Different views of the MiST unit; (c) a compacted sample is placed in the MiST tank; (d, e) the water in the chamber is pressurized by means of piston, which inflates and deflates a flexible air bladder located below the sample.

Figure 4.2 shows schematically the various stages of the combined moisture conditioning protocol. First the samples were immersed in a bath with distilled water at a temperature of 60°C, in order to expedite the diffusion of water into the asphalt samples. At specified time intervals of 2, 4, 6 and 8 weeks three samples per mixture were removed from the bath, placed in water at 20°C for 2 hours and then stored in a climatic chamber at 20°C until tested. An additional three samples per mixture were removed from the bath and further conditioned in MiST; 4000 cycles of pressure were applied at a temperature of 60°C and a pressure of 70 psi (0.48 MPa). After MiST conditioning, the samples were placed in a water bath at 20°C for 2 hours.

The additional step of placing the samples in a water bath at room temperature (20°C) was found to be essential, considering that the samples were bath conditioned at high temperature and therefore, they were soft after bath or before MiST application. This extra step allowed the stabilization and further handling of the samples. The degradation of the mechanical properties due to moisture conditioning can be evaluated by several mechanical tests performed before and after moisture conditioning. In this research, indirect tensile tests (ITT) were performed in accordance with the EN 12697-23 European standard. The indirect tensile strength tests were performed at 20°C at a loading rate of 50 mm/min.

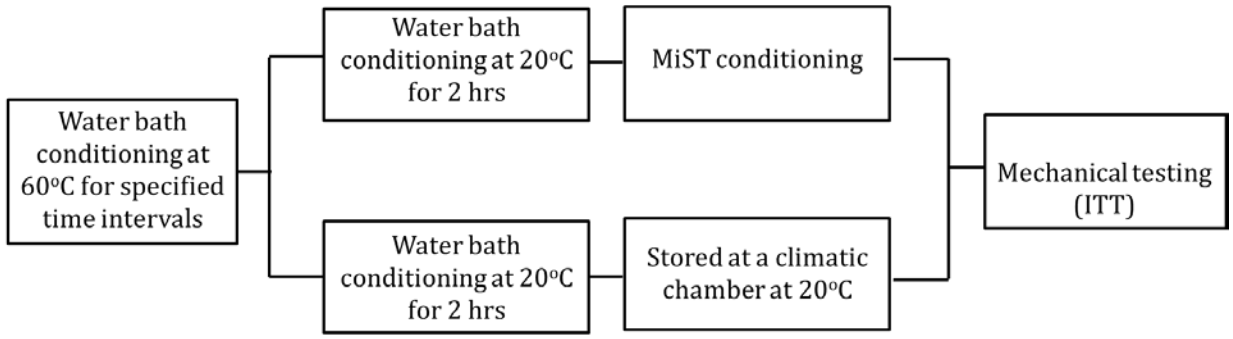

Figure 4.2. Schematic of the applied moisture conditioning protocol.

4.2.2 Duration of bath conditioning phase

The duration of the moisture conditioning phase in the water bath is a critical parameter that can influence significantly the results of the indirect tensile test. In an attempt to minimize any variations in the ITT results, finite element simulations of moisture diffusion into an asphalt sample were performed so as to ensure that a homogenized moisture concentration profile exists in the body of the samples before testing. The FE diffusion analysis tool developed in *chapter two* was used for simulating moisture diffusion. From the results, the time required for moisture to diffuse into the asphalt sample was estimated and a decision on the duration of the bath conditioning phase for the suggested protocol was made.

The analysis was performed on 3D microscale meshes obtained from real cylindrical asphalt samples. X-ray computed tomography (CT) was utilised as a non-destructive technique in order to obtain the digital description of the internal structure of the asphalt samples. Then, Simpleware® software was used to enable the conversion of CT scan images into FE meshes‡. The developed microscale meshes comprised three components, namely aggregates, binder (bitumen plus filler and fines) and air voids.

For the analysis, a specific moisture diffusion coefficient was assigned to each material phase. Each material phase was assumed to be isotropic and a constant diffusion coefficient was assigned. The diffusivity values were adopted from a study by Kringos et al. (2008). Diffusion coefficients equal to 11.08×10^{-3} mm^2/hr and $0.72 mm^2/hr$ were assigned to the mortar and aggregate phases,

‡More details on the generation of the 3D finite element meshes are given in chapter six.

respectively. The diffusion coefficient of the air void phase was assumed as 93.6×10^3 mm^2/hr, a value reported in Kassem et al. (2009). For the simulations, a constant moisture boundary condition (θ=1) was applied on the top surface and the periphery of the asphalt samples.

A number of nodes were selected as output locations for the moisture concentration values. All selected nodes are lying on the diameter of the sample and are located 1 mm above the bottom surface of the sample as shown in Figure 4.3(a). Figure 4.3(b) illustrates the distribution and the connectivity of the air voids in the sample. The interconnected voids and the inaccessible air voids are shown in blue and red colour, respectively.

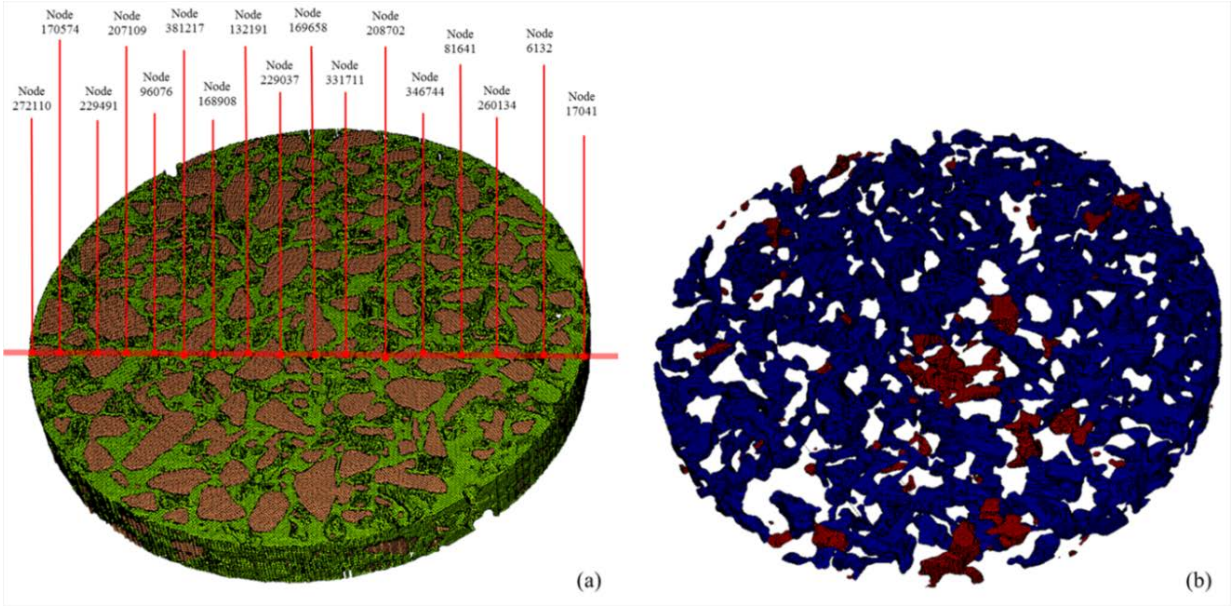

Figure 4.3. (a) Output locations for normalized moisture concentration and (b) volume rendering of the air void phase of the porous asphalt sample.

Figure 4.4 presents the results of the moisture diffusion analysis; based on these, key observations about the homogeneity of the moisture concentration profile can be made. On the whole it was observed that the concentration profile of moisture is non-uniform and various parts of the sample require longer conditioning times to reach full saturation. Also, the peak, which consistently appears at every time interval, coincides spatially with the presence of isolated voids in the sample, Figure 4.3b. This discontinuity in the air void network is a hindrance to diffusion of moisture in that specific location of the sample; hence the overall time required for the sample to reach full saturation is prolonged. The numerical analysis indicated that a total of 14 days of moisture conditioning is required for the normalized moisture concentration to attain its maximum value at each location in the sample. Therefore, to make sure that a spatially homogenized moisture profile is present within the asphalt samples, the first interval of the bath conditioning phase was chosen to be two weeks.

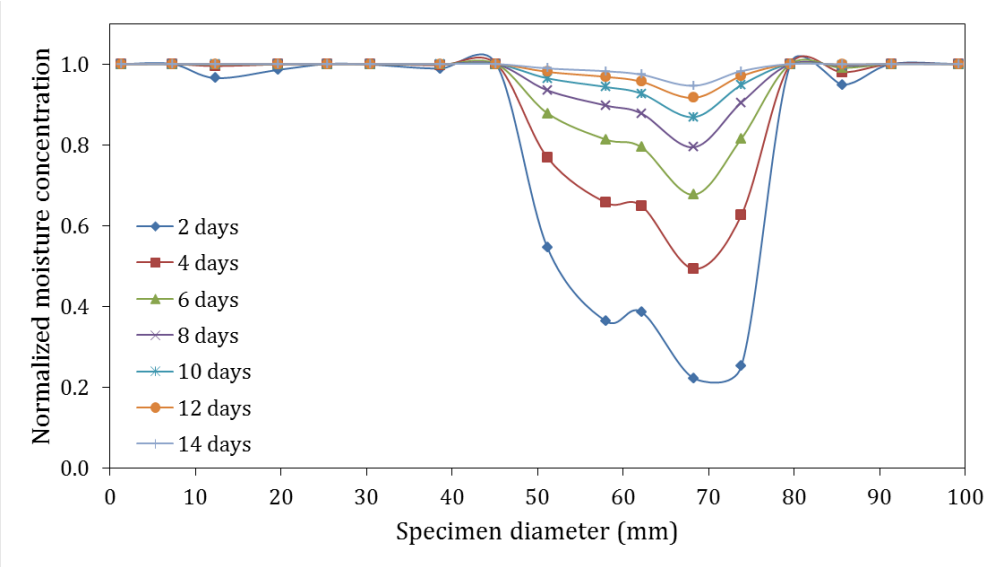

Figure 4.4. Results from the moisture diffusion analysis: Normalized moisture concentration profile along the diameter of the sample at various time intervals.

In reality, for a given asphalt mixture, the diffusion of moisture into a mixture is greatly affected by the content, distribution and interconnectivity of the air void phase (Varveri et al. 2015). Furthermore, the type of binder, filler and aggregates can influence the diffusion of moisture into the mixture due to the unique coefficients of diffusion associated with the particular physico-chemical characteristics of each material phase. However the results of the numerical analysis can be used in order to gain a better insight into the conditioning times required for full saturation of the various asphalt types. In this manner, extremely short or long conditioning periods can be avoided when setting up testing protocols and specifications.

4.2.3 Optimum number of MiST conditioning cycles

In setting up the new moisture conditioning protocol, apart from the duration of the bath conditioning phase, the final parameter to be considered was the optimum number of MiST conditioning cycles. The objective was to apply the fewer number of MiST cycles, which corresponds to shorter testing times, while maintaining the ability to distinguish among mixtures with different moisture damage susceptibility. For the investigation, a porous asphalt mixture prepared with sandstone aggregate and SBS modified binder was selected. Based on field data and laboratory tests, this particular combination is expected to have the best performance against moisture damage (Kringos et al. 2008). Assuming that degradation in strength would be observed for this highly moisture resistant mixture, it was ensured that all mixtures would show a reduction in strength after MiST application.

The samples were subjected to MiST conditioning without any prior bath conditioning. Three sets of samples were utilised in replicates of three. The first set of samples was subjected to 1000 cycles, while the second and third set of samples to 4000 and 8000 cycles, respectively. The test was performed at 60°C temperature and 0.48 MPa pressure. Figure 4.5 shows the average tensile

strength out of three replicate samples (black solid line). The dashed lines show the maximum and minimum strength obtained for the three replicates at each conditioning regime. The graph shows that strength decreases with increasing number of MiST cycles, indicating damage development due to the repetitive pressure application. The samples showed an average reduction in strength of about 16% after 1000 cycles, 18% after 4000 cycles and 31% after 8000 cycles of MiST conditioning.

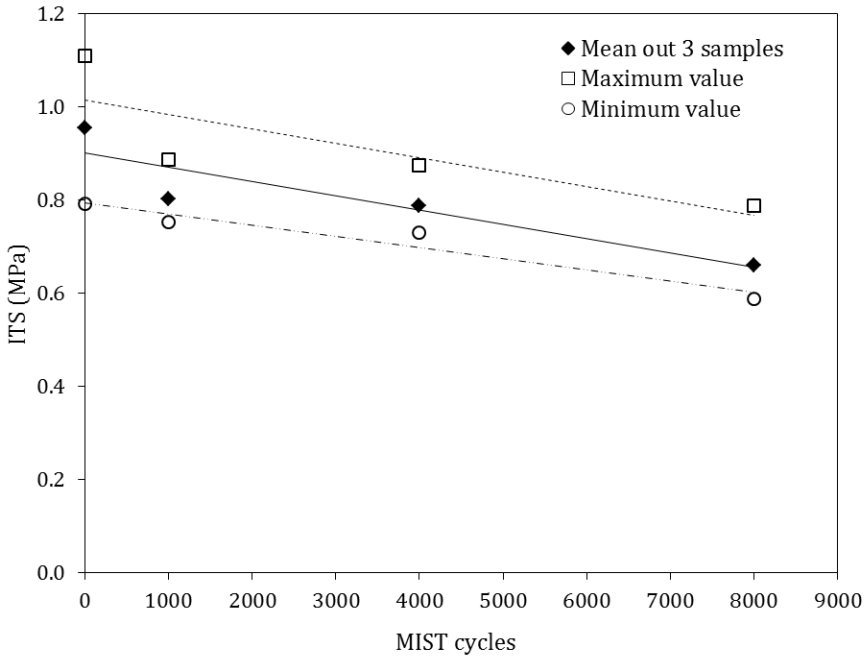

Figure 4.5. Strength reduction with increasing number of MIST cycles.

On the basis of the results, the optimum number of cycles was selected to be 4000, which results to a testing period of eight hours. Even though the application of 1000 cycles resulted in an almost equal reduction in strength as after 4000 cycles, it was considered too short to sufficiently condition the asphalt sample. A higher reduction in strength was obtained after 8000 cycles. However, the above investigation was performed on dry unconditioned samples while MiST is intended to be used as a second stage conditioning method. The additional reduction in strength due to first stage bath conditioning might cause a significant disintegration of the sample, making it thus impossible to perform a mechanical test.

4.3 Materials and sample preparation

Porous asphalt (PA) samples were produced according to Dutch specifications (CROW 2010). The requirements for porous asphalt mixtures and the actual composition of the mixtures prepared for this study are shown in Table 4.1. It should be noted that the values in the Table represent the composition by weight, while the weight of the bitumen is expressed relatively to 100% weight of the mineral aggregates.

Table 4.1. Mixture composition based on Dutch specifications (CROW 2010)

Aggregate size [mm]	Material density [kg/m^3]	RAW specification cumulative retained [%]	Retained by weight [%]	Cumulative retained [%]	Material weight [gr]	Cumulative by weight [gr]
C 22.4 - 16.0	2778	0 -7	1.7	1.7	85.4	85.4
C 16 - 11.2	2774	15 - 30	20.9	22.6	1049.7	1135.1
C 11.2 - 8	2762	50 - 65	42.3	64.9	2124.5	3259.6
C 8 - 5.6	2765	70 - 85	12.9	77.8	647.9	3907.5
C 5.6 - 2	2677	85	6.2	84	311.4	4218.9
2 - 0.063	2781	95.5	11.2	95.2	562.6	4781.5
Filler (<0.063)			4.8	100	241.1	5022.6
Bitumen	1030		4.5% by weight		226	5248.6

A total of six variants of the PA mixture were prepared, which differed in terms of the aggregate and bitumen types used. For a better control of the test variables the gradation was kept the same for the various mixtures. The samples were compacted to a target air void content of 20% using a gyratory compactor. The gyratory samples had a 150 mm diameter and height; samples with a 101.6 mm diameter were cored along the vertical axis of the gyratory samples and further sliced into 50 mm thickness samples in order to be used for moisture conditioning and subsequent testing. Figure 4.6 shows steps of the sample preparation procedure.

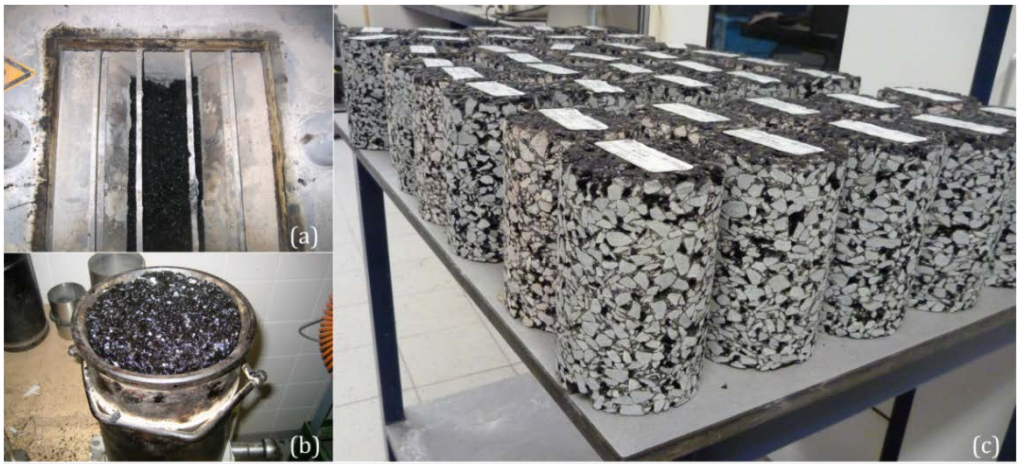

Figure 4.6. Mixture preparation: (a) mixing of the asphaltic components, (b) sample in the gyratory compactor, (c) gyratory compacted samples.

The constituent materials, namely bitumen, mineral filler and aggregates were selected based on experience from previous studies, which have shown that different moisture sensitivity is expected for the various combinations of the materials. Specifically, two aggregate types were used; granite which is known to be prone to moisture damage and sandstone with known good field moisture damage performance. The bitumens used were Total 70/100 penetration grade bitumen, 45/80 SBS modified Sealoflex 5-50 (PA) bitumen and 60/90 SBS modified Cariphalte XS bitumen. The filler was hydrated lime filler (Wigro 60K). In *chapter three*, the same bitumens were used for cohesion tests. The different mixtures are denoted as GP, GS, GC, SP, SS, SC, with the letters G and S

denoting the granite and sandstone aggregates respectively, while letters P, S and C denote the bitumen types used (Pen 70/100, Sealoflex 5-50 (PA) and Cariphalte XS). For each mixture, 30 replicates were produced, which were further divided into 10 sets of 3 samples for conditioning in combinations of water bath immersion and cyclic pore pressure application.

4.4 Quantification of long- and short-term moisture damage

Table 4.2 shows the strength of all asphalt mixtures after the various combinations of bath immersion and MiST conditioning. Each data point represents the average strength out of three replicate samples. Also, the minimum and maximum strength, standard deviation and coefficient of variation of each set of measurements are given.

Table 4.2. Tensile strength at 20°C of asphalt mixtures exposed to various combinations of moisture conditioning.

Mixture	Conditioning method	Bath immersion					Bath immersion & MiST				
	Duration of bath conditioning [days]	0	14	28	42	56	0	14	28	42	56
GP	Mean strength [MPa]	0.67	0.62	0.59	0.51	0.51	0.63	0.59	0.55	0.50	0.43
	Min strength [MPa]	0.62	0.58	0.48	0.40	0.44	0.53	0.53	0.49	0.43	0.38
	Max strength [MPa]	0.74	0.68	0.74	0.59	0.58	0.72	0.70	0.59	0.57	0.49
	SD [MPa]	0.05	0.04	0.11	0.08	0.06	0.08	0.08	0.04	0.06	0.05
	CV [%]	7.8	7.2	18.7	15.5	11.2	12.3	12.9	7.9	11.5	10.5
GS	Mean strength [MPa]	0.89	0.84	0.80	0.74	0.71	0.86	0.79	0.75	0.72	0.62
	Min strength [MPa]	0.78	0.75	0.75	0.66	0.64	0.80	0.72	0.69	0.62	0.53
	Max strength [MPa]	0.95	0.98	0.87	0.78	0.81	0.90	0.88	0.82	0.84	0.67
	SD [MPa]	0.08	0.10	0.05	0.05	0.07	0.04	0.07	0.05	0.09	0.06
	CV [%]	8.5	12.1	6.3	7.4	10.0	5.0	8.5	7.1	12.5	9.9
GC	Mean strength [MPa]	0.92	0.91	0.90	0.90	0.84	0.85	0.82	0.81	0.80	0.71
	Min strength [MPa]	0.86	0.87	0.83	0.78	0.75	0.82	0.74	0.71	0.69	0.65
	Max strength [MPa]	0.99	0.98	0.95	0.99	0.89	0.89	0.91	0.98	0.93	0.79
	SD [MPa]	0.05	0.05	0.05	0.09	0.06	0.03	0.07	0.12	0.10	0.06
	CV [%]	5.8	5.3	5.8	9.7	7.6	3.9	8.5	15.1	12.4	8.2
SP	Mean strength [MPa]	0.63	0.61	0.61	0.56	0.55	0.57	0.55	0.52	0.50	0.45
	Min strength [MPa]	0.55	0.52	0.51	0.49	0.48	0.50	0.49	0.45	0.43	0.37
	Max strength [MPa]	0.72	0.71	0.69	0.63	0.62	0.65	0.64	0.59	0.58	0.51
	SD [MPa]	0.07	0.08	0.07	0.06	0.06	0.06	0.06	0.06	0.06	0.06
	CV [%]	11.3	12.8	12.3	10.2	10.4	10.8	11.8	11.0	12.4	13.2
SS	Mean strength [MPa]	0.82	0.79	0.78	0.69	0.65	0.80	0.78	0.77	0.61	0.60
	Min strength [MPa]	0.79	0.72	0.73	0.62	0.61	0.71	0.73	0.74	0.56	0.54
	Max strength [MPa]	0.85	0.85	0.87	0.74	0.70	0.87	0.84	0.80	0.65	0.69
	SD [MPa]	0.02	0.05	0.07	0.05	0.04	0.07	0.05	0.02	0.04	0.06
	CV [%]	3.1	6.7	8.5	7.4	5.7	8.3	5.8	3.2	6.0	10.6
SC	Mean strength [MPa]	0.97	0.94	0.88	0.89	0.88	0.91	0.88	0.83	0.80	0.76
	Min strength [MPa]	0.92	0.89	0.84	0.82	0.82	0.88	0.81	0.78	0.78	0.68
	Max strength [MPa]	1.02	1.01	0.91	0.95	0.97	0.94	0.94	0.87	0.83	0.84
	SD [MPa]	0.04	0.05	0.03	0.05	0.06	0.02	0.05	0.04	0.02	0.07
	CV [%]	4.2	5.3	3.3	6.0	7.4	2.8	6.1	4.5	2.7	8.6

Table 4.2 is quite revealing in several ways. First, long-term bath conditioning resulted in significant reduction in mixture strength with respect to their initial strength at dry conditions. For example, the mean strength of the GP mixture changed from 0.67 to 0.51 MPa after 56 days of moisture conditioning, a reduction of about 24%. In addition, the data clearly show that, depending on mixture composition, the effect of bath conditioning may vary substantially. Diverse results were also obtained based on the type of the applied conditioning method. In the following, the influence of both conditioning type and mixture composition on mixture strength is discussed.

4.4.1 Influence of conditioning type

The evaluation of the asphalt samples for their moisture damage susceptibility was performed on the basis of the indirect tensile strength (ITS) and the indirect tensile strength ratio (ITSR). Figure 4.7 shows the mean ITSR values (from 3 replicate samples) after long periods of bath conditioning for all mixtures. The coefficient of variation (%) is reported on the top of each column. The dashed red line represents the threshold value below which an asphalt mixture is considered to be more susceptible to moisture damage according to the Dutch standards (CROW 2010).

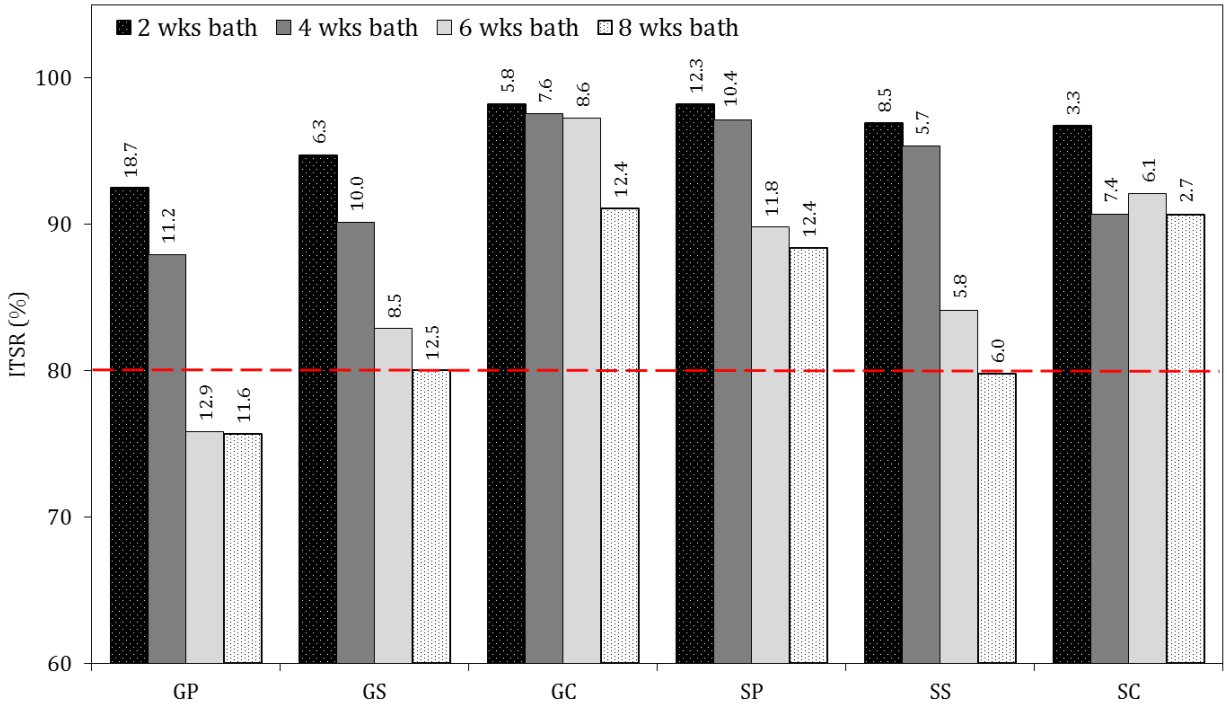

Figure 4.7. Mean ITSR values after the application of the various moisture conditioning regimes.

The ITSR results suggest that mixtures prepared with SBS modified binders have a better performance with respect to moisture damage. Specifically, the GP (granite aggregate; Pen 10/100 bitumen) and SP (sandstone aggregate; unmodified bitumen) mixtures were found to be more susceptible to moisture damage compared to the polymer modified mixture variants. Quite the opposite trend is observed for mixtures GC and SC (granite or sandstone aggregate; SBS modified bitumen), which showed the best performance among all mixtures after the application of the

several moisture conditioning scenarios. Overall, the TSR values after 56 days of bath conditioning (longest conditioning period) showed that all mixtures are expected to perform satisfactorily against moisture damage. However, if one considers also the dynamic effect of pore pressures it is observed that all mixtures exhibited a further decrease in their strength, which resulted to TSR values far lower than the threshold, suggesting thus that the mixtures are prone to moisture damage, Figure 4.8.

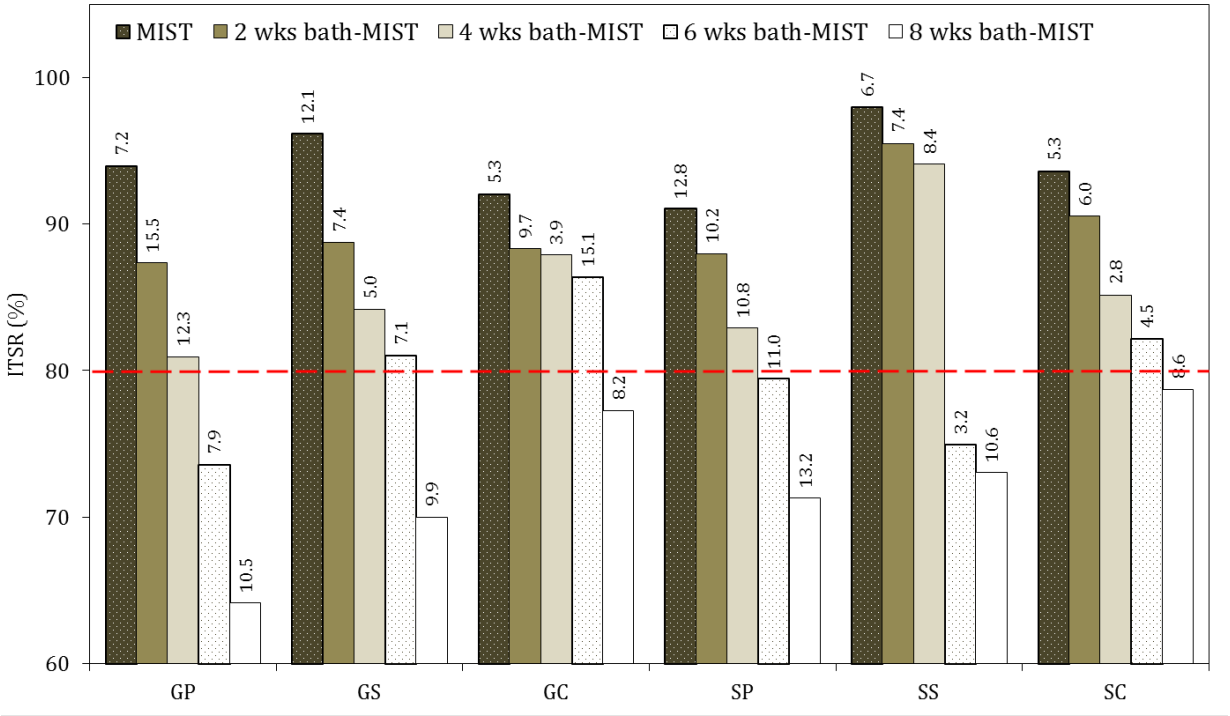

Figure 4.8. Mean ITSR values after the application of the various moisture conditioning regimes.

The test results are plotted in the graphs shown in Figures 4.9-4.11 and the contributions of the short- and long-term moisture damage on the tensile strength of the samples were quantified. The solid curves demonstrate the effect of moisture diffusion on tensile strength due to bath conditioning alone, while the dashed curves show the influence of the combined conditioning protocol (bath and MiST) on tensile strength. Each data point represents the average strength out of three replicate samples.

The contribution of the cyclic pore pressure to the total strength degradation of the samples is given as the gap between the solid and the dashed curves (curves with identical colours represent the same mixture) that correspond to the different moisture conditioning protocols. The combined protocol represents two different damage inducing mechanisms, i.e. moisture diffusion and pore pressures. Moisture diffusion, which is a slow process and requires long periods to occur, can cause a softening of asphalt binders, change their rheological properties and eventually result to debonding of the aggregate-binder interface, thus causing a reduction in terms of strength and stiffness. On the other hand, pressure increase in the saturated macro pores of a mixture can lead to the development of additional tensile stresses to the surrounding aggregates causing them to separate and hence initiate the formation or propagation of cracks in the binder film.

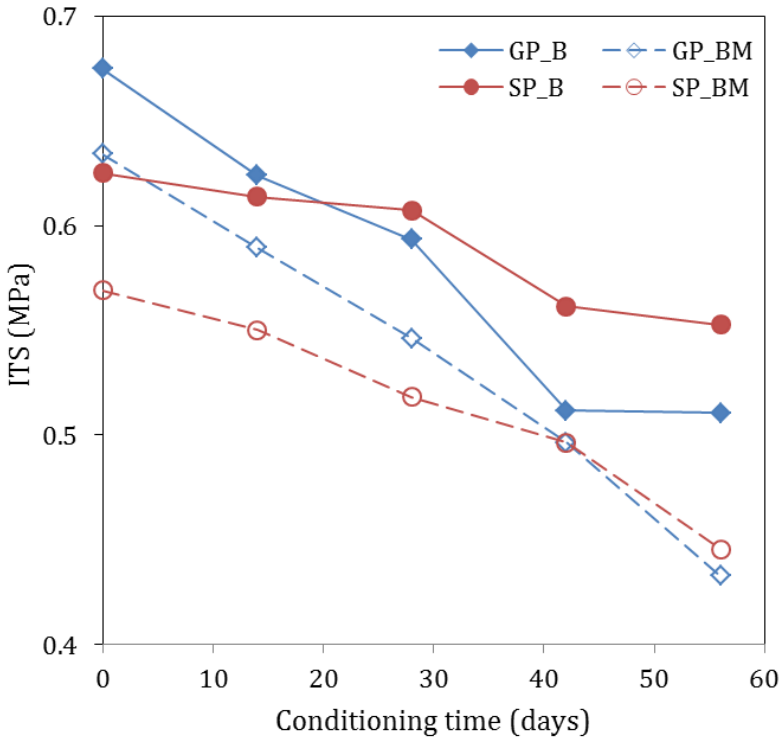

Figure 4.9. Strength degradation curves after bath (B) and bath-MiST (BM) conditioning for mixtures containing a standard 70/100 penetration grade bitumen plus granite and sandstone aggregates.

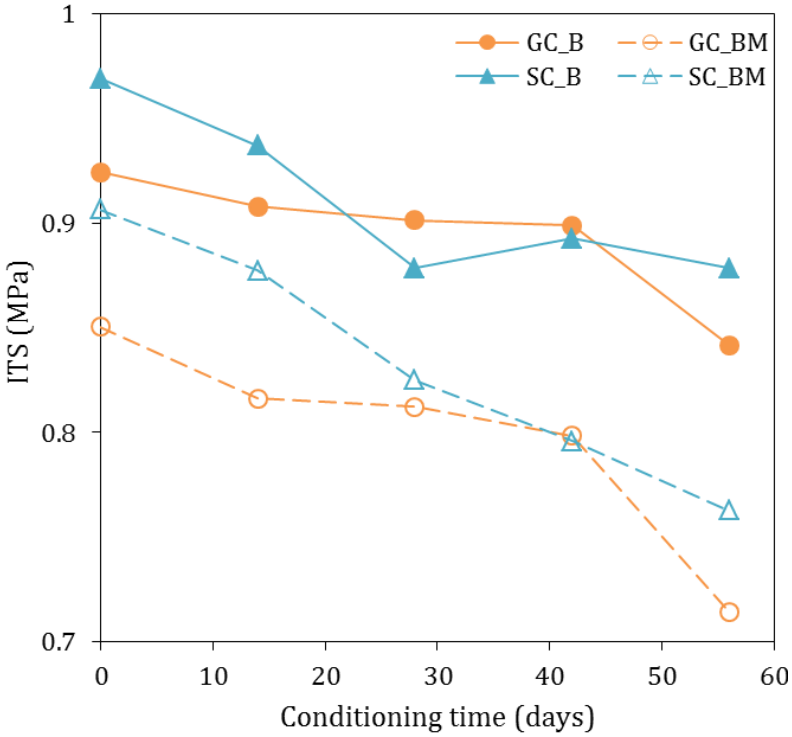

Figure 4.10. Strength degradation curves after bath (B) and bath-MiST (BM) conditioning for mixtures containing a 60/90 SBS modified bitumen Cariphalte XS plus granite and sandstone aggregates.

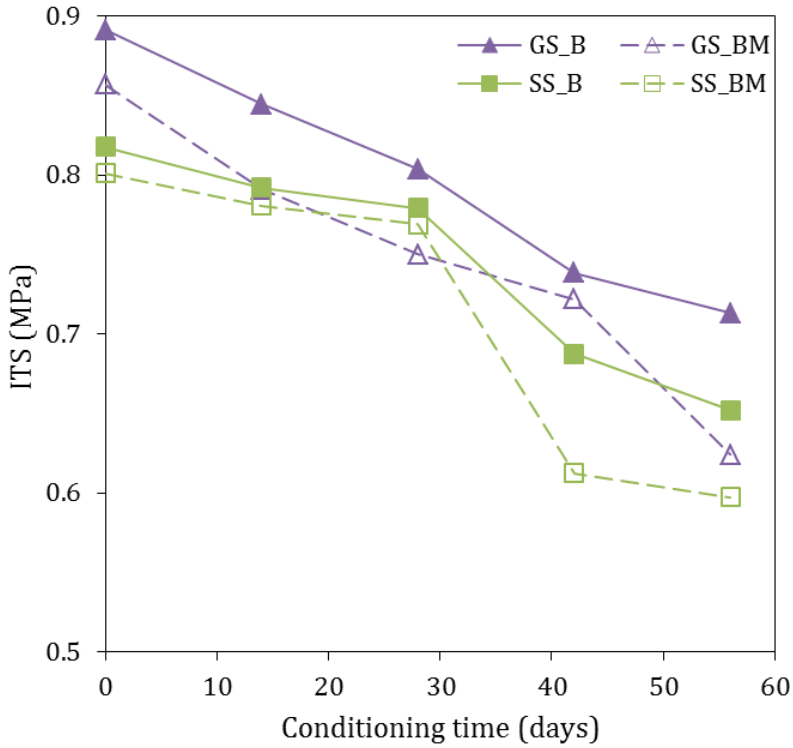

Figure 4.11. Strength degradation curves after bath (B) and bath-MiST (BM) conditioning for mixtures containing 45/80 SBS modified bitumen Sealoflex 5-50 (PA) plus granite and sandstone aggregates.

The graphs show that the distance between the two curves for each mixture increases with extended periods of long-term bath conditioning. This can be explained if one considers the different damage patterns associated with moisture diffusion and pore pressure application. As the duration of the long-term moisture conditioning increased, the cohesive and adhesive properties of the binder degraded further, hence making it more vulnerable to the application of short-term pore pressures. As a result, a higher reduction in strength for the same number of MiST cycles was observed.

Table 4.3 presents the reduction in strength after the application of both conditioning methods, i.e. bath and bath-MiST protocol. Furthermore the reduction in strength due to MiST conditioning only, which is calculated as the difference between the two protocols, is reported. The data revealed the detrimental effect of moisture on the mixtures. Specifically, a high reduction in strength was observed for the GP mixture (granite plus unmodified bitumen) after just about every conditioning protocol. The strength of the samples decreased approximately by 24% after 56 days of conditioning, and then, after MiST application, further reduced to 35% with respect to their original dry strength. On the contrary, the mixtures prepared with PmB had a superior performance against moisture damage irrespectively of the aggregate type used. Even though a SBS modifier was used in both bitumen types, the behaviour of the mixtures against long- and short-term moisture conditioning differed significantly. The mixtures containing Cariphalte XS bitumen exhibited higher reduction in strength after MiST application in comparison to the mixtures prepared with Sealoflex 5-50 (PA) bitumen. Quite the opposite trend was observed after long-term bath conditioning. The results show that the effect of moisture diffusion was not significant for the GC and SC mixtures and

did not result to high levels of damage, whereas the strength reduction was about two times higher for the GS and SS mixtures. These results suggest that the two moisture damage inducing mechanisms are relatively independent from each other. It may be that an asphalt mixture is more prone to one damage mode than the other based on its composition. However, when one damage mode is activated, the other can accentuate the phenomena. In the next section, the effect of mixture composition on moisture sensitivity is discussed in more detail.

Table 4.3. Average reduction (%) in tensile strength.

Conditioning method	Conditioning time[days]	GP	GS	GC	SP	SS	SC
Bath immersion	0	0.0	0.0	0.0	0.0	0.0	0.0
	14	7.6	5.3	1.8	1.8	3.1	3.3
	28	12.1	9.9	2.5	2.9	4.7	9.3
	42	24.2	17.1	2.8	10.2	15.9	7.9
	56	24.3	20.0	9.0	11.6	20.3	9.3
Bath immersion & MiST	0	6.0	3.9	8.0	9.0	2.0	6.4
	14	12.6	11.3	11.7	12.0	4.5	9.5
	28	19.1	15.9	12.1	17.1	5.9	14.9
	42	26.4	19.0	13.6	20.6	25.1	17.9
	56	35.9	30.0	22.7	28.7	27.0	21.3
MiST contribution	0	6.0	3.9	8.0	9.0	2.0	6.4
	14	5.1	6.0	9.9	10.2	1.4	6.2
	28	7.0	6.0	9.6	14.3	1.3	5.5
	42	2.3	1.9	10.9	10.4	9.2	10.0
	56	11.5	10.0	13.8	17.1	6.7	12.0

4.4.2 Influence of mixture composition

The constituents of a mixture and the way they interact with each other are of great importance when discussing moisture damage. As discussed earlier, in chapter two, the type of mineral aggregate used plays a major role on the moisture susceptibility characteristics of a mixture. In this study, two aggregates, namely granite and sandstone, were investigated. The graphs in Figures 4.9-4.11 show that, in general, the dry strength of the granite mixtures was higher than this of sandstone mixtures. However, the reduction of strength due to moisture conditioning was more severe for granite mixtures than for those containing sandstone aggregates. After 28 days of bath conditioning the granite mixtures, depending on the bitumen type, lost from 2.5% to 12.1% of their original strength, while the strength loss was 2.9% to 9.3% for the sandstone mixtures. These results are consistent with those of Kringos et al. (2008) who used the same combinations of materials and showed, based on laboratory tests and field performance, that there was a significant difference in the performance of mixtures with sandstone and granite aggregates, with the first performing better in the field than the latter.

To investigate the effect of polymer modification on the moisture susceptibility of asphalt mixtures three mortar types were used, in combination with granite and sandstone aggregates, to

produce asphalt mixtures. The same mortars denoted as mortar B, C and D were used in chapter two. The mortars were prepared with hydrated lime filler and Norwegian sand; for binder B a Total 70/100 penetration grade bitumen was used, while for mortar C and D two polymer modified bitumen types were used, the Cariphalte XS and the Sealoflex 5-50 (PA) bitumen, respectively. In this study, mortar B was used for the production of the SP and GP mixtures, while mortar C and mortar D were used for mixtures SC and GC, and mixtures SS and GS, respectively.

In the second chapter, the long-term moisture susceptibility characteristics of these asphalt mortars were investigated through moisture uptake measurements. From the results, it was observed that the amount and the rate of moisture absorption varied with bitumen type. The use of polymer modified bitumen had a substantial effect on the uptake of moisture. After long-term bath conditioning the mortars that contained polymer modified bitumen absorbed two times lesser moisture in comparison to the mortar, which was prepared with standard penetration grade bitumen. A different behaviour was also observed with respect to the rate of moisture absorption. The SBS modified mortars absorbed moisture in a lower rate compared to the unmodified mortar. As a result, the modified mortars are expected to saturate slower compared to the mortar with the standard bitumen type.

In mixture level, the results demonstrated that the degradation in strength is lower for asphalt mixtures with polymer modified mortars, irrespective of the aggregate type used, thus indicating that the use of polymer modified bitumen increases the resistance of the mixture to moisture damage. This observation can be explained on the basis of the moisture uptake measurements obtained in Chapter two for the asphalt mortars. Two possible explanations can be considered. Bearing in mind that moisture diffusion progresses slower for polymer modified mortars (likely due to the presence of polymer particles that are hydrophobic in nature), it may be that moisture cannot easily reach the aggregate-mortar interface and therefore cause a strength degradation of the aggregate-mortar bond, which in turn would degrade the overall mechanical properties of the mixture. At the moment moisture is present in the interface other phenomena related to the adhesion properties of the specific aggregate- mortar combinations become the dominating factor that governs mixture degradation due to moisture. Similarly, the improved moisture characteristics of modified mixtures can be attributed to the fact that modified mortars can hold minor amount of water compared to the unmodified mortars, and consequently the level of moisture damage at asphalt mixture level will be lower. Analogous results were obtained in a study by Cheng et al. (2003), in which the differences found in the damage levels for asphalt mixtures with the same type of aggregate were attributed to the moisture absorption ability of the binders. Also, the high resistivity of polymer modified binders against moisture is supported by earlier studies. Kringos et al. (2008) and Poulikakos & Partl (2009) investigated the performance of several combinations of asphaltic materials against moisture damage susceptibility with different test methods at micro- and macro-level. Their work demonstrated the positive effect of using polymer modified binders on the moisture susceptibility of bituminous mixtures. It was reported that polymer modified binders were found to be less susceptible to moisture damage compared to the unmodified ones.

Moreover differences were observed for the mixtures prepared with SBS modified binders. Specifically, the mixtures prepared with mortar D (60/90 Sealoflex 5-50 (PA)) showed a high reduction in strength after long-term bath conditioning, while the extra stresses developed due to

the short-term conditioning regime (MiST) appeared to have a minor effect on their tensile strength. On the contrary, the mixtures with mortar C (45/80 Cariphalte XS) were affected by cyclic pore pressure application, while their performance was not greatly diminished by bath conditioning. These results are likely to be related to the nature of the conditioning methods. Prolonged bath conditioning is associated with changes in the physico-chemical nature of the binders (and mortars), which result in cohesive or adhesive types of failure; these results may suggest that there is an incompatibility between mortar D and the aggregate that results in a weaker adhesive bond (than with mortar C), which is further compromised in moist conditions. On the other hand, cyclic pore pressures have a mechanical effect on the mixture. It is, therefore, possible that a softer mortar like D is more flexible and as a result can resist better the pressure-induced stresses compared to a stiffer mortar like mortar C.

4.5 Characterization of pore pressure damage by means of X-ray CT scans

X-ray computed tomography (CT) and imaging techniques were used to characterize the effect of cyclic pore pressure on asphalt mixtures. In the previous section, the effect of pore pressure application was quantified through indirect tensile strength tests. It was observed that increasing bath conditioning time and number of MiST cycles caused a reduction in the tensile strength of the samples without any visible sign of failure, thus suggesting that damage develops at the micro scale leading to a decline of the overall loading capacity of the asphalt sample. Moisture damage due to the build-up of excess water pressure in the voids may lead to the initiation of cracks in the binder film and further to the propagation and expansion of existing micro cracks which merge to form macro cracks. In this section, damage due to pore pressure application was evaluated on the basis of visual evaluation (nucleation and development of cracks, debonding at the aggregate-binder interface) and of the variations in the air voids content and percentage of interconnected void network.

A porous asphalt sample with sandstone aggregates and SBS modified binder was prepared. The sample was scanned when at dry conditions and after MiST conditioning (at 0.48 MPa pressure and 60°C temperature) for various numbers of cycles without any prior bath conditioning. MiST conditioning was interrupted at specified numbers of cycles, the sample was scanned and 2D images were collected for image analysis.

4.5.1 Image analysis

X-Ray computed tomography was employed as a non-destructive technique in order to obtain information on the internal structure of asphalt specimens in the form of 2D images. The asphalt core sample had a diameter and a height of 100mm. The scanning resolution was 756 x 760 (pixels) with a slice thickness of 100 micrometres and a total of 1000 CT scans. The sample was scanned at dry conditions and after 1000, 4000 and 8000 cycles of MiST conditioning. At each specified number of cycles - prior to scanning - the sample was removed from the MiST device, then surface dried with

a damp towel and placed in a climate chamber at ambient conditions of 20°C and 50% RH in a perforated self to dry for two days.

The obtained 2D scans were used for the reconstruction of the 3D internal morphology of the sample. The air void content and interconnectivity of the asphalt sample were quantified using Simpleware® software. First filters were applied to reduce noise and therefore improve image quality. Then segmentation of the various material phases, i.e. aggregates, binder and air voids, was performed by selecting pixels with the same grayscale value from those with a different value. In this study, the air voids were segmented using a threshold segmentation algorithm. An upper and a lower threshold value of 0 and 96, respectively, were assigned to segment the air void phase. Figure 4.12 shows the 3D rendering of the asphalt sample from a stack of CT sectional images and the air void phase.

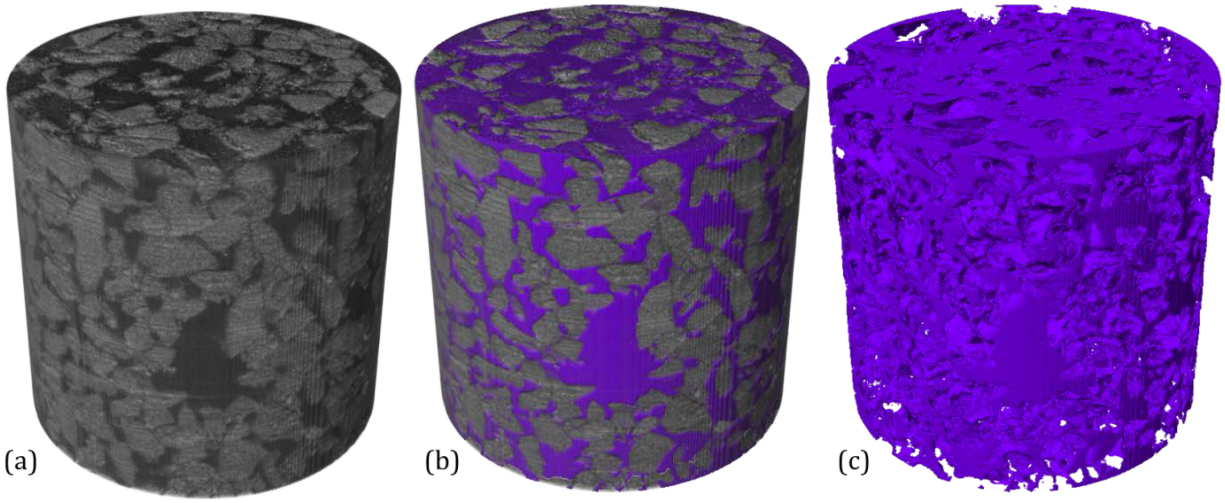

Figure 4.12. (a) 3D rendering from the reconstruction of the CT scan images, (b) reconstructed 3D image showing the air voids in the asphalt sample and (c) segmented air void phase.

After the segmentation process was completed, image analysis was performed so as to extract quantitative information on the microstructure of the asphalt mixture. Figure 4.13 illustrates the changes in air void content and interconnectivity after MiST conditioning. Overall, the results obtained from the image analysis showed that the air voids content increased with increasing number of MiST cycles. Therefore, it seems that MiST has a fracturing effect resulting to the opening of new flow paths due to crack initiation and propagation. As expected, the interconnectivity of the sample was already high and did not vary significantly after MiST application.

After 4000 cycles, however, it was observed that the air voids decreased. A possible explanation may be that binder and finer particles were eroded by the action of water and then transported by advection through the body of the sample, thus causing clogging of the pore network. To investigate this hypothesis, the sample was divided in three pieces namely the bottom (0-33mm in height), the middle (33-66mm) and the top (66-100mm) part and specific information for the various parts of the sample were obtained. Figure 4.14 illustrates the air void content and interconnectivity of the three specific parts of the sample.

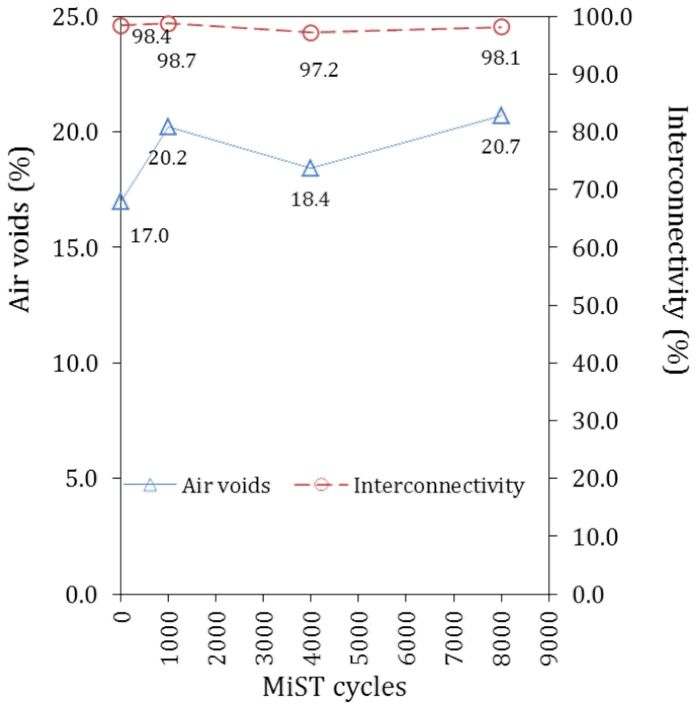

Figure 4.13. Air voids content and interconnectivity after MiST conditioning.

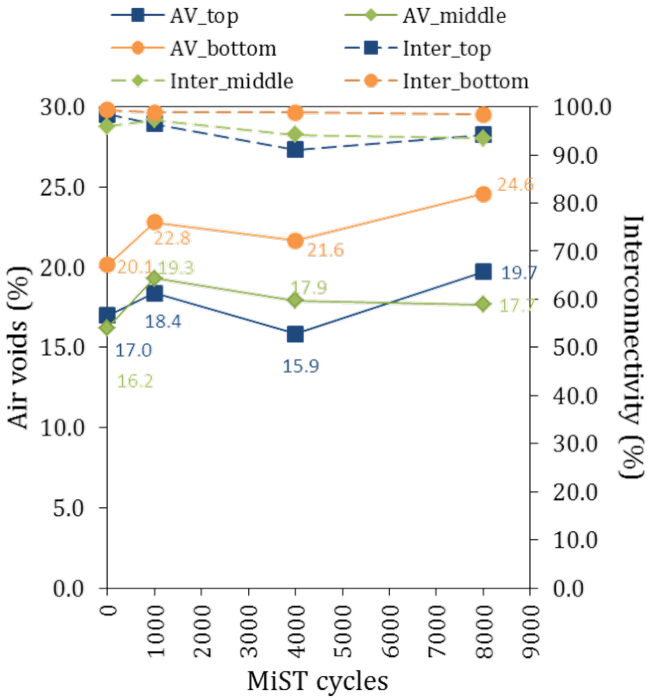

Figure 4.14. Air voids content and interconnectivity for the top, middle and bottom part of the sample after MiST conditioning.

For the middle part of sample, small variations in the air void content were observed, while its interconnectivity reduced with increasing MiST cycles. On the other hand, from the data it is shown that the percentage of air voids increased for the top and bottom part of the sample as the number of MiST cycles increased. A possible explanation for this might be that eroded particles are transported from the top and bottom parts and are trapped in the middle part of the sample, thus reducing the interconnectivity of this fragment (and therefore affect the pore network connectivity of the whole sample). Also, after 8000 cycles an amount of the eroded particles was transported out of the sample and was found in the water in the MiST tank. Figure 4.15 shows the particles collected by filtering the water once MiST conditioning was completed.

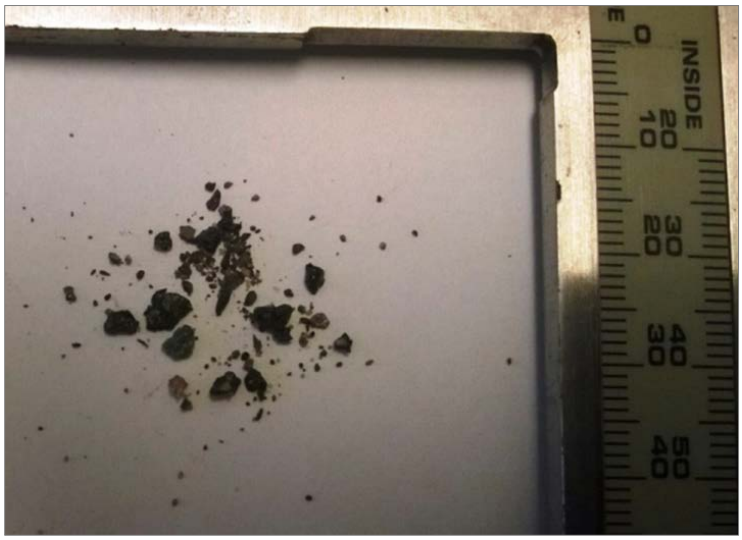

Figure 4.15. Fine particles collected by filtering the water after 8000 MiST conditioning cycles (the scale is given in mm).

4.5.2 Visual evaluation

The qualitative evaluation of the degree of degradation of the porous asphalt after MiST conditioning was attempted through visual observations. The scanning parameters were kept identical for all scanning rounds. Also, great care was given in positioning the sample in exactly the same location before scanning, so as to ensure that the scans obtained will be comparable. The evaluation was made on the basis of the following features: (i) roughness of the binder edges and (ii) cracks in the binder and aggregates.

Figure 4.16 shows a CT scan of the sample, which located in the middle part at a height of 65mm from the bottom surface of the sample. It is apparent that water has an effect on the roughness of the binder film. It was observed that the action of water, as it is pumped in and out of the sample, has a smoothening effect on the binder surface surrounding the air voids. In some scans, it was seen that the coating had been lost and the aggregates were exposed. Also, even though the samples were allowed to dry before scanning, water was still present in the some of the voids of the sample, Figure 4.16.

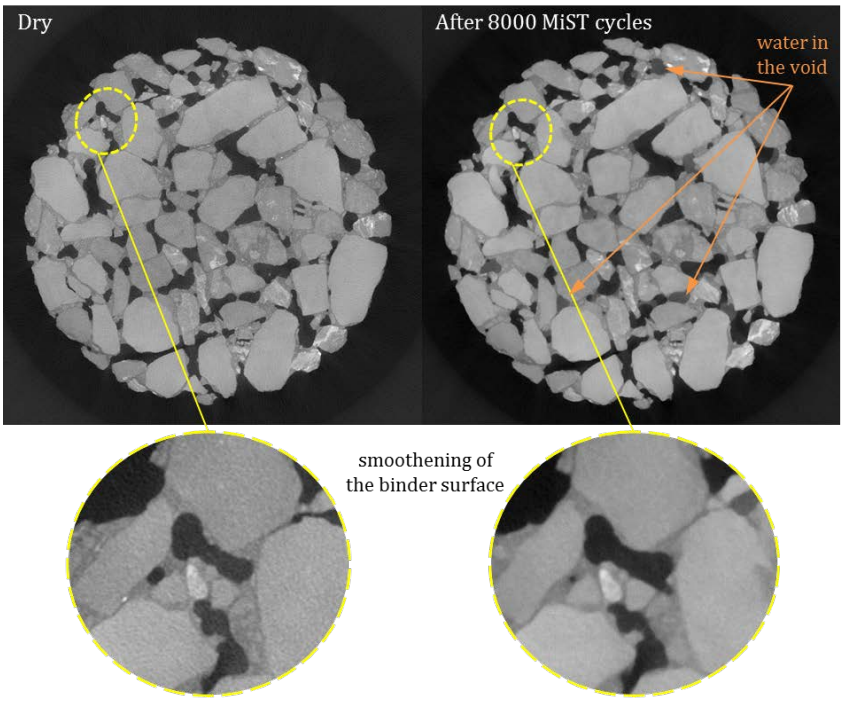

Figure 4.16. Smoothening effect of water on the edges of the binder coating.

In Figure 4.17, the red square, in the top left picture, highlights the location of an existing crack that was detected when the sample was scanned at dry conditions. The slice is located in the middle part of the sample at 59mm height. The rest of the pictures show the crack in magnification. It was observed that the crack was gradually filled in with water and widened due to the repeated pore pressure application after 1000, 4000 and 8000 MiST cycles.

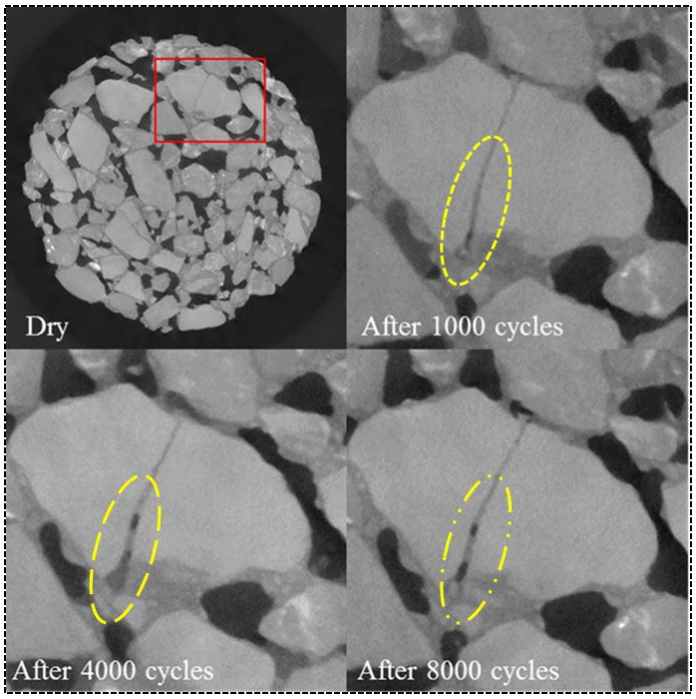

Figure 4.17. Widening of an existing crack after MIST conditioning.

These findings demonstrate the mechanical action of repeated pore pressure application. It is evident that, unlike moisture diffusion (which results in a change of physico-chemical properties leading to weakening of the binder or the binder-aggregate bond strength) pumping action promotes the development of additional internal stresses that can ultimately result to cracking initiation and propagation, as well as erosion of the binder.

4.6 Summary

In this study, the aim was to develop a moisture conditioning protocol that combines the two main moisture-induced damage mechanisms, namely moisture diffusion and pumping action, and furthermore to demonstrate the importance of including the short-term moisture damage processes when considering moisture damage in asphalt pavements. Asphalt samples produced with various aggregate and bitumen types were conditioned in combinations of water bath immersion and cyclic pore pressures by means of the Moisture Induced Stress Tester (MiST). The degradation in strength was quantified through indirect tensile strength tests. The Indirect Tensile Strength (ITS) and the Indirect Tensile Strength Ratio (ITSR) were used for the evaluation of the moisture sensitivity of the mixtures. Based on the results the contributions of long- and short-term moisture damage were quantified.

The experiments presented in this chapter showed that the degradation of mixture strength due to moisture is influenced by the conditioning method (i.e. bath conditioning and pore pressure application) as well as the conditioning time. The results indicate that the two damage inducing mechanisms are relatively independent from each other. It may, therefore, be that an asphalt mixture is more prone to one damage mode than the other. In specific cases though, the duration of the bath conditioning phase was found to intensify the effect of short-term pore pressure application. Longer conditioning times resulted in higher strength reduction for the same number of MiST cycles.

The influence of constituent materials on the moisture susceptibility characteristics of the mixtures was also investigated. Mixture composition was found to have a significant effect on the response of the mixtures against the two moisture damage modes. The use of PmB was observed to improve the resistance of mixtures to moisture. The enhanced performance was attributed to the moisture uptake characteristics of the polymer modified binders, as discussed in Chapter three. On the one hand, the rate of moisture diffusion was found to be lower for the SBS modified binders possibly due to the presence of polymer particles that are hydrophobic in nature, and on the other hand PmBs can hold a minor amount of water compared to the unmodified binders, which results in lesser damage in the mixture scale. Hence, it can be stated that the diffusivity characteristics of asphalt binders, and therefore mortars, can provide insights on the moisture sensitivity of asphalt mixtures.

As a next phase of the study, X-ray computed tomography and image analysis were used to further understand damage induced by pore pressure build-up. The volumetric analysis of the reconstructed 3D sample showed that repeated pore pressures lead to higher air void content with increasing number of pressure cycles, indicating thus the opening of new flow paths in the mixture.

Image analysis revealed the mechanical effects of pore pressure application; pore pressure induces additional internal stresses that can ultimately lead to cracking of the binder films or the widening of existing cracks in a mixture. In contrast, long-term diffusion phenomena can change the rheological and therefore the mechanical properties of the aggregate-binder systems; nevertheless those effects on strength degradation generally become apparent after the application of mechanical loading.

The findings indicate that the two moisture-induced damage mechanisms have diverse effects on asphalt mixture degradation. Moreover, mixtures with variable composition and morphological characteristics (air void content, interconnectivity etc.) can be susceptible to long- or short-term conditioning in a lesser or greater degree. Therefore disregarding the short-term effects of pumping action may lead to erroneous conclusions when designing and developing specifications for testing asphalt mixtures for their moisture damage susceptibility. In addition to the importance of these findings in characterizing the effect of moisture on mixture degradation, the results presented in this chapter may serve as input parameters for the calibration and validation of computational models that simulate moisture damage phenomena in asphalt pavements.

4.7 References

Airey, G.D. and Choi, Y.C. (2002). State of the art report on moisture sensitivity test methods for bituminous pavement materials. *Road Materials and Pavement Design*, 3:4, 355–372.

Airey, G.D., Choi, Y.C., Collop, A.C., Moore, A.J.V. and Elliott, R.C. (2005). Combined laboratory ageing/moisture sensitivity assessment of high modulus base asphalt mixtures. Proceedings of the association of Asphalt Paving Technologists, 74, 307–346.

Aschenbrener, T., Terrel, R.L. and Zamora, R.A. (1994). Comparison of the Hamburg wheel-tracking device and the environmental conditioning system to pavements of known stripping performance. Colorado Department of Transportation, Denver, Colorado.

Azari, H. (2010). Precision Estimates of AASHTO T283: Resistance of Compacted Hot Mix Asphalt (HMA) to Moisture-Induced Damage. National Cooperative Highway Research Program, Transportation Research Board of the National Academies, USA.

Birgisson, B., Roque, R., Tia, M. and Masad, E.A. (2005). Development and Evaluation of Test Methods to Evaluate Water Damage and Effectiveness of Antistripping Agents (Final report). Gainesville: University of Florida.

Caro, S., Masad, E.A. Bhasin, A. and Little, D.N. (2008a). Moisture susceptibility of asphalt mixtures, part 1: Mechanisms. *International Journal of Pavement Engineering,* 9:2, 81–98.

Caro, S., Masad, E.A., Bhasin, A. and Little, D.N. (2008b). Moisture susceptibility of asphalt mixtures, part 2: characterisation and modelling. *International Journal of Pavement Engineering,* 9:2, 99-114.

Cheng, D., Little, D.N., Lytton, R.L. and Holste, J.C. (2003). Moisture damage evaluation of asphalt mixtures by considering both moisture diffusion and repeated-load conditions. *Transportation Research Record: Journal of the Transportation Research Board,* 1832, 42–49.

Choi, Y.C. (2005). Development of the saturation aging tensile stiffness SATS test for high modulus base materials. PhD dissertation. School of Civil Engineering, University of Nottingham, U.K.

Collop, A.C., Choi, Y.C. and Airey, G.D. (2004). Development of a combined aging/moisture sensitivity laboratory test. Proceedings of Eurasphalt and Eurobitume Congress, Vienna, Austria.

Collop, A., Choi, Y.C., and Airey, G.D. (2007). Effects of Pressure and Aging in SATS Test. *Journal of Transportation Engineering*, 133:11, 618–624.

Copeland, A. (2011), *Reclaimed asphalt pavement in asphalt mixtures: state of the practice*, Report No. FHWA-HRT-11-021, Federal Highway Administration, Washington D.C.

Cox, J.A., VanFrank, K.M. and Romero, P. (2013). On the variability of results from the Hamburg Wheel Tracker Device. Proceedings of the 49th ASC Annual International Conference.

CROW (2010). *Standaard RAW Bepalingen. Publicatie 470*. The Netherlands.

Grönniger, J., Wistuba, M.P. and Renken, P. (2010). Adhesion in Bitumen-Aggregate-Systems. *Road Materials and Pavement Design*, 11:4, 881-898.

Hicks, R.G. (1991). NCHRP Synthesis of Highway Practice 175: Moisture Damage in Asphalt Concrete. Washington D.C.: TRB & National Research Council.

Hicks, R.G., Santucci, L. and Aschenbrener, T. (2003). Moisture sensitivity of asphalt pavements - A national seminar. San Diego, California.

InstroTek Inc. (2012). Moisture Induced Sensitivity Test Operators Guide, Version 10. Raleigh NC.

Kandhal, P.S., Lubold, C.W. and Roberts, F.L. (1989). Water damage to asphalt overlays: Case histories. Proceedings of the Association of Asphalt Paving Technologists, 58:40, 67.

Kandhal, P.S. and Rickards, I.J. (2001). *Premature failure of asphalt overlays from stripping: Case histories* (Report 01-01). Alabama: National Center for Asphalt Technology of Auburn University.

Kanitpong, K. and Bahia, H.U. (2008). Evaluation of HMA moisture damage in Wisconsin as it relates to pavement performance. *International Journal of Pavement Engineering,* 9:1, 9-17.

Kassem, E., Masad, E.A., Lytton, R.L. and Bulut, R. (2009). Measurements of the moisture diffusion coefficient of asphalt mixtures and its relationship to mixture composition. *International Journal of Pavement Engineering,* 10:6, 389-399.

Kiggundu, B.M. and Roberts, F.L. (1988). Stripping in HMA mixtures: state-of-the-art and critical review of test methods (Report 88-02). Alabama: National Center for Asphalt Technology of Auburn University.

Kringos, N. and Scarpas, A. (2005). Raveling of asphaltic mixes due to water damage: Computational identification of controlling parameters. *Transportation Research Record: Journal of the Transportation Research Board,* 1929, 79–87.

Kringos, N., Scarpas, A., Kasbergen, C. and Selvadurai, P. (2008). Modelling of combined physical mechanical moisture-induced damage in asphaltic mixes, part 1: Governing processes and formulations. *International Journal of Pavement Engineering,* 9:2, 115-118.

Kringos, N., Scarpas, A. and De Bondt, A. (2008). Determination of moisture susceptibility of mastic-stone bond strength and comparison to thermodynamical properties. *Journal of the Association of Asphalt Paving Technologists, 77*, 435–478.

Kringos, N., Azari, H. and Scarpas, A. (2009). Identification of parameters related to moisture conditioning that cause variability in modified Lottman test. *Transportation Research Record: Journal of the Transportation Research Board,* 2127, 1–11.

Lu, Q. and Harvey, J. (2006). Evaluation of Hamburg wheel-tracking device test with laboratory and field performance data. *Transportation Research Record: Journal of the Transportation Research Board,* 1970, 25–44.

Poulikakos, L.D. and Partl, M.N. (2009). Evaluation of moisture susceptibility of porous asphalt concrete using water submersion fatigue tests. *Construction and Building Materials,* 23:12, 3475-3484.

Simpleware +ScanFE (v6.0) [computer software]. Exeter, United Kingdom.

Solaimanian, M., Harvey, J., Tahmoressi, M. and Tandon, V. (2003). Test methods to predict moisture sensitivity of hot-mix asphalt pavements. In: Moisture sensitivity of asphalt pavements, National Seminar, San Diego. Washington, DC: Transportation Research Board.

Terrel, R.L. and Al-Swailmi, S. (1994). Water sensitivity of asphalt–aggregate mixes: Test selection (SHRP Report A-403). Washington D.C.: National Research Council.

Varveri, A., Avgerinopoulos, S., Kasbergen, C., Scarpas, A. and Collop, A. (2015). Influence of air void content on moisture damage susceptibility of asphalt mixtures: A computational study. *Transportation Research Record: Journal of the Transportation Research Board,* 2446, 8-16.

5

Modelling moisture damage of asphalt mixtures

"If people do not believe that mathematics is simple, it is only because they do not realize how complicated life is."
— John von Neumann (1903-1957)

Modelling damage due to moisture allows for a better understanding of the fundamental processes that govern moisture damage and the key factors that control these processes over the service life of a pavement. Such model can serve as a tool to investigate a great variety of parameters before a pavement structure is actually built. This allows for new materials and mixture designs to be investigated and the risks involved with these to be minimized. This chapter presents an energy-based large strain three-dimensional elasto-visco-plastic model with softening for modelling the coupled effects of moisture and mechanical loading. The mathematical details of the model in addition to the numerical approach followed for its implementation are provided.

Part of this chapter contains published material from the article "Influence of air void content on moisture damage susceptibility of asphalt mixtures: Computational study" by A. Varveri, S. Avgerinopoulos, C. Kasbergen, A. Scarpas and A. Collop, published in the Transportation Research Record: Journal of the Transportation Research Board, volume 2446, issue 3, pp. 8-16 © 2015.

5.1 Introduction

Constitutive modelling is a significant way to help understand the possible fundamental processes that govern moisture damage and to identify the key factors that control these processes in asphalt mixtures. With the advent of today's computer power, computation times and space issues have largely been reduced. An effective model can be used to estimate in-time performance of asphalt pavements under specific environmental conditions and traffic loading. This means that, relatively fast and at low costs, a great variety of parameters can be investigated before the structure is actually built. This allows for new material and new designs to be investigated and the risks involved with these to be minimized.

Over the years, researchers have developed computational models to simulate the response of bituminous materials under the combined effect of long-term moisture diffusion and mechanical loading. Although different geometries, material properties and constitutive models were used, all studies focused on the principle of coupling the physical and mechanical processes into a single moisture-induced damage model for asphalt mixtures. Kringos (2007) developed a computational tool, named RoAM (Raveling of Asphaltic Mixes) to model the combined physical-mechanical moisture damage in asphalt mixtures. An elasto-visco-plastic model was adjusted to incorporate the degradation effects of moisture. The moisture damage functions were expressed, for all components of asphalt mixtures, i.e. asphalt mastics, aggregates and mastic-aggregate interfaces, as

$$d_\theta = f(\theta) \qquad [5.1]$$

, where θ is the moisture content, which is defined as the ratio of moisture concentration with respect to the maximum moisture concentration that the material can absorb. Expressions for the moisture damage functions were determined for both adhesive and cohesive failure. Copeland et al. (2007) and Kringos et al. (2008) studied the relationship between moisture content and damage at the mastic-aggregate interface. Based on these studies, it was postulated that the development of moisture damage at the interface increases as a function of moisture concentration and was defined as

$$d_\theta^{if} = 1 - e^{-\alpha_\theta^{if}\sqrt{\theta}} \qquad [5.2]$$

, where α_θ^{if} is the moisture susceptibility parameter of mastic-aggregate interfaces. The susceptibility parameter for the particular mastic-aggregate combinations tested was found as $\alpha_\theta^{if} = 3.76$. For simplicity, and due to the lack of experimental evidence, the evolution of damage for asphalt mastics due to the presence of moisture, was at that time defined as

$$d_\theta^{mst} = 1 - e^{-\alpha_\theta^{mst}\sqrt{\theta}} \qquad [5.3]$$

Based on the above, moisture diffusion and the resulted damage were simulated using a 2D finite element mesh consisting of two stones coated with a mastic film. The aggregate-mastic interface was also modeled to simulate the response of the adhesive bond. Figure 5.1 illustrates the infiltration of moisture into the asphalt mastic and towards the mastic-aggregate interface as modeled by Kringos (2007).

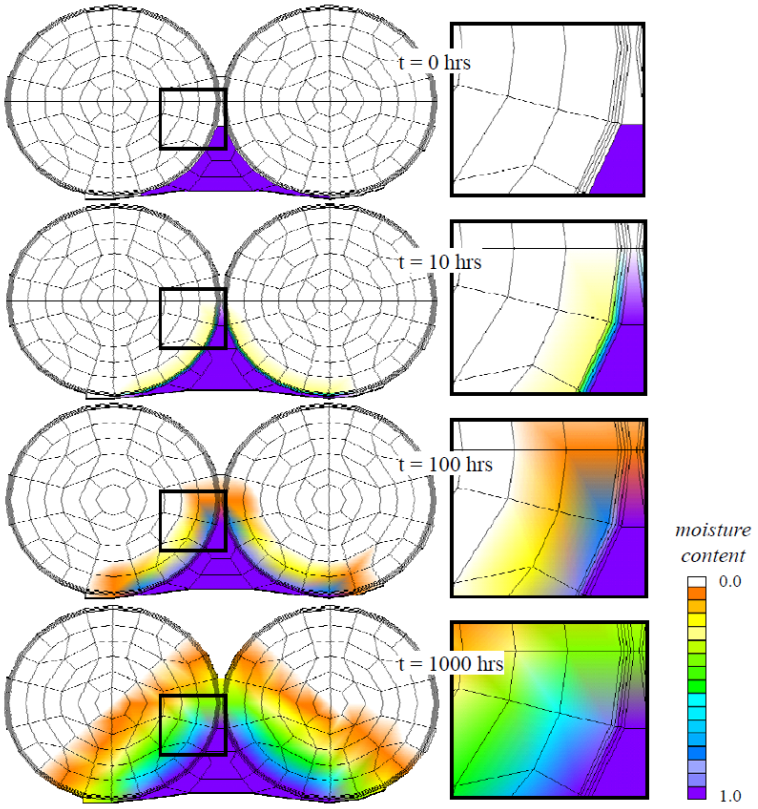

Figure 5.1 Moisture diffusion simulation with Dagg=0.01 mm2/hr and Dmst= 0.015 mm2/hr (after Kringos 2007).

In another study, Caro (2009) coupled the effects of moisture diffusion and mechanical loading to quantify the level of damage within asphalt mixtures. The adhesive failures at the mastic-aggregate interfaces and the cohesive failure of the mastic were simulated using the cohesive zone modeling technique. Damage was evaluated based on the location and time for crack initiation and propagation at the mastic-aggregate interfaces and on the level of strains and stresses within the bulk of asphalt mastics. Figure 5.2 illustrates the response of two types of mastics after mechanical loading for the dry case and for the moisture conditioned cases.

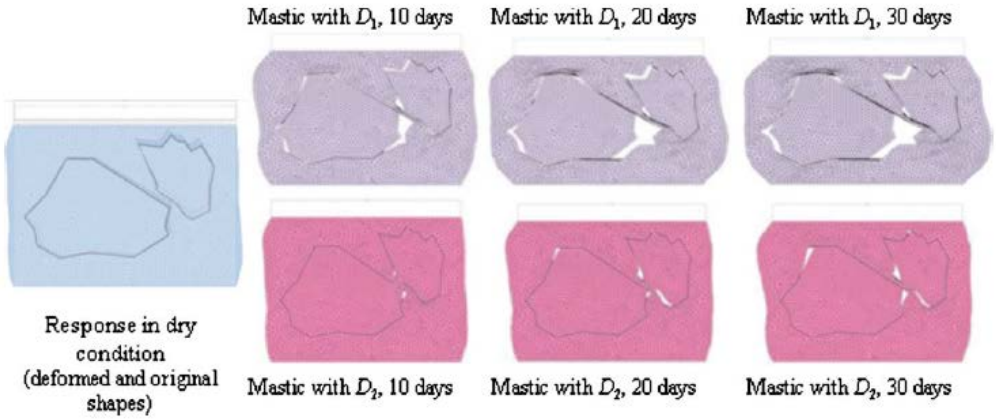

Figure 5.2 Response of the aggregate-mastic system after application of mechanical loading of 0.2 N/s for a total time of 30s for specimens subjected to different moisture conditioning periods (after Caro 2009).

Graham (2009) modified the nonlinear viscoelastic-viscoplastic model developed by Huang (2008) to couple the effects of moisture and mechanical loading on asphalt mixtures. In this study, the moisture history was taken into consideration by introducing the moisture content as a function of time. However, Mehrara and Khodaii (2013) stated that moisture-induced damage in asphalt mixtures may be partly healed during the absence of moisture and suggested that a parameter related with the healing of the material needs to be included.

5.2 Elasto-visco-plastic model with softening due to coupled moisture-mechanical damage

This section describes an energy-based, finite strain, three-dimensional elasto-visco-plastic model with softening used for the prediction of damage due to the combination of moisture and mechanical loading. The model consists of a generalized Maxwell model, with hyperelastic springs and viscous time-dependent components, in series with an inelastic component driven by coupled moisture-mechanical damage, Figure 5.3(a). The model response is illustrated in Figure 5.3(b). The model is implemented into the CAPA-3D Finite Element (FE) system developed at Delft University of Technology (Scarpas 2005).

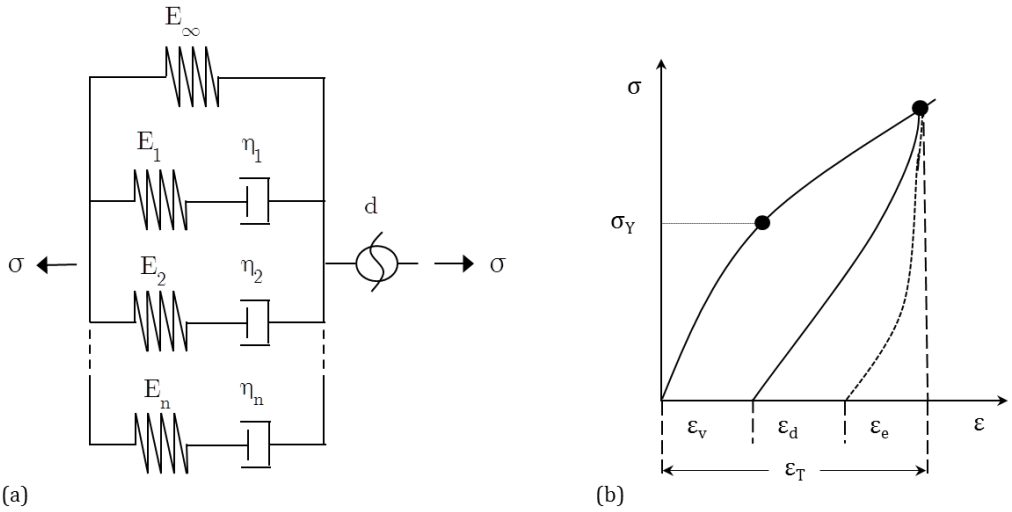

Figure 5.3 (a) Schematic of elasto-visco-plastic model with softening due to mechanical-moisture damage. (b) Model response: σ is the stress; σ_Y is the yield stress; $\varepsilon=\varepsilon_d+\varepsilon_v+\varepsilon_e$, where ε is the total strain, ε_d is the strain due to damage, ε_v is the viscous strain and ε_e is the elastic strain.

5.2.1 Formulation of the damage model: Kinematics

Inelastic response in bituminous mixtures leading to material failure can be described by a combination of elastic, viscous and inelastic dissipative components. To formulate the elasto-visco-plastic model with softening due to coupled mechanical-moisture damage, the multiplicative decomposition of the deformation gradient tensor is applied. The motion of a continuum particle

from the reference configuration B^o to the current configuration B, Figure 5.4, is mapped by the total deformation gradient F. During elastic deformation the bituminous material is intact and, therefore, the reference configuration will be obtained from the deformed configuration as soon as the forces acting on the material are removed.

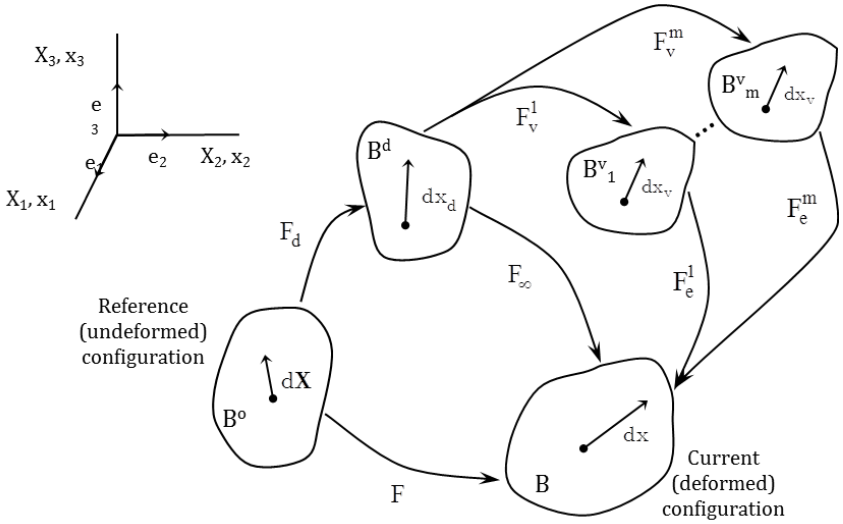

Figure 5.4 Proposed multiplicative decomposition: The intermediate configuration B^d is obtained from the deformed configuration B^o by elastic un-stressing to zero stress.

To include the notion of material damage into a large deformation viscoelastic framework, the following multiplicative decomposition of the total deformation gradient tensor F is proposed and the intermediate configuration B^d is introduced, Figure 5.4.

$$F = F_\infty F_d \qquad [5.4]$$

, where F is the total deformation gradient, F_d is the damage deformation gradient and F_∞ is the undamaged elastic deformation gradient. The material undergoes damage from B^o to the intermediate configuration B^d, which is mapped by the damage deformation gradient F_d. The intermediate configuration is obtained from the current configuration by elastic un-stressing to zero stress state. It differentiates from the reference configuration by an (irreversible) damage deformation and from the current configuration by a reversible deformation represented by the undamaged elastic deformation gradient F_∞. Furthermore, it is postulated that the undamaged rheological response is due to the contribution of elastic and viscoelastic components such that

$$F_\infty = F_e^i F_v^i \quad \text{for every } i = 1....m \qquad [5.5]$$

, where F_e^i and F_v^i denote the elastic deformation gradient and the viscous deformation gradient of the i^{th} Maxwell component of the viscoelastic formulation. On the basis of the proposed multiplicative decomposition Eq. [5.4] can be expressed as follows

$$F = F_e^i F_v^i F_d \quad \text{for every } i = 1....m \qquad [5.6]$$

Following the definition of the spatial velocity gradient $L = \dot{F}F^{-1}$ (Holzapfel 2000) and on the basis of the proposed decomposition of the total deformation gradient F, the velocity gradient from the reference to the current configuration is expressed as

$$\begin{aligned} L = \dot{F}F^{-1} &= \frac{\partial}{\partial t}\left(F_e^i F_v^i F_d\right)\left(F_d^{-1}\left(F_v^i\right)^{-1}\left(F_e^i\right)^{-1}\right) = \left[\dot{F}_e^i F_v^i F_d + F_e^i \frac{\partial}{\partial t}\left(F_v^i F_d\right)\right]\left(F_d^{-1}\left(F_v^i\right)^{-1}\left(F_e^i\right)^{-1}\right) \\ &= \left[\dot{F}_e^i F_v^i F_d + F_e^i\left(\dot{F}_v^i F_d + F_v^i \dot{F}_d\right)\right]\left(F_d^{-1}\left(F_v^i\right)^{-1}\left(F_e^i\right)^{-1}\right) \\ &= \left(\dot{F}_e^i F_v^i F_d + F_e^i \dot{F}_v^i F_d + F_e^i F_v^i \dot{F}_d\right)\left(F_d^{-1}\left(F_v^i\right)^{-1}\left(F_e^i\right)^{-1}\right) \\ &= \dot{F}_e^i\left(F_e^i\right)^{-1} + F_e^i \dot{F}_v^i\left(F_v^i\right)^{-1}\left(F_e^i\right)^{-1} + F_e^i F_v^i \dot{F}_d F_d^{-1}\left(F_v^i\right)^{-1}\left(F_e^i\right)^{-1} \end{aligned} \quad [5.7]$$

Hence the elastic, damage and viscous velocity gradient tensors expressed in the current configuration can be obtained

$$L_e^i = \dot{F}_e^i\left(F_e^i\right)^{-1} \quad [5.8]$$

$$L_v^i = F_e^i \dot{F}_v^i\left(F_v^i\right)^{-1}\left(F_e^i\right)^{-1} \qquad \text{for every } i = 1...m \quad [5.9]$$

$$L_d = F_e^i F_v^i \dot{F}_d F_d^{-1}\left(F_v^i\right)^{-1}\left(F_e^i\right)^{-1} \quad [5.10]$$

One can now introduce various strain measures. The right and left Cauchy-Green deformation tensors C and B for the deformation components F_∞ and F_e^i are defined, with respect to the reference configuration, as

$$C_\infty = {F_\infty}^T F_\infty, \quad b_\infty = F_\infty {F_\infty}^T \quad [5.11]$$

$$C_e = {F_e}^T F_e, \qquad b^i e = F_e^i\left(F_e^i\right)^T \qquad \text{for every } i = 1...m \quad [5.12]$$

, where ${F_\infty}^T$ and $\left(F_e^i\right)^T$ are the transpose of the deformation tensors F_∞ and F_e^i, respectively. Therefore the total Cauchy-Green deformation tensors *C* and B can be written as

$$\begin{aligned} C = {F}^T F &= {F_d}^T C_\infty F_d \\ &= {F_d}^T\left(F_v^i\right)^T C_e^i F_v^i F_d \qquad \text{for every } i = 1...m \end{aligned} \quad [5.13]$$

Similarly the Lagrange-Green strain tensor E is defined as

$$\begin{aligned} E &= \frac{1}{2}(C - I) = \frac{1}{2}(F^{T}F - I) = \\ &= \frac{1}{2}(F_d{}^{T} C_{\infty} F_d - I) \\ &= \frac{1}{2}(F_d{}^{T} \left(F_v^i\right)^{T} C_e^i F_v^i F_d - I) \qquad \text{for every } i = 1...m \end{aligned} \tag{5.14}$$

5.2.2 Thermodynamics

For a constitutive model to be thermodynamically consistent, the Clausius-Planck dissipation inequality or second law of thermodynamics has to be fulfilled. The inequality, as shown in Eq. [5.15], states that a material can either be non-dissipative (undergoes a reversible process) or dissipative (undergoes an irreversible process), but it cannot produce energy.

$$D = P : \dot{F} - \dot{e} + \Theta\dot{\eta} \geq 0 \tag{5.15}$$

, where the D denotes the internal dissipation energy, $P : \dot{F}$ represents the work conjugate pair (or rate of internal mechanical work per unit reference volume), P is the first Piola-Kirchhoff stress, $\dot{e}$ denotes the rate of internal energy and $\Theta\dot{\eta}$ is the absolute temperature multiplied by the rate of entropy.

The inequality holds for irreversible processes, whereas is equal to zero for reversible processes. For a purely mechanical case, where the thermal effects are ignored, Eq. [5.15] becomes

$$D = P : \dot{F} - \dot{e} = P : \dot{F} - \dot{\Psi} \geq 0 \tag{5.16}$$

, where $\dot{\Psi}$ denotes the time derivative of the Helmholtz free-energy function that coincides with the rate of internal energy. For the proposed model the strain-energy function Ψ is defined as

$$\Psi = \sum_{i=1}^{m} \Psi_v^i \left(C_e^i\right) + \Psi_{\infty}\left(C_{\infty}, d\right) \tag{5.17}$$

, where Ψ_v is the strain-energy function related to the spring of the ith viscoelastic Maxwell component, Ψ_{∞} is the strain-energy function related to the single elastic spring and *d* is the damage function. The time derivative of the strain-energy function is then

$$\dot{\Psi} = \sum_{i=1}^{m}\left(C_e^i\right) + \dot{\Psi}_{\infty}\left(C_{\infty}, d\right) = \sum_{i=1}^{m} \frac{\partial \Psi_v^i}{\partial C_e^i} : \dot{C}_e^i + \frac{\partial \Psi_{\infty}}{\partial C_{\infty}} : \dot{C}_{\infty} + \frac{\partial \Psi_{\infty}}{\partial d} \cdot \dot{d} \tag{5.18}$$

, where $\dot{C}_{\infty}$ and $\dot{C}_e^i$ are the time derivatives of the elastic right Cauchy deformation tensor for the single spring and of the elastic right Cauchy deformation tensor for the ith Maxwell component, respectively. Substituting Eq. [5.18] into the Clausius-Planck local dissipation inequality gives

$$D = P : \dot{F} - \sum_{i=1}^{m} \frac{\partial \Psi_v^i}{\partial C_e^i} : \dot{C}_e^i - \frac{\partial \Psi_{\infty}}{\partial C_{\infty}} : \dot{C}_{\infty} - \frac{\partial \Psi_{\infty}}{\partial d} \cdot \dot{d} \geq 0 \tag{5.19}$$

The time derivatives of the Cauchy-Green deformation tensors C_∞ and C_e^i are defined as

$$\begin{aligned}\dot{C}_\infty &= \frac{d}{dt}\left(F_\infty^T F_\infty\right) = \dot{F}_\infty^T F_\infty + F_\infty^T \dot{F}_\infty = \\ &= \frac{d}{dt}\left(F_d^{-T} F^T\right) F_\infty + F_\infty^T \frac{d}{dt}\left(F F_d^{-1}\right) = \\ &= \dot{F}_d^{-T} F^T F_\infty + F_d^{-T} \dot{F}^T F_\infty + F_\infty^T \dot{F} F_d^{-1} + F_\infty^T F \dot{F}_d^{-1} =^{(*)} \\ &= -F_d^{-T} \dot{F}_d^T F_d^{-T} F^T F_\infty + F_d^{-T} \dot{F}^T F_\infty + F_\infty^T \dot{F} F_d^{-1} - F_\infty^T F F_d^{-1} \dot{F}_d F_d^{-1}\end{aligned} \quad [5.20]$$

$$\begin{aligned}\dot{C}_e^i &= \frac{d}{dt}\left(\left(F_e^i\right)^T F_e^i\right) = \left(\dot{F}_e^i\right)^T F_e^i + \left(F_e^i\right)^T \dot{F}_e^i = \\ &= \frac{d}{dt}\left(\left(F_v^i\right)^{-T} F_\infty^T\right) F_\infty \left(F_v^i\right)^{-1} + \left(F_v^i\right)^{-T} F_\infty^T \frac{d}{dt}\left(F_\infty \left(F_v^i\right)^{-1}\right) = \\ &= \left(\dot{F}_v^i\right)^{-T} F_\infty^T F_\infty \left(F_v^i\right)^{-1} + \left(F_v^i\right)^{-T} \dot{F}_\infty^T F_\infty \left(F_v^i\right)^{-1} + \left(F_v^i\right)^{-T} F_\infty^T \dot{F}_\infty \left(F_v^i\right)^{-1} + \left(F_v^i\right)^{-T} F_\infty^T F_\infty \left(\dot{F}_v^i\right)^{-1} = \\ &= \left(\dot{F}_v^i\right)^{-T} C_\infty \left(F_v^i\right)^{-1} + \left(F_v^i\right)^{-T} \dot{C}_\infty \left(F_v^i\right)^{-1} + \left(F_v^i\right)^{-T} C_\infty \left(\dot{F}_v^i\right)^{-1} = \\ &= -\left(\left(F_v^i\right)^{-1} \dot{F}_v^i \left(F_v^i\right)^{-1}\right)^T C_\infty \left(F_v^i\right)^{-1} + \left(F_v^i\right)^{-T} \dot{C}_\infty \left(F_v^i\right)^{-1} - \left(F_v^i\right)^{-T} C_\infty \left(F_v^i\right)^{-1} \dot{F}_v^i \left(F_v^i\right)^{-1} = \\ &= -\left(F_v^i\right)^{-T} \dot{F}_v^T \left(F_v^i\right)^{-T} C_\infty \left(F_v^i\right)^{-1} + \left(F_v^i\right)^{-T} \dot{C}_\infty \left(F_v^i\right)^{-1} - \left(F_v^i\right)^{-T} C_\infty \left(F_v^i\right)^{-1} \dot{F}_v^i \left(F_v^i\right)^{-1} = \\ &= -\left(\bar{L}_v^1\right)^T \left(F_v^i\right)^{-T} C_\infty \left(F_v^i\right)^{-1} + \left(F_v^i\right)^{-T} \dot{C}_\infty \left(F_v^i\right)^{-1} - \left(F_v^i\right)^{-T} C_\infty \left(F_v^i\right)^{-1} \bar{L}_v^1\end{aligned}$$

$$\text{for every } i = 1...m \quad [5.21]$$

, where $\bar{L}_v^1 = \dot{F}_v^i \left(F_v^i\right)^{-1}$ and $\left(\bar{L}_v^1\right)^T = -\left(F_v^i\right)^{-T} \left(\dot{F}_v^i\right)^T$.

As shown in Appendix A, after substituting Eqs. [5.20] and [5.21] and rearranging the terms, the Clausius-Planck inequality can be written as

(*) We can postulate that $F_d^{-1} F_d = I \Rightarrow \dot{F}_d^{-1} F_d + F_d^{-1} \dot{F}_d = 0 \Rightarrow \dot{F}_d^{-1} + F_d^{-1} \dot{F}_d F_d^{-1} = 0 \Rightarrow \dot{F}_d^{-1} = -F_d^{-1} \dot{F}_d F_d^{-1}$. Hence the transpose of the inverse of the time derivative of F_d becomes $(\dot{F}_d^{-1})^T = -F_d^{-T} \dot{F}_d^T F_d^{-T}$.

$$D = P : \dot{F} - \dot{\Psi} = \left(P - 2F_{\infty} \left(\frac{\partial \Psi_{\infty}}{\partial C_{\infty}} + \sum_{i=1}^{m} \left(F_v^i \right)^{-1} \frac{\partial \Psi_v^i}{\partial C_e^i} \left(F_v^i \right)^{-T} \right) F_d^{-T} \right) : \dot{F} + \\ + 2C_{\infty} \left(\frac{\partial \Psi_{\infty}}{\partial C_{\infty}} + \sum_{i=1}^{m} \left(F_v^i \right)^{-1} \frac{\partial \Psi_v^i}{\partial C_e^i} \left(F_v^i \right)^{-T} \right) : \dot{F}_d F_d^{-1} + \\ + \sum_{i=1}^{m} 2 \left(F_v^i \right)^{-T} C_{\infty} \left(F_v^i \right)^{-1} \frac{\partial \Psi_v^i}{\partial C_e^i} : \dot{F}_v^i \left(F_v^i \right)^{-1} - \frac{\partial \Psi_{\infty}}{\partial d} \cdot \dot{d} \geq 0 \qquad [5.22]$$

Utilizing the standard thermodynamic arguments (Coleman & Gurtin 1967) the first Kirchhoff-Piola tensor P can be obtained as

$$P = 2F_{\infty} \left(\frac{\partial \Psi_{\infty}}{\partial C_{\infty}} + \sum_{i=1}^{m} \left(F_v^i \right)^{-1} \frac{\partial \Psi_v^i}{\partial C_e^i} \left(F_v^i \right)^{-T} \right) F_d^{-T} = \tau F^{-T} \qquad [5.23]$$

, where τ is the Kirchhoff stress. The derivation of the reduced form of Eq. [5.23] can be found in Appendix B. In addition, on the basis of Eq. [5.22], the complementary inequality can be postulated as

$$2C_{\infty} \left(\frac{\partial \Psi_{\infty}}{\partial C_{\infty}} + \sum_{i=1}^{m} \left(F_v^i \right)^{-1} \frac{\partial \Psi_v^i}{\partial C_e^i} \left(F_v^i \right)^{-T} \right) : \dot{F}_d F_d^{-1} + \sum_{i=1}^{m} 2 \left(F_v^i \right)^{-T} C_{\infty} \frac{\partial \Psi_v^i}{\partial C_e^i} : \dot{F}_v^i \left(F_v^i \right)^{-1} - \frac{\partial \Psi_{\infty}}{\partial d} \cdot \dot{d} \geq 0 \qquad [5.24]$$

As shown in Appendix C, the reduced form of the inequality is expressed as

$$\Sigma_d : \bar{L}_d + \sum_{i=1}^{m} \left(\Sigma_e^i : \bar{L}_v^i \right) - q \cdot \dot{d} \geq 0 \quad , \quad q = \frac{\partial \Psi_{\infty}}{\partial d} \qquad [5.25]$$

, where Σ_e^i is the Mandel stress tensor of the ith Maxwell viscoelastic component and Σ_d is the Mandel stress tensor of the damage component, q is the stress component due to damage, and $\bar{L}_v^i$ and $\bar{L}_d$ are the corresponding viscous and damage velocity gradients defined in the intermediate configurations.

On the basis of the principle of maximum energy dissipation (Scarpas 2005), the following minimization problem is defined

$$\text{minimize} \qquad -\left(\Sigma_d : \bar{L}_d + \sum_{i=1}^{m} \Sigma_e^i : \bar{L}_v^i - q \cdot \dot{d} \right) \qquad [5.26]$$

$$\text{subject to} \qquad g\left(\Sigma_d, q \right) \leq 0 \qquad [5.27]$$

To ensure that for every Maxwell component $\Sigma_e^i : \bar{L}_v^i \geq 0$ the following choice is made for $\bar{L}_v^i$

$$\bar{L}_v^i = \dot{F}_v^i \left(F_v^i\right)^{-1} = \left(C_v^i\right)^{-1} : \Sigma_e^i \qquad \text{for every } i = 1...m \tag{5.28}$$

, where $\left(C_v^i\right)^{-1} = \frac{1}{2\eta_d^i}\left(I^4 - \frac{1}{3} I \otimes I\right) + \frac{1}{9\eta_v^i}(I \otimes I)$ is a symmetric fourth order tensor representing viscosity, as proposed by Reese & Govindjee (1998) and found in Scarpas (2005). Here, I^4 is the fourth order symmetric identity tensor, while η_d^i and η_v^i represent the viscosity parameters for the deviatoric and volumetric parts of the i^{th} Maxwell component. Therefore, the minimization problem is reduced to the following equations

$$\text{minimize} \qquad f\left(\Sigma_d, q\right) = -\left(\Sigma_d : \bar{L}_d - q \cdot \dot{d}\right) \tag{5.29}$$

$$\text{subject to} \qquad g\left(\Sigma_d, q\right) \le 0 \tag{5.30}$$

Damage flow surface

At this point a choice for $g\left(\Sigma_d, q\right)$ should be made. An extended Ducker-Prager yield surface, in the compression and tension zone, is used in the proposed model formulation considering that asphalt concrete has a strong dependence on hydrostatic pressure. The conventional Drucker-Prager yield function is given in the form

$$f = \sqrt{J_2} - \alpha I_1 - \beta \tag{5.31}$$

, where J_2 is the deviatoric shear stress, I_1 the hydrostatic stress, α is a material parameter that reflects the internal friction of the material and β is a parameter related to the combined effect of the cohesive and frictional properties.

The Drucker-Prager yield function is modified to include damage due to moisture and mechanical loading as follows

$$g\left(\sigma, q\right) = \sqrt{J_2\left(\sigma\right)} - \alpha_o I_1\left(\sigma\right)(1-d)^a - \gamma(1-d)q_o \tag{5.32}$$

, in which the Cauchy stress is equal to $\sigma = J^{-1} F_\infty^{-T} \Sigma_d F_\infty^T$, $q_o = \frac{\beta_o}{\gamma}(1-d)^{b-1}$ denotes softening due to damage, d is the coupled mechanical-moisture damage, $0 \le a \le b$, $b \ge 1$ and γ are parameters that control the softening rate due to damage. The parameters α_o and β_o are defined in terms of the compressive and tensile yield stresses as

$$\alpha_o = \frac{2}{\sqrt{3}}\left(\frac{f_c f_t}{f_c + f_t}\right) \qquad \text{and} \qquad \beta_o = \frac{1}{\sqrt{3}}\left(\frac{f_t - f_c}{f_c + f_t}\right) \tag{5.33}$$

, where f_c and f_t are the compressive and the tensile yield stress at undamaged conditions respectively. Figure 5.5 shows the influence of parameters a and b on the yield surface.

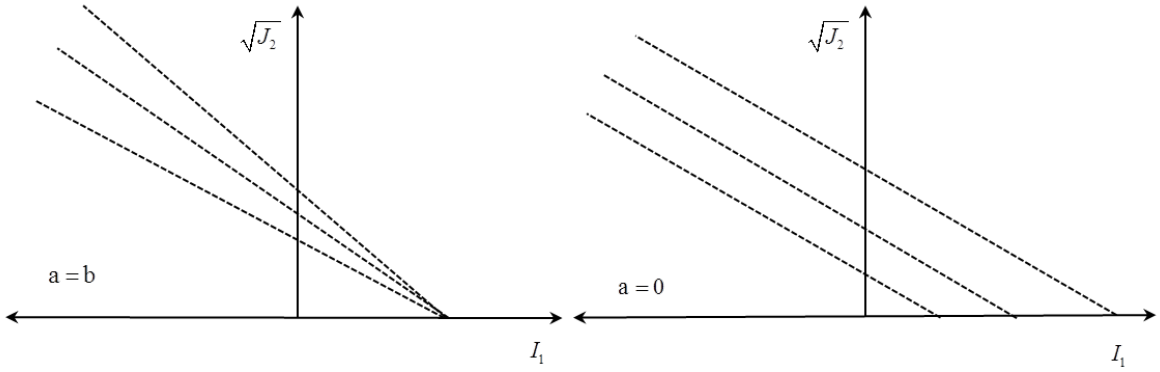

Figure 5.5 Influence of a and b on the shape of the flow surface plotted in $I_1 - \sqrt{J_2}$ space.

When $0 < a < b$ then the response of the yield function is a combination of the responses shown in Figure 5.5. In this case, damage affects both the cohesive and frictional properties of the material. The deviatoric shear stress and the hydrostatic stress are expressed as

$$J_2 = \frac{1}{2}(s_d)_{ij}(s_d)_{ij}, \quad I_1 = (\Sigma_d)_{ii} \tag{5.34}$$

, in which

$$(s_d)_{ij} = (\Sigma_d)_{ij} - p_d\delta_{ij} \quad \text{and} \quad p_d = \frac{1}{3}(\Sigma_d)_{ii} \tag{5.35}$$

Set up of constrained optimization using Lagrange multipliers

The method of Lagrange multipliers is used to set up a group of equations that satisfy the reduced minimization problem, as described by Eqs. [5.29] and [5.30]. The Lagrangian function is introduced as

$$\mathcal{L}\{\Sigma_d, q, \lambda\} = f(\Sigma_d, q) - \dot{\lambda} g(\Sigma_d, q) \tag{5.36}$$

, where $\dot{\lambda}$ is the time derivative of the Lagrange multiplier. Then Eq. [5.31] is solved for

$$\nabla_{\Sigma_d, q, \lambda}\mathcal{L}\{\Sigma_d, q, \lambda\} = 0 \tag{5.37}$$

, which implies that $g(\Sigma_d, q) = 0$ Therefore, the solution of Eq. [5.32] gives

$$\begin{aligned} \nabla_{\Sigma_d}\mathcal{L}\{\Sigma_d, q, \lambda\} &= \frac{\partial \mathcal{L}\{\Sigma_d, q, \lambda\}}{\partial \Sigma_d} + \dot{\lambda}\frac{\partial g(\Sigma_d, q)}{\partial \Sigma_d} = -\bar{L}_d + \dot{\lambda}\frac{\partial g(\Sigma_d, q)}{\partial \Sigma_d} = \\ &= -\dot{F}_d F_d^{-1} + \dot{\lambda}\frac{\partial g(\Sigma_d, q)}{\partial \Sigma_d} = 0 \Rightarrow \qquad \dot{F}_d = \dot{\lambda}\frac{\partial g(\Sigma_d, q)}{\partial \Sigma_d} F_d \end{aligned} \tag{5.38}$$

and also

$$\nabla_q \mathcal{L}\{\Sigma_d, q, \lambda\} = \frac{\partial \mathcal{L}\{\Sigma_d, q, \lambda\}}{\partial q} + \dot{\lambda}\frac{\partial g(\Sigma_d, q)}{\partial q} = \\ = \dot{d} - \dot{\lambda}\gamma(1-d) = 0 \Rightarrow \qquad \dot{d} = \dot{\lambda}\gamma(1-d) \tag{5.39}$$

Stating that $\mu = \dot{\lambda}$, the following equivalent set of evolution equations are postulated

$$\dot{F}_d = \mu\frac{\partial g(\Sigma_d, q)}{\partial \Sigma_d}F_d, \quad \dot{d} = \mu\frac{\partial g(\Sigma_d, q)}{\partial q} = \mu\gamma(1-d), \\ \dot{F}_v^i = \left(\left(C_v^i\right)^{-1} : \Sigma_e^i\right)F_v^i \qquad \text{for every } i = 1...m \tag{5.40}$$

, where μ is the damage consistency parameter. The standard Kuhn-Tucker conditions can be applied

$$\mu g(\Sigma_d, q) = 0, \quad \mu \geq 0, \quad \text{and} \quad g(\Sigma_d, q) \leq 0 \tag{5.41}$$

5.2.3 Stress reduction procedure

5.2.3.1 Trial elastic state

The finite element method is used to solve the system of equations, as described in Eq. [5.29] and Eq. [5.30]. For this, the temporal and spatial discretization of the equations must be realized. Hence the elastic deformation gradient F_∞, as defined in Eq. [5.4], is expressed as

$${}^{t+\Delta t}F_\infty = {}^{t+\Delta t}F\,{}^{t+\Delta t}F_d^{-1} \tag{5.42}$$

Assuming that during the motion in the time interval [t, t+Δt] no further damage occurs, and hence

$${}^{t+\Delta t}F_d = {}^{t}F_d, \qquad {}^{t+\Delta t}\mu = {}^{t}\mu \tag{5.43}$$

, then the approximate elastic deformation gradient can be calculated as

$${}^{t+\Delta t}_{\text{trial}}F_\infty = {}^{t+\Delta t}F\,{}^{t}F_d^{-1} \tag{5.44}$$

Similarly, assuming that during the time interval [t, t+Δt] no further viscous deformation occurs, the approximate viscous deformation gradient for the i^{th} Maxwell component can be calculated as

$${}^{t+\Delta t}F_e^i = {}^{t+\Delta t}F\,{}^{t}\left(F_v^i\right)^{-1} \qquad \text{for every } i = 1...m \tag{5.45}$$

5.2.3.2 Flow rule discretization

The time discretized solution of the evolution Eq. $[5.405]_1$ is given as

$$ {}^{t+\Delta t}F_d = \exp\left(\Delta t \ \mu \frac{\partial g(\Sigma_d, q)}{\partial \Sigma_d}^{t} \right) F_d \qquad [5.46] $$

To solve Eq. [5.47], the inverse of the damage deformation gradient is required, hence Eq. [5.49] becomes

$$ {}^{t+\Delta t}F_d^{-1} = {}^{t}F_d^{-1} \exp\left(-\Delta\mu \frac{\partial g(\Sigma_d, q)}{\partial \Sigma_d} \right) \qquad [5.47] $$

, in which $\Delta\mu = \Delta t \ \mu$. Substituting Eq. [5.50] into Eq. [5.45], considering Eq. [5.47], yields

$$ \begin{aligned} {}^{t+\Delta t}F_\infty &= {}^{t+\Delta t}F \, {}^{t}F_d^{-1} \exp^{t+\Delta t}\left(-\Delta\mu \frac{\partial g(\Sigma_d, q)}{\partial \Sigma_d} \right) = \\ &= {}^{t+\Delta t}_{trial}F_\infty \exp^{t+\Delta t}\left(-\Delta\mu \frac{\partial g(\Sigma_d, q)}{\partial \Sigma_d} \right) \end{aligned} \qquad [5.48] $$

In a similar way, the evolution problem defined by Equation $[5.40]_3$ can be solved in the time interval [t, t+Δt] as follows

$$ {}^{t+\Delta t}F_v^i = \exp\left(-\Delta t \ \left(C_v^i\right)^{-1} : \Sigma_e^i \right) {}^{t}F_v^i \qquad \text{for every } i = 1...m \qquad [5.49] $$

To solve Eq. [5.48], the inverse of the viscous deformation gradient is required, hence

$$ {}^{t+\Delta t}\left(F_v^i\right)^{-1} = {}^{t}\left(F_v^i\right)^{-1} \exp\left(-\Delta t \left(C_v^i\right)^{-1} : \Sigma_e^i \right) \qquad \text{for every } i = 1...m \qquad [5.50] $$

Substituting Eq. [5.53] into Eq. [5.48], considering that ${}^{t+\Delta t}\mathbf{F}_e^i = {}^{t+\Delta t}\mathbf{F} \ {}^{t}\left(\mathbf{F}_v^i\right)^{-1}$, yields

$$ {}^{t+\Delta t}F_e^i = {}^{t+\Delta t}F_\infty \ {}^{t}\left(F_v^i\right)^{-1} \exp^{t+\Delta t}\left(-\Delta t \left(C_v^i\right)^{-1} : \Sigma_e^i \right) \qquad \text{for every } i = 1...m \qquad [5.51] $$

The evolution law for the damage flow surface as expressed in Eq. $[5.40]_2$ is defined as

$$ \dot{d} = \mu \frac{\partial g}{\partial q} = \mu\gamma\left(1 - d\right) \qquad [5.52] $$

In Eq. [5.32], material damage d due to the coupled mechanical-moisture effects is a scalar quantity, which is bound between the undamaged state for d=0 to the fully damaged state when d=1. Moisture damage is a function of moisture content at various times and can be described as (Kringos 2007)

$$ d_\theta = 1 - e^{-a\sqrt{\theta}} \qquad [5.53] $$

, where α is the moisture damage susceptibility parameter and θ is the normalized moisture concentration in the material at a specific time. The general solution of Eq. [5.52] gives

$$d = 1 - e^{-\mu\gamma t} + ce^{-\mu\gamma t} \quad [5.54]$$

, where c is the differentiation constant.

Due to the different time scales associated with the diffusion of moisture and the application of mechanical loading, the proposed model is meant to be used in a staggered computational analysis. First, moisture diffusion analysis is performed to obtain the moisture content in the material and then the elasto-visco-plastic model is used to obtain the mechanical response due to coupled moisture-mechanical damage. As a result, moisture damage d_θ is treated as a constant and can be used as a boundary condition for solving Eq. [5.54]. Therefore, considering that $d_{(t=0)} = d_\theta$ Eq. [5.54] yields

$$d = 1 - e^{-\mu\gamma t} + d_\theta e^{-\mu\gamma t} \quad [5.55]$$

, or alternatively, taking into account the definition of moisture damage

$$\begin{aligned} d &= 1 - e^{-\mu\gamma t} + \left(1 - e^{-a\sqrt{\theta}}\right)e^{-\mu\gamma t} = \\ &= 1 - e^{-a\sqrt{\theta}}e^{-\mu\gamma t} \\ &= 1 - (1 - d_\theta)(1 - d_{mech}) \end{aligned} \quad [5.56]$$

The evolution problem defined by Equation [5.40]$_2$ can be solved in the time interval [t, t+Δt] as follows

$${}^{t}d = 1 - e^{-a\sqrt{\theta}}e^{-\mu\gamma t} \Rightarrow \begin{cases} e^{-a\sqrt{\theta}}e^{-\mu\gamma t} = 1 - {}^{t}d, \text{ at time } t \\ e^{-a\sqrt{\theta}}e^{-\mu\gamma(t+\Delta t)} = 1 - {}^{t+\Delta t}d, \text{ at time } t + \Delta t \end{cases} \quad [5.57]$$

Dividing the two equations, yields

$$\frac{1 - {}^{t+\Delta t}d}{1 - {}^{t}d} = \frac{e^{-\mu\gamma(t+\Delta t)}}{e^{-\mu\gamma t}} = e^{-\mu\gamma\Delta t} = e^{-\gamma\Delta\mu} \quad [5.58]$$

Hence the time discretized form of the total damage evolution equation is

$${}^{t+\Delta t}d = 1 - e^{-\gamma\Delta\mu}\left(1 - {}^{t}d\right) \quad [5.59]$$

Finally, the incremental form of the Eq. [5.32], which defines the damage flow surface, is obtained. At time [t+Δt], the evolution equation for total damage is written as

$${}^{t+\Delta t}g(\sigma, q) = {}^{t+\Delta t}\sqrt{J_2(\sigma)} - \alpha_o I_1(\sigma)(1 - {}^{t+\Delta t}d)^a - \beta_o(1 - {}^{t+\Delta t}d)^b \quad [5.60]$$

Substituting Eq. [5.56] and Eq. [5.57] in the evolution equation of the total damage yields

$${}^{t+\Delta t}g(\sigma, q) = {}^{t+\Delta t}\sqrt{J_2(\sigma)} - \alpha_o I_1(\sigma)\left(e^{-a\sqrt{\theta}}e^{-\gamma\Delta\mu}\left(1 - {}^{t}d_{mech}\right)\right)^a - \beta_o\left(e^{-a\sqrt{\theta}}e^{-\gamma\Delta\mu}\left(1 - {}^{t}d_{mech}\right)\right)^b \quad [5.61]$$

5.2.4 Return mapping algorithm

The Newton-Raphson method is used to solve the minimization problem described in the above. In order to compute the updates of the damage parameter $\Delta\mu$ and of the deformation tensors F_∞ and F_e by means of a Newton-Raphson scheme, the residual form of Eq. [5.47], Eq. [5.50] and Eq. [5.56] has to be specified. The residual equation for the undamaged elastic deformation tensor F_∞ is defined as

$$R_{F_\infty} = {}^{t+\Delta t}F_\infty - {}^{t+\Delta t}_{trial}F_\infty \exp^{t+\Delta t}\left(-\Delta\mu \frac{\partial g(\Sigma_d, q)}{\partial \Sigma_d}\right) \qquad [5.62]$$

In the same way, the residual equation for the elastic deformation tensor F_e of the viscoelastic component is defined as

$$R^i_{F_e} = {}^{t+\Delta t}F^i_e - {}^{t+\Delta t}F_\infty \; {}^{t}\left(F^i_v\right)^{-1} \exp^{t+\Delta t}\left(-\Delta t\left(C^i_v\right)^{-1} : \Sigma^i_e\right) \qquad \text{for every } i = 1...m \qquad [5.63]$$

Lastly, the residual equation for the damage flow surface is

$$R_d = {}^{t+\Delta t}\sqrt{J_2(\sigma)} - \alpha_o I_1(\sigma)\left(e^{-a\sqrt{\theta}}e^{-\gamma\Delta\mu}\left(1 - {}^{t}d_{mech}\right)\right)^a - \beta_o\left(e^{-a\sqrt{\theta}}e^{-\gamma\Delta\mu}\left(1 - {}^{t}d_{mech}\right)\right)^b \qquad [5.64]$$

An iterative Newton-Raphson procedure is employed to minimize the set of residual equations, shown in Eq. [5.65], solving simultaneously for F_∞, F^i_e and $\Delta\mu$. Initially F_∞ gets a trial value based on the previous converged time step, and $\Delta\mu = 0$.

$$\begin{bmatrix} \frac{\partial R_{F_\infty}}{\partial F_\infty} & \frac{\partial R_{F_\infty}}{\partial F^1_e} & \cdots & \frac{\partial R_{F_\infty}}{\partial F^m_e} & \frac{\partial R_{F_\infty}}{\partial \Delta\mu} \\ \frac{\partial R^1_{F_e}}{\partial F_\infty} & \frac{\partial R^1_{F_e}}{\partial F^1_e} & \cdots & \frac{\partial R^1_{F_e}}{\partial F^m_e} & \frac{\partial R^1_{F_e}}{\partial \Delta\mu} \\ \vdots & \vdots & & \vdots & \vdots \\ \frac{\partial R^m_{F_e}}{\partial F_\infty} & \frac{\partial R^m_{F_e}}{\partial F^1_e} & \cdots & \frac{\partial R^m_{F_e}}{\partial F^m_e} & \frac{\partial R^m_{F_e}}{\partial \Delta\mu} \\ \frac{\partial R_d}{\partial F_\infty} & \frac{\partial R_d}{\partial F^1_e} & \cdots & \frac{\partial R_d}{\partial F^m_e} & \frac{\partial R_d}{\partial \Delta\mu} \end{bmatrix} \begin{bmatrix} \Delta F_\infty \\ \Delta F^1_e \\ \vdots \\ \Delta F^m_e \\ \Delta\Delta\mu \end{bmatrix} = - \begin{bmatrix} R_{F_\infty} \\ R^1_{F_e} \\ \vdots \\ R^m_{F_e} \\ R_d \end{bmatrix} \qquad [5.65]$$

The analytical expressions for the individual derivatives are given in Appendix D.

5.2.5 Model response

An equilibrium-based driver was set up that allows the simulation of any state of uniaxial or multiaxial testing conditions. The required model parameters α_o and β_o, which are a function of the tensile and compressive strength as defined in Eq. [5.33], and the softening related parameters a, b,

and γ can be determined via regression analysis on the basis of uniaxial tension and compression tests at different moisture contents, temperatures and strain rates.

To verify the model response uniaxial tension tests were performed. The strain level was 20% and the input model parameters for the analysis were selected as: tensile strength f_t= 4.0 MPa and compressive strength f_c=12.0 MPa. The damage parameters b and γ varied to demonstrate their influence on the response of the model. Dynamic Shear Rheometer tests were performed to determine the material properties in terms of Prony's series of the asphalt mortar. The Prony coefficients were then determined using a methodology described in Srirangam (2015) and are listed in Table 5.1.

Table 5.1 Prony coefficients for viscoelastic mortar at 20°C

Maxwell component i	**E_i [MPa]**	**η [MPa·s]**
1	209.89	4.36
2	26.91	2103.93
3	152.55	19.04
4	32.33	82.42
5	85.41	60.83
6	43.27	324.43
∞ (single spring)	1.21	-

Figure 5.6 shows the non-linear behaviour of asphalt mortar as simulated in uniaxial tension under displacement control at dry conditions. In the case of tension loading, depending on the strain rate the softening response of the material is obtained.

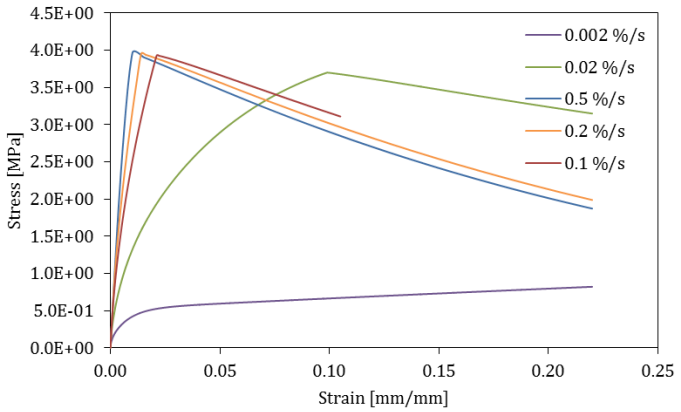

Figure 5.6 Model response during a tension test at various strain rates.

Damage propagation starts after the peak stress is reached. When damage starts, the loading surface begins to shrink. This is achieved by means of the softening law as described in Eq. [5.32]. Figure 5.7 illustrates the response of the model at various moisture contents. It can be observed that the strength of the material decreases with increasing moisture content.

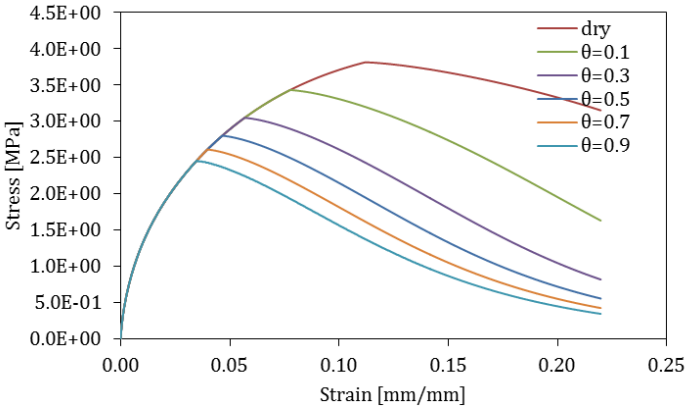

Figure 5.7 Model response at various moisture contents. The strain amplitude was 20% and strain rate was 0.02 %/s. Parameter γ=5, parameter a=b=2, moisture damage parameter α=0.35.

Figure 5.8 shows the effect of parameter γ on the response degradation phase. It can be observed that parameter γ strongly influences the post-peak behaviour of the curve. The rate of degradation increases with increasing γ values. Figure 5.9 shows that parameter b controls the peak stress; an increase in the value of parameter b softens the material.

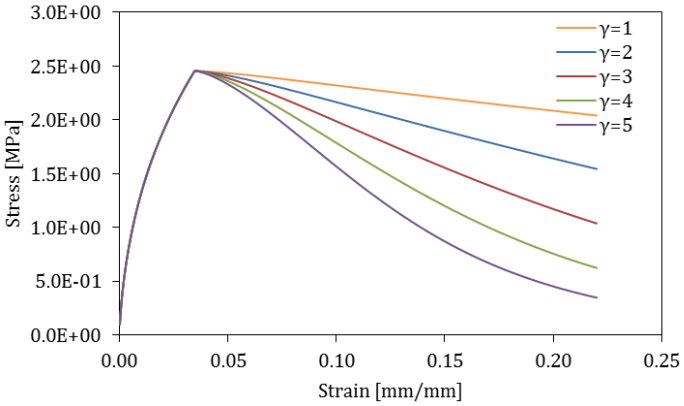

Figure 5.8 Influence of softening parameter γ at a strain rate of 0.02%/s. Parameters a and b are set equal to 2. Moisture damage parameter α=0.35 and moisture content θ=0.9.

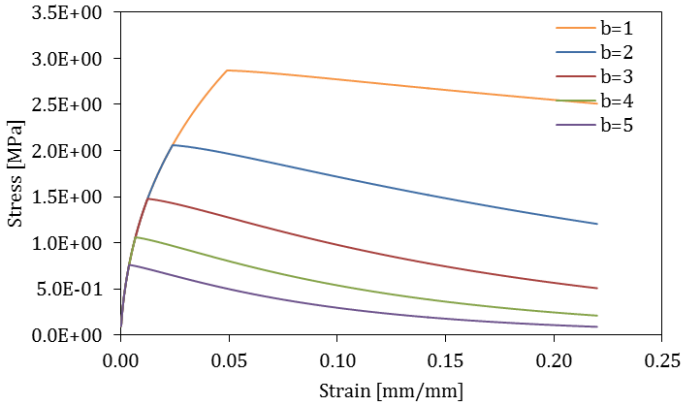

Figure 5.9 Influence of parameter b at a strain rate of 0.02%/s. Parameter γ=2 and parameter a=0. Moisture damage parameter α=0.35 and moisture content θ=0.9.

5.3 Summary

In this chapter, the formulations of the elasto-visco-plastic model with softening driven by coupled moisture-mechanical damage model were derived and formulated in a way that are suitable for implementation into a finite element method framework. The model was implemented into the CAPA-3D Finite Element (FE) system. The availability of the model enables modern pavement engineers to understand the fundamental processes that govern moisture damage and identify the key factors that control these processes, both over short- and long-term periods. Such model can serve as a relatively fast and inexpensive way, to investigate a great variety of parameters before the pavement structure is actually built. This allows for new materials and mixture designs to be investigated and the risks involved with these to be minimized. An application of the model is presented in Chapter six.

5.4 References

Caro, S. (2009). A coupled micromechanical model of moisture-induced damage in asphalt mixtures: Formulations and applications. PhD dissertation. Texas A&M University, USA.

Coleman, B.D., and Gurtin, M.E. (1967). Thermodynamics with Internal Variables. *Journal of Chemical Physics*, 47, 597.

Copeland, A., Kringos, N., Youtcheff, J. and Scarpas, A. (2007). Measurement of aggregate-mastic bond strength in the presence of moisture: a combined experimental - computational study. Transportation Research Board 86th Annual Meeting Compendium of Papers, No. 07-1829, Washington, D.C.

Graham, M.A. (2009). *Viscoelastic-viscoplastic damage model for asphalt concrete*. MSc thesis. Texas A&M University, USA.

Holzapfel, G.A. (2000). Nonlinear solid mechanics: A continuum approach for engineering. John Wiley & Sons Ltd. West Sussex, England.

Huang, C.W. (2008). *Development and numerical implementation of nonlinear viscoelastic-viscoplastic model for asphalt materials.* PhD dissertation. Texas A&M University, USA.

Kringos, N. (2007). *Modeling of combined physical-mechanical moisture induced damage in asphaltic mixes*. PhD dissertation. Delft University of Technology, Netherlands.

Kringos, N., Scarpas, A., Copeland, A., and Youtcheff, J. (2008). Modelling of combined physical–mechanical moisture-induced damage in asphaltic mixes, part 2: moisture susceptibility parameters. *International Journal of Pavement Engineering*, 9:2, 129-151.

Mehrara, A., and Khodaii, A. (2013). A review of state of the art on stripping phenomenon in asphalt concrete. *Construction and Building Materials*, 38, 423-442.

Reese, S., and Govindjee, S. (1998). A theory of finite viscoelasticity and numerical aspects. *International Journal of Solid Structures*, 35, 3455-3482.

Scarpas, A. (2005). *CAPA-3D: A mechanics based computational platform for pavement engineering.* PhD dissertation. Delft University of Technology, Netherlands.

Srirangam, S. K. (2015). *Numerical simulation of tire-pavement interaction*. PhD dissertation. Delft University of Technology, Netherlands.

6

Influence of air voids on moisture susceptibility of asphalt mixtures

"Essentially, all models are wrong, but some are useful."
— George E. P. Box (1919-2013)

Apart from the physicochemical properties of the mixture constituents, moisture sensitivity of asphalt pavements is significantly influenced by mixture morphology. It is known that the air voids content and interconnectivity can have a great effect on the rate and magnitude of moisture damage in pavements. It is, therefore, essential to understand the interplay among the mix design parameters and use this information to develop new mixture designs with enhanced characteristics against moisture damage. To this end, the computational model described in Chapter five is implemented and used to provide useful insights on the effect of the microscale characteristics on the macroscopic mechanical behaviour of asphalt mixtures.

Part of this chapter contains published material from the article "Influence of air void content on moisture damage susceptibility of asphalt mixtures: Computational study" by A. Varveri, S. Avgerinopoulos, C. Kasbergen, A. Scarpas and A. Collop, published in the Transportation Research Record: Journal of the Transportation Research Board, volume 2446, issue 3, pp. 8-16 © 2015.

6.1 Introduction

As soon as moisture is introduced into an asphalt pavement, in the form of liquid or vapor water, the diffusion of moisture into the structure becomes a critical process that needs to be understood. Damage due to moisture is greatly dependent on the properties of the constituent materials and mixture morphology. The spatial distribution and physicochemical properties of the individual material phases, as well as the interplay among the phases are key elements that ultimately dictate the mechanical response of the composite material in moist conditions.

To date, several experimental studies exist in literature regarding the influence of air voids on moisture damage (Masad et al. 2006, Arambula et al. 2007, Kassem et al. 2009, and Kassem et al. 2011). In Chapter two, the importance of air void content and distribution, as well as of the diffusivity properties of the mixture constituents on moisture diffusion, and consequently on moisture sensitivity of asphalt mixtures, has been already discussed. However, in all modelling efforts presented in Chapter five asphalt mixtures were simulated as two-phase materials (aggregates and mastic); hence the air void phase was excluded. Moreover, for all simulations 2D representations of the internal structure of the samples were used for creating the finite element meshes. Because the behaviour of multiphase materials, such as asphalt concrete, is determined by the contribution and interaction of the constituents in addition to their morphological and geometrical characteristics, the inclusion of air voids in finite element simulations is of paramount importance. Especially since, in the case of moisture diffusion, air voids facilitate the ingress of moisture to the binder and eventually to the aggregate-binder interface.

In this chapter a staggered computational procedure is used to demonstrate the influence of the air void phase on the moisture susceptibility of asphalt mixtures. This procedure combines the moisture diffusion model described in Chapter two and the elasto-visco-plastic model with softening due to coupled moisture-mechanical damage described in Chapter five. All simulations were performed on 3D finite element (FE) meshes obtained via X-ray Computed Tomography (CT) scans.

6.2 Geometry and FE mesh generation

The accurate representation of the internal structure of asphalt mixtures is quite significant in modelling moisture damage at the microscale, since each mix component has its particular diffusion coefficient and mechanical properties, and therefore the geometry of every single phase plays an important role on the propagation of moisture into the mixture and on its mechanical response. To this end, three dimensional micromechanical FE meshes were produced from X-Ray CT scans by means of Simpleware® software (Simpleware 2011). A Siemens Somatom Volume Zoom CT scanner was used to obtain the digital information of the internal morphology of the asphalt samples in the form of 2D CT scans. Typically, the process for the creation of 3D voxel-based meshes from a set of CT scans includes data preparation and filtering, segmentation of the individual masks, mask filtering and mesh generation. Figure 6.1 shows schematically the process for the generation of 3D voxel-based FE meshes.

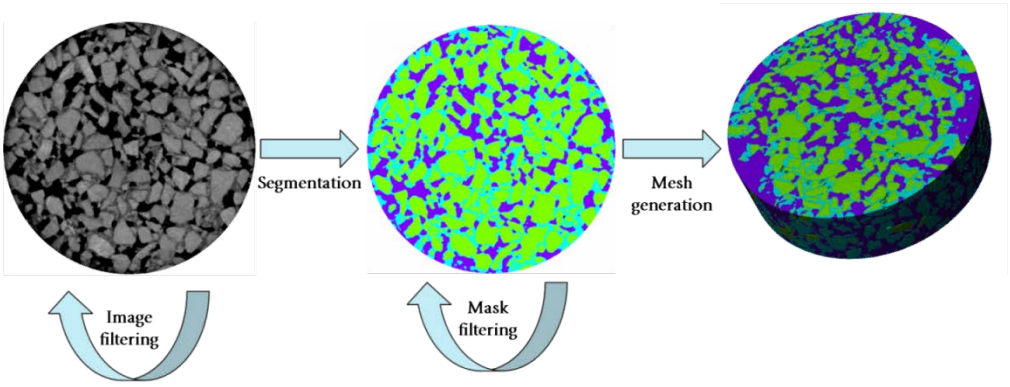

Figure 6.1 Process flow for the development of FE meshes.

In this study, the moisture sensitivity of two mixtures with dissimilar morphology, namely a dense stone mastic asphalt (SMA) and a porous asphalt (PA) mixture, were investigated. First, asphalt slabs for both mixtures were prepared in the laboratory using a roller compactor and specimens of 60 mm in height and 100 mm in diameter were cored out of the slabs and scanned in the CT scanner. The SMA and PA mixtures had a nominal maximum aggregate size of 10 mm. The binder content (P_b) and the air void percentage (AV) were 6.4 and 4.4% , respectively, for the SMA; for the PA mixture P_b was 5.3 and AV was 23.7%. Figure 6.2 presents the volume renderings of the FE meshes and the air void phase.

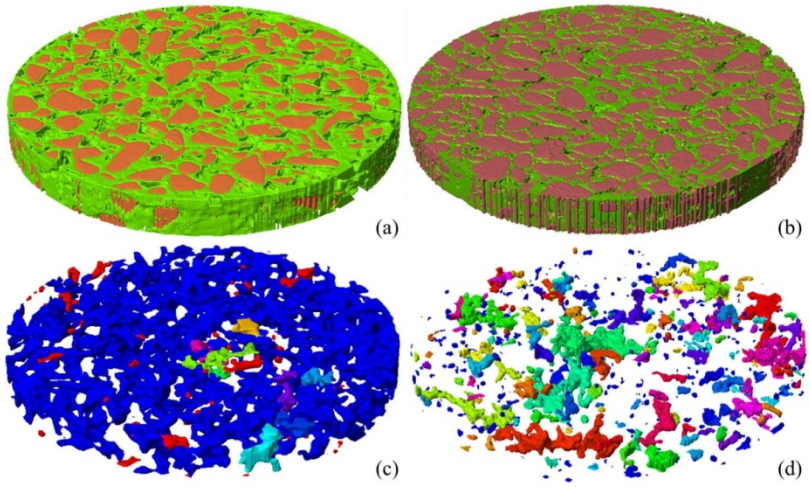

Figure 6.2 Reconstructed geometry of the porous (a) and dense (b) samples and their air void phase (c, d).

In asphalt mixtures part of the air void network is interconnected, while there are voids that are isolated and bounded by the mortar (a mix of bitumen, filler and sand). The distribution and interconnectivity of the air void network depends primarily on the mix design (i.e. volumetric properties and aggregate gradation) and compaction level. Figure 6.3 and Figure 6.4 show the distribution and interconnectivity of the air void network along the height of the samples. In the case of the open-graded porous sample, Figure 6.3, there is almost no difference between the distribution of the total and interconnected air voids. This reveals the high interconnectivity of the mixture which is 90% by volume of the total air void phase. In Figure 6.4, a large gap is observed between the total and interconnected air voids curves that indicate the presence of isolated voids in

the sample. The interconnectivity of the dense SMA sample was 10% by volume of the total air-void, whereas the rest of the air void phase was divided in volume fractions of less than 2% each, Figure 6.2(d).

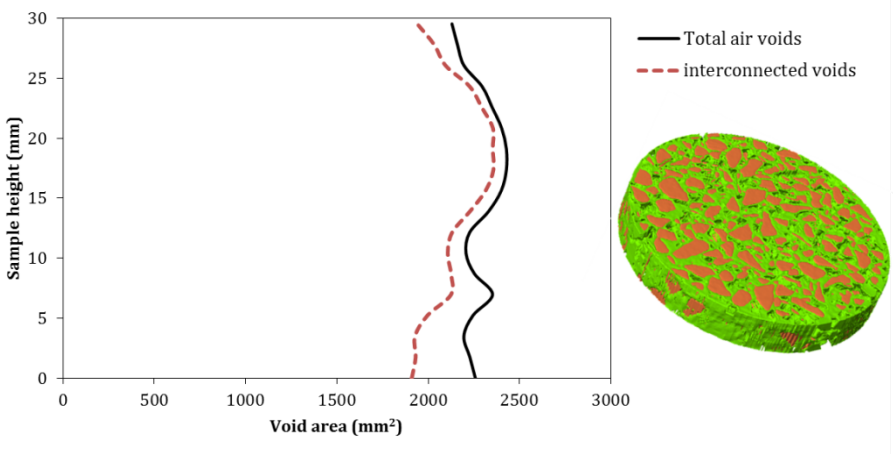

Figure 6.3 Air void distribution along the height of the porous sample.

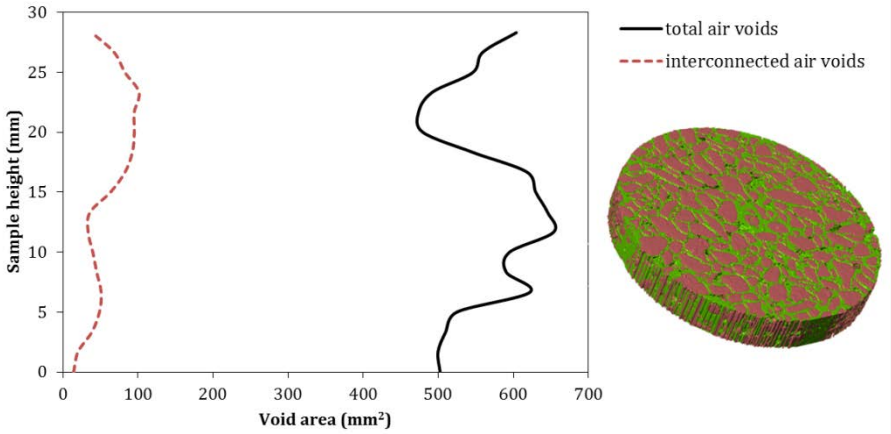

Figure 6.4 Air void distribution along the height of the dense stone mastic sample.

After cropping the segmented data to the desired dimensions, a robust meshing algorithm was applied to enable the conversion of the 2D images into FE meshes. For the analysis, both meshes were discretized by using 3D linear four-node tetrahedral elements. Specifically, the SMA mesh consists of 3,645,835 elements and the PA mesh consists of 2,223,084 elements. It is clear that when such detailed microscale meshes are employed for analysis, the computation time increases dramatically and the use of parallel computing resources is essential.

6.3 Moisture diffusion analysis

Due to the different time scales associated with the diffusion of moisture into the mixtures and the application of mechanical loading, a staggered computational scheme was implemented. In the first step, moisture diffusion simulations were performed to obtain moisture concentration profiles within the asphalt samples at specific time intervals. The diffusion model described in Chapter two was implemented in the CAPA-3D computational platform (Scarpas 2005) and used to investigate the effect of the aforementioned mixture morphologies on the propagation of moisture.

6.3.1 Boundary conditions and input parameters

The boundary conditions for the analysis were defined as follows: the top surface and the periphery of the samples were exposed to continuous moisture supply while the bottom surface was considered to be impermeable to moisture. In this way, the interconnected air voids have a continuous flow of moisture from the top and the sides of the samples. In the beginning of the analysis, the samples were assumed to be dry; hence the value of moisture in the isolated air voids was zero. With time moisture was allowed to reach the isolated voids by diffusing through the mortar and aggregates. Moreover, the coarse aggregates were assumed to be fully coated with mortar, and therefore moisture had to diffuse first through the mortar film in order to reach the aggregates.

The parameters required for modelling diffusion are essentially the moisture diffusion coefficients of each material phase. Thus far, several studies determined the coefficients of moisture diffusion in bituminous materials utilizing various techniques as summarized in Table 2.3. For the analysis, the moisture diffusion coefficients of the mortar and aggregates were adopted by a study from Kringos et al. (2008). The diffusivity of the mortar and aggregates was chosen to be 11.08×10^{-3} mm^2/hr and 0.72 mm^2/hr, respectively. The coefficient of moisture diffusion of air voids phase was chosen as 93.6×10^3 mm^2/hr (Kassem et al. 2009). Since the rate of diffusion in each phase depends on their associated diffusion coefficient, moisture will diffuse through the mortar at a slower rate compared to the aggregates and air voids phase. Given that the purpose of the simulations was to investigate the influence of mixture morphology on moisture damage, the materials properties were kept constant.

6.3.2 Moisture diffusion analysis

The moisture diffusion simulations have been performed for a period of 5 days. Figure 6.5 and Figure 6.6 present the normalized moisture concentration profiles in the open-graded PA and dense SMA samples, respectively. A number of nodes were selected as output locations for the moisture concentration values. The selected nodes are lying on the diameter of the sample and are located 1mm above the bottom surface.

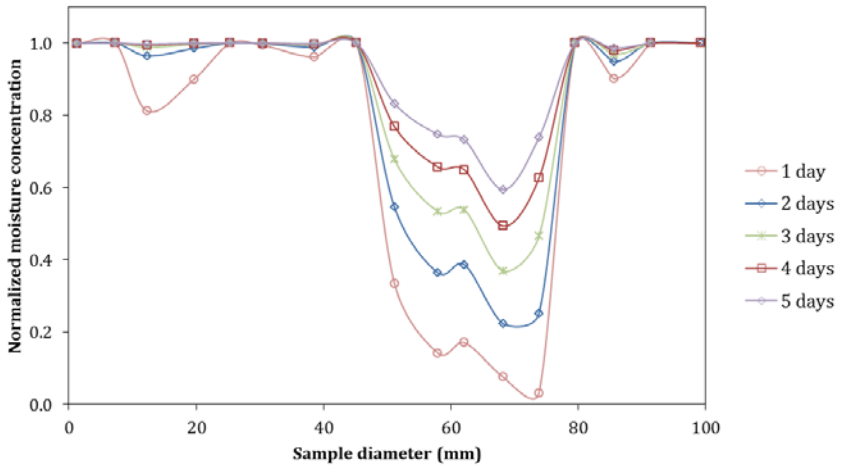

Figure 6.5 Propagation of moisture in the porous sample with time.

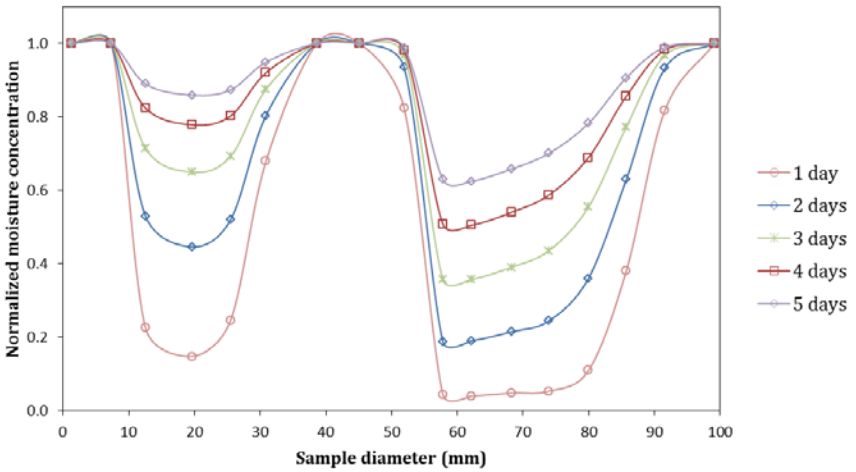

Figure 6.6 Propagation of moisture in the dense sample with time.

The results demonstrate the effect of air void content and interconnectivity on the amount of moisture that is present in the samples at any given time. After five days of diffusion the porous mixture appeared to have higher moisture values in comparison to the dense SMA sample, as the high interconnectivity of the air void network of the porous mixture creates channels that facilitate moisture to enter the sample. Although this was expected, it is interesting to note that the moisture profile in the porous mixture is more uniform than this in the dense mixture. Again, this can be attributed to the high percentage of the connected voids that allows moisture to diffuse in a homogeneous way through the body of the sample. The generated moisture profiles can be explained by the air void distribution of the samples. Figure 6.2(c), the air void distribution of the porous sample is illustrated. The blue colour denotes the interconnected voids, whereas the isolated air voids are shown in different colours. It is observed that the peak shown in the graph for the porous mixture, Figure 6.5, coincides spatially with the presence of isolated voids in the sample. This discontinuity in the air void network is a hindrance to the diffusion of moisture in that specific location of the sample. Similar observations can be made for the SMA sample. The higher amount of

interconnected voids is located in the middle of the sample, Figure 6.2 (d), and this is the location with the higher moisture content as illustrated in the graph in Figure 6.6.

6.4 Computational parametric analysis of long-term moisture damage

The effect of moisture on the mechanical response of the mixtures was investigated by performing simulations using the elasto-visco-plastic model with softening due to coupled moisture-mechanical damage described in Chapter five, which was implemented in CAPA-3D (Scarpas 2005). After the generation of moisture profiles the microscale meshes, with their material properties updated for moisture damage, were subjected to virtual displacement controlled tests.

6.4.1 Boundary conditions and input parameters

The analysis was carried out with the following boundary conditions: Displacement constrains were specified for the bottom and back surface of the samples. The bottom surface was constrained vertically, and the back surface was constrained horizontally. During the simulation, the prescribed displacement was applied diametrically across the circular cross section of the cylindrical sample with a constant rate of 50 mm/min, replicating thus the loading conditions during an Indirect Tension Test (ITT). To apply and distribute the load uniformly along the entire length of the sample, the width of the loading strip was 12 mm.

The input parameters required for the analysis were the viscoelastic material properties, the moisture damage susceptibility parameter and the mechanical damage related parameters of the asphalt mortar, as described in Chapter six. An instantaneous modulus of 3.5 MPa was specified for the purely elastic component. For the viscoelastic component, an elastic modulus of 550 MPa and a viscosity of 2200 MPa·s were specified. The moisture susceptibility parameter can be back-calculated by curve fitting experimental damage degradation curves with respect to moisture content (Kringos et al. 2011). In this study, the moisture damage susceptibility parameter (α_1) was selected as 0.7. The aggregate phase was modeled as an isotropic elastic material, with an elastic modulus of 18.1 GPa and a Poisson's ratio of 0.171 (Artamendi et al. 2011).

6.4.2 Modelling damage due to moisture

The effect of moisture on the tensile strength of the mixtures was quantified through FE simulations. Figure 6.7 and Figure 6.8 illustrate the results of the simulations for the porous and the dense mixture, respectively. Figure 6.7(a) and Figure 6.8(a) show the finite element mesh of the PA and SMA samples at dry conditions, i.e. before any moisture conditioning; for both samples, aggregates are in yellow, mortar in red and air voids in blue color. The damage distribution of the mixtures, at dry state, after the application of the mechanical load in depicted in Figure 6.7(d) and Figure 6.8(d). It can be observed that damage concentrates along the diameter of the samples in the

direction of loading. Also, a high accumulation of damage is observed at the location of the sample that is in contact with the loading strips.

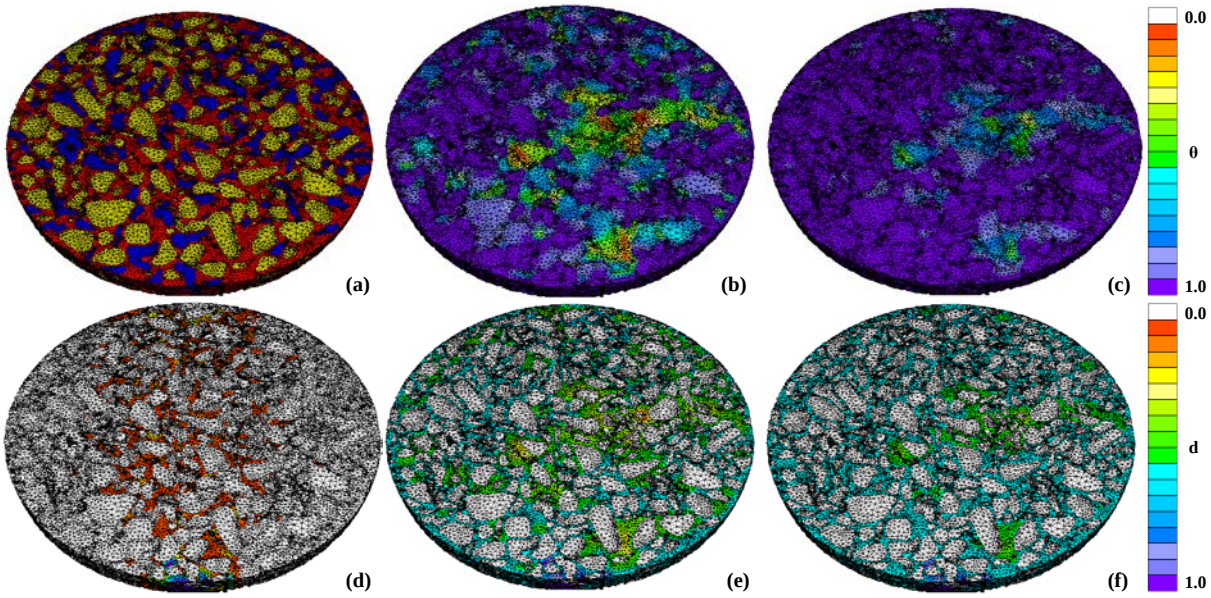

Figure 6.7 Porous mixture: moisture content contours and damage distribution at dry state (a, d), after 48 hours (b, e) and after 120 (c, f) hours of diffusion.

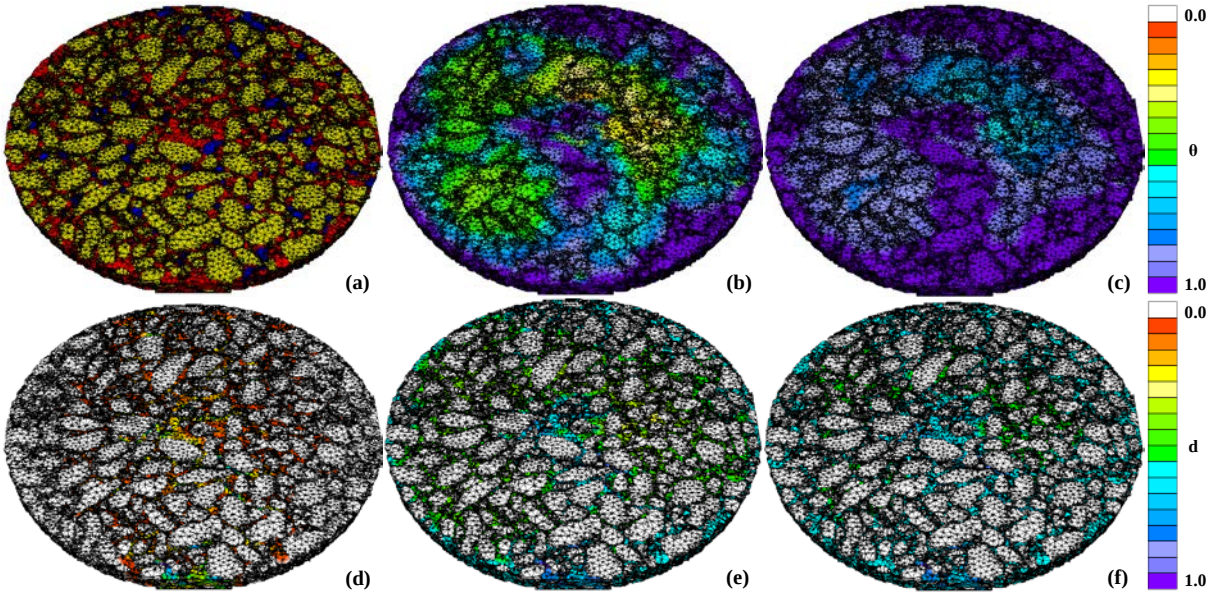

Figure 6.8 Dense mixture: moisture content contours and damage distribution at dry state (a, d), after 48 hours (b, e) and after 120 (c, f) hours of diffusion.

Figure 6.7(b-c) and Figure 6.8(b-c) illustrate the spatial distribution of moisture in the porous and dense samples after 48 and 120 hrs of conditioning. As discussed in paragraph 6.4, the porous mixture has higher moisture content in time than the dense; therefore damage development is expected to be higher for the porous sample. Figure 6.7(e-f) and Figure 6.8(e-f) show the damage distribution in the samples after moisture conditioning. These figures illustrate that mechanical

damage gradually localized near the edges of the samples and at those areas where the material was already degraded by moisture, as the conditioning time increased. This phenomenon may be observed in the field in the form of local pavement failures after long rainy periods.

Overall, the results demonstrate the strong relationship between the amount of moisture in the material and the damage levels in the asphalt samples. The strength of the samples with conditioning time is plotted in Figure 6.9. At dry conditions, the dense mixture exhibited higher ITT strength than the porous. This was to be expected as the presence of high air voids content decreases the loading capacity of the asphalt samples.

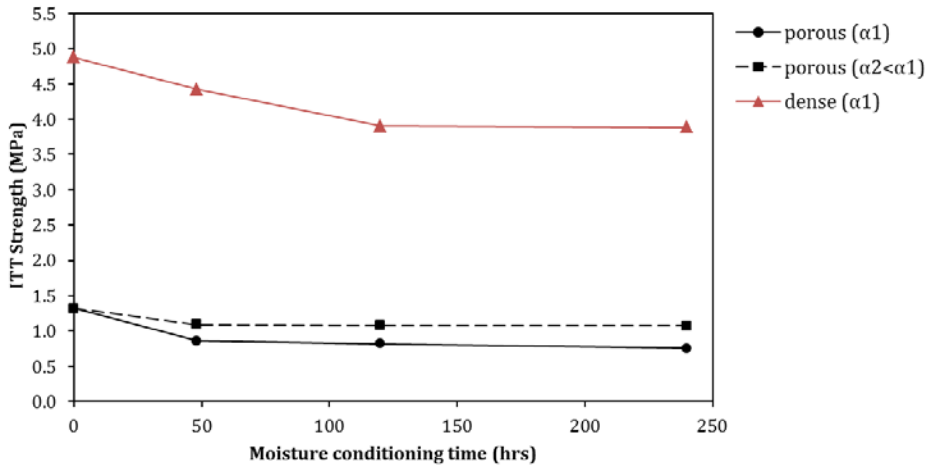

Figure 6.9 Change in tensile strength with conditioning time for the porous and dense samples. For the porous sample, two mortars with different sensitivity to moisture were tested. The moisture susceptibility parameter $\alpha 1 > \alpha 2$; hence mortar 2 is more resistant to moisture than mortar 1.

The figure shows that as the time of moisture conditioning increases, the tensile strength of the porous and dense samples decreases. The strength of the porous sample reduced by 43% after 240 hrs (10 days) of conditioning, whereas for the dense sample the reduction was lower and equal to 21%. Then, the same analysis were carried out for the porous samples using a mortar that is less sensitive to moisture, i.e. the moisture susceptibility parameter $\alpha_2 < \alpha_1$. The analysis showed that strength reduction of the moisture resistant mortar was 18.5% after 240 hrs of conditioning, which is much lower compared to the 43% of the original mortar. These results highlight the importance of selecting mixture components that are less susceptible to moisture, especially when considering porous mixtures that have an intrinsic sensitivity to moisture damage due to their high air voids content and interconnectivity.

6.5 Summary

The aim of this study was to investigate the effect of mixture morphology on moisture sensitivity. A finite element analysis was performed in a staggered scheme: first a moisture diffusion model (Chapter two) was used to obtain the moisture profiles within the asphalt samples, and then an elasto-visco-plastic model with softening due to coupled moisture-mechanical damage (Chapter five) was used to investigate the influence of air voids and interconnectivity to the moisture

sensitivity of the mixtures. The analysis was carried out for a porous and a dense sample and the simulations were performed on 3D finite element (FE) meshes obtained via X-ray Computed Tomography (CT) scans.

The results of the moisture diffusion analysis showed that moisture content was higher for the porous sample than for the dense sample, indicating thus that the amount of moisture in a mixture is strongly dependent on its morphology. Isolated air voids and low interconnectivity of the void network was shown to be a hindrance in the propagation of moisture in mixtures.

The mechanical analysis showed that the tensile strength of the mixtures decreased with increasing conditioning time. Moreover, it has been observed that the areas with high levels of damage were those that had been already degraded by moisture. This observation is likely the reason why moisture damage is associated with local and premature failures in the field. Furthermore, the results suggest that there is a strong relationship between the moisture sensitivity of the mortars and the overall damage levels of asphalt mixtures. The use of a less moisture sensitive mortar resulted in lower reduction in strength, from 43% to 18.5%, for the porous mixture. These results demonstrate the effect of using mortars with high resistivity against moisture and quantify the benefits that would arise due to this choice, especially when designing porous mixtures that have an intrinsic sensitivity to moisture damage.

Overall, this study suggests that the moisture susceptibility of asphalt mixtures is governed by the contribution, the interaction and the geometry of the mixture constituents. Hence it is of great importance to treat asphalt concrete as a three-phase composite in microscale finite element simulations. The use of microscale models, on contrast to macroscale models, enables the investigation of different mixtures types, such as gap- and open-graded mixtures. Moreover, such micromechanical models may serves as a way to provide physical insight into the dependability of composite properties and behaviour on material microstructures. Imaging techniques are used to capture the particularities of the internal structure of mixtures and to obtain a better observation of their characteristics such as air void connectivity, structure of the aggregate skeleton, and binder film thickness. Availability of the model enables the evaluation and ranking of asphalt mixtures subjected to combinations of mechanical loading and moisture. Along these lines, engineers can reduce the amount of empiricism in materials engineering and opt for critical selection of mineral aggregates, binder and other additives to produce high performance materials, thus reducing the risk of failure.

6.6 References

Arambula, E., Masad, E.A. and Martin A. (2007). Influence of air void distribution on the moisture susceptibility of asphalt mixes. *Journal of Materials in Civil Engineering*, 19:8, 655–664.

Artamendi, I., Kane, M., Scarpas A. and Villani, M.M. (2011). *Measurement of the interface component characteristics*. EU FP7 SKIDSAFE project report 1.1.

Kassem, E., Masad, E.A., Lytton, R.L. and Chowdhury, A. (2011). Influence of air voids on mechanical properties of asphalt mixtures. *Road Materials and Pavement Design*, 12:3, 493-524.

Kassem, E., Masad, E.A., Lytton, R.L. and Bulut, R. (2009). Measurements of the moisture diffusion coefficient of asphalt mixtures and its relationship to mixture composition. *International Journal of Pavement Engineering*, 10: 6, 389-399.

Kringos, N., Khedoe, R., Scarpas, A. and de Bondt, A. (2011). New asphalt concrete moisture susceptibility test methodology. Transportation Research Board 90th Annual Meeting Compendium of Papers, Washington, D.C.

Kringos, N., Scarpas, A. and de Bondt, A. (2008). Determination of moisture susceptibility of mastic-stone bond strength and comparison to thermodynamical properties. *Journal of the Association of Asphalt Paving Technologists*, 77, 435-478.

Masad, E.A., Castelblanco, A. and Birgisson, B. (2005). Effects of air void size distribution, pore pressure, and bond energy on moisture damage. *Journal of Testing and Evaluation*, 34:1.

Scarpas, A. (2005). *CAPA-3D: A mechanics based computational platform for pavement engineering.* PhD dissertation. Delft University of Technology, Netherlands.

Simpleware (2011), ScanIP, +ScanFE.

7

Frost damage in asphalt mixtures

"The purpose of models is not to fit the data but to sharpen the questions."
— Samuel Karlin (1924-2007)

Frost damage is one of the major concerns in pavement design particularly in cold regions. During their service life, asphalt pavements are continuously exposed to various environmental conditions such as moisture, oxidation and ultraviolet radiation. The joint effects of mechanical and environmental loading progressively degrade the mechanical properties of asphalt pavements, resulting thus to frost damage when ice crystals form in the pavement. This chapter presents a three-dimensional energy based micromechanical model for the simulation of volume expansion that occurs during the water-to-ice phase change in the macro pores of a mixture.

Part of this chapter contains published material from the article "A constitutive model for simulation of water-to-ice phase change in asphalt mixtures." by A. Varveri, S. Avgerinopoulos, C. Kasbergen, A. Scarpas and A. Collop, published in Y.R. Kim (Ed.), Proceedings of the 12th International conference on Asphalt Pavements (ISAP), pp. 531-539 © 2014.

7.1 Introduction

A major concern for asphalt pavements in cold regions is freeze-thaw damage. The detrimental effects of freeze-thaw cycles involve stripping of aggregates from the asphalt mixture, which in time results to pothole formation and deterioration of the pavement surface. Hence the way frost damage manifests itself is similar to moisture damage. In addition, for frost damage to occur, water and low temperatures have to be concurrently present in a pavement. Therefore, one can classify frost damage as part of the moisture damage related mechanisms.

Freeze-thaw damage is the result of excess pressure when water expands at low temperature. Unlike the majority of substances, water expands upon freezing and its volume increases approximately by 9% under atmospheric pressure. On the basis of thermodynamics, volume expansion of water-to-ice is the result of a phase change from a liquid state to a solid one, Figure 7.1. Phase change takes place in a very narrow temperature range around zero degrees and for this reason temperatures below zero have very little influence on volume change.

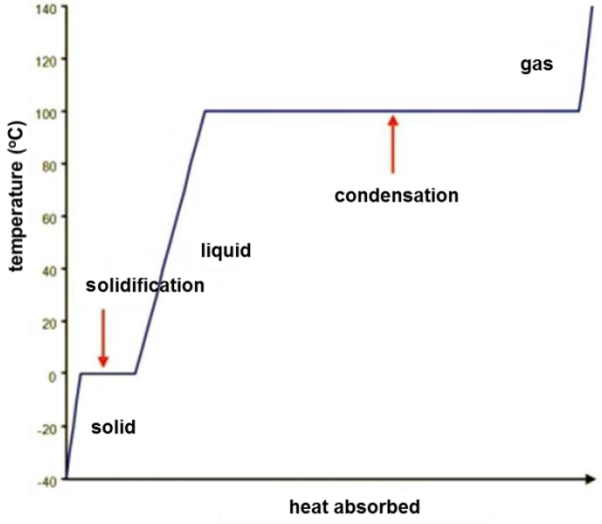

Figure 7.1 Heating curve for water.

Depending on the design characteristics, air void content in an asphalt mixture can vary from 3-5% for a dense mixture and up to 20% for a porous mixture. Because of precipitation and other reasons, moisture can accumulate inside the air voids and the micro-cracks in the top layers of the pavement, Figure 7.2(b). As the temperature drops below zero, the pavement freezes from the surface downwards and a phase change of water-to-ice takes place followed by volume expansion, Figure 7.2(c). The expanding ice crystals impose compressive stresses to the adjacent aggregates, Figure 7.2(d), causing thus the expansion of cracks and pores and eventually the deterioration of the pavement.

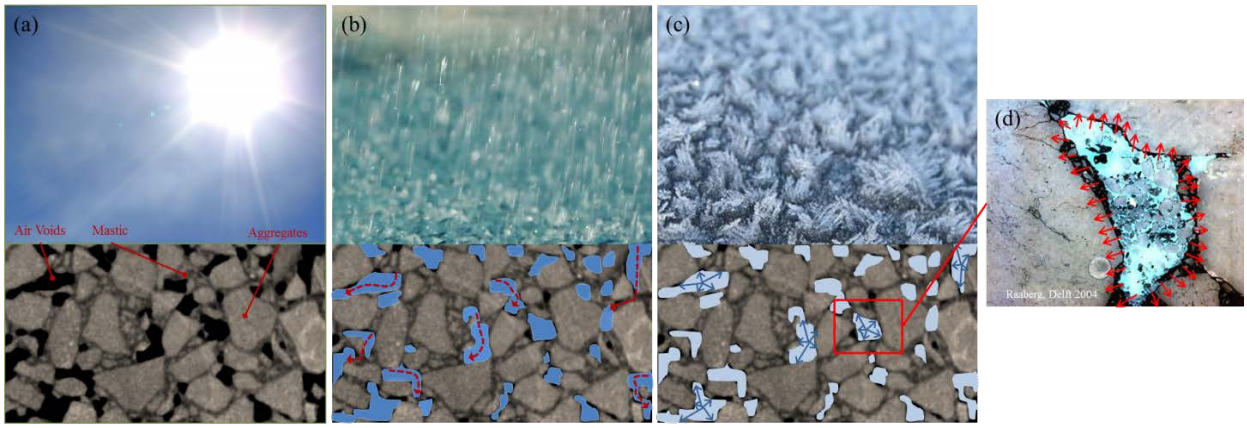

Figure 7.2 Frost damage: (a) mixture components, (b) moisture infiltration, (c) ice expansion, (d) developed stresses.

There are several models in literature that are used to simulate the freeze-thaw damage mechanisms for soils (Michalowski & Zhu 1993, Selvadurai et al. 1999, Fourie et al. 2007) and cement concrete (Bazant et al. 1988, Duan et al. 2013). For asphalt pavements, previous studies focused primarily on characterizing the degradation of mixture performance under the influence of freeze-thaw cycles (Feng et al. 2009, Wang et al. 2009, and Maudit et al. 2010).

7.2 Modelling frost damage in pavements

The computational scheme proposed for the simulation of frost damage combines a phase-change model capable of simulating the volume expansion of water upon freezing and a thermal diffusion model. To simulate binder damage the model presented in Chapter five is used. The new model is implemented in the CAPA-3D computational platform (Scarpas 2005).

7.2.1 Water-to-ice phase change model

This section describes an energy-based, large strain, three-dimensional model used for the simulation of the expansion of the ice crystals during the water-to-ice phase-change. As shown in Figure 7.3, the model consists of a hyperelastic spring that represents the mechanical stiffness of the ice crystal and a growth element which, when active, simulates the phase-change driven expansion ε_c. For a constrained total deformation case (i.e. $\varepsilon = \text{cnst}$), as ε_c in the growth component increases due to phase-change, the hyperelastic spring is compressed and hence it exerts compressive stresses in the surrounding.

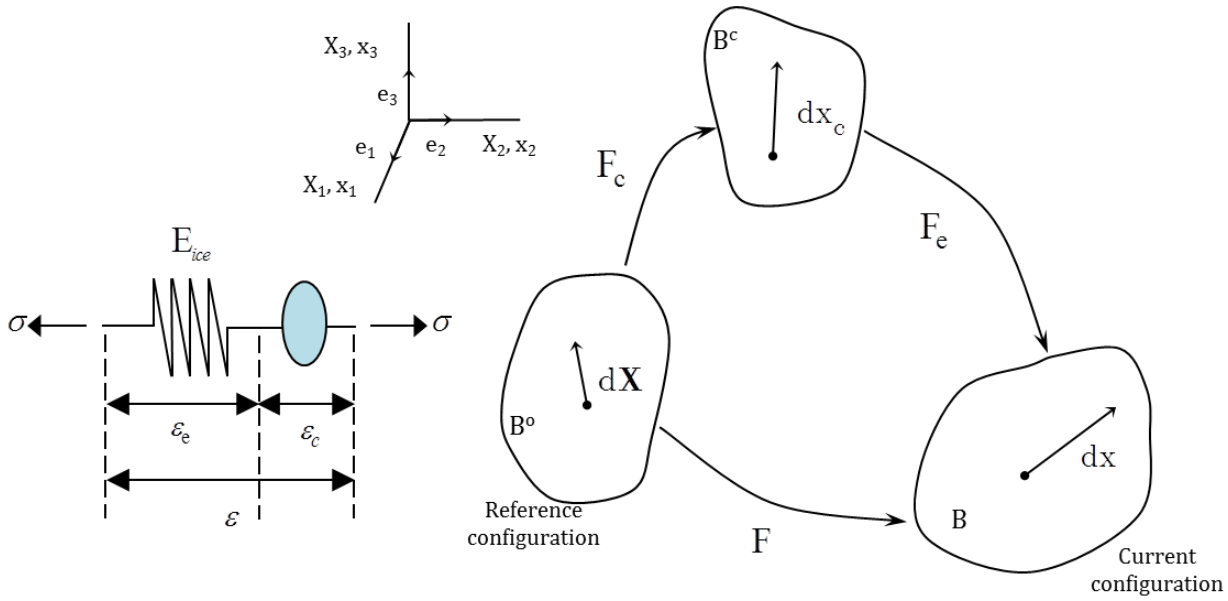

Figure 7.3 Schematic of the phase-change material model.

To formulate the phase-change model, the multiplicative decomposition of the deformation gradient tensor is applied. In this way, the relevant processes that occur during the water-to-ice phase change can be taken into consideration. The following multiplicative decomposition of the total deformation gradient tensor *F* is proposed and the intermediate configuration B^c is introduced, Figure 7.3.

$$F = F_e F_c \qquad [7.1]$$

, where F is the total deformation gradient, F_c is the deformation gradient for the 'ice expansion' component and F_e is the elastic deformation gradient.

The material undergoes a phase transformation from B^o to the intermediate configuration B^c, which is mapped by the deformation gradient F_c. The intermediate configuration is obtained from the current configuration by elastic un-stressing to zero stress state. The equation describing the evolution of the water-to-ice phase change driven expansion is postulated as

$$\frac{\partial \xi}{\partial t} = \frac{1}{t_c}(1-\xi) \qquad [7.2]$$

, where ξ denotes the expansion in time and t_c denotes the characteristic time of the phenomenon. Assuming that the initial condition $\xi|_{t=0} = 0$ holds, the expansion of the ice crystal in time is defined as

$$\xi = 1 - \exp\left(\frac{t}{t_c}\right) \qquad [7.3]$$

Then, the evolution equation of expansion, as stated in Eq. [7.3] is incorporated into the deformation gradient tensor related to the 'ice expansion' component as

$$\mathbf{F}_c = (1 + k\xi)\mathbf{I} \qquad [7.4]$$

, where k is the maximum expansion and $\mathbf{I}$ the second order identity tensor. Substituting Eq. [7.3] into Eq. [7.1] an expression for the elastic deformation tensor is obtained as

$$\mathbf{F}_e = \mathbf{F}\mathbf{F}_c^{-1} = \frac{\mathbf{F}}{1 + k\xi} \qquad [7.5]$$

With regard to the reference configuration, the right Cauchy-Green strain tensors for the hyperelastic and the growth component are described by

$$\mathbf{C}_c = \mathbf{F}_c^{\mathrm{T}}\mathbf{F}_c \qquad [7.6]$$

$$\mathbf{C}_e = \mathbf{F}_e^{\mathrm{T}}\mathbf{F}_e \qquad [7.7]$$

For a purely mechanical case, the Clausius-Planck dissipation inequality defines the dissipation of energy D as

$$D = \mathbf{P} : \dot{\mathbf{F}} - \dot{\Psi} \geq 0 \qquad [7.8]$$

, where $\mathbf{P}$ is the first Piola-Kirchhoff stress, $\dot{\Psi}$ is the time derivative of the Helmholtz strain energy function. For the proposed model the Helmholtz free energy can defined as

$$\Psi = \Psi_c(\xi) + \Psi_e(\mathbf{C}_e) \qquad [7.9]$$

, in which Ψ_c is the strain energy function of the swelling component, Ψ_e is the strain energy function for the hyperelastic spring. Substituting Eq. [7.9] into the dissipation inequality results to

$$D = \mathbf{P} : \dot{\mathbf{F}} - \frac{\partial \Psi_e}{\partial \mathbf{C}_e} : \dot{\mathbf{C}}_e - \frac{\partial \Psi_c}{\partial \xi} \cdot \dot{\xi} \geq 0 \qquad [7.10]$$

Similar to what described in paragraph 5.2.2, the first Piola-Kirchhoff stress tensor and the complementary dissipation inequality can be obtained as

$$\mathbf{P} = 2\mathbf{F}_e \frac{\partial \Psi}{\partial \mathbf{C}_e}\mathbf{F}_c^{-\mathrm{T}} \qquad \text{and} \qquad 2\mathbf{C}_e \frac{\partial \Psi}{\partial \mathbf{C}_e} : \mathbf{L}_c + \frac{\partial \Psi_c}{\partial \xi} \cdot \dot{\xi} \geq 0 \qquad [7.11]$$

, where $\mathbf{L}_c = \dot{\mathbf{F}}_c\mathbf{F}_c^{-1}$ is the velocity gradient. After defining the Mandel stress tensor for the hyperelastic component

$$\Sigma_e = \mathbf{C}_e\mathbf{S}_e = 2\mathbf{C}_e \frac{\partial \Psi}{\partial \mathbf{C}_e} \qquad [7.12]$$

Eq. [7.11][2] becomes

$$\Sigma_e : L_c + \frac{\partial \Psi_c}{\partial \xi} \cdot \dot{\xi} \geq 0 \qquad [7.13]$$

To comply with the 2nd law of thermodynamics it should hold that

$$\Sigma_e : L_c \geq 0 \qquad [7.14]$$

$$\frac{\partial \Psi_c}{\partial \xi} \frac{\partial \xi}{\partial t} \geq 0 \qquad [7.15]$$

, where the following form for the velocity gradient of the ice component is defined

$$L_c = \dot{F}_c F_c^{-1} = \frac{\kappa t_c (1-\xi)}{1+\kappa\xi} I = c\, I, \quad c \geq 0 \qquad [7.16]$$

Substitution of Eq. [7.16] into Eq. [7.14] gives

$$\left.\begin{array}{l} \Sigma_e : c\, I \geq 0 \\ d\, tr(\Sigma_e) \geq 0 \end{array}\right\} \Rightarrow c = tr(\Sigma_e) \qquad [7.17]$$

If c is chosen like this, Eq. [7.14] evaluates to $\Sigma_e : L_c = \Sigma_e : (tr\Sigma_e) I = tr\Sigma_e (\Sigma_e : I) = (tr(\Sigma_e))^2 \geq 0$, which is always bigger than zero. By combining Eq. [7.16] and Eq. [7.17] the Mandel stress can be directly expressed as a function of the parameters ξ, κ and t_c.

$$tr(\Sigma_e) = \frac{\kappa t_c (1-\xi)}{1+\kappa\xi} \qquad [7.18]$$

7.2.2 Thermal conduction model

The governing partial differential equations for thermal conduction are similar to those of moisture diffusion as described in Chapter two. Thermal conduction is governed by the following equation

$$q = -k \nabla T \qquad [7.19]$$

, where q is the heat flux vector (W/m^2), k is the thermal conductivity (W/m·^{o}C) and T is the temperature (^{o}C) at a point within the medium. Equation [7.19] is similar to Equation [2.5] which describes the steady-state flux of moisture per unit area. By combining Fourier's law for the conduction of heat Equation [7.19] and the law for conservation of energy, assuming a constant thermal conductivity k, one can obtain the heat conduction equation

$$\frac{\partial T}{\partial t} = \alpha \nabla^2 T \qquad [7.20]$$

, where ∇^2 is the Laplace operator in three dimensional rectangular Cartesian coordinates and α is the thermal diffusivity (m^2/s) of the material. Thermal diffusivity can be further expressed as

$$\alpha = \frac{k}{\rho C_s} \quad [7.21]$$

, where ρ is the mass density (kg/m^3) and C_s is the specific heat capacity of the conductive medium (J/kg·^{o}C). A comparison between Equation [7.20] and Equation [2.8] reveals that there exists a direct analogy between the two equations. However, similar to the assumption of uniform diffusivity for Equation [2.8], this analogy is valid only for homogeneous materials. For anisotropic materials, another analogy should be considered. The conduction model was implemented in the CAPA-3D finite element software (Scarpas 2005).

7.2.3 Asphalt binder model

To simulate the damage in the binder due to the pressure induced by ice expansion the elasto-visco-plastic model with softening due to coupled moisture-mechanical damage described in Chapter five was used. The model was implemented in such way that the user can select to activate one or both damage modes for an analysis. This study considers damage to be only the result of the mechanical action of the expanding ice crystals.

7.3 Geometry and FE mesh generation

Two different geometries, those of a porous (PA) and a dense (SMA) mixture, were studied. The samples were scanned and FE meshes were made by means of Simpleware® software (Simpleware 2011) following the procedure described in Chapter six.

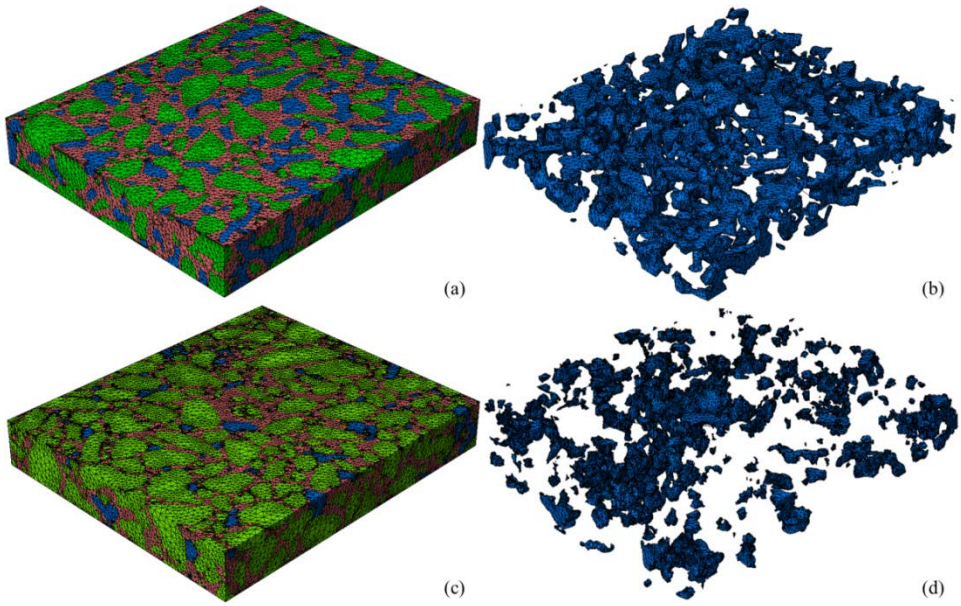

Figure 7.4 Volume renderings of the (a) porous and (c) dense mixtures. Figures (b) and (d) illustrate the corresponding air voids network.

For the spatial discretization of the meshes, three-dimensional linear four-node tetrahedral elements were used. Specifically, the PA and the SMA meshes consist of 412,304 and 1,286,806 elements, respectively. Figure 7.4 shows the volume renderings of the FE meshes.

7.4 Frost damage simulations

The computational scheme as described in paragraph 7.2 was used to study the mechanical degradation of the samples as a result of the phase-driven volume expansion of water in the macro pores.

7.4.1 Boundary conditions and input parameters

The following boundary conditions were imposed on the FE mesh: Displacement constrains were specified for the bottom and side surfaces of the samples, as shown in Figure 7.5. During the analysis, the top surface of the samples was exposed to a constant temperature T = -2°C to simulate top-down freezing. For all other surfaces, adiabatic thermal flow conditions were specified. In the beginning of the analysis, the samples were assumed to have a temperature of 10°C.

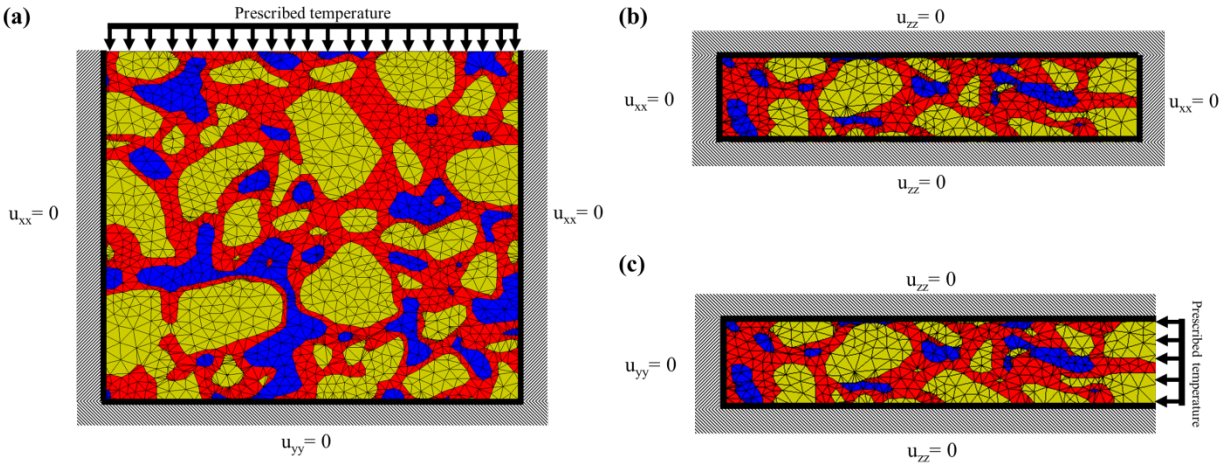

Figure 7.5 Specified boundary conditions in (a) X-Y, (b) X-Z and (c) Y-Z planes.

The parameters required for modelling thermal conduction are the volumetric heat capacity and thermal conductivity. For the analysis, the thermal parameters differed for every material phase i.e. aggregates (ag), asphalt binder (ab), air voids (av). The thermal conductivity for each phase was selected as k^{ag}=0.576, k^{ab}=0.6173 and k^{av}=0.09 (J/mm·hr·°C). Similarly the volumetric heat capacity ρC_s was selected as $\rho C_s{}^{ag}$=2.024x10^{-3}, $\rho C_s{}^{ab}$=2.275x10^{-3}, and $\rho C_s{}^{av}$=1.189x10^{-6}, (J/mm^3·°C). The materials properties were kept constant for both mixtures. For the ice material, the elastic modulus and the Poisson's ratio were selected as 9.0GPa and 0.31 (at 0 °C), respectively. The mechanical model parameters for the viscoelastic binder and the hyperelastic aggregates were the same as in Chapter six (paragraph 6.4.1.).

7.4.2 Modelling frost damage

Damage due to freeze-thaw depends, among others, on the degree of saturation of the voids with liquid water (Maudit et al. 2010). This analysis simulates the utmost case where all accessible voids are fully saturated with water. Figure 7.6(a) and Figure 7.6(c) show the meshes for the porous and dense sample in their undamaged condition, i.e. before freezing; for both meshes, yellow colours denotes the aggregates, red colour the asphalt binder and the air voids are shown in blue color. Similarly, Figure 7.6(b) and Figure 7.6(d) illustrate the damage distribution due to the action of the expanding ice crystals for the porous and the dense mixture, respectively.

The results show that damage accumulates in those areas of the binder located around the macro pores of the mixtures. It is observed that damage is higher for the porous than for the dense mixture. This finding is fairly obvious because porous mixtures have a high air voids content and interconnectivity that allow more water to enter the structure and hence the mixture becomes more susceptible to frost damage.

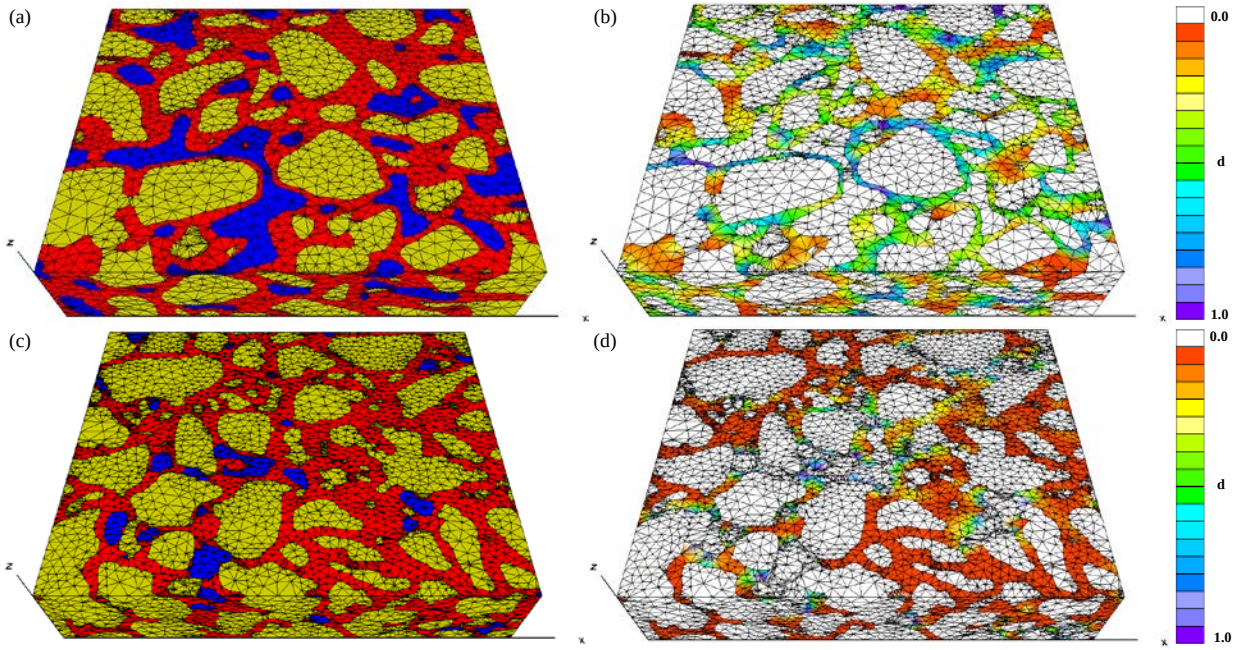

Figure 7.6 Three-phase finite element mesh and damage distribution due to water expansion in the porous (a-b) and the dense (c-d) mixture.

Figure 7.7 and Figure 7.8 show the expansion of the samples in the vertical direction as a result of water expansion in the pores upon freezing. The black horizontal line indicates the height of the samples in their initial undamaged configuration.

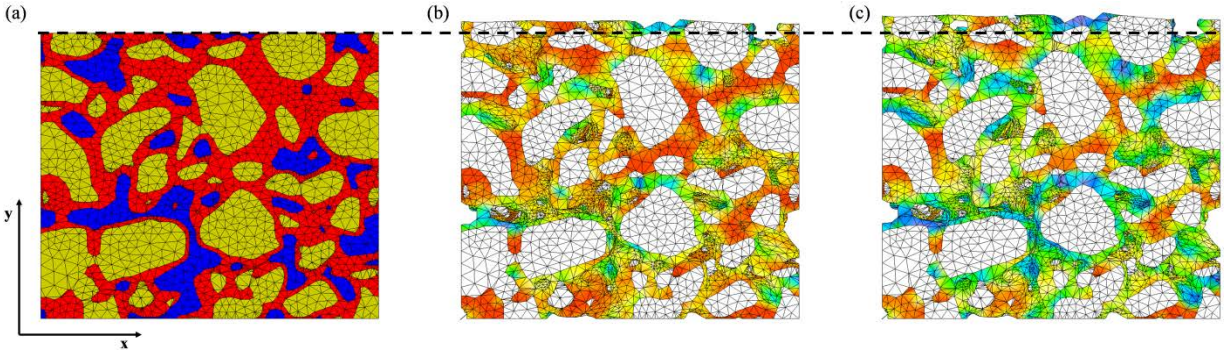

Figure 7.7 (a) Initial undamaged configuration. Displacement in vertical direction after (b) three and (c) five hours of freezing for the porous mixture.

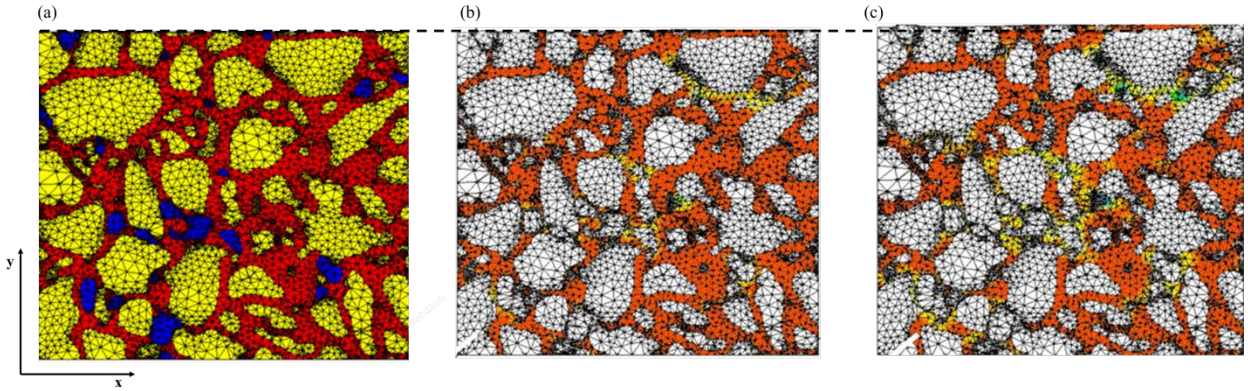

Figure 7.8 (a) Initial undamaged configuration. Displacement in vertical direction after (b) three and (c) five hours of freezing for the dense mixture.

Damage develops in the binder as the phase-change process takes places and until the volumetric expansion reaches the maximum value of 9% water-to-ice volume expansion. The displacement of the top surface of the samples is not uniform. It is expected that the highest displacement will occur in those areas where the air voids content is high and the pores are filled with water. In the field, this can occur in areas that are clogged and water collects in the pores of the pavement. Then, at freezing temperatures, these locations can be shifted upwards as a result of ice expansion.

In Figure 7.9, the average displacement u_{yy} of the top surface is plotted against the compressive reaction forces developed in the horizontal boundary of the samples. The u_{yy} values at any given time correspond to the average shift of all nodes, in the vertical direction, for the aggregate and binder material phases.

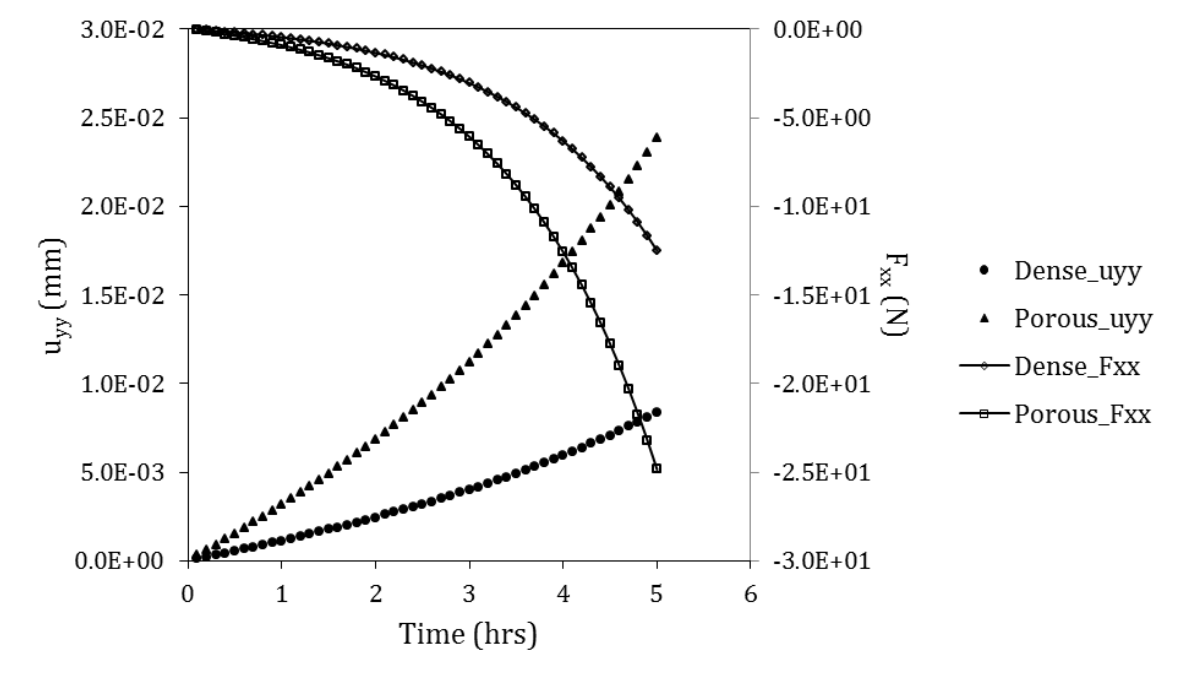

Figure 7.9 Influence of phase-change driven volume expansion on the mixtures.

7.5 Summary

The aim of this study was to develop a computational scheme to simulate damage due to freeze-thaw cycles. This scheme involves (i) formulation of a model that simulates the volume expansion of water during its phase-change from liquid to solid at freezing conditions, (ii) formulation of a thermal conduction model to simulate the temperature distribution in the pavement, and finally (iii) utilization of the elasto-visco-plastic model with softening, described in Chapter five, for calculating stresses in the pavement structure and modelling binder damage due to the additional stresses as a result of water expansion upon freezing. The model makes it, in principle, feasible to determine critical areas with a propensity to cracking on the basis of the stresses in the asphalt pavement. The model was used to investigate the influence of mixtures characteristics on frost damage susceptibility. The analysis considered the utmost case where the pores of the pavement are fully saturated with water. The results showed that damage is developed in the areas around the pores of the samples. The intensity of damage and the expansion of the sample upon freezing were higher for the porous than for the dense sample, suggesting thus that porous mixtures may be more sensitive to freeze-thaw damage due to their geometry. It is necessary to calibrate the model by carrying out tests, which would have to include application of monotonic and freeze-thaw cycles on samples with various types of asphalt mixtures and freezing rates.

7.6 References

Bazant, Z.P., Chern, J.C., Rosenberg, A.M. and Gaidis, J.M. (1988). Mathematical model for freeze-thaw durability of concrete. *Journal of the American Ceramic Society*, 71:9, 776-783.

Duan, A., Chen, J. and Jin, W. (2013). Numerical simulation of the freezing process of concrete. *Journal of Materials in Civil Engineering*, 25:9, 1317-1325.

Feng, D., Yi, J., Wang, L. and Wang, D. (2009). Impact of gradation types on freeze-thaw performance of asphalt mixtures in seasonal frozen region. 9th International Conference of Chinese Transportation Professionals (ICCTP), Harbin, China, 1-7.

Fourie, W.J., Barnes, D.L. and Shur, Y. (2007). The formation of ice from infiltration of water into a frozen coarse grained soil. *Cold Regions Science and Technology*, 48, 118-128.

Maudit, C., Hammoum, F., Piau, J.M., Maudit, V., Ludwig, S. and Hamon, D. (2010). Quantifying expansion effects induced by freeze-thaw cycles in partially water saturated bituminous mix. *Road Materials and Pavement Design*, 11:1, 443-457.

Michalowski, R.L. and Zhu, M. (1993). A constitutive model of saturated soils for frost heave simulations. *Cold Regions Science and Technology*, 22, 47-63.

Scarpas, A. (2005). *CAPA-3D: A mechanics based computational platform for pavement engineering.* PhD dissertation. Delft University of Technology, Netherlands.

Selvadurai, A.P.S., Hu, J. and Konuk, I. (1999). Computational modelling of frost heave induced soil-pipeline interaction I. Modelling frost heave. *Cold Regions Science and Technology*, 29, 215-228.

Simpleware (2011), ScanIP, +ScanFE.

Wang, D., Yi, J. and Feng, D. (2009). Impact of freeze-thaw cycles on the performance of asphalt mixture based permeability. Advanced Testing and Characterization of Bituminous Materials, Rhodes, Greece, 205-213.

8

Conclusions and recommendations

"Every new beginning comes from other beginnings end."
— Lucius Annaeus Seneca (ca. 4 BC-65 AD)

Chapter 8 summarizes the findings of this dissertation and highlights the main conclusions and insights gained by this research. Moreover, recommendations are made for the continuation of this research topic and for implementation by practitioners.

8.1 Conclusions

The incentives for this research thesis were the practical problems related to the use of porous asphalt pavements: (i) the reduced durability of porous asphalt pavements compared to dense asphalt pavements and (ii) the need for regular maintenance works due to the deterioration of the pavement surface as a result of ravelling. Both problems can be reduced to the moisture-induced damage problem, which is considered as a key degradation mechanism in porous pavements, together with oxidative ageing. The focus of this thesis was to broaden the knowledge of moisture damage sensitivity of asphalt mixtures, with a view to developing a set of tools and methodologies that can be used to optimize the design of durable bituminous composites.

Damage due to moisture diffusion can be considered as a multiscale phenomenon. Moisture diffusion within the constituents of asphalt mixtures causes a reduction in their stiffness and strength (material level). This leads to the overall degradation of the composite material (mixture level) compromising the durability and loading capacity of pavement structures (structure level). Through the literature review process of previous studies, the main parameters that influence moisture diffusion were identified and their importance to the evolution of the physical process was discussed. It can be concluded that the estimation of moisture content in a pavement is no trivial task mainly because it is essentially the result of interplay among the physicochemical properties of the constituents, the mixture microstructure, and the environmental conditions. For that reason, an algorithm was developed to simulate three-dimensional moisture diffusion in asphalt mixtures. The model especially contributes to enhance our understanding of the relationship between the mixture structure and composition and its macroscopic behaviour with respect to moisture sensitivity.

The effect of prolonged moisture diffusion on the cohesion properties of asphalt mortar was studied by means of uniaxial tension tests. A new data analysis procedure was proposed with the aim of obtaining a more accurate calculation of fracture energy. The procedure uses nonlinear finite element analysis to specify the unloading response outside the fracture zone, and then utilizes this information to compute the fracture energy of the material. This methodology yields a framework for the calculation of fracture energy provided that only force-displacement data are available and therefore the estimation of the true stress-strain curve is not feasible.

Through the experimental investigation, it was established that moisture has detrimental consequences on the fracture properties of asphalt mortars, especially with respect to their low temperature characteristics. At intermediate temperatures, moisture resulted in softening of the mortars as suggested by the observed reduction in strength and increase in fracture energy after prolonged bath conditioning. At low temperatures, however, the unfavorable effect of moisture was more pronounced. The strength and fracture energy of the mortars reduced significantly, indicating that moisture increases the propensity to low temperature cracking. The use of additives such as hydrated lime filler and SBS modifiers improved the fracture properties of the moisture conditioned mortar samples. Particularly, at low temperatures, the use of SBS modified bitumen was found to have a favorable influence on the wet response of the mortar, possibly due to the overall increase in their elasticity caused by the addition of the SBS modifiers.

The moisture uptake measurements confirmed that depending on the chemical composition of the mortar, the moisture absorption and desorption rates in addition to the maximum moisture

uptake can vary substantially among dissimilar mortar types. However, the amount of moisture that is present in the mortar was found to control the intensity of moisture damage, mainly at the intermediate testing temperature. At low temperature, though, such relation could not be established; it is likely that other phenomena dominate at these temperatures.

The reversibility of the fracture properties of asphalt mortar was not supported from the findings of this study. At intermediate temperature, after the application of a drying cycle, the strength of the desiccated mortar samples was higher than their dry strength; nevertheless a reduction (or no change) in their fracture energy was observed. Also, the low temperature properties were not restored upon drying; on the contrary, the mortars exhibited particularly poor fracture properties. Hence, these findings demonstrated that damage due to moisture diffusion causes embrittlement of the mortars and suggest that the continuous wet and drying cycles, which bituminous mixtures experience in the field, may have a fatigue-like effect that can result in materials with inferior performance characteristics.

The effect of freeze-thaw cycles on the fracture properties was observed to depend on the conditioning state (dry or wet) of the mortars and vary significantly with testing temperature. Overall, the application of freeze-thaw cycles was observed to deteriorate the low temperature properties of the mortar samples, suggesting thus higher susceptibility to low temperature cracking. Interestingly, at intermediate temperature, an increase in strength and fracture energy of the dry mortars was observed, indicating that thermal cycles may have a positive effect on the properties of the mortar at this temperature. When tested at wet conditions though, a reduction in cohesive strength was observed for all mortar types. The combination of moisture and thermal conditioning was found to have a softening effect for the SBS modified mortars, as their fracture energy increased; in contrast, the unmodified mortars demonstrated a substantial decrease in their fracture energy.

At mixture level, apart from damage induced by moisture diffusion, other moisture damage mechanisms such as pumping action may take place depending on the mixture type, traffic loading and environmental conditions. X-ray computed tomography and image analysis demonstrated that pore pressure induces additional internal stresses that can lead to cracking of mortar or widening of existing cracks, thus increasing the air void content and causing an overall degradation of the material. Hence, a moisture conditioning protocol that combines the two main moisture-induced damage mechanisms was proposed for evaluating moisture susceptibility of asphalt mixtures. The experimental results revealed the major influence of conditioning method (i.e. bath conditioning and pore pressure application) and conditioning time on the degradation of mixture strength. The two damage inducing mechanisms were found to be relatively independent from each other. It may, therefore, be that an asphalt mixture is more prone to one damage mode than the other. However, in specific cases, the duration of the bath conditioning phase was found to increase the extent of damage due to pore pressures. Longer conditioning times resulted in higher strength reduction for the same number of pore pressure cycles. These findings support the importance of including the short-term damage process when considering moisture damage in asphalt pavements.

It has been discussed that moisture damage depends on the properties of the constituent materials and on the morphology of asphalt mixtures. Therefore, it is essential to deepen the understanding of the way the spatial distribution and physicochemical properties of the individual

material phases, as well as the interplay among the phases, dictate the mechanical response of the composite material in moist conditions. To this end, an energy-based elasto-visco-plastic model with softening was proposed to model damage due to the coupled effects of moisture diffusion and mechanical loading. The model introduces material damage as an internal variable, which represents the dissipative (irreversible) processes within the microstructure of the material. It consists of a generalized Maxwell model, with hyperelastic springs and viscous time-dependent components, in series with an inelastic component driven by coupled moisture-mechanical damage.

The model was used in a computational scheme to study the influence of air voids content and interconnectivity on moisture sensitivity. The analysis was performed using a staggered approach: first the moisture diffusion model, presented in Chapter two, was used to obtain the moisture profiles within the asphalt samples and then the elasto-visco-plastic model was used to quantify binder damage due to moisture diffusion. The results of the diffusion analysis demonstrated that the amount of moisture present in a mixture is strongly dependent on its morphology and that the interconnectivity of the air voids network controls the rate of damage development. The mechanical analysis revealed the positive effect of using mortars with high resistivity against moisture and quantified the benefits that would arise due to this choice, especially when designing porous mixtures that have an intrinsic sensitivity to moisture damage due to their morphological characteristics. The availability of the model is expected to constitute a tool for the design of mixtures with optimized moisture susceptibility properties and allow for the addition of new materials and mix designs to be investigated. Moreover, such a model can provide physical insight into the dependability of composite behaviour on material microstructures.

The influence of freeze-thaw cycles on asphalt binders was discussed earlier. Nevertheless, the observed degradation of the mechanical properties of the binders, which results to the overall degradation of the pavement, commonly occurs gradually during the lifetime of the pavement. The sudden manifestation of frost damage that has been observed to occur in the field can be mainly attributed to the freezing of water that is accumulated in the pores of the pavement. At sub-zero temperatures the water freezes and expands causing additional stresses to the pavement structure. Driven by these observations, a computational scheme to simulate frost damage was proposed. This scheme involves the formulation of a model that simulates the volume expansion of water during the water-to-ice phase-change at freezing conditions, the formulation of a thermal conduction model to simulate temperature distribution in the pavement, and finally the utilization of the elasto-visco-plastic model to determine critical areas with a susceptibility to cracking on the basis of the stresses in the pavement. This computational scheme can serve as a base for future studies on the effect of the various parameters, such as the degree of pore saturation, material properties, and mixture morphology on frost damage susceptibility.

This thesis contributes to our understanding of the fundamental moisture damage processes and establishes a relationship between the physico-mechanical properties of the constituent materials and mixture morphology and the moisture susceptibility of the pavement structure. In addition, the tools, i.e. experimental methods and computational models, developed in this research could be used to help the optimization of mixture design in relation to moisture damage and the engineering of asphalt binders with enhanced durability.

8.2 Recommendations

The susceptibility of a mixture to moisture damage is governed by several parameters such as the physicochemical properties of bitumen and aggregates and their interaction, the mixture morphology, the environmental conditions, the type of traffic loading and the quality control during construction. The variability of the aforementioned parameters introduces a high level of complexity to the problem and causes additional difficulties in mitigating moisture induced damage in asphalt pavements. In the following, recommendations are made for the continuation of this research on the basis of the obtained results. Moreover, general guidelines and suggestions are given for practitioners.

Recommendations for future research

In this research, the effects of moisture and freeze-thaw cycles on asphalt mortar were evaluated by means of monotonic uniaxial tests. In reality, however, pavement failure normally occurs due to the repetitive action of loads with lower magnitude. It would therefore be interesting to evaluate the effects of moisture on the fatigue performance of asphalt mortars using cyclic tests. Moreover, the findings of this study demonstrated the irreversibility of the fracture properties of the mortars upon drying. It is suggested that a more extended experimental program is undertaken to investigate the impact of continuous wet-drying cycles on the performance of bituminous mixtures.

More broadly, given that the changes in the mechanical response of mortars due to moisture essentially take place as a result of the alteration of their chemical and rheological properties, it is suggested that further research should focus on obtaining greater insight into the chemo-mechanic processes of moisture damage. In this way, a turn into more fundamental theories can be accomplished, which would contribute to engineer binders with enhanced performance characteristics.

Considering that the main degradation mechanisms related to the durability of asphalt pavements is moisture damage and oxidative ageing, and that these processes occur in a relevant time frame, it is suggested that the diffusion model is expanded to a coupled moisture-oxygen diffusion model. Damage evolution functions similar to those defined for moisture damage can be then introduced and implemented in the elasto-visco-plastic model for the degradation of material properties due to oxidative ageing. Moreover, future research should investigate the impact of ageing on the diffusivity properties, and therefore the moisture susceptibility characteristics of asphalt mortars. The resulting observations should then be incorporated into the aforementioned models.

Further research should also focus on developing a model for the simulation of water flow through asphalt pavements. Along these lines, the magnitude of stresses developed in the undrained case due to pumping action and the erosion of the binder due to flow-induced stresses in the pavement structure can be determined.

Recommendations for practitioners

A key parameter in preventing moisture damage of asphalt mixtures is the careful selection of individual mixture components. Based on the findings of this research, it has been established that the diffusivity properties of the constituents of an asphalt mixture dictate its moisture sensitivity characteristics. Moreover, nowadays, the use of unconventional materials like rubber, fibers, polyurethane resins, epoxy, and other additives, either as a supplement or replacement for conventional materials has gained a lot of interest. The use of these materials aims to increase the strength and impart desirable characteristics to a mixture such as noise reduction, improved rutting resistance, production of mixtures at lower temperature etc. Nevertheless, the introduction of these materials necessitates an understanding of their diffusivity characteristics and mechanical properties at moist conditions, so that the desirable characteristics are attained without compromising the durability of the pavement.

Therefore, it is recommended that the determination of moisture diffusion coefficients should become part of the standard practice. To this end, the pavement engineering community should focus on the development of easily implementable testing protocols, similar to those available for mechanical asphalt tests, which designate the test conditions, sample preparation and provide the analytical tools to determine the physical properties related to moisture. This information can serve as a screening tool for the selection of aggregates, asphalt binders, mineral fillers as well as additives with inherent resistivity against moisture and enable the development of mix designs with improved characteristics against moisture damage. Especially for porous mixtures, which are significantly affected by moisture damage, constituent materials with enhanced properties should be further considered.

As soon as this information becomes available, one can use the proposed computational tools to investigate the influence of both specific material combinations as well as the addition of new materials on mixture performance and moisture damage susceptibility, thus reducing the risk of failure. Moreover, these models can be used as computational platforms where simulations of laboratory tests can be performed that will provide useful insights and practical recommendations to the pavement community. For example, the diffusion model, presented in Chapter two, can be used to gain a better insight into the conditioning times required for full saturation of various mixture types. In this way, extremely short or long conditioning periods can be avoided when setting up testing protocols and specifications for the evaluation of moisture damage susceptibility.

Furthermore, based on the results of this study the main moisture-induced damage mechanisms were found to be relatively independent from each other, indicating that an asphalt mixture may be more prone to one damage mode than the other. It is, therefore, recommended to include the pumping action mechanism into the current specifications for moisture damage susceptibility. Disregarding the pore pressure mechanism, might lead to erroneous conclusions when evaluating mixtures for their susceptibility to moisture damage.

Appendix A

Clausius-Planck inequality

The Clausius-Planck inequality for the elasto-visco-plastic with softening model is defined as

$$D = P : \dot{F} - \sum_{i=1}^{m} \frac{\partial \Psi_v^i}{\partial C_e^i} : \dot{C}_e^i - \frac{\partial \Psi_\infty}{\partial C_\infty} : \dot{C}_\infty - \frac{\partial \Psi_\infty}{\partial d} \cdot \dot{d} \geq 0 \qquad [A.1]$$

, where D denotes the internal dissipation energy, $P : \dot{F}$ represents the work conjugate pair (or rate of internal mechanical work per unit reference volume), P is the first Piola-Kirchhoff stress, Ψ_v^i is the strain-energy function related to the spring in the ith viscoelastic Maxwell component, Ψ_∞ is the strain-energy function related to the single elastic spring, $\dot{C}_\infty$ and $\dot{C}_e^i$ are the time derivatives of the elastic right Cauchy deformation tensor for the single spring and of the elastic right Cauchy deformation tensor for the ith Maxwell component, respectively, and *d* is the damage function.

The time derivatives of the Cauchy-Green deformation tensors C_∞ and C_e^i are defined as

$$\dot{C}_\infty = \frac{d}{dt}\left(F_\infty^T F_\infty\right) = -F_d^{-T}\dot{F}_d^T F_d^{-T} F^T F_\infty + F_d^{-T}\dot{F}^T F_\infty + F_\infty^T \dot{F} F_d^{-1} - F_\infty^T F F_d^{-1}\dot{F}_d F_d^{-1} \qquad [A.2]$$

$$\dot{C}_e^i = \frac{d}{dt}\left(\left(F_e^i\right)^T F_e^i\right) = -\left(\bar{L}_v^i\right)^T \left(F_v^i\right)^{-T} C_\infty \left(F_v^i\right)^{-1} + \left(F_v^i\right)^{-T} \dot{C}_\infty \left(F_v^i\right)^{-1} - \left(F_v^i\right)^{-T} C_\infty \left(F_v^i\right)^{-1} \bar{L}_v^i$$

$$\text{for every } i = 1...m \qquad [A.3]$$

, where $\overline{L}_v^i = \dot{F}_v^i \left(F_v^i\right)^{-1}$ and $\left(\overline{L}_v^i\right)^T = -\left(F_v^i\right)^{-T}\left(\dot{F}_v^i\right)^T$. By substituting these time derivatives into the contraction terms of Equation [A.1] and using the tensor identity $A:BC = B^TA:C = AC^T:B$ gives

$$\begin{aligned}
\frac{\partial \Psi_v^i}{\partial C_e^i}:\dot{C}_e^i &= \frac{\partial \Psi_v^i}{\partial C_e^i}:\left(-\left(\overline{L}_v^i\right)^T\left(F_v^i\right)^{-T}C_\infty\left(F_v^i\right)^{-1}+\left(F_v^i\right)^{-T}\dot{C}_\infty\left(F_v^i\right)^{-1}-\left(F_v^i\right)^{-T}C_\infty\left(F_v^i\right)^{-1}\overline{L}_v^i\right)= \\
&= -\frac{\partial \Psi_v^i}{\partial C_e^i}:\left(\overline{L}_v^i\right)^T\left(\left(F_v^i\right)^{-T}C_\infty\left(F_v^i\right)^{-1}\right)+\frac{\partial \Psi_v^i}{\partial C_e^i}:\left(F_v^i\right)^{-T}\dot{C}_\infty\left(F_v^i\right)^{-1}-\frac{\partial \Psi_v^i}{\partial C_e^i}:\left(\left(F_v^i\right)^{-T}C_\infty\left(F_v^i\right)^{-1}\right)\overline{L}_v^i= \\
&= -\frac{\partial \Psi_v^i}{\partial C_e^i}\left(\left(F_v^i\right)^{-T}C_\infty\left(F_v^i\right)^{-1}\right)^T:\left(\overline{L}_v^i\right)^T+\left(F_v^i\right)^{-1}\frac{\partial \Psi_v^i}{\partial C_e^i}\left(F_v^i\right)^{-T}:\dot{C}_\infty-\left(\left(F_v^i\right)^{-T}C_\infty\left(F_v^i\right)^{-1}\right)^T\frac{\partial \Psi_v^i}{\partial C_e^i}:\overline{L}_v^i= \\
&= -\frac{\partial \Psi_v^i}{\partial C_e^i}\left(F_v^i\right)^{-T}C_\infty\left(F_v^i\right)^{-1}:\left(\overline{L}_v^i\right)^T+\left(F_v^i\right)^{-1}\frac{\partial \Psi_v^i}{\partial C_e^i}\left(F_v^i\right)^{-T}:\dot{C}_\infty-\left(F_v^i\right)^{-T}C_\infty\left(F_v^i\right)^{-1}\frac{\partial \Psi_v^i}{\partial C_e^i}:\overline{L}_v^i= \\
&= \left(F_v^i\right)^{-1}\frac{\partial \Psi_v^i}{\partial C_e^i}\left(F_v^i\right)^{-T}:\dot{C}_\infty-2\left(F_v^i\right)^{-T}C_\infty\left(F_v^i\right)^{-1}\frac{\partial \Psi_v^i}{\partial C_e^i}:\overline{L}_v^i \qquad \text{for every } i=1...m
\end{aligned} \tag{A.4}$$

$$\begin{aligned}
\frac{\partial \Psi_\infty}{\partial C_\infty}:\dot{C}_\infty &= \frac{\partial \Psi_\infty}{\partial C_\infty}:\left(-F_d^{-T}\dot{F}_d^TF_d^{-T}F^TF_\infty+F_d^{-T}\dot{F}^TF_\infty+F_\infty^T\dot{F}F_d^{-1}-F_\infty^TFF_d^{-1}\dot{F}_dF_d^{-1}\right)= \\
&= -\frac{\partial \Psi_\infty}{\partial C_\infty}:F_d^{-T}\dot{F}_d^TF_d^{-T}F^TF_\infty+\frac{\partial \Psi_\infty}{\partial C_\infty}:F_d^{-T}\dot{F}^TF_\infty+\frac{\partial \Psi_\infty}{\partial C_\infty}:F_\infty^T\dot{F}F_d^{-1}-\frac{\partial \Psi_\infty}{\partial C_\infty}:F_\infty^TFF_d^{-1}\dot{F}_dF_d^{-1}= \\
&= -\frac{\partial \Psi_\infty}{\partial C_\infty}:\overline{L}_d^TF_\infty^TF_\infty+\frac{\partial \Psi_\infty}{\partial C_\infty}:F_d^{-T}\dot{F}^TF_\infty+\frac{\partial \Psi_\infty}{\partial C_\infty}:F_\infty^T\dot{F}F_d^{-1}-\frac{\partial \Psi_\infty}{\partial C_\infty}:F_\infty^TF_\infty\overline{L}_d= \\
&= -\frac{\partial \Psi_\infty}{\partial C_\infty}:\overline{L}_d^TC_\infty+\frac{\partial \Psi_\infty}{\partial C_\infty}:F_d^{-T}\dot{F}^TF_\infty+\frac{\partial \Psi_\infty}{\partial C_\infty}:F_\infty^T\dot{F}F_d^{-1}-\frac{\partial \Psi_\infty}{\partial C_\infty}:C_\infty\overline{L}_d= \\
&= -\frac{\partial \Psi_\infty}{\partial C_\infty}C_\infty:\overline{L}_d^T+F_d^{-1}\frac{\partial \Psi_\infty}{\partial C_\infty}F_\infty^T:\dot{F}^T+\frac{\partial \Psi_\infty}{\partial C_\infty}F_d^{-T}:F_\infty^T\dot{F}-C_\infty\frac{\partial \Psi_\infty}{\partial C_\infty}:\overline{L}_d= \\
&= -C_\infty\frac{\partial \Psi_\infty}{\partial C_\infty}:\overline{L}_d+F_\infty\frac{\partial \Psi_\infty}{\partial C_\infty}F_d^{-T}:\dot{F}+F_\infty\frac{\partial \Psi_\infty}{\partial C_\infty}F_d^{-T}:\dot{F}-C_\infty\frac{\partial \Psi_\infty}{\partial C_\infty}:\overline{L}_d= \\
&= 2F_\infty\frac{\partial \Psi_\infty}{\partial C_\infty}F_d^{-T}:\dot{F}-2C_\infty\frac{\partial \Psi_\infty}{\partial C_\infty}:\overline{L}_d
\end{aligned} \tag{A.5}$$

With the above expressions the dissipation inequality, Equation [A.1], can be rewritten as

$$D = P : \dot{F} - \left(\sum_{i=1}^{m} \left(\left(F_v^i \right)^{-1} \frac{\partial \Psi_v^i}{\partial C_e^i} \left(F_v^i \right)^{-T} : \dot{C}_\infty - 2 \left(F_v^i \right)^{-T} C_\infty \left(F_v^i \right)^{-1} \frac{\partial \Psi_v^i}{\partial C_e^i} : \bar{L}_v^i \right) + \frac{\partial \Psi_\infty}{\partial C_\infty} : \dot{C}_\infty + \frac{\partial \Psi_\infty}{\partial d} \cdot \dot{d} \right) =$$

$$= P : \dot{F} - \left[\left(\frac{\partial \Psi_\infty}{\partial C_\infty} + \sum_{i=1}^{m} \left(\left(F_v^i \right)^{-1} \frac{\partial \Psi_v^i}{\partial C_e^i} \left(F_v^i \right)^{-T} \right) \right) : \dot{C}_\infty - \sum_{i=1}^{m} \left(2 \left(F_v^i \right)^{-T} C_\infty \left(F_v^i \right)^{-1} \frac{\partial \Psi_v^i}{\partial C_e^i} : \bar{L}_v^i \right) + \frac{\partial \Psi_\infty}{\partial d} \cdot \dot{d} \right] =$$

$$= P : \dot{F} - 2F_\infty \left(\frac{\partial \Psi_\infty}{\partial C_\infty} + \sum_{i=1}^{m} \left(\left(F_v^i \right)^{-1} \frac{\partial \Psi_v^i}{\partial C_e^i} \left(F_v^i \right)^{-T} \right) \right) F_d^{-T} : \dot{F} + 2C_\infty \left(\frac{\partial \Psi_\infty}{\partial C_\infty} + \sum_{i=1}^{m} (\ ) \right) : \bar{L}_d +$$

$$+ \sum_{i=1}^{m} \left(2 \left(F_v^i \right)^{-T} C_\infty \left(F_v^i \right)^{-1} \frac{\partial \Psi_v^i}{\partial C_e^i} : \bar{L}_v^i \right) - \frac{\partial \Psi_\infty}{\partial d} \cdot \dot{d} \qquad \text{for every } i = 1...m$$

[A.6]

Finally, after rearrangement of terms, the following expression for the Clausius-Plank inequality is obtained

$$D = P : \dot{F} - \dot{\Psi} = \left(P - 2F_\infty \left(\frac{\partial \Psi_\infty}{\partial C_\infty} + \sum_{i=1}^{m} \left(\left(F_v^i \right)^{-1} \frac{\partial \Psi_v^i}{\partial C_e^i} \left(F_v^i \right)^{-T} \right) \right) F_d^{-T} \right) : \dot{F} +$$

$$+ 2C_\infty \left(\frac{\partial \Psi_\infty}{\partial C_\infty} + \sum_{i=1}^{m} \left(\left(F_v^i \right)^{-1} \frac{\partial \Psi_v^i}{\partial C_e^i} \left(F_v^i \right)^{-T} \right) \right) : \bar{L}_d + \qquad [A.7]$$

$$+ \sum_{i=1}^{m} \left(2 \left(F_v^i \right)^{-T} C_\infty \left(F_v^i \right)^{-1} \frac{\partial \Psi_v^i}{\partial C_e^i} : \bar{L}_v^i \right) - \frac{\partial \Psi_\infty}{\partial d} \cdot \dot{d} \geq 0$$

Appendix B

Reduced form of the first Piola-Kirchhoff stress tensor

The Clausius-Planck inequality for the proposed elasto-visco-plastic model with softening is written as

$$\begin{aligned} D = P : \dot{F} - \dot{\Psi} = & \left(P - 2F_{\infty} \left(\frac{\partial \Psi_{\infty}}{\partial C_{\infty}} + \sum_{i=1}^{m} \left(\left(F_v^i \right)^{-1} \frac{\partial \Psi_v^i}{\partial C_e^i} \left(F_v^i \right)^{-T} \right) \right) F_d^{-T} \right) : \dot{F} + \\ & + 2C_{\infty} \left(\frac{\partial \Psi_{\infty}}{\partial C_{\infty}} + \sum_{i=1}^{m} \left(\left(F_v^i \right)^{-1} \frac{\partial \Psi_v^i}{\partial C_e^i} \left(F_v^i \right)^{-T} \right) \right) : \bar{L}_d + \\ & + \sum_{i=1}^{m} \left(2 \left(F_v^i \right)^{-T} C_{\infty} \left(F_v^i \right)^{-1} \frac{\partial \Psi_v^i}{\partial C_e^i} : \bar{L}_v^i \right) - \frac{\partial \Psi_{\infty}}{\partial d} \cdot \dot{d} \geq 0 \end{aligned} \qquad [B.1]$$

Utilizing the standard thermodynamic arguments the first Piola-Kirchhoff tensor P is defined as

$$P = \left(2F_{\infty} \frac{\partial \Psi_{\infty}}{\partial C_{\infty}} + 2F_{\infty} \sum_{i=1}^{m} \left(\left(F_v^i \right)^{-1} \frac{\partial \Psi_v^i}{\partial C_e^i} \left(F_v^i \right)^{-T} \right) \right) F_d^{-T} \qquad [B.2]$$

Rearranging the terms and utilizing the fact that $F_d = F_{\infty}^{-1} F \Rightarrow F_d^{-T} = \left(F_{\infty}^{-1} F \right)^T$, the reduced form of the first Piola-Kirchhoff stress tensor P is obtained

$$
\begin{aligned}
P &= 2F_{\infty}\left(\frac{\partial \Psi_{\infty}}{\partial C_{\infty}} + \sum_{i=1}^{m}\left(\left(F_v^i\right)^{-1}\frac{\partial \Psi_v^i}{\partial C_e^i}\left(F_v^i\right)^{-T}\right)\right)F_d^{-T} = \\
&= 2F_{\infty}\left(\frac{\partial \Psi_{\infty}}{\partial C_{\infty}} + \sum_{i=1}^{m}\left(\left(F_v^i\right)^{-1}\frac{\partial \Psi_v^i}{\partial C_e^i}\left(F_v^i\right)^{-T}\right)\right)F_{\infty}^{-T}F^{-T} = \\
&= \left(2F_{\infty}\frac{\partial \Psi_{\infty}}{\partial C_{\infty}}F_{\infty}^{T} + \sum_{i=1}^{m}\left(2F_{\infty}\left(F_v^i\right)^{-1}\frac{\partial \Psi_v^i}{\partial C_e^i}\left(F_v^i\right)^{-T}F_{\infty}^{T}\right)\right)F^{-T} = \\
&= \left(2F_{\infty}\frac{\partial \Psi_{\infty}}{\partial C_{\infty}}F_{\infty}^{T} + \sum_{i=1}^{m}\left(2F_e^i\frac{\partial \Psi_v^i}{\partial C_e^i}\left(F_e^i\right)^{T}\right)\right)F^{-T} = \\
&= \left[F_{\infty}\left(2\frac{\partial \Psi_{\infty}}{\partial C_{\infty}}\right)F_{\infty}^{T} + \sum_{i=1}^{m}\left(F_e^i\left(2\frac{\partial \Psi_v^i}{\partial C_e^i}\right)\left(F_e^i\right)^{T}\right)\right]F^{-T}
\end{aligned}
\qquad [B.3]
$$

, or, after defining the second Piola-Kirchhoff stress tensor as

$$S = 2\frac{\partial \Psi}{\partial C} \qquad [B.4]$$

, and the Kirchhoff stress tensor as

$$\tau = FSF^{T} \qquad [B.5]$$

the inequality expressed by Equation [B.3] becomes

$$
\begin{aligned}
P &= \left[F_{\infty}\left(2\frac{\partial \Psi_{\infty}}{\partial C_{\infty}}\right)F_{\infty}^{T} + \sum_{i=1}^{m}\left(F_e^i\left(2\frac{\partial \Psi_v^i}{\partial C_e^i}\right)\left(F_e^i\right)^{T}\right)\right]F^{-T} = \\
&= \left[F_{\infty}S_{\infty}F_{\infty}^{T} + \sum_{i=1}^{m}\left(F_e^iS_e^i\left(F_e^i\right)^{T}\right)\right]F^{-T} = \\
&= \left[\tau_{\infty} + \sum_{i=1}^{m}\tau_e^i\right]F^{-T} = \tau F^{-T}
\end{aligned}
\qquad [B.6]
$$

, where S_{∞} is the second Piola-Kirchhoff stress tensor related to the single spring, S_e is the second Piola-Kirchhoff stress tensor related to the spring of the viscoelastic Maxwell components, and τ_{∞}, τ_e and τ are the elastic, viscous and total Kirchhoff stress tensors.

Appendix C

Reduced form of the Clausius-Planck inequality

The complementary inequality to the Clausius-Planck equation is postulated as

$$2C_\infty\left(\frac{\partial\Psi_\infty}{\partial C_\infty}+\sum_{i=1}^{m}\left(F_v^i\right)^{-1}\frac{\partial\Psi_v^i}{\partial C_e^i}\left(F_v^i\right)^{-T}\right):\dot{F}_d F_d^{-1}+\sum_{i=1}^{m}2\left(F_v^i\right)^{-T}C_\infty\frac{\partial\Psi_v^i}{\partial C_e^i}:\dot{F}_v^i\left(F_v^i\right)^{-1}-\frac{\partial\Psi_\infty}{\partial d}\cdot\dot{d}\geq 0 \qquad [C.1]$$

Rearranging the terms and utilizing the fact that $\bar{L}_v^i=\dot{F}_v^i\left(F_v^i\right)^{-1}$ and $\bar{L}_d=\dot{F}_d F_d^{-1}$, Equation [C.1] is expressed as

$$\begin{aligned}&2C_\infty\left(\frac{\partial\Psi_\infty}{\partial C_\infty}+\sum_{i=1}^{m}\left(F_v^i\right)^{-1}\frac{\partial\Psi_v^i}{\partial C_e^i}\left(F_v^i\right)^{-T}\right):\bar{L}_d+\sum_{i=1}^{m}2\left(F_v^i\right)^{-T}C_\infty\frac{\partial\Psi_v^i}{\partial C_e^i}:\bar{L}_v^i-\frac{\partial\Psi_\infty}{\partial d}\cdot\dot{d}=\\&C_\infty\left[2\frac{\partial\Psi_\infty}{\partial C_\infty}+\sum_{i=1}^{m}\left(F_v^i\right)^{-1}\left(2\frac{\partial\Psi_v^i}{\partial C_e^i}\right)\left(F_v^i\right)^{-T}\right]:\bar{L}_d+\sum_{i=1}^{m}\left(\left(\left(F_v^i\right)^{-T}F_\infty^T F_\infty\left(F_v^i\right)^{-1}\left(2\frac{\partial\Psi_v^i}{\partial C_e^i}\right)\right):\bar{L}_v^i\right)-\frac{\partial\Psi_\infty}{\partial d}\cdot\dot{d}\geq 0\end{aligned} \qquad [C.2]$$

After defining the second Piola-Kirchhoff stress tensor as

$$S=2\frac{\partial\Psi}{\partial C} \qquad [C.3]$$

, the inequality as shown in Equation [C.2] becomes

$$C_\infty\left[S_\infty+\sum_{i=1}^{m}\left(\left(F_v^i\right)^{-1}S_e^i\left(F_v^i\right)^{-T}\right)\right]:\bar{L}_d+\sum_{i=1}^{m}\left(\left(\left(F_v^i\right)^{-T}F_\infty^T F_\infty\left(F_v^i\right)^{-1}S_e^i\right):\bar{L}_v^i\right)-\frac{\partial\Psi_\infty}{\partial d}\cdot\dot{d}\geq 0 \qquad [C.4]$$

Finally, after defining the Mandel stress tensor as

$$\Sigma = 2C\frac{\partial \Psi}{\partial C} = CS \qquad [C.5]$$

, the reduced form of the inequality is obtained as

$$\begin{aligned}
&C_\infty\left[S_\infty + \sum_{i=1}^{m}\left(\left(F_v^i\right)^{-1} S_e^i \left(F_v^i\right)^{-T}\right)\right]:\bar{L}_d + \sum_{i=1}^{m}\left(\left(\left(F_v^i\right)^{-T} F_\infty^T F_\infty \left(F_v^i\right)^{-1} S_e^i\right):\bar{L}_v^i\right) - \frac{\partial \Psi_\infty}{\partial d}\cdot \dot{d} = \\
&= C_\infty\left[S_\infty + \sum_{i=1}^{m} S_{ve}^i\right]:\bar{L}_d + \sum_{i=1}^{m}\left(\left(\left(F_e^i\right)^T F_e^i S_e^i\right):\bar{L}_v^i\right) - \frac{\partial \Psi_\infty}{\partial d}\cdot \dot{d} = \\
&= \left(C_\infty S_\infty + C_\infty \sum_{i=1}^{m} S_{ve}^i\right):\bar{L}_d + \sum_{i=1}^{m}\left(C_e^i S_e^i : \bar{L}_v^i\right) - \frac{\partial \Psi_\infty}{\partial d}\cdot \dot{d} = \\
&= \left(\Sigma_\infty + \sum_{i=1}^{m} \Sigma_e^i\right):\bar{L}_d + \sum_{i=1}^{m}\left(\Sigma_e^i : \bar{L}_v^i\right) - \frac{\partial \Psi_\infty}{\partial d}\cdot \dot{d} = \\
&= \Sigma_d : \bar{L}_d + \sum_{i=1}^{m}\left(\Sigma_e^i : \bar{L}_v^i\right) - \frac{\partial \Psi_\infty}{\partial d}\cdot \dot{d} \geq 0
\end{aligned} \qquad [C.6]$$

, or alternatively

$$\Sigma_d : \bar{L}_d + \sum_{i=1}^{m}\left(\Sigma_e^i : \bar{L}_v^i\right) - q\cdot \dot{d} \geq 0 \quad , \quad q = \frac{\partial \Psi_\infty}{\partial d} \qquad [C.7]$$

, where Σ_e^i is the Mandel stress tensor of the ith viscoelastic Maxwell component and Σ_d is the Mandel stress tensor of the damage component, q is the stress component due to damage and $\bar{L}_v^i$ and $\bar{L}_d$ are the corresponding viscous and damage velocity gradients defined in the intermediate configurations.

Appendix D

Newton-Raphson iterative scheme

An iterative Newton-Raphson procedure is employed to minimize the set of residual equations, shown in Eq. [D.1], solving simultaneously for F_∞, F_e^i and $\Delta\mu$. Initially F_∞ gets a trial value based on the previous converged time step, and $\Delta\mu = 0$.

$$\begin{bmatrix} \frac{\partial R_{F_\infty}}{\partial F_\infty} & \frac{\partial R_{F_\infty}}{\partial F_e^1} & \cdots & \frac{\partial R_{F_\infty}}{\partial F_e^m} & \frac{\partial R_{F_\infty}}{\partial \Delta\mu} \\ \frac{\partial R_{F_e}^1}{\partial F_\infty} & \frac{\partial R_{F_e}^1}{\partial F_e^1} & \cdots & \frac{\partial R_{F_e}^1}{\partial F_e^m} & \frac{\partial R_{F_e}^1}{\partial \Delta\mu} \\ \vdots & \vdots & & \vdots & \vdots \\ \frac{\partial R_{F_e}^m}{\partial F_\infty} & \frac{\partial R_{F_e}^m}{\partial F_e^1} & \cdots & \frac{\partial R_{F_e}^m}{\partial F_e^m} & \frac{\partial R_{F_e}^m}{\partial \Delta\mu} \\ \frac{\partial R_d}{\partial F_\infty} & \frac{\partial R_d}{\partial F_e^1} & \cdots & \frac{\partial R_d}{\partial F_e^m} & \frac{\partial R_d}{\partial \Delta\mu} \end{bmatrix} \begin{bmatrix} \Delta F_\infty \\ \Delta F_e^1 \\ \vdots \\ \Delta F_e^m \\ \Delta\Delta\mu \end{bmatrix} = - \begin{bmatrix} R_{F_\infty} \\ R_{F_e}^1 \\ \vdots \\ R_{F_e}^m \\ R_d \end{bmatrix} \qquad [D.1]$$

The analytical expressions for the individual derivatives are presented in the following.

(A) Computation of terms $\frac{\partial R_{F_\infty}}{\partial F_\infty}$, $\frac{\partial R_{F_\infty}}{\partial F_e}$, $\frac{\partial R_{F_\infty}}{\partial \Delta\mu}$

The residual equation for the undamaged elastic deformation tensor F_∞ is defined as

$$R_{F_\infty} = {}^{t+\Delta t}F_\infty - {}^{t+\Delta t}_{trial}F_\infty \exp^{t+\Delta t}\left(-\Delta\mu\frac{\partial g(\Sigma_d, q)}{\partial \Sigma_d}\right) \quad [D.2]$$

, or in index notation, where for sake of notation simplification, the superscript t+Δt is omitted,

$$R_{F_\infty} = \left(F_\infty\right)_{ij} - {}_{trial}\left(F_\infty\right)_{ik} \exp\left(-\Delta\mu\frac{\partial g(\Sigma_d, q)}{\partial \Sigma_d}\right)_{kj} \quad [D.3]$$

The derivative of this with respect to $\left(F_\infty\right)_{mn}$ gives

$$\frac{\partial\left(R_{F_\infty}\right)_{ij}}{\partial\left(F_\infty\right)_{mn}} = \frac{\left(F_\infty\right)_{ij}}{\partial\left(F_\infty\right)_{mn}} - {}_{trial}\left(F_\infty\right)_{ik}\frac{\exp\left(-\Delta\mu\frac{\partial g(\Sigma_d, q)}{\partial \Sigma_d}\right)_{kj}}{\partial\left(F_\infty\right)_{mn}} = \quad [D.4]$$

$$= \delta_{im}\delta_{jn} - {}_{trial}\left(F_\infty\right)_{ik}\frac{\partial \exp\left(-\Delta\mu\frac{\partial g(\Sigma_d, q)}{\partial \Sigma_d}\right)_{kj}}{\partial\left(\Sigma_d\right)_{pq}}\frac{\partial\left(\Sigma_d\right)_{pq}}{\partial\left(F_\infty\right)_{mn}}$$

Similarly, the derivatives of R_{F_∞} with respect to $\left(F_e^i\right)_{mn}$ and $\Delta\mu$ give

$$\frac{\partial\left(R_{F_\infty}\right)_{ij}}{\partial\left(F_e^i\right)_{mn}} = -{}_{trial}\left(F_\infty\right)_{ik}\frac{\partial \exp\left(-\Delta\mu\frac{\partial g(\Sigma_d, q)}{\partial \Sigma_d}\right)_{kj}}{\partial\left(\Sigma_d\right)_{pq}}\frac{\partial\left(\Sigma_d\right)_{pq}}{\partial\left(F_e^i\right)_{mn}} \quad \text{for every } i = 1...m \quad [D.5]$$

$$\frac{\partial\left(R_{F_\infty}\right)_{ij}}{\partial\Delta\mu} = -{}_{trial}\left(F_\infty\right)_{ik}\frac{\partial \exp\left(-\Delta\mu\frac{\partial g(\Sigma_d, q)}{\partial \Sigma_d}\right)_{kj}}{\partial\Delta\mu} \quad [D.6]$$

The exponential terms in Eqs. [D.4], [D.5] and [D.6] are expanded by means of the Cayley-Hamilton theorem. According to the theorem, the exponential term of a tensor $\left(A\right)_{ij}$ can be written as

$$\exp\left(At\right)_{ij} = \alpha_2 t^2 A_{ik}A_{kj} + \alpha_1 t A_{ij} + \alpha_o I_{ij} \quad [D.7]$$

, where α_o, α_1 and α_2 are functions of *t* that are determined on the basis of A . Using this definition, the derivative of $\exp\left(At\right)_{ij}$ with respect to a tensor $\left(A\right)_{pq}$ can be defined as

$$\frac{\partial \exp(At)_{ij}}{\partial (A)_{pq}} = \alpha_2 t^2 \left(\frac{\partial A_{ik}}{\partial A_{pq}} A_{kj} + A_{ik} \frac{\partial A_{kj}}{\partial A_{pq}} \right) + \alpha_1 t \frac{\partial A_{ij}}{\partial A_{pq}} + \alpha_o \frac{\partial I_{ij}}{\partial A_{pq}} =$$
$$= \alpha_2 t^2 \left(\delta_{ip}\delta_{kq} A_{kj} + A_{ik}\delta_{kp}\delta_{jq} \right) + \alpha_1 t \delta_{ip}\delta_{jq} = \quad [D.8]$$
$$= \alpha_2 t^2 \left(\delta_{ip} A_{qj} + A_{ip}\delta_{jq} \right) + \alpha_1 t \delta_{ip}\delta_{jq}$$

, where δ_{ij} is the Kronecker delta defined as $\delta_{ij} = \begin{cases} 0, & \text{if } i \neq j \\ 1, & \text{if } i = j \end{cases}$.

Also, the derivative of $\exp(At)_{ij}$ with respect to a scalar quantity z is

$$\frac{\partial \exp(At)_{ij}}{\partial z} = \alpha_2 t^2 \left(\frac{\partial A_{iq}}{\partial z} A_{qj} + A_{ip} \frac{\partial A_{pj}}{\partial z} \right) + \alpha_1 t \frac{\partial A_{ij}}{\partial z} \quad [D.9]$$

Therefore the derivative of the exponential term, in Eqs. [D.4] and [D.5], with respect to $(\Sigma_d)_{pq}$ can be written as

$$\frac{\partial \exp\left(-\Delta\mu \frac{\partial g(\Sigma_d, q)}{\partial \Sigma_d} \right)_{kj}}{\partial (\Sigma_d)_{pq}} = \frac{\partial \exp\left(-\Delta\mu \frac{\partial g(\Sigma_d, q)}{\partial \Sigma_d} \right)_{kj}}{\partial \left(-\Delta\mu \frac{\partial g(\Sigma_d, q)}{\partial \Sigma_d} \right)_{rs}} \frac{\partial \left(-\Delta\mu \frac{\partial g(\Sigma_d, q)}{\partial \Sigma_d} \right)_{rs}}{\partial (\Sigma_d)_{pq}} \quad [D.10]$$

Furthermore, the terms $\frac{\partial (\Sigma_d)_{pq}}{\partial (F_\infty)_{mn}}$ and $\frac{\partial (\Sigma_d)_{pq}}{\partial (F_e)_{mn}}$ have to be defined. By definition it holds that

$$\Sigma_d = \Sigma_\infty + \sum_{i=1}^{m} \Sigma_{ve}^i = C_\infty S_\infty + \sum_{i=1}^{m} C_\infty \left(F_v^i \right)^{-1} S_e^i \left(F_v^i \right)^{-T} =$$
$$= C_\infty S_\infty + \sum_{i=1}^{m} C_\infty \left(\left(F_e^i \right)^{-1} F_\infty \right)^{-1} S_e^i \left(\left(F_e^i \right)^{-1} F_\infty \right)^{-T} =$$
$$= C_\infty S_\infty + \sum_{i=1}^{m} F_\infty^T F_\infty F_\infty^{-1} F_e^i S_e^i \left(F_e^i \right)^T F_\infty^{-T} =$$
$$= C_\infty S_\infty + \sum_{i=1}^{m} F_\infty^T F_e^i S_e^i \left(F_e^i \right)^T F_\infty^{-T} = \quad \text{multiplying by } \left(F_e^i \right)^{-T} \left(F_e^i \right)^T \quad [D.11]$$
$$= \Sigma_\infty + \sum_{i=1}^{m} F_\infty^T \left(F_e^i \right)^{-T} \left(F_e^i \right)^T F_e^i S_e^i \left(F_e^i \right)^T F_\infty^{-T} =$$
$$= \Sigma_\infty + \sum_{i=1}^{m} \left(\left(F_e^i \right)^{-1} F_\infty \right)^T \Sigma_e^i \left(F_\infty^{-1} F_e^i \right)^T$$

,or, in index notation,

$$\left(\Sigma_d\right)_{ij} = \left(\Sigma_\infty\right)_{ij} + \sum_{i=1}^{m}\left(\left(\left(F_e^i\right)^{-1}F_\infty\right)_{ki}\left(\Sigma_e^i\right)_{kl}\left(F_\infty^{-1}F_e^i\right)_{jl}\right) \qquad [D.12]$$

Then the term $\frac{\partial\left(\Sigma_d\right)_{pq}}{\partial\left(F_\infty\right)_{mn}}$ can be expressed as

$$\begin{aligned}
\frac{\partial\left(\Sigma_d\right)_{pq}}{\partial\left(F_\infty\right)_{mn}} &= \frac{\partial\left(\Sigma_\infty\right)_{pq}}{\partial\left(F_\infty\right)_{mn}} + \sum_{i=1}^{m}\left(\left(F_e^i\right)^{-1}\right)_{kr}\frac{\partial\left(F_\infty\right)_{rp}}{\partial\left(F_\infty\right)_{mn}}\left(\Sigma_e^i\right)_{kl}\left(F_\infty^{-1}F_e^i\right)_{ql} + \sum_{i=1}^{m}\left(\left(F_e^i\right)^{-1}F_\infty\right)_{kp}\left(\Sigma_e^i\right)_{kl}\frac{\partial\left(F_\infty^{-1}\right)_{qr}}{\partial\left(F_\infty\right)_{mn}}\left(F_e^i\right)_{rl} = \\
&= \frac{\partial\left(\Sigma_\infty\right)_{pq}}{\partial\left(F_\infty\right)_{mn}} + \sum_{i=1}^{m}\left(\left(F_e^i\right)^{-1}\right)_{kr}\delta_{rm}\delta_{pn}\left(\Sigma_e^i\right)_{kl}\left(F_\infty^{-1}F_e^i\right)_{ql} - \sum_{i=1}^{m}\left(\left(F_e^i\right)^{-1}F_\infty\right)_{kp}\left(\Sigma_e^i\right)_{kl}\left(F_\infty^{-1}\right)_{qm}\left(F_\infty^{-1}\right)_{nr}\left(F_e^i\right)_{rl} = \\
&= \frac{\partial\left(\Sigma_\infty\right)_{pq}}{\partial\left(F_\infty\right)_{mn}} + \sum_{i=1}^{m}\left(\left(F_e^i\right)^{-1}\right)_{km}\left(\Sigma_e^i\right)_{kl}\left(F_\infty^{-1}F_e^i\right)_{ql}\delta_{pn} - \sum_{i=1}^{m}\left(\left(F_e^i\right)^{-1}F_\infty\right)_{kp}\left(\Sigma_e^i\right)_{kl}\left(F_e^i\right)_{rl}\left(F_\infty^{-1}\right)_{nr}\left(F_\infty^{-1}\right)_{qm} = \\
&= \frac{\partial\left(\Sigma_\infty\right)_{pq}}{\partial\left(F_\infty\right)_{mn}} + \sum_{i=1}^{m}\left(\left(F_e^i\right)^{-T}\Sigma_e^i\left(F_e^i\right)^{T}F_\infty^{-T}\right)_{mq}\delta_{pn} - \sum_{i=1}^{m}\left(F_\infty^{T}\left(F_e^i\right)^{-T}\Sigma_e^i\left(F_e^i\right)^{T}F_\infty^{-T}\right)_{pn}\left(F_\infty^{-T}\right)_{mq} = \\
&= \frac{\partial\left(\Sigma_\infty\right)_{pq}}{\partial\left(F_\infty\right)_{mn}} + \sum_{i=1}^{m}\left(F_\infty^{-T}\left(F_e^i\right)^{-T}\Sigma_e^i\left(F_e^i\right)^{T}F_\infty^{-T}\right)_{mq}\delta_{pn} - \sum_{i=1}^{m}\left(F_\infty^{-T}\right)_{mq}\left(F_\infty^{T}\left(F_e^i\right)^{-T}\Sigma_e^i\left(F_e^i\right)^{T}F_\infty^{-T}\right)_{pn} = \\
&= \frac{\partial\left(\Sigma_\infty\right)_{pq}}{\partial\left(F_\infty\right)_{mn}} + \sum_{i=1}^{m}\left(F_\infty^{-T}\Sigma_{ve}^i\right)_{mq}\delta_{pn} - \sum_{i=1}^{m}\left(F_\infty^{-1}\right)_{qm}\left(\Sigma_{ve}^i\right)_{pn}
\end{aligned} \qquad [D.13]$$

, where $\Sigma_{ve}^i = \left(\left(F_e^i\right)^{-1}F_\infty\right)^{-1}S_e^i\left(\left(F_e^i\right)^{-1}F_\infty\right)^{-T}$, as results from Eq. [D.8].

Similarly, the term $\frac{\partial\left(\Sigma_d\right)_{pq}}{\partial\left(F_e^i\right)_{mn}}$ can be obtained as

$$\begin{aligned}
\frac{\partial\left(\Sigma_d\right)_{pq}}{\partial\left(F_e^i\right)_{mn}} = &-\left(\left(F_e^i\right)^{-1}F_\infty\right)_{np}\left(\left(\Sigma_{ve}^i\right)^{T}F_\infty^{-1}\right)_{qm} + \left(\left(F_e^i\right)^{-1}F_\infty\right)_{pk}\frac{\partial\left(\Sigma_e^i\right)_{kl}}{\partial\left(F_e^i\right)_{mn}}\left(F_\infty^{-1}F_e^i\right)_{lq} \\
&+\left(\left(\left(F_e^i\right)^{-1}F_\infty\right)\left(\Sigma_{ve}^i\right)^{T}\right)_{np}\left(F_\infty^{-1}\right)_{qm} \qquad \text{for every } i = 1...m
\end{aligned} \qquad [D.14]$$

Lastly, the derivative $\frac{\partial(\Sigma_\infty)_{pq}}{\partial(F_\infty)_{mn}}$, in Eq. [D.13], is calculated. Using the Neo-Hookean formulation for the strain energy function Ψ_∞ of the hyperelastic spring is defined as

$$\Psi_\infty = \frac{\mu_\infty}{2}\left[I_1 - 3 + \frac{1}{\alpha_\infty}\left(I_3^{-\alpha_\infty} - 1 \right) \right] \quad [D.15]$$

, where $\alpha_\infty = \frac{\lambda_\infty}{2\mu_\infty}$, λ_∞ and μ_∞ denote the Lamé parameters, $I_1 = \mathrm{tr}(C_\infty)$ and $I_3 = \det(C_\infty)$ is the first and third invariant of the right Cauchy-Green deformation tensor C_∞. After defining the second Piola-Kirchhoff stress tensor S_∞

$$\begin{aligned} S_\infty &= 2\frac{\partial \Psi_\infty}{\partial (C_\infty)_{ij}} = \\ &= 2\frac{\mu_\infty}{2}\left(\frac{\partial I_1}{\partial C_\infty} - \frac{\alpha_\infty}{\alpha_\infty} I_3^{-\alpha_\infty - 1}\frac{\partial I_3}{\partial C_\infty} \right) = \\ &= \mu_\infty \left(I - I_3^{-\alpha_\infty - 1}\frac{\partial I_3}{\partial C_\infty} \right) = \\ &= \mu_\infty \left(I - I_3^{-\alpha_\infty - 1} I_3 C_\infty^{-1} \right) = \\ &= \mu_\infty \left(I - I_3^{-\alpha_\infty} C_\infty^{-1} \right) \end{aligned} \quad [D.16]$$

, where I is the identity tensor. Then the Mandel stress tensor can be calculated as

$$\begin{aligned} \Sigma_\infty &= C_\infty S_\infty = \mu_\infty C_\infty \left(I - I_3^{-\alpha_\infty} C_\infty^{-1} \right) \\ &= \mu_\infty \left(C_\infty - I_3^{-\alpha_\infty} I \right) \end{aligned} \quad [D.17]$$

Finally, the derivative $\frac{\partial(\Sigma_\infty)_{pq}}{\partial(F_\infty)_{mn}}$ is expressed, on the basis of Eq. [D.17] as

$$\frac{\partial\left(\Sigma_{\infty}\right)_{ij}}{\partial\left(F_{\infty}\right)_{mn}}=\frac{\partial\left(\Sigma_{\infty}\right)_{ij}}{\partial\left(C_{\infty}\right)_{pq}}\frac{\partial\left(C_{\infty}\right)_{pq}}{\partial\left(F_{\infty}\right)_{mn}}=$$

$$=\mu_{\infty}\left[\frac{\partial\left(C_{\infty}\right)_{ij}}{\partial\left(C_{\infty}\right)_{pq}}+\alpha_{\infty}I_3^{-\alpha_{\infty}-1}I_3\left(C_{\infty}^{-1}\right)_{pq}\delta_{ij}\right]\frac{\partial\left(C_{\infty}\right)_{pq}}{\partial\left(F_{\infty}\right)_{mn}}=$$

$$=\mu_{\infty}\left[\delta_{ip}\delta_{jq}+\alpha_{\infty}I_3^{-\alpha_{\infty}}\delta_{ij}\left(C_{\infty}^{-1}\right)_{pq}\right]\left[\frac{\partial\left(\left(F_{\infty}\right)_{pr}^{T}\left(F_{\infty}\right)_{rq}\right)}{\partial\left(F_{\infty}\right)_{mn}}\right]=$$

$$=\mu_{\infty}\left[\delta_{ip}\delta_{jq}+\alpha_{\infty}I_3^{-\alpha_{\infty}}\delta_{ij}\left(C_{\infty}^{-1}\right)_{pq}\right]\left[\delta_{rm}\delta_{pn}\left(F_{\infty}\right)_{rq}+\left(F_{\infty}\right)_{rp}\delta_{rm}\delta_{qn}\right]= \qquad [D.18]$$

$$=\mu_{\infty}\delta_{rm}\delta_{pn}\left(F_{\infty}\right)_{rq}\left(\delta_{ip}\delta_{jq}+\alpha_{\infty}I_3^{-\alpha_{\infty}}\delta_{ij}\left(C_{\infty}^{-1}\right)_{pq}\right)+$$

$$+\mu_{\infty}\left(F_{\infty}\right)_{rp}\delta_{rm}\delta_{qn}\left(\delta_{ip}\delta_{jq}+\alpha_{\infty}I_3^{-\alpha_{\infty}}\delta_{ij}\left(C_{\infty}^{-1}\right)_{pq}\right)=$$

$$=\mu_{\infty}\left(F_{\infty}\right)_{mj}\delta_{in}+\mu_{\infty}\left(F_{\infty}\right)_{mi}\delta_{jn}+2\mu_{\infty}\alpha_{\infty}I_3^{-\alpha_{\infty}}\left(F_{\infty}^{-1}\right)_{nm}\delta_{ij}$$

Similarly, the derivative $\frac{\partial\left(\Sigma_e^i\right)_{pq}}{\partial\left(F_e^i\right)_{mn}}$ is written as

$$\frac{\partial\left(\Sigma_e^i\right)_{ij}}{\partial\left(F_e^i\right)_{mn}}=\mu_e\left(F_e^i\right)_{mj}\delta_{in}+\mu_{\infty}\left(F_e^i\right)_{mi}\delta_{jn}+2\mu_e\alpha_e I_3^{-\alpha_{\infty}}\left(\left(F_e^i\right)^{-1}\right)_{nm}\delta_{ij}\qquad \text{for every } i=1...m \qquad [D.19]$$

Hence, summarizing the above, Eq. [D.4], Eq. [D.5] and Eq. [D.6] are written as

$$\frac{\partial\left(R_{F_{\infty}}\right)_{ij}}{\partial\left(F_{\infty}\right)_{mn}}=\delta_{im}\delta_{jn}-{}_{\text{trial}}\left(F_{\infty}\right)_{ik}\frac{\partial\exp\left(-\Delta\mu\frac{\partial g(\Sigma_d,q)}{\partial\Sigma_d}\right)_{kj}}{\partial\left(-\Delta\mu\frac{\partial g(\Sigma_d,q)}{\partial\Sigma_d}\right)_{rs}}\frac{\partial\left(-\Delta\mu\frac{\partial g(\Sigma_d,q)}{\partial\Sigma_d}\right)_{rs}}{\partial\left(\Sigma_d\right)_{pq}}\left[\frac{\partial\left(\Sigma_{\infty}\right)_{pq}}{\partial\left(F_{\infty}\right)_{mn}}+\right. \qquad [D.20]$$

$$\left.+\left(F_{\infty}^{-T}\sum_{i=1}^{m}\Sigma_{ve}^{i}\right)_{mq}\delta_{in}-\left(F_{\infty}^{-1}\right)_{qm}\left(\sum_{i=1}^{m}\Sigma_{ve}^{i}\right)_{in}\right]$$

$$\frac{\partial\left(R_{F_{\infty}}\right)_{ij}}{\partial\left(F_e^i\right)_{mn}}=-{}_{\text{trial}}\left(F_{\infty}\right)_{ik}\frac{\partial\exp\left(-\Delta\mu\frac{\partial g(\Sigma_d,q)}{\partial\Sigma_d}\right)_{kj}}{\partial\left(-\Delta\mu\frac{\partial g(\Sigma_d,q)}{\partial\Sigma_d}\right)_{rs}}\frac{\partial\left(-\Delta\mu\frac{\partial g(\Sigma_d,q)}{\partial\Sigma_d}\right)_{rs}}{\partial\left(\Sigma_d\right)_{pq}}\frac{\partial\left(\Sigma_d\right)_{pq}}{\partial\left(F_e^i\right)_{mn}}\qquad \text{for every } i=1...m \qquad [D.21]$$

$$\frac{\partial\left(R_{F_\infty}\right)_{ij}}{\partial\Delta\mu} = -\,{}_{trial}\left(F_\infty\right)_{ik}\frac{\partial \exp\left(-\Delta\mu\frac{\partial g(\Sigma_d,q)}{\partial\Sigma_d}\right)_{kj}}{\partial\Delta\mu} \qquad [D.22]$$

(B) Computation of terms $\frac{\partial R_{F_e}}{\partial F_\infty}$, $\frac{\partial R_{F_e}}{\partial F_e}$, $\frac{\partial R_{F_e}}{\partial\Delta\mu}$

The residual equation for the elastic deformation tensor F_e^i of the i[th] viscoelastic component is defined as

$$\begin{aligned} R^i_{F_e} &= {}^{t+\Delta t}F_e^i - {}^{t+\Delta t}_{trial}F_e^i \exp^{t+\Delta t}\left(-\Delta t\ \left(C_v^i\right)^{-1} : \Sigma_e^i\right) = \\ &= \left({}^{t+\Delta t}F_\infty\ {}^{t}\left(F_v^i\right)^{-1}\right) - \left({}^{t+\Delta t}_{trial}F_\infty\ {}^{t}\left(F_v^i\right)^{-1}\right)\exp^{t+\Delta t}\left(-\Delta t\ \left(C_v^i\right)^{-1} : \Sigma_e^i\right) \quad \text{for every } i=1...m \end{aligned} \qquad [D.23]$$

, or in index notation

$$R^i_{F_e} = \left(F_e^i\right)_{ij} - {}_{trial}\left(F_\infty\right)_{ik}\left({}^{t}\left(F_v^i\right)^{-1}\right)_{kl}\exp\left(-\Delta t\ \left(C_v^i\right)^{-1} : \Sigma_e^i\right)_{lj} \quad \text{for every } i=1...m \qquad [D.24]$$

The derivative of $R^i_{F_e}$ with respect to $\left(F_\infty\right)_{mn}$ gives

$$\begin{aligned} \frac{\partial\left(R^i_{F_e}\right)_{ij}}{\partial\left(F_\infty\right)_{mn}} &= -\delta_{im}\delta_{kn}\left(\left(F_v^i\right)^{-1}\right)_{kl}\exp\left(-\Delta t\ \left(C_v^i\right)^{-1} : \Sigma_e^i\right)_{lj} = \\ &= -\delta_{im}\left(\left(F_v^i\right)^{-1}\right)_{nl}\exp\left(-\Delta t\ \left(C_v^i\right)^{-1} : \Sigma_e^i\right)_{lj} \quad \text{for every } i=1...m \end{aligned} \qquad [D.25]$$

Similarly, the derivatives of R_{F_∞} with respect to $\left(F_e^i\right)_{mn}$ and $\Delta\mu$ give

$$\frac{\partial\left(R^i_{F_e}\right)_{ij}}{\partial\left(F_e^i\right)_{mn}} = \delta_{im}\delta_{jn} - \left(F_\infty\right)_{ik}\left(\left(F_v^i\right)^{-1}\right)_{kl}\frac{\partial\left(\exp\left(-\Delta t\ \left(C_v^i\right)^{-1} : \Sigma_e^i\right)_{lj}\right)}{\partial\left(F_e^i\right)_{mn}} \qquad [D.26]$$

for every $i=1...m$

$$\frac{\partial\left(R^i_{F_e}\right)_{ij}}{\partial\Delta\mu} = 0 \quad \text{for every } i=1...m \qquad [D.27]$$

The derivative of the exponential term with respect to $\left(F_e^i\right)_{mn}$ in Eq. [D.26] is written as

$$\frac{\partial\left(\exp\left(-\Delta t\ \left(C_v^i\right)^{-1}:\Sigma_e^i\right)_{lj}\right)}{\partial\left(F_e^i\right)_{mn}}=\frac{\partial\left(\exp\left(-\Delta t\ \left(C_v^i\right)^{-1}:\Sigma_e^i\right)_{lj}\right)}{\partial\left(\Sigma_e^i\right)_{pq}}\frac{\partial\left(R_{F_e}^i\right)_{ij}}{\partial\left(F_e^i\right)_{mn}}=\delta_{im}\delta_{jn}-\left(F_\infty\right)_{ik}\left(\left(F_v^i\right)^{-1}\right)_{kl}$$

$$\text{for every } i=1...m \qquad \text{[D.28]}$$

Hence Eq. [D.26] is written as

$$\frac{\partial\left(R_{F_\infty}\right)_{ij}}{\partial\left(F_\infty\right)_{mn}}=\delta_{im}\delta_{jn}-{}_{\text{trial}}\left(F_\infty\right)_{ik}\frac{\partial\exp\left(-\Delta\mu\dfrac{\partial g(\Sigma_d,q)}{\partial\Sigma_d}\right)_{kj}}{\partial\left(-\Delta\mu\dfrac{\partial g(\Sigma_d,q)}{\partial\Sigma_d}\right)_{rs}}\frac{\partial\left(-\Delta\mu\dfrac{\partial g(\Sigma_d,q)}{\partial\Sigma_d}\right)_{rs}}{\partial\left(\Sigma_d\right)_{pq}}\left[\frac{\partial\left(\Sigma_\infty\right)_{pq}}{\partial\left(F_\infty\right)_{mn}}+\right.$$

$$\left.+\left(F_\infty^{-T}\sum_{i=1}^{m}\Sigma_{ve}^i\right)_{mq}\delta_{in}-\left(F_\infty^{-1}\right)_{qm}\left(\sum_{i=1}^{m}\Sigma_{ve}^i\right)_{in}\right] \qquad \text{for every } i=1...m \qquad \text{[D.29]}$$

(C) Computation of terms $\frac{\partial R_d}{\partial F_\infty}$, $\frac{\partial R_d}{\partial F_e}$, $\frac{\partial R_d}{\partial\Delta\mu}$

The residual equation for the equation for the damage flow surface is defined as

$$R_d={}^{t+\Delta t}\sqrt{J_2(\sigma)}-\alpha_0 I_1(\sigma)e^{-a\sqrt{\theta}}\left(e^{-\gamma\Delta\mu}\left(1-{}^{t}d_{mech}\right)\right)^a-\beta_o e^{-a\sqrt{\theta}}\left(e^{-\gamma\Delta\mu}\left(1-{}^{t}d_{mech}\right)\right)^b \qquad \text{[D.30]}$$

The derivative of R_d with respect to $\left(F_\infty\right)_{mn}$ gives

$$\frac{\partial R_d}{\partial\left(F_\infty\right)_{mn}}=\frac{\partial R_d}{\partial(\sigma)_{rs}}\frac{\partial(\sigma)_{rs}}{\partial\left(\Sigma_d\right)_{pq}}\frac{\partial\left(\Sigma_d\right)_{pq}}{\partial\left(F_\infty\right)_{mn}} \qquad \text{[D.31]}$$

Similarly, the derivatives of R_d with respect to $\left(F_e^i\right)_{mn}$ and $\Delta\mu$ give

$$\frac{\partial R_d}{\partial\left(F_e^i\right)_{mn}}=\frac{\partial R_d}{\partial(\sigma)_{rs}}\frac{\partial(\sigma)_{rs}}{\partial\left(\Sigma_d\right)_{pq}}\frac{\partial\left(\Sigma_d\right)_{pq}}{\partial\left(F_e^i\right)_{mn}} \qquad \text{for every } i=1...m \qquad \text{[D.32]}$$

$$\frac{\partial R_d}{\partial\Delta\mu}=\alpha_o I_1\gamma a e^{-a\sqrt{\theta}}\left(e^{-\gamma\Delta\mu}\left(1-{}^{t}d_{mech}\right)\right)^a+\beta_o\gamma b e^{-a\sqrt{\theta}}\left(e^{-\gamma\Delta\mu}\left(1-{}^{t}d_{mech}\right)\right)^b \qquad \text{[D.33]}$$

Summary

A well-functioning, long-lasting and safe highway infrastructure network ensures the mobility of people and facilitates the transport of goods, promoting thus environmental, economic, and social sustainability. The development of sustainable highway infrastructure requires, among other activities, the construction of pavement systems with enhanced durability. Moisture damage in asphalt pavements is associated with inferior performance, unexpected failures and reduced service life. All of these contribute to the increase of operational and maintenance costs in order to fulfill the intended service life of the pavement system. Moreover, global warming and climate change events such as temperature extremes, high mean precipitation and rainfall intensity may further increase the probability and rate of pavement deterioration.

This dissertation aims to obtain an advanced understanding of the influence of moisture on pavement durability by developing a set of tools, i.e. experimental methods and computational models, which will provide insight into the fundamental moisture damage processes and on their impact on pavement systems. Based on this knowledge, researchers and practitioners will be able not only to design pavements with increased resiliency, thereby providing reliable services to road users, but also to minimize the risks in the face of changing climate conditions.

Moisture diffusion is well-known to degrade the mechanical properties of asphalt mortars, namely bitumen, filler and sand, thus increasing the propensity of pavements to cracking. To determine the changes in the cohesion properties of the mortar, uniaxial tension tests were performed. Mortar samples were prepared and then subjected to five combinations of moisture and thermal conditioning, in an attempt to reproduce the various conditioning states that pavements undergo in the field, before being tested. Tensile strength and fracture energy were used to evaluate the changes in mechanical properties due to the various conditioning protocols. To post-process the experimental data, a new data analysis procedure was suggested in order to obtain a more accurate calculation of fracture energy. The procedure uses nonlinear finite element analysis to specify the unloading response outside the fracture zone, and then utilizes this information to compute the fracture energy of the binders. This methodology yields a framework for the calculation of fracture energy when only force-displacement data are available and therefore the estimation of the true stress-strain curve is not feasible.

The experimental investigation revealed the deteriorating impact of moisture on the fracture characteristics of asphalt mortars, especially as regards to their low temperature properties. These effects were not reversible upon drying. On the contrary, the application of a drying cycle caused embrittlement of the mortars and indicated that continuous wet and drying cycles in the field may result in materials with poor performance characteristics. Also, the application of freeze-thaw cycles was shown to increase the susceptibility of mortars to low temperature cracking. Nevertheless, on the whole, the effect of freeze-thaw on fracture properties was observed to depend on the conditioning state (dry or wet) and composition of the mortars. The use of additives, such as hydrated lime filler and SBS modifiers, were found to improve the wet strength and fracture energy of the mortars. On the basis of moisture uptake measurements, it was confirmed that the chemical composition influences significantly the diffusivity characteristics of the mortars. Also, the

maximum moisture uptake was found to be the main parameter that dictates the intensity of mortar damage.

In addition, moisture susceptibility was studied at mixture level. At this level, besides moisture diffusion, excess pore pressure can contribute to the degradation of mixture performance depending on the mixture type, the traffic loading and the environmental conditions. Hence, a moisture conditioning protocol that comprises two conditioning types, namely bath immersion and pore pressure application, was proposed for evaluating susceptibility of asphalt mixtures to moisture. Also, evidence was collected of the effect that dynamic pore pressure has on mixture degradation by means of X-ray computed tomography and image analysis techniques. The two damage mechanisms were found to be relatively independent from each other, suggesting that an asphalt mixture can be more prone to one damage mode than the other, depending on its composition. The proposed protocol captures both processes that occur when water interacts with a pavement and can provide more reliable conclusions with regard to mixture sensitivity.

In order to improve our perception of the influence of material microstructures on moisture sensitivity of the asphalt composite, an energy-based elasto-visco-plastic model with softening was implemented to model damage due to the coupled effects of moisture diffusion and mechanical loading. The model consists of a generalized Maxwell model, with hyperelastic springs and viscous time-dependent components, in series with an inelastic component that accounts for the irreversible processes within the microstructure of the material. Then, a computational scheme was proposed by means of a staggered approach: first a three-dimensional diffusion model was applied to obtain information on the accumulation of moisture within the mixtures and then the elasto-visco-plastic model was used to quantify mortar damage due to moisture diffusion. This method was successfully applied to study the influence of mixture morphology on moisture sensitivity. The results demonstrated that moisture content in a mixture strongly depends on its morphology, whereas the interconnectivity of the voids network controls the rate of damage development. Also, the analysis revealed the positive effect of using binders with high resistivity against moisture and quantified the benefits that would arise due to this choice, especially when designing porous mixtures that have an intrinsic sensitivity to moisture due to their morphological characteristics.

More broadly, frost damage can be classified as part of the moisture damage related mechanisms. In the field, frost damage can be mainly attributed to the expansion of water accumulated in the pores of the pavement at sub-zero temperatures that causes additional stresses to the pavement structure. A numerical scheme to simulate frost damage was proposed. This scheme comprises a model that simulates the volume expansion of water during the water-to-ice phase-change, a thermal conduction model to simulate temperature distribution in the pavement, and the elasto-visco-plastic model to determine critical areas with a propensity to cracking on the basis of the pavement stresses.

In conclusion, this thesis contributes to establishing a relationship of the physico-mechanical properties of the constituent materials and mixture morphology with the moisture susceptibility of pavement structures. The proposed experimental methods and computational models can serve as tools to investigate a great variety of parameters before a pavement structure is actually built. This allows for new materials and mixture designs to be investigated and the risks involved with their use to be minimized.

Samenvatting

Een goed functionerend, duurzaam en veilig wegeninfrastructuur netwerk zorgt voor de mobiliteit van mensen en faciliteert het vervoer van goederen, bevorderen aldus milieutechnische, economische en sociale duurzaamheid. De ontwikkeling van duurzame snelweg infrastructuur, vereist onder andere de aanleg van wegverhardingen met een langere levensduur. Vochtschade in asfaltverhardingen wordt geassocieerd met inferieure prestaties, onverwachte schade en een verminderde levensduur. Al deze effecten dragen bij aan de verhoging van de beheer- en onderhoudskosten nodig om de beoogde levensduur van de verharding te realiseren. Bovendien kunnen opwarming van de aarde en extreme weersomstandigheden zoals extreme temperaturen, een hoge gemiddelde neerslag en neerslag intensiteit, verder de kans op en snelheid van materiaal achteruitgang verder verhogen.

Dit proefschrift streeft er naar een diepgaand begrip van de invloed van vocht op de duurzaamheid van wegconstructies te verkrijgen door het ontwikkelen van een set van gereedschappen, dat wil zeggen experimentele methoden en numerieke modellen, die inzicht geven in de fundamentele vochtschade processen en hun impact op wegconstructies. Op basis van deze kennis zullen onderzoekers en wegenbouwers wegconstructies kunnen ontwerpen met verhoogde weerstand tegen vochtschade, teneinde betrouwbare diensten aan de weggebruikers te bieden en de risico's van klimaatverandering voor wegconstructies te minimaliseren.

Het is bekend dat vochtdiffusie de mechanische eigenschappen van asfaltmortels verslechterd, waardoor het wegdek gevoeliger wordt voor scheurvorming. Om de veranderingen in de cohesie-eigenschappen van de mortels te bepalen, zijn uniaxiale trekproeven uitgevoerd. Proefstukken van mortel (een mengsel van bitumen, vulstof en zand) werden bereid en vervolgens onderworpen aan vijf combinaties van vocht- en thermische conditionering, in een poging verschillende van de condities die mortels in de praktijk ondergaan, te reproduceren voordat wordt ze worden getest. De treksterkte en breukenergie zijn gebruikt om de veranderingen in mechanische eigenschappen ten gevolge van de verschillende conditioneringsprotocollen te beoordelen. Voor het verwerken van de experimentele gegevens is een nieuw data-analyse procedure ontwikkeld om een nauwkeurigere berekening van de breukenergie te verkrijgen. De procedure maakt gebruik van een niet-lineaire eindige elementenanalyse om het ontlasten van de proefstukdelen buiten de scheurzone te bepalen, en gebruikt deze informatie om de breukenergie van de mortels te berekenen. Deze methode maakt het mogelijk de breukenergie te berekenen in het geval dat alleen kracht-verplaatsingsgegevens beschikbaar zijn en dus de benadering van de werkelijke spanningsrekcurve niet mogelijk is.

Het experimentele onderzoek toonde aan dat vocht een negatieve invloed heeft op de breukeigenschappen van mortel, met name wat betreft hun lage temperatuur eigenschappen. Deze effecten waren niet omkeerbaar na drogen. Integendeel, de toepassing van een droogcyclus veroorzaakte verbrossing van de mortels, wat er op wijst dat aanhoudende afwisseling van natte en droge cycli kan leiden tot materialen met slechte prestaties. Ook werd aangetoond dat vorst-dooicycli de gevoeligheid van mortel voor lage temperatuur scheurvorming verhogen. Niettemin is over het algemeen het effect van vorst-dooi cycli op de breukeigenschappen afhankelijk van de conditioneringstoestand (droog of nat) en de samenstelling van de bindmiddelen. Het gebruik van

additieven, zoals vulstof met calcium hydroxide en SBS modificaties in bitumen, bleken de natte sterkte en de breukenergie van de mortel te verbeteren. Op basis van vochtopnamemetingen werd bevestigd dat de chemische samenstelling een significante invloed heeft op de diffusieparameters van de mortel. Ook bleek de maximale vochtopname de voornaamste parameter te zijn die de intensiteit van mortel schade bepaald.

Aanvullend werd de vochtgevoeligheid op asfaltmengsel niveau bestudeerd. Op dit niveau kan , naast vochtdiffusie, ook wateroverspanning bijdragen aan de afname van de asfaltprestaties, afhankelijk van het mengsel, de verkeersbelasting en omgevingsfactoren. Vandaar dat een vochtconditioneringsprotocol dat twee vormen van conditionering omvat, namelijk onderdompeling in een waterbad en het aanbrengen van een wisselende waterspanning, is gebruikt voor het evalueren van de gevoeligheid van asfaltmengsels voor vocht. Ook werd bewijs verzameld van het effect dat de wisselende waterspanning heeft op de degradatie van asfalt door middel van X-ray computertomografie en beeldanalyse technieken. De twee schademechanismen bleken relatief onafhankelijk van elkaar te zijn, wat suggereert dat een asfaltmengsel gevoeliger kan zijn voor schade in de ene of de andere modus, afhankelijk van de mengselsamenstelling. Het ontwikkelde protocol simuleert beide processen die plaatsvinden wanneer water interacteert met een asfaltmengsel en kan daardoor tot meer betrouwbare conclusies leiden met betrekking tot de vochtgevoeligheid van asfalt in de praktijk.

Om de kennis van de wijze waarop de microstructuur van een asfaltmengsel de gevoeligheid van het mengsel voor vochtschade beïnvloed te vergroten, is een elasto-visco-plastisch schademodel op energiebasis geïmplementeerd om de schade als gevolg van de gekoppelde effecten van vochtdiffusie en mechanische belasting te modelleren. Het model bestaat uit een gegeneraliseerd Maxwell-model met hyper-elastische veren en viskeuze tijdsafhankelijke componenten, in serie met een onelastische component die de onomkeerbare processen binnen de microstructuur van het materiaal beschrijft. Vervolgens werd een methode door middel van een getrapte aanpak ontwikkeld: eerst wordt een driedimensionaal diffusiemodel toegepast om informatie te verkrijgen over de ontwikkeling van het vochtgehalte in het asfalt en vervolgens wordt het elasto-visco-plastisch schademodel gebruikt om de mortel degradatie door vochtdiffusie te kwantificeren. Deze methode is succesvol toegepast voor het bestuderen van de invloed van mengselmorfologie op vochtgevoeligheid. De resultaten toonden aan dat het vochtgehalte in een mengsel sterk afhankelijk is van de morfologie, terwijl de interconnectiviteit van de holle ruimte bepalend is voor de snelheid van de schadeontwikkeling. Ook bleek uit de analyse het positieve effect van het gebruik van mastiek met een hoge weerstand tegen vocht en werden de voordelen van deze keuze gekwantificeerd, met name bij het ontwerpen open mengsels die een intrinsieke gevoeligheid voor vocht hebben als gevolg van hun morfologische kenmerken.

Meer in het algemeen, kan vorstschade worden aangemerkt als onderdeel van de vochtgerelateerde schademechanismen. In de weg wordt vorstschade vooral veroorzaakt door water dat zich ophoopt in de poriën van het wegdek en uitzet bij temperaturen onder nul, die uitzetting veroorzaakt extra spanningen in de wegverharding. Een numerieke methode om vorstschade te simuleren is ontwikkeld. Deze methode omvat een model dat de volumevergroting water simuleert in de water-ijs faseovergang, een warmtegeleidingsmodel om de temperatuurverdeling in het wegdek te simuleren en het elasto-visco-plastisch schademodel om

kritieke gebieden in de mastiek met een risico op scheurvorming te bepalen op basis van de spanningen in de verharding.

Tot slot, dit proefschrift draagt bij aan het ontwikkelen van een verband tussen de fysisch-mechanische eigenschappen van de bouwstoffen en mengselmorfologie aan de ene en de vochtgevoeligheid van asfaltverhardingen aan de andere kant. De voorgestelde experimentele methoden en computermodellen kunnen dienen als hulpmiddelen voor onderzoek aan een groot aantal parameters voor een wegverharding daadwerkelijk wordt gebouwd. Dit maakt het mogelijk nieuwe materialen en mengselontwerpen te onderzoeken en de risico's van het gebruik ervan te minimaliseren.

Curriculum vitae

Aikaterini (Katerina) Varveri

25 May 1983	Born in Kavala, Greece
Sept. 2002 - Sept. 2007	MEng in Environmental Engineering Democritus University of Thrace, Greece
Jan. 2007 - Jul. 2008	Laboratory researcher Democritus University of Thrace, Greece Faculty of Environmental Engineering
Sept. 2007- Sept. 2008	MSc in Hydraulics Engineering Democritus University of Thrace, Greece Faculty of Civil Engineering
Oct. 2008 - Oct. 2009	MSc in Environmental Protection & Sustainable Development Aristotle University of Thessaloniki, Greece Faculty of Civil Engineering
Nov.2008 - Nov. 2010	Environmental-Hydraulics Engineer Varveri, Independent engineering firm, Thessaloniki, Greece
Dec. 2010 – Dec. 2016	PhD candidate Delft University of Technology, the Netherlands Section of Pavement Engineering
Jan. 2015 – present	Post-doctoral research fellow Delft University of Technology, the Netherlands Section of Pavement Engineering

List of publications

Journal publications

Varveri, A., Avgerinopoulos, S., Kasbergen, C., Scarpas, A. & Collop (2015). Influence of air void content on moisture damage susceptibility of asphalt mixtures: Computational study. Journal of Transportation Research Board, Transportation Research Record, 2446:3, 8-16.

Varveri, A., Avgerinopoulos, S. & Scarpas, A. (2016). Experimental evaluation of long- and short-term moisture damage characteristics of asphalt mixtures. Road Materials and Pavement Design 17:1, 168-186.

Anupam, K., Srirangam, S.K., Varveri, A., Kasbergen, C. & Scarpas, A. (2016). Microstructural analysis of porous asphalt concrete mix subjected to rolling truck tire loads. Journal of Transportation Research Board, Transportation Research Record, 2575, 113-122.

Refereed conference proceedings (selected)

Varveri, A., Avgerinopoulos, S. & Scarpas, A. (2016). Durability of European asphalt mixtures containing reclaimed asphalt and warm-mix additives. 95th Transportation Research Board Annual Meeting Compendium of Papers, Washington, D.C., Paper no. 16-0624.

Varveri, A., Avgerinopoulos, S., Kasbergen, C., Scarpas, A. & Collop, A. (2014). A constitutive model for simulation of water to ice phase change in asphalt mixtures. In Y.R. Kim (Ed.), Proceedings of the 12th International conference on Asphalt Pavements (ISAP), 531-539.

Nicholls, C., Wayman, M., Mollenhauer, K., McNally, C., Tabaković, A., Gibney, A., Varveri, A., Cassidy, S., Shahmohammadi, R. & Gilbert, K. (2014). Effect of using of reclaimed asphalt and/or lower temperature asphalt on the availability of the road network. Proceedings of the Transport Research Arena (TRA), 1-10.

Pauli, A., Schmets, A.J.M., Kasbergen, C., Varveri, A. & Scarpas, A. (2013). Microstructural Self-healing of bituminous materials: combined experimental and numerical study. Proceedings of the 4th International Conference on Self-Healing Materials, Ghent, Belgium.

Srirangam, S.K., Varveri, A. Scarpas, A., Kasbergen, C. & Kane, M. (2012). Micromechanical analysis of the effect of asphalt mix characteristics on rubber friction. Proceedings of the 7th Symposium on Pavement Surface Characteristics (SURF), Virginia, USA.

Srirangam, S.K., Varveri, A., Scarpas, A. Kasbergen, C. & Anupam, K. (2012). Numerical investigation of the effect of hydroplaning on braking and directional stability of passenger car tires. ECCOMAS-2012 conference, Vienna, Austria.

Other publications

Varveri, A., Zhu, J. & Kringos, N. (2015). Moisture Damage in Asphaltic Mixtures in Huang and Di Benedetto (Eds.), Advances in Asphalt Materials: Road and Pavement Construction. Woodhead Publishing, ISBN: 9780081002698.